# Reservoir Characterization of the Realgrunnen Subgroup in Wisting Central III (7425/8-3), SW Barents Sea

*Controls on Reservoir Quality in the Triassic-Jurassic Transition*

**Kara Hua Meunier**


Master Thesis in Geosciences
Petroleum Geology and Petroleum Geophysics
30 credits

Department of Geosciences
Faculty of Mathematics and Natural Sciences
UNIVERSITY OF OSLO

01.06.2019

# Reservoir Characterization of the Realgrunnen Subgroup in Wisting Central III (7324/8-3), SW Barents Sea

*Controls on Reservoir Quality in the Triassic-Jurassic Transition*

**Kara Hua Meunier**


Master Thesis in Geosciences
Petroleum Geology and Petroleum Geophysics
30 credits

Department of Geosciences
Faculty of Mathematics and Natural Sciences
UNIVERSITY OF OSLO

01.06.2019

Reservoir Characterization of the Realgrunnen Subgroup in Wisting Central III (7324/8-3), SW Barents Sea

Kara Hua Meunier

Supervisors: Prof. Jens Jahren and PhD Lina Hedvig Line

This work is published digitally through DUO – Digitale Utgivelser ved UiO
http://www.duo.uio.no/

It is also catalogued in BIBSYS (http://www.bibsys.no/english)

Print: Reprosentralen, Universitetet i Oslo

# Acknowledgements

Completing this study has been a challenging and educational process. I am so grateful to have had the opportunity to attain this experience – it has not only contributed in developing my skills as a geologist, but has also played a role in developing my character as a person. I wish to extend my sincerest gratitude to my supervisors, Professor Jens Jahren, and co-supervisor Lina Hedvig Line for their support, guidance, and encouragement throughout the progression of this thesis.

I would like to thank OMV Norge AS, particularly Eirik Stueland, for permission to log and collect samples of the core, enabling me to heighten my knowledge of the sandstones found in Wisting Central III. I really appreciated to opportunity to present at the OMV offices.

I would also like to express my gratitude to Salahalladin Akhavan, Kristian Backer-Owe, Thanusha Naidoo, and Siri Simonsen for their support and technical assistance in development of this thesis.

I am also very grateful to Stina Rosseland Skretting, whom I conducted this study alongside. I enjoyed comparing my results with yours and presenting with you both in Spain and at OMV. Your calm and collected nature is really something I can learn from. Vilde Bjørnebye was also kind in assisting me with interpreting the transgressive lag in Wisting Central III. It was also nice to have those in room 217 to empathize with. Thank you.

Finally, I would like to thank my boyfriend, Torgeir Rimstad. Thank you for being my rock through thick and thin in the duration of this degree. Thank you for your unwavering support and encouragement. And thank you for always believing in me more than I believe in myself. I love you.

2019

Kara Hua Meunier

# Abstract

Although the Triassic-Jurassic sandstones of the Realgrunnen Subgroup form the primary reservoir units in the Barents Sea, there are relatively few published studies targeting these formations in the central and northern parts of the southwestern Barents Sea. This thesis documents reservoir properties in the sandstones of the Wisting Central III (7324/8-3) drill core, thereby aiming to academically contribute to the understanding of the geological development in this area. Additionally, lateral variations in the vicinity of the Wisting field are studied, particularly with respect to the Gemini North (7325/4-1) wellbore.

Wisting Central III is the 6th and most recent appraisal well of the Wisting discovery, located in the Hoop Fault Complex in the southwestern Barents Sea. In Wisting Central III, the Realgrunnen Subgroup comprises Triassic-Jurassic deposits of the Fruholmen, Nordmela and Stø formations. The aim of this thesis is to describe reservoir properties and gain insights on factors influencing the reservoir quality of these formations, such as climate, provenance, depositional environment and diagenesis. This is achieved by employing sedimentological, petrographical, and petrophysical methods with use of the Wisting Central III drill core.

Based on observations from the drill core, facies associations of the Realgrunnen Subgroup are described and interpreted to record a range of shallow marine to coastal depositional environments. The Fruholmen Formation is interpreted to represent the overall progradation of a delta system, with a low-order transgression at the top. The Nordmela Formation is interpreted to record the migration of a tidal dune complex, while the Stø Formation is interpreted to comprise upper shoreface deposits.

Petrographic results show that there are stark changes across the Triassic-Jurassic transition. This is strongly reflected in XRD results, which show that the Triassic Fruholmen Formation has a high mineralogical diversity as opposed to the mineralogically mature Jurassic Nordmela and Stø formations. Point counting yields similar results. The Fruholmen Formation is significantly more immature than the Jurassic Stø and Nordmela Formations, with moderate proportions of lithic rock fragments and feldspars. These constituents are virtually absent in the Jurassic formations. Textural maturity is also found to increase across the boundary.

Differences across the T-J boundary are concluded to relate to a change in provenance, from the primarily Uralian-sourced Fruholmen Formation to the primarily Caledonian/Fennoscandian-sourced Nordmela and Stø formations. A change in provenance area is likely accompanied by forebulge uplift in the area, creating a regime of reduced accommodation, promoting extensive reworking. These events changed the initial sandstone composition towards higher maturity. The first-generation Uralian sourced Fruholmen Formation deposits are heavily affected by diagenetic reactions such as kaolinitization and chloritization. Sandstones of the highly reworked Caledonian/Fennoscandian sourced Stø and Nordmela Formations are almost entirely absent of such diagenetic reactions, having exclusively evidence of quartz cementation. Results from this study demonstrate the fundamental importance of sediment provenance, accommodation, depositional environment, and burial diagenesis in determining reservoir quality seen today.

# Table of Contents

# Chapter 1: Introduction

## 1.1 Background

The Barents Sea is a marginal sea of the Arctic Ocean, located off the northern coasts of Norway and Russia (Figure 1.1). Comprising an area of about 1.3 million km$^2$, it constitutes one of the largest continental shelves on Earth at present, having an average water depth of only 300 m (Doré, 1995). Motivated by the success of the North Sea in the 1960's, oil and gas exploration in the Barents Sea was initiated in 1969, consisting of the acquisition of seismic reflection surveys and exploration wells – the first of which was drilled in 1980 (Doré, 1995). At present, Snøhvit and Goliat are the only producing fields in the Norwegian Barents Sea. A third, Johan Castberg, has been scheduled to start production in 2022 (NPD, 2019). To this day, the extreme geographic setting has presented challenges to the operators that wish to explore in the Barents Sea.

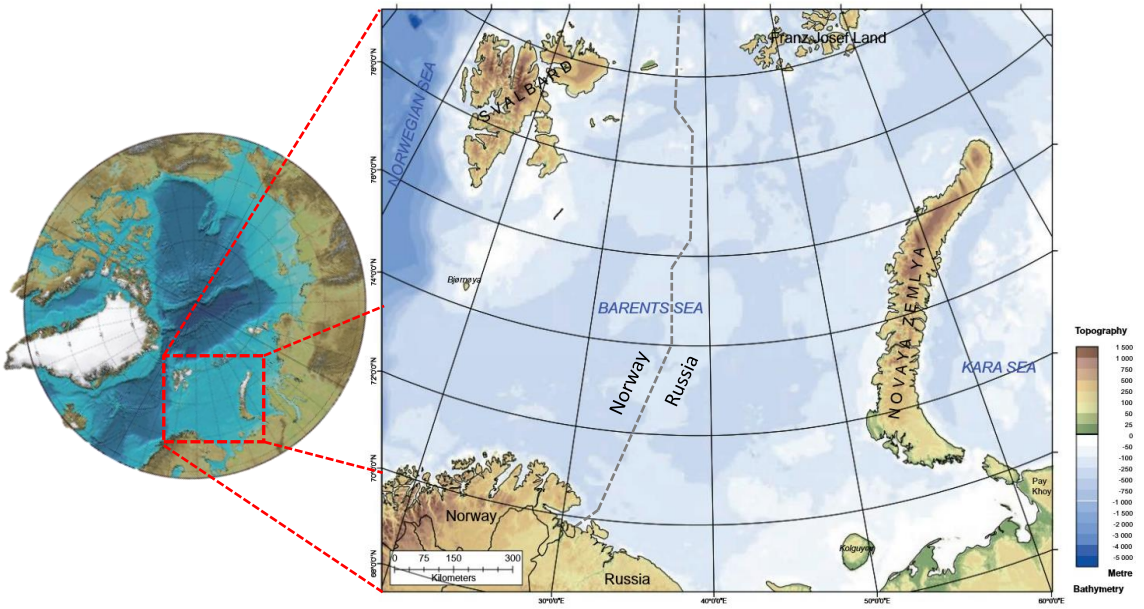


**Figure 1.1:** Left – the location of the Barents Sea in relation to geographical elements as shown in the International Bathymetric Chart of the Arctic Ocean, modified after Jakobsson (2012). Right – close-up of the Barents Sea, marked with the political maritime boundary between Norway and Russia and coloured with respect to topography and bathymetry; modified after Smelror et al. (2009).

Today, the southern portion of the Norwegian part of the Barents Sea is open for petroleum activities; this area totals approximately 245,000 km$^2$ (Ohm et al, 2008). Interest in the area has increased in recent years, and in the years since 2015, the Norwegian Petroleum Directorate has estimated that over 60 percent of undiscovered resources on the NCS are situated in the Barents Sea (NPD, 2019). The most recent estimate from 2017 is shown in figure 1.2. Triassic and Jurassic sandstones serve as primary reservoirs, which are located at shallow depths due to significant Cenozoic uplift.

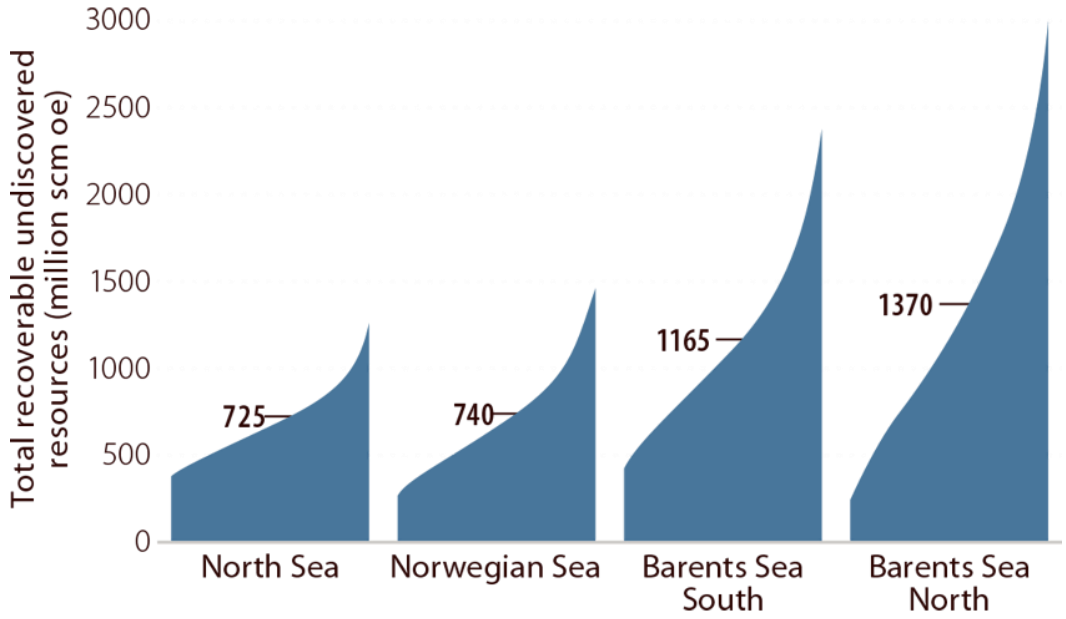


**Figure 1.2:** Undiscovered resources by area on the NCS; numbers shown are the expected values. Estimates were made 31 December 2017, and are taken from NPD (2019). The figure demonstrates that more than 60 percent of undiscovered resources are expected to lie in the Barents Sea, with the remainder divided approximately equally between the North and Norwegian Seas.

# 1.2 Motivation and Objective

Wisting Central III (7324/8-3) is the 6th and most recent appraisal well of the Wisting discovery, located in the Hoop Fault Complex of the SW Barents Sea (OMV, 2019a). To date, the Wisting discoveries are estimated to contain more than 1 billion barrels of oil in place, and an estimated range of 300 – 500 million barrels of recoverable resources (OMV, 2019a).

Although the Triassic-Jurassic sandstones of the Realgrunnen Subgroup form the main reservoir units in the Barents Sea, there are relatively few published studies targeting these formations in the central and northern parts of the southwestern Barents Sea. The primary objective of this study is to describe the properties of the reservoir sandstones of the Realgrunnen Subgroup, comprising the Fruholmen, Nordmela, and Stø Formations, within the Wisting Central III drill core – thereby aiming to academically contribute to the understanding of the geologic development in the area. In order to characterize reservoir sandstones, sedimentological, petrographical, and petrophysical analyses are employed.

Porosity and permeability are of primary importance because they control the potential capacity to store hydrocarbons and the capability of the rock to transmit them. Initial reservoir properties are governed by a number of parameters, foremost of which are the provenance, depositional environment, and climate. In turn, these factors determine the mineralogical composition, sorting, shape, and grain size which consequently influence the diagenetic processes that occur both near surface and with increased burial. All aforementioned parameters impact the porosity and permeability and therefore reservoir quality seen today, and as such are of interest in this study. Results will be compared with information from similar studies, particularly from Gemini North (7325/4-1), to observe lateral and temporal variations.

# 1.3 Study Area

The Wisting discovery is located in the Hoop Fault Complex of the southwestern Barents Sea, situated in the PL537 exploration license (OMV, 2019a). It lies approximately 310 kilometers off mainland Norway. Primary structural elements in the Barents Sea are shown in figure 1.3. The zoom-in at the top left corner of figure 1.3 displays the structural elements found in and around the study area, as well as the location of Wisting Central III. The Wisting Central exploration well (7324/8-1), drilled in 2013, marked the first encounter with oil in the Hoop-Maud Basin in the Barents Sea (OMV, 2019b). Since then, 6 appraisal wells have been drilled, the most recent being Wisting Central III, the object of this study (OMV, 2019a). Wisting Central III was drilled 315 kilometers north of the Norwegian city of Hammerfest in mid-August 2017 by Island Innovator (NPD, 2019). The well encountered an oil column of about 55 meters in sandstones of Late Triassic to Middle Jurassic age (the Fruholmen, Nordmela, and Stø formations) (NPD, 2019).

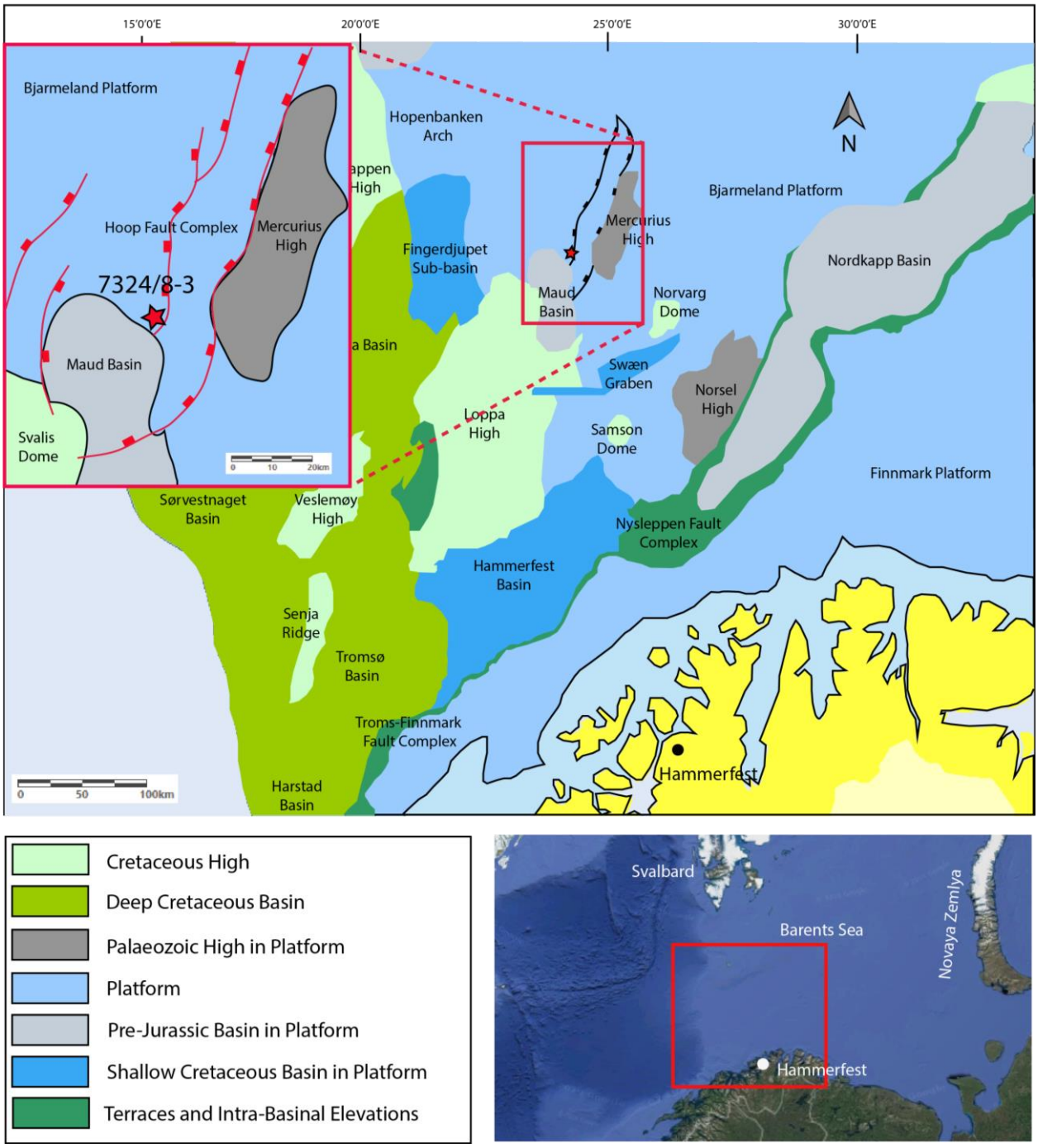


**Figure 1.3:** Primary structural elements in the southwest Barents Sea, labelled in accordance with Gabrielsen et al. (1990). Colour key is adapted from NPD (2019). Pictured area comprises the red boxed area in the satellite image in the lower right corner. Upper left hand corner displays a zoom-in of the study area, with a red star marking Wisting Central III (7324/8-3). Satellite image is modified from Google Earth (2019).

# 1.4 Data and Methods

The data implemented in this study comes from the drill core and petrophysical logs from Wisting Central III. Access to this data is provided by OMV Norge AS. To determine reservoir quality, the core will be sedimentologically logged and subsequently sampled to conduct petrographical studies; these include bulk XRD, thin section analysis, cathode luminescence (CL), and scanning electron microscopy (SEM). Furthermore, petrophysical logs will be employed to estimate the maximum burial depth and temperature. The results from these sedimentological, petrographical, and petrophysical analyses with be used in concert to discuss provenance, depositional environments, climate, and diagenesis – all of which determine the reservoir properties and potential of the Fruholmen, Nordmela, and Stø formations in Wisting Central III.

# Chapter 2: Geological Background

## 2.1 Introduction

At present, the Barents Shelf is subdivided into numerous basins, platforms, and highs (see Figure 1.3) (Gabrielsen et al., 1990). The eastern portion of the Barents Shelf is dominated by two large basins (the Northern and Southern Barents Basins), located to the west of Novaya Zemlya (Worsley, 2008). To the western part of the Barents Sea, a significant change in structural style occurs, with the area dominated by relatively narrow northeast-southwest trending extensional basins generated by intermittent rifting episodes (Gernigon et al., 2014). These areas are separated by a suture thought to originate from the Caledonian orogeny (Henriksen et al., 2011b). The Hoop Fault Complex is located in the southwestern portion of the Barents Sea (see figure 1.3). As such, focus is given to this area of the Barents Sea in this chapter.

The present day geological complexity is accounted for by plate tectonics and changes in depositional and climatic conditions over hundreds of millions of years (Smelror, 2009). Smelror et al. (2009) and Worsley (2008) provide reviews of the evolution and regional geology of the Barents Sea. In addition, detailed studies focusing on the development of the Barents Sea have been conducted by a number of authors (e.g. Faleide et al., 2015; Gabrielsen et al., 1990; Henriksen et al., 2011b). This chapter aims firstly to give a brief outline of the tectonostratigraphic development of the western Barents Sea based on previously listed references, and secondly to hone in on the Triassic-Jurassic stratigraphic framework and the Hoop Fault Complex area. Uplift ramifications on the petroleum system are additionally addressed.

# 2.2 Tectonostratigraphic Development

A description of the main tectonostratigraphic proceedings taking place from the Caledonian orogeny to the present is reviewed with respect to geological time periods in chronological order. The left-hand side of figure 2.1 offers a summary of the main tectonic events affecting the western Barents Sea, which are related to the geographical and structural trends shown on the right-hand side.

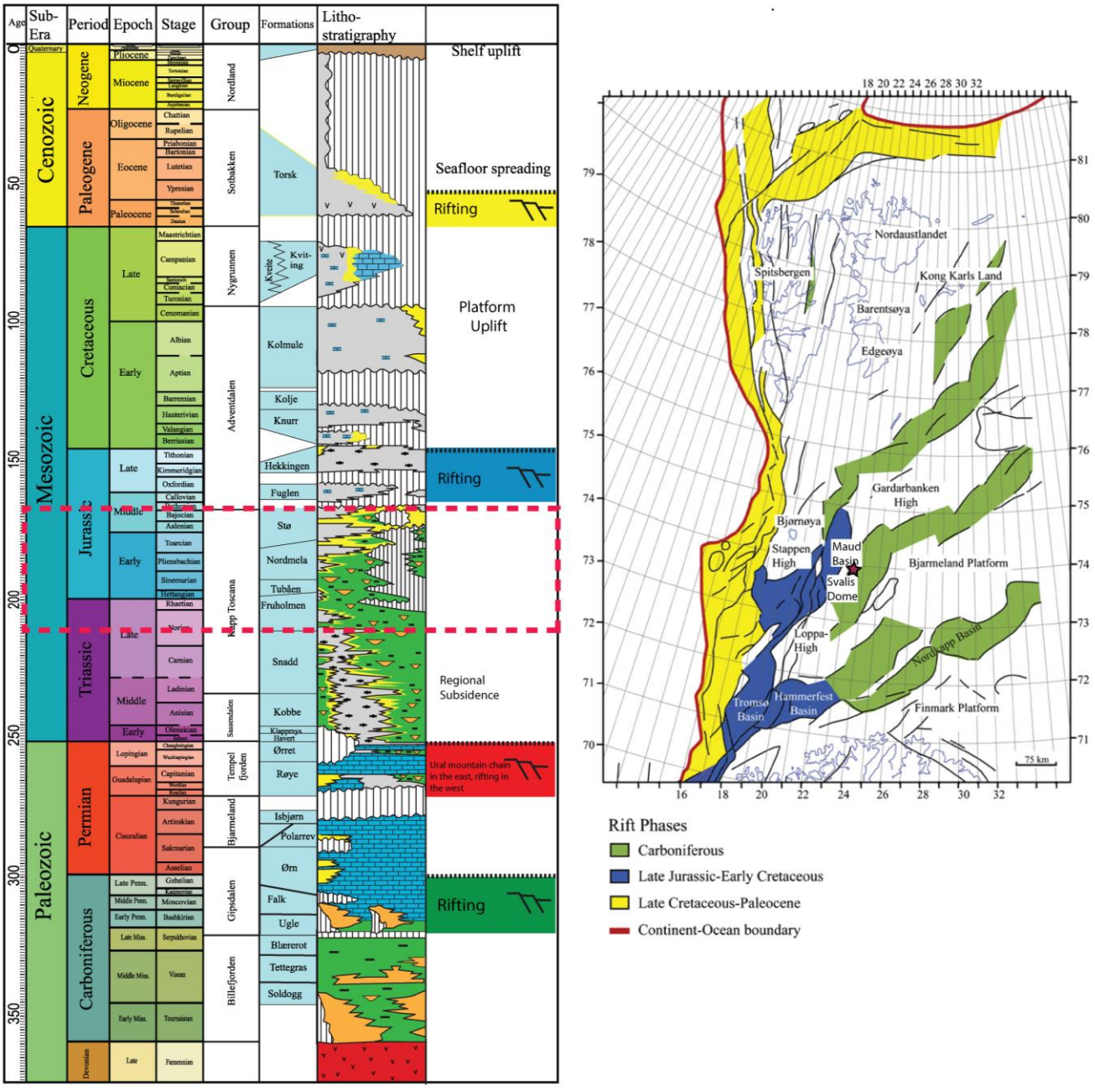


**Figure 2.1:** (Left) Tectonostratigraphic chart showing the lithostratigraphy in the western Barents Sea. Time period of interest is boxed in red. (Right) Main structural elements in the Barents Sea, colour coded to reflect the focus of tectonic activity. Star denotes approximate location of Wisting Central III.

(Right) is modified from Glørstad-Clark et al. (2010). Glørstad-Clark et al. (2010) modified the stratigraphy from Nøttvedt et al. (1993) and Larssen et al. (2002) and used formation names from Mørk et al. (1999)

(Left) is modified from Glørstad-Clark et al. (2010), which is modified after Gabrielsen et al. (1990) and Faleide et al. (2008).

## 2.2.1 Paleozoic

*Ordovician-Devonian*

The Caledonian orogeny began during the Middle Ordovician and had culminated by the Early Devonian (Gernigon et al., 2014). This major mountain building event resulted in the closure of the Iapetus Ocean and the merging of Laurentia (Greenland, North America) and Baltica (Scandinavia, western Russia), creating the Laurasian continent (Smelror et al., 2009). Much of the basement rocks on mainland Norway are metamorphic rocks generated during the Caledonian orogeny. It is likely that these rocks extend offshore into the Barents Sea, and are seen to reappear on Svalbard (Breivik, 1998). The basement of the Barents Sea is largely dominated by Caledonian trends, seen in the NE-SW structural grain of the southwestern Barents Sea (Doré, 1995).

In the Early Devonian, following the Caledonian orogeny, the rapidly exhumated hinterland was extensively eroded. This resulted in the deposition of continental siliciclastic sediments into intracratonic and foreland basins (Smelror et al., 2009). This denudation was concurrent with a change from a compressional system to a left-lateral shear regime (Faleide et al., 1984). These subsequent tectonic events exploited the areas of weakened crust generated by the Caledonian orogeny (Smelror et al., 2009). Transpression and transtension by the end of Devonian time led to the development of fault-bounded basins as seen on Svalbard (Faleide et al., 1984; Nøttvedt et al. 1993). Continental siliciclastic sediments are preserved in these grabens (Smelror et al., 2009). A paleogeographic reconstruction of the Late Devonian is presented in figure 2.1. By the end of the Devonian, the western Barents Sea was dominated by land areas with structures orientated NE-SW (Smelror et al., 2009).

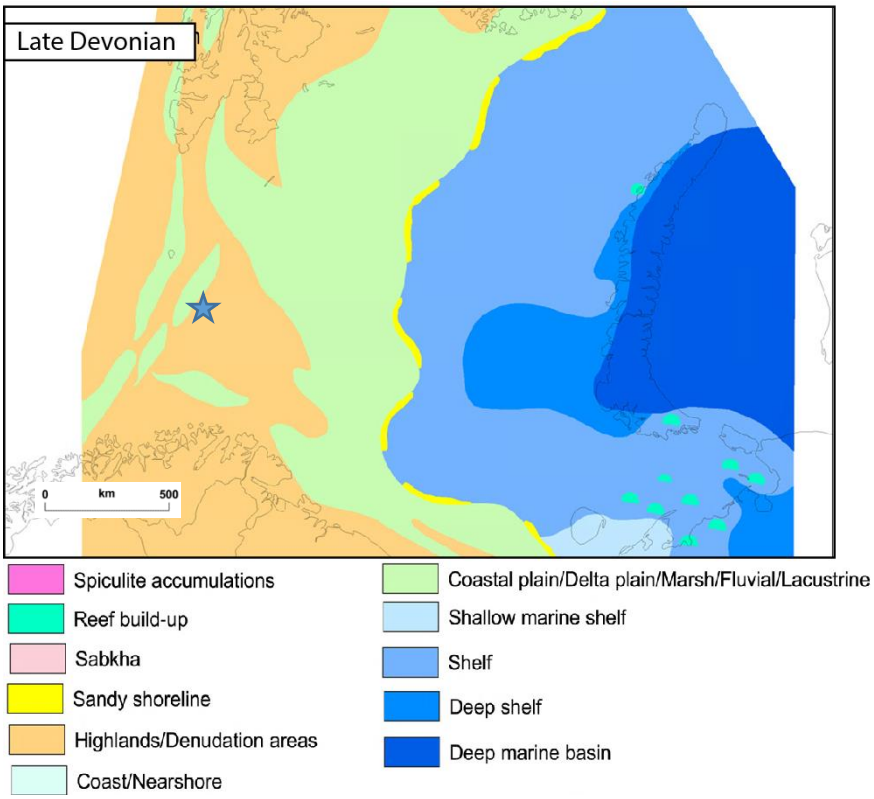


**Figure 2.1:**

Palaeogeographic reconstruction of Late Devonian (Frasnian) times, demonstrating extensive continental siliciclastic deposition to the west and a marine shelf and deeper marine conditions in the east. Modified after Henriksen et al. (2011b).

Stars in paleogeographic maps in this chapter denote the approximate position of Wisting Central III.

## *Carboniferous*

The Barents Sea and Svalbard underwent further rifting during Carboniferous times, following commencement in the Devonian (Worsley, 2008). The rifts formed a fan-shaped array of half grabens, and continued to be influenced by zones of weakness in the basement corresponding to the Caledonian orogeny, producing NE-SW trending geometries (Henriksen et al., 2011b). Gudlaugsson et al. (1998) inferred a major rift pulse in the Middle Carboniferous in the southwest Barents Sea. This likely initiated the formation of several sedimentary basins, including the Tromsø, Bjørnøya, Nordkapp, Fingerdjupet and Maud Basins (Gudlaugsson et al., 1998). Lower Carboniferous deposits comprise continental siliciclastic strata to the west, which is replaced by marine carbonates in the east (Henriksen et al., 2011b). Tropical humid climatic conditions prevailed during the Lower Carboniferous (Henriksen et al., 2011b). Denudation of the post-Caledonian highlands continued during this time, with coal-bearing alluvial strata accumulating in half grabens (Ehrenberg et al., 1998). In the Late Carboniferous, the climate shifted from tropical humid to subtropically arid (Smelror et al., 2009). This was accompanied by a shift to regional subsidence and higher sea levels, with the development of a regional sag basin covering the entire Barents Shelf (Gudlaugsson et al., 1998; Smelror et al., 2009). This enabled an expansion of the carbonate shelf, evaporite deposition in deep marine environments, as well as sabkhas and salinas (Smelror et al., 2009). Henriksen et al. (2011b) relates this shift in subsidence to the closure of the Uralian Ocean along the eastern margin of Baltica.

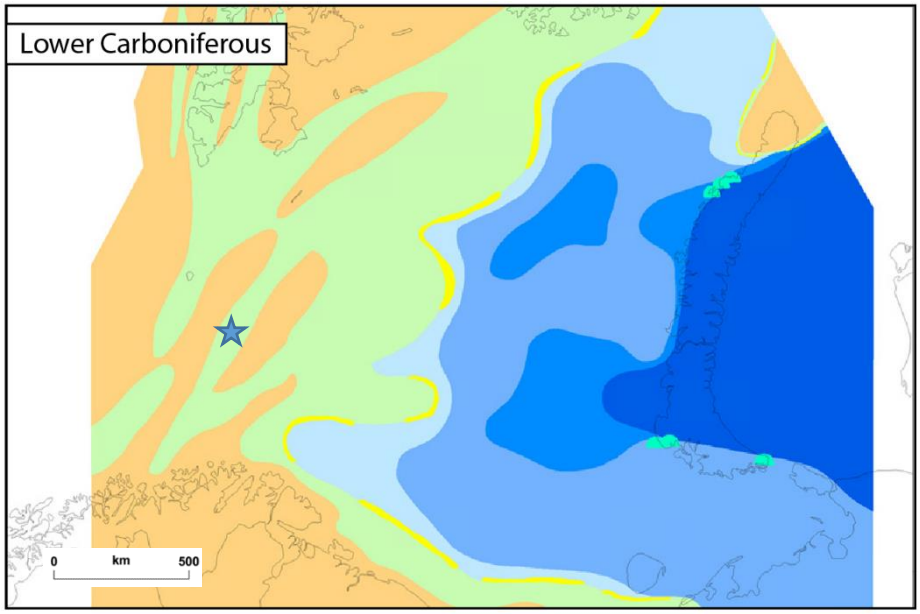


**Figure 2.2:**

Legend found in figure 2.1.

Lower Carboniferous (Visean) paleogeographic reconstruction of the SW Barents Sea, showing a continued continental regime in the west and a broad marine carbonate shelf in the east. Modified after Henriksen et al. (2011b).

*Permian*

By Permian times, the climate continued to dry in the Barents Sea (Smelror et al., 2009). The continental post-Caledonian landscape in the western part of the Barents Shelf was transgressed, and warm water carbonate shelf conditions dominated (Henriksen et al., 2011b). Widespread evaporite deposition also occurred both in deep basins and in shallower salinas and sabkhas (Stemmerik and Worsley, 2005). The deposition of carbonates occurred in an 'ice-house' world, with high frequency and amplitude eustatic sea level changes due to glaciations on Gondwana (figure 2.3)(Henriksen et al., 2011b; Smelror et al., 2009). At highstands, thick sequences of platform carbonates developed, whereas during sea level lows, subaerial exposure along with karst development occurred (Henriksen et al., 2011b). The high sea level fluctuations ceased by the end of the Early Permian, marked by a major transgressive event. This has been attributed to the disappearance of the Gondwanan ice cap (Worsley, 2008).

The Early Permian carbonate deposition was replaced by a siliciclastic regime in the Late Permian, accompanied by a change from a warm and arid climate to a cooler, temperate climate (Smelror et al., 2009). This is related to drastic changes in marine circulation systems. The Norwegian-Greenland rift system was developing by Late Permian times, opening a continuous seaway between the Arctic in the north and the northwest European basins to the south (Glørstad-Clark et al., 2010; Henriksen et al., 2011b). This allowed cool water to flow across the Barents Shelf (Stemmerik and Worsley, 2010). The change may also be related to the development of the Urals and the associated closure of connections to the warm waters of Tethys to the east (Worsley, 2008). The temperate climate, together with deep-water shelf depositional environments brought about by subsidence, allowed rich siliceous sponge fauna to dominate strata across the western shelf (figure 2.3) (Henriksen et al., 2011b; Worsley, 2008).

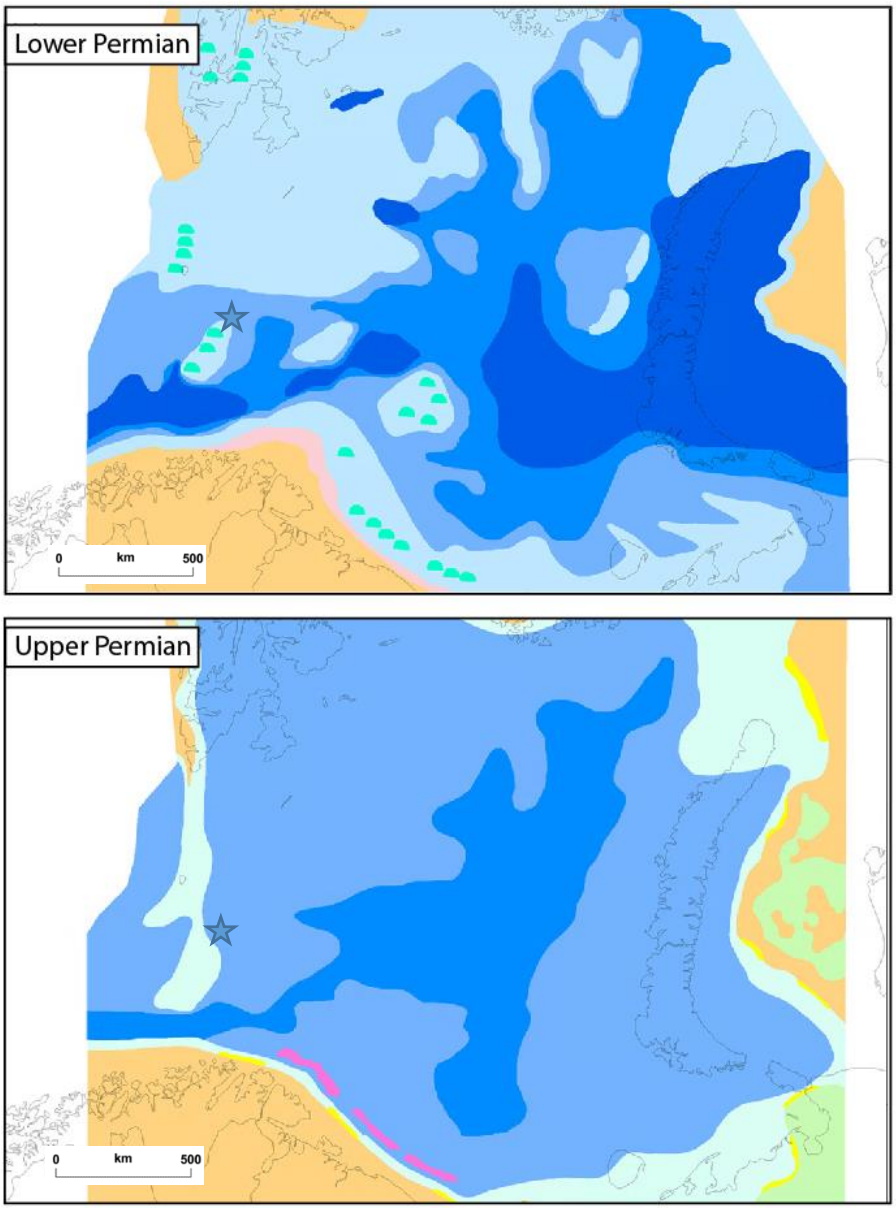


**Figure 2.3:**

Legend found in figure 2.1.

Paleogeographic reconstructions of the Lower (Asselian) and Upper (Kazanian) Permian, demonstrating the large-scale transgression of the Barents shelf as well as the effects relating to the change in climate brought about by the development of the Norwegian-Greenland rift system. Carbonate build ups cease, and siliceous fauna become dominating. Modified after Henriksen et al. (2011b).

## 2.2.2 Mesozoic

*Triassic*

By the start of the Triassic, tectonic movements of the Uralian orogeny had led to a closure of the marine connection from the southeast to the Barents Sea (Smelror et al., 2009; Worsley, 2008). The Barents Sea basin generally experienced regional sag subsidence during the entire Triassic Period (Glørstad-Clark et al., 2010). Subsidence was greatest in the southern Barents Sea, while the western Barents Sea was more quiescent, with passive regional subsidence (Henriksen et al., 2011b). However, local zones of fault activity persisted during this time, including the southern Loppa High Fault System (Indrevær et al., 2017) and the Hoop Graben (Mahajan et al., 2014, as cited by Mulrooney et al., 2018).

Subsidence resulted in the accommodation of kilometer-thick successions of Triassic strata, consisting of siliciclastic deltaic deposits characterized by platform scale clinoforms (Glørstad-Clark et al., 2010). Sediments were sourced primarily from the ongoing Uralian Orogen in the southeast, but Fennoscandia to the south and exposed areas to the west and northwest contributed sediment as well (Pozer Bue and Andresen, 2014). This change in main provenance area effectively reversed sedimentation patterns, as can be observed when comparing figure 2.2 to figure 2.4 (Henriksen et al., 2011b). Deposition was also affected by palaeotopography from Late Paleozoic rifting, with the Loppa and Stappen highs representing barriers to the west to sediments prograding from the south (Faleide et al., 1984).

Lithostratigraphic formations in the Triassic are related to transgressive-regressive cycles of deltaic progradation from SE to NW, bounded by flooding surfaces (Glørstad-Clark et al., 2010). Reservoir rocks are generally present at the approximate maximum regression in these cycles, whereas source rocks are associated with marine anoxia during periods of flooding (Henriksen et al., 2011b). Figure 2.4 shows paleogeographical reconstructions of both the Early and Late Triassic maximum regressions. Reservoir quality has been shown to increase stratigraphically up section throughout the Triassic because of extensive diagenetic alterations in more deeply buried successions (Worsley et al., 2008).

In the Late Triassic, a major change in climate occurs, with an abrupt change to more humid conditions in the Early Carnian, related to the 'Carnian Pluvial Event' (Hochuli and Vigran, 2010; Mueller et al., 2016). The Late Triassic also saw a change in basin infill pattern, likely due to the uplift of the Novaya Zemlya fold and thrust belt (Müller et al., 2019). This changed sedimentation patterns that had controlled supply of sediment prior to the Norian stage, and generated foreland basins in the eastern Barents Sea and forebulge uplift in the west (Müller et al., 2019). Forebulge uplift led to low accommodation and the development of distinct angular unconformities between the Upper Triassic strata and the overlying Lower Jurassic strata, showing that large parts of it formed topographic highs (Müller et al., 2019). The stratigraphic units of the Late Triassic will be elaborated upon in section 2.3 (Realgrunnen Subgroup), as this includes the Fruholmen Formation.

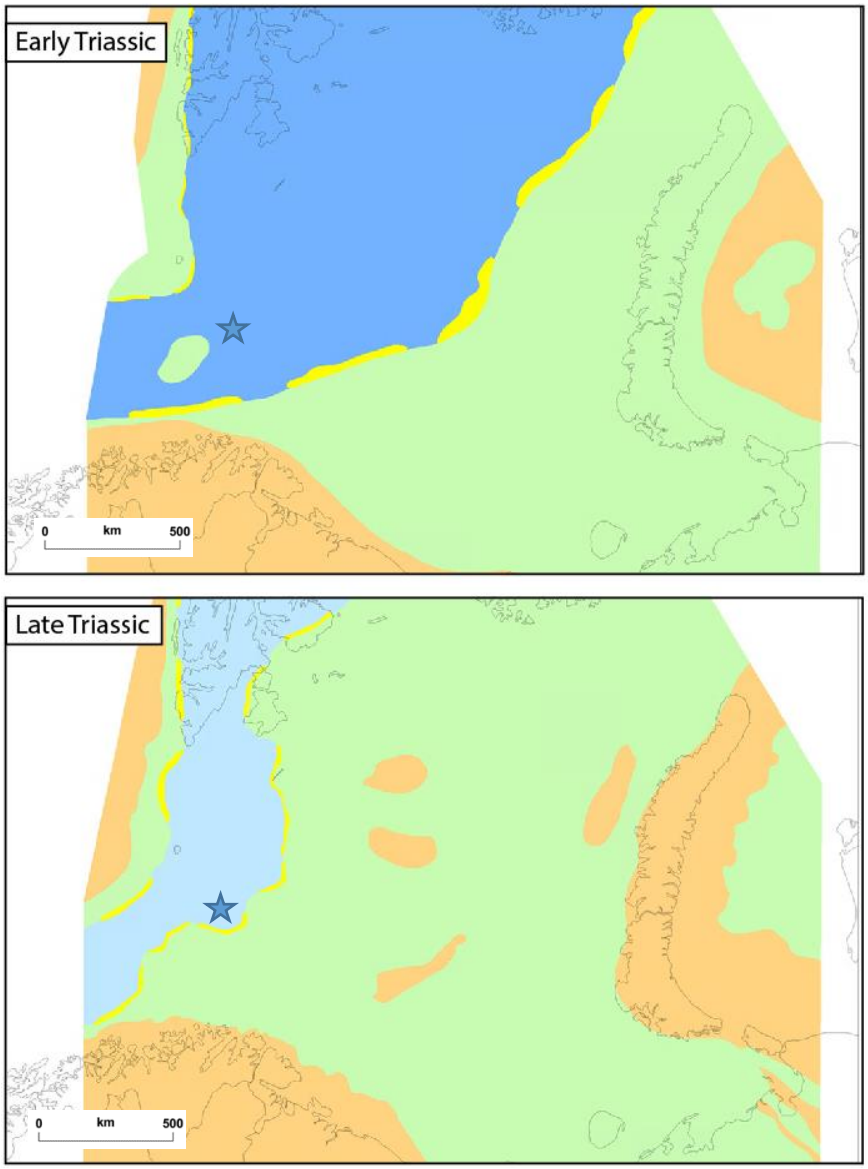


**Figure 2.4:**
Legend found in figure 2.1.

Paleogeographic reconstruction of the Early and Late Triassic, reflecting the Early Triassic (Induan) and Late Triassic (Carnian) regressive maximums. The Late Triassic shoreline reached a position much further west, showing extensive progradation of near-shore and coastal environments. Modified after Henriksen et al. (2011b).

## *Jurassic*

Large parts of the Barents Sea were uplifted and eroded during the Late Triassic-Early Jurassic time. This time frame corresponds to the deposition of the main reservoir units of the Realgrunnen Subgroup, which are bounded by the Early Norian maximum flooding surface (MFS) and a regional Middle Jurassic condensed section below the overlying Fuglen Formation mudrocks (Henriksen et al., 2011b). In the Early Jurassic, the central parts of the Barents Sea area, including Loppa High and Svalbard, comprised wide continental lowlands (Smelror et al., 2009). This reflects a change from gradual subsidence with high sediment supply to a more condensed secession characterized by limited accommodation and bypass in the Early Jurassic (Ryseth, 2014). The Early Jurassic is associated with a yet more humid climate than in the latest Triassic, possibly related to the widespread release of $CO_2$ into the atmosphere as a result of volcanism from the breakup of Pangaea (Ryseth, 2014). Mineralogical

differences occurring in the late Triassic and across the Triassic-Jurassic boundary in the Barents Sea are of great interest due to differences in reservoir quality.

Late in Early Jurassic, the continental lowlands that had developed through uplift were flooded during sea-level rise from both the west and east (Smelror et al., 2009). During the early transgression stage, a change from flood-plain environments to a prograding coastal setting in the southwestern Barents Sea occurred (Smelror et al., 2009). In the late transgression stage, shallow-marine depositional environments were established over most of the western Barents Sea region (Smelror et al., 2009). This resulted in a succession consisting of amalgamated shoreface deposits with excellent reservoir quality, which are primary targets for exploration wells (Smelror et al., 2009). Figure 2.5 shows a paleogeographic reconstruction from Henriksen et al. (2011b) of this period of time, which corresponds to the Stø Formation.

In the Middle Jurassic, regression was caused by central uplift in the Barents Sea, and large parts of the shelf were exposed (Smelror et al., 2009). This led to a depositional gap observed over much of the Barents Sea, and caused coastlines to prograde both to the west and the east (Smelror et al., 2009). The late Middle Jurassic to Early Cretaceous was characterized by widespread rifting, forming rift basins such as the Bjørnøya, Tromsø, and Harstad basins (Faleide et al., 1993; Glørstad-Clark et al., 2010). In the Late Jurassic, differential subsidence and uplift led to the formation of deep basins flanked by exposed platforms and highs in the western Barents Sea (Henriksen et al., 2011b). Organic rich shale and mudstone deposits were deposited in anoxic conditions present in the basins, forming the Hekkingen Formation, an important source rock in the Barents Sea (Henriksen et al, 2011b; Worsley, 2008).

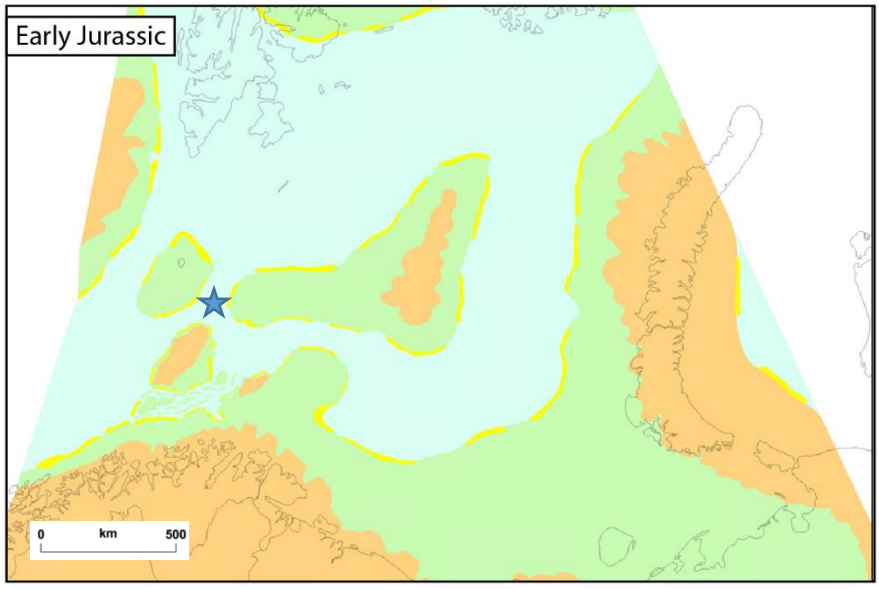


**Figure 2.5:**

Legend found in figure 2.1.

Paleogeographic reconstruction of the Early Jurassic (Toarcian) Barents Sea. A shoreline is located along the Norwegian margin and deflects to the North along Novaya Zemlya. Structural highs such as Stappen high and the central Barents arch may have formed positive relief with internal drainage systems. Modified after Henriksen et al. (2011b).

*Cretaceous*

Widespread rifting that had commenced in the Jurassic continued into the Cretaceous, resulting in very deep basins in the southwestern Barents Sea (Glørstad-Clark et al., 2010). These deep-water shelf and deep basin environments dominating the southwestern Barents Sea at this time deposited thick units of clay with thin limestone and dolomite layers (Smelror et al., 2009). Some submarine fan deposits are found near uplifted structural highs (e.g. Loppa High) (Smelror et al., 2009). This rift system laid the foundation of present day basins and highs. Substantial coal deposits in continental and coastal areas point to shift to a humid climate at this time (Smelror et al., 2009).

Significant subsidence persisted throughout the Late Cretaceous along the western margin of the Barents Sea (Henriksen et al., 2011b). This accommodated thick successions of sediments originating from uplifted continental areas in the east, exceeding 2 km in the Tromsø and Sørvestnaget Basins (Henriksen et al., 2011b). These strata comprise marine mudrocks, however it appears that the oceanic depositional setting present at the time did not favour the creation of source rocks (Henriksen et al., 2011b).

### 2.2.3 Cenozoic

Cenozoic development of the Barents Sea, especially at the western margin, is closely related to the opening of the Norwegian-Greenland Sea (Henriksen et al., 2011b). Considerable shearing along the ocean-continent boundary (the Senja Fracture Zone) occurred as the spreading ridge propagated northwards (Henriksen et al., 2011b). This spreading eventually formed a passive margin in the Oligocene (Henriksen et al., 2011b), with seafloor spreading commencing in the Eocene (Smelror et al., 2009). After the Atlantic opening and general uplift, the major central and eastern parts of the Barents Shelf became tectonically stable, but the basins on the westernmost Barents Shelf (e.g. Tromsø and Sørvestsnaget Basins) continued to subside and receive significant amounts of sediment from the east (Smelror et al., 2009).

The late Pliocene-Pleistocene marks the onset of large-scale glaciation (Smelror et al., 2009). Repeated glaciations and subsequent periods of isostatic uplift resulted in the development of a major unconformity, where uplift and erosion led to the shedding of large amounts of sediments into major submarine depositional depocenters along the western margin (Smelror et al., 2009). Maximum uplift and erosion took place in the northern platform areas and around Svalbard, where up to 3 km of sediments have been removed. Southern parts of the basin (e.g. Nordkapp basin and on the Loppa High) have experienced no more than 2km of uplift (Smelror et al., 2009).

# 2.3 Realgrunnen Subgroup

The Realgrunnen subgroup consists four formations: the normal regressive offshore to deltaic Fruholmen Formation (Norian-Rhaetian), the forced regressive Tubåen Formation (Rhaetian-Sinemurian), and the overall transgressive Nordmela (Sinemurian-Pleinsbachian) and Stø (Pleinsbachian-Bajocian) formations (Figure 2.6) (Gjelberg et al., 1987; Mørk et al, 1999; Müller et al., 2019; Mulrooney et al., 2018).

In the Hoop Fault Complex area, the Fruholmen Formation is found to be immature and supplied from the east, while the overlying Jurassic succession of the Realgrunnen Subgroup comprise reworked and dominantly southerly derived sediments (Klausen et al., 2017). The base of the Realgrunnen subgroup is the Early Norian MFS between the Snadd and Fruholmen formations, while the top is defined by early Bathonian flooding, marked by a condensed section between the Stø and Fuglen formation. This condensed section corresponds to the Brentskardhaugen bed on Svalbard (Henriksen et al., 2011b; Koevoets et al., 2018; Mørk et al., 1999; Worsley, 2008).

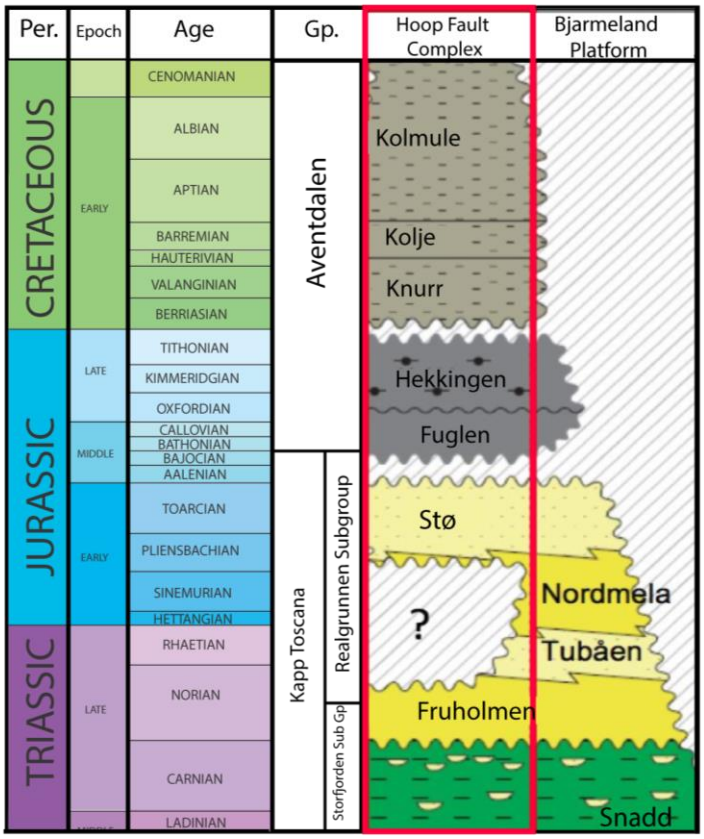


**Figure 2.6:** Lithostratigraphy of Triassic-Cretaceous sediments in the Hoop Fault Complex area and the adjacent Bjarmeland platform. The figure demonstrates completely missing Tubåen and partly missing Nordmela strata in the Hoop Fault Complex area. Modified from OMV Norge (2016).

The thickness of the Realgrunnen Subgroup is 424 m in the type well (7121/5-1) (Halland et al., 2014). Thicknesses of up to 871m have been drilled in the southern part of the Bjørnøyrenna Fault Complex (well 7219/9-1) (Halland et al., 2014). The subgroup is thinly developed on the Bjarmeland Platform, and is mostly eroded on the Troms-Finnmark Platform (Halland et al., 2014). Figure 2.7 demonstrates the thickness variations in the Realgrunnen Subgroup. Westward thickening may be the result of early

Kimmerian subsidence and tilting towards the Tromsø and Bjørnøya Basins (Halland et al., 2014). The successions comprising the Realgrunnen Subgroup are of great interest for further exploration due to recent oil discovery.

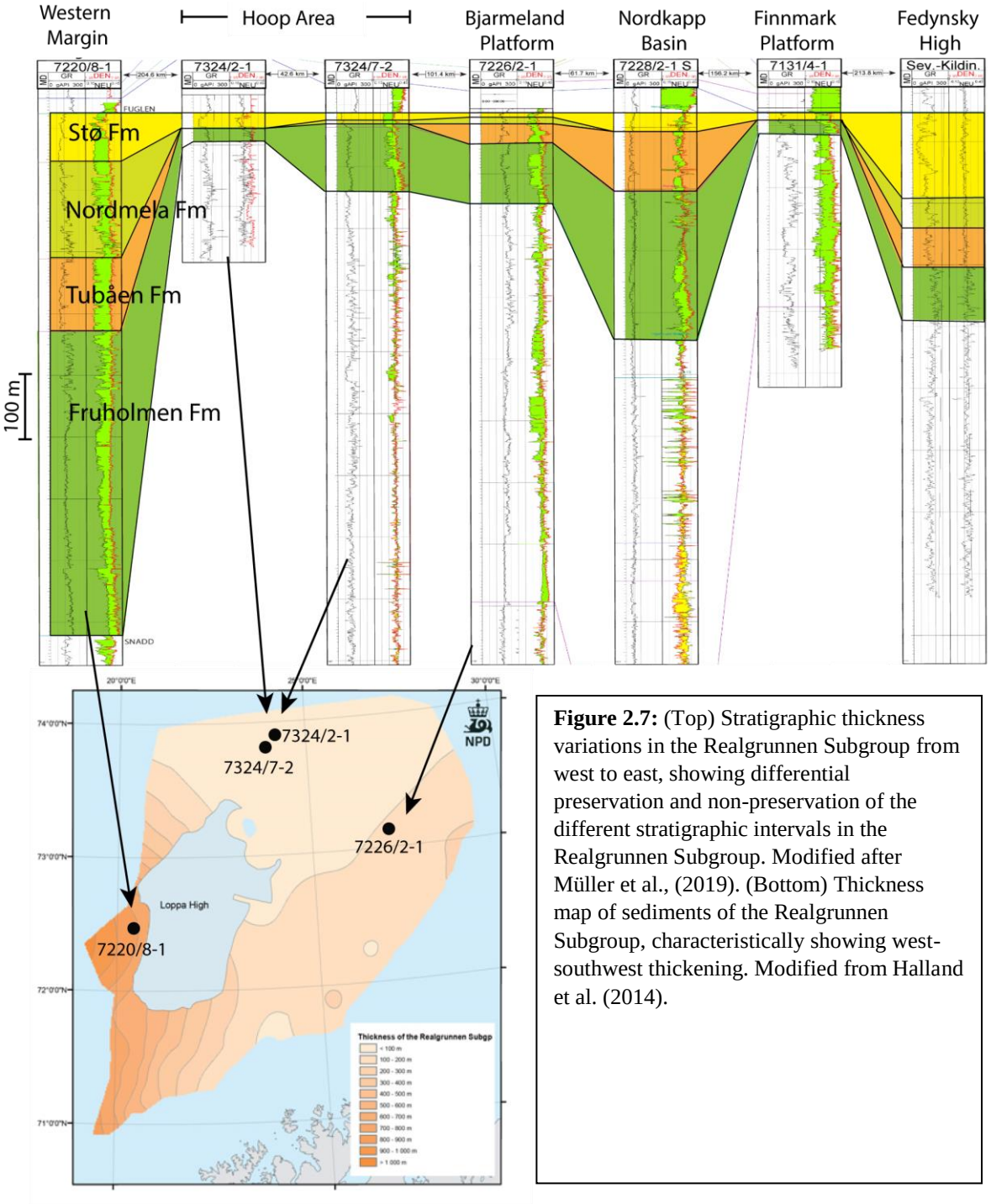


**Figure 2.7:** (Top) Stratigraphic thickness variations in the Realgrunnen Subgroup from west to east, showing differential preservation and non-preservation of the different stratigraphic intervals in the Realgrunnen Subgroup. Modified after Müller et al., (2019). (Bottom) Thickness map of sediments of the Realgrunnen Subgroup, characteristically showing west-southwest thickening. Modified from Halland et al. (2014).

*Fruholmen Formation (Norian – Rhaetian)*

The Fruholmen Formation is subdivided into three members, comprising the prodeltaic Akkar Member, the fluvio-tidal Reke Member, and the deltaic Krabbe Member (Dalland et al., 1988; Müller et al., 2019). This depicts a coarsening upwards trend relating to northward fluvio-deltaic progradation with a depocenter to the south (Halland et al., 2014). As the main deltaic input shifted laterally, the majority of the central and southern parts of the basin became the site of flood-plain deposition, with more marine environments to the north (Halland et al., 2014). The type well for the Fruholmen Formation is well (7121/5-1), where the thickness of the formation is 221m. The thickest sequence of the Fruholmen Formation drilled thus far is 572m (well 7219/9-1) located in the Bjørnøyrenna Fault Complex (Halland et al., 2014). Variations in thickness from west to east are shown in figure 2.7.

*Tubåen Formation (Late Rhaetian to Early Hettangian)*

The Tubåen Formation is absent in Wisting Central III, as well as in other wells in the Hoop Fault Complex area (Clark, 2017; Müller et al., 2019; Skretting, *in prep*), representing a prominent hiatus. With reference to areas where the Tubåen Formation is present (e.g. Bjarmeland Platform, Nordkapp Basin), the Tubåen Formation is dominated by sandstones with subordinate shales and coals (Halland et al., 2014). The formation can be divided into three parts, comprising a lower and upper sand-rich unit separated by a shalier interval (Halland et al., 2014). The sandy units are interpreted to be fluviodeltaic in origin, with a variety of fluvial and distributary facies represented (Ryseth, 2014). The Tubåen Formation shows a distinct change in fluvial style in relation to underlying units, holding more sandstone and less interbedded fine-grained deposits (Ryseth, 2014). To the northwest, the shale content increases, where the Tubåen Formation may interfinger with a lateral shale equivalent (Halland et al., 2014). The absence of the Tubåen Formation observed in Wisting Central III represents millions of years of missing data, during which a vast change in mineral composition is seen in the subsequent Nordmela and Stø Formations. Variations in thickness from west to east are shown in figure 2.7.

*Nordmela Formation (Sinemurian-Late Pleinsbachian)*

The Nordmela Formation is interpreted to represent a 3.25 m interval in Wisting Central III (E. Stueland, Personal Communication, December 21st, 2018), and is consequently logged in this study. The Nordmela Formation typically consists of interbedded sandstones, siltstones, and shales with occurrences of coal (Halland et al., 2014). The depositional environment is interpreted to be a tidal flat to floodplain environment, with estuarine and tidal channels representing sandstone sequences (Halland et al., 2014). Thickness variations illustrate a south-westwards thickening wedge (Halland et al., 2014). Variations in thickness from west to east can be seen in figure 2.7.

*Stø Formation (Late Pliensbachian to Bajocian)*

The dominant lithology of the Stø Formation consists of mineralogically mature and well-sorted sandstone. The Stø Formation encompasses shallow marine, coastal, and fluvial environments deposited in an overall transgressive regime, punctuated by progradation of individual parasequences (Klausen et al., 2018). Linear clastic coast features are identified (Halland et al., 2014). Thin units of shale represent regional transgressive pulses (Halland et al., 2014). Persistent low accommodation settings throughout Stø times resulted in a highly condensed succession, characterized by a high degree of reworking (Klausen et al., 2018). Transgressive lag conglomerates are found at the top, indicating that while the formation was being transgressed there was little accommodation space available (Klausen et al., 2018). This transgressive lag is an equivalent to the Brentskardhaugen bed on Svalbard (Klausen et al., 2018). In general the Stø Formation thickens westwards, consistent with the underlying previous two formations. Variations in thickness can be seen in figure 2.7.

# 2.4 Hoop Fault Complex

The Hoop Fault Complex is characterized by normal faulting in a deep-seated zone of weakness that cuts across Loppa High and Bjarmeland Platform and separates Mercurius High from the Maud Basin (figure 2.8)( Gabrielsen et al., 1990). It is geographically located between located between 720 50’ N, 21050’ E and 740 N, 260 E (Gabrielsen et al., 1990). The fault complex follows a NE-SW trending lineament, corresponding with the structural grain of the Caledonian orogeny within the southwestern Barents Sea (Gabrielsen et al., 1990; Smelror et al., 2009). The northern part of the fault complex consists of a swarm of normal faults cutting the Bjarmeland Platform (Gabrielsen et al., 1990). The central part relates to the development of the Maud Basin, Mercurius High, and the Svalis Dome (Gabrielsen et al., 1990). The southern part comprises a narrow graben on the northern part of Loppa High (Gabrielsen et al., 1990).

The Hoop Fault Complex has experienced multiple phases of extension, forming a complex network of faults (Gabrielsen et al., 2016). Activity in the central part of the complex may have played a role in controlling Late Carboniferous to Permian sedimentation pattern associated with the subsidence of the Maud basin (Gabrielsen et al., 1990). The complex was reactivated in the Middle Triassic, Late Jurassic to Early Cretaceous, and possibly during the Tertiary ages (Gabrielsen et al., 1990). These reactivations took place along listric faults associated with fault movements in the Maud basin (Gabrielsen et al., 1990).

Gabrielsen et al. (2016) conducted experimental studies with reference to the Hoop Fault Complex to investigate the effects of multistage extension on rock sequences of different strength. The style of faulting seen in the Hoop Fault Complex was found to be dependent on the heterogeneity of strata, caused by the presence of layers with contrasting mechanical strength (Gabrielsen et al., 2016).

Evaporites, located primarily in Permian sequences, form weak interlayers within the sedimentary pile, which may form detachment horizons that mechanically decouple and impact the geometry and growth of faults (Gabrielsen et al., 2016). Typically in multistage extensional systems, a systematic increase in accumulated heave is observed with depth because older sequences have experienced greater momentum. However, the presence of mechanically weaker layers can relieve strain that would have otherwise caused offset. This results in accumulated heave that varies from one stratigraphic level to another and does not increase systematically with stratigraphic depth – such is the case for faults within the Hoop Fault Complex (Gabrielsen et al., 2016).

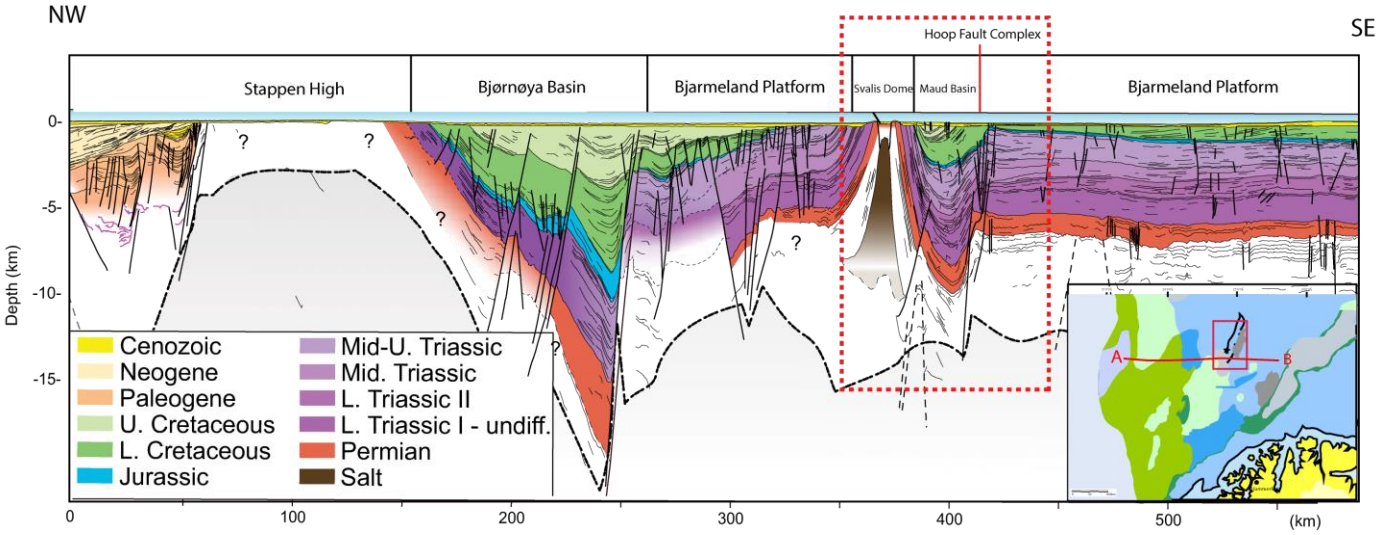


**Figure 2.8:** Regional NW–SE cross-section of the southwestern Barents Sea (line A–B in bottom right-hand corner). Red boxed area highlights structures in the vicinity of the study area, including the Hoop fault complex, Maud Basin, and Svalis Dome. Modified from Gernigon et al. (2012). An enlarged map of the bottom right-hand corner can be found in figure 1.3.

# 2.5 Petroleum System in the Barents Sea

Essential elements comprising the petroleum system are the source rock, reservoir rock, seal rock, and overburden rock (Magoon and Dow, 1994). The Norwegian Barents Sea is a prime example of an overfilled petroleum system, having numerous source rock intervals (Ohm et al., 2008). A high proportion of wells drilled in the Barents Sea have hydrocarbon shows, but few are considered commercial discoveries (Ohm et al., 2008). This is attributed to the aforementioned uplift episodes from the Paleocene until the Pliocene-Pleistocene, causing depletion of hydrocarbons (see section 2.6). This has resulted in a redistribution of petroleum to distal parts of hydrocarbon-generating basins, charging traps which would otherwise have not been reached (Ohm, 2008). The undiscovered hydrocarbons are agreed to be high in the Barents Sea, with the primary exploration target being Triassic to Middle Jurassic sandstones (NPD, 2019).

*Source Rocks*

A source rock is a sedimentary unit from which hydrocarbons have been generated or are capable of being generated (Tissot and Welte, 1984). Source rocks in the Norwegian Barents Sea are found in every stratigraphic interval, from the Carboniferous to Cretaceous, and hydrocarbon generation has occurred over a long period of geologic history (Ohm et al., 2008). As a result, discovered petroleum may comprise a mixture originating from several source rocks and correlation may be challenging (Ohm et al., 2008).

Upper Jurassic and Triassic organic rich shales serve as some of the most significant source rocks in the Barents Sea (Faleide et al., 2015). The most prolific is the Upper Jurassic Hekkingen Formation (Ohm et al., 2008). Petroleum systems connected to this source rock dominate western parts of the Barents Shelf, however have some degree of mixing (Ohm et al., 2008).

Well-developed Early to Middle Triassic Source rocks are also extant, however major contributions from Triassic shales have not been observed (Doré, 1995)

*Reservoir rocks*

The main reservoir rocks in the western Barents Sea comprise the Late Triassic-Middle Jurassic Realgrunnen Subgroup (section 2.3). The Stø Formation usually has very good reservoir properties, and Larsen et al. (1993) has estimated that about 85% of the hydrocarbons in the Norwegian Barents Sea are in this formation.

Other candidate reservoir rocks include those underlying the Realgrunnen Subgroup, namely the Triassic Snadd, Kobbe, and Klappmyss Formations. However, these typically have lower sand contents, and have a stronger tendency to be both laterally and vertically discontinuous in nature (Doré, 1995).

Some potential may also exist in Paleozoic carbonates, Paleogene deep marine sandstones, and Cretaceous rocks (Faleide et al., 2015).

### *Petroleum Plays*

Most traps in the Barents Sea are related to extensional fault blocks or folded domes that have formed due to the multiple tectonic episodes (Henriksen, 2011a). Table 2.1 displays petroleum plays that have been suggested for the Hoop Fault Complex area in NPD (2019).

| | **Triassic** | **Jurassic** |
|---|---|---|
| **Source** | Middle Triassic Shale (Steinkobbe Formation), Permian shales (Tempelfjorden group) | Middle Triassic Shale (Steinkobbe Formation), Permian shales (Tempelfjorden group) |
| **Reservoir** | Klappmyss, Havert, Kobbe, and Snadd, and Fruholmen Formations | Stø Formation |
| **Trap** | Stratigraphic (rotated fault blocks and halokinetic | Stratigraphic (rotated fault blocks and halokinetic |

**Table 2.1:** Petroleum plays suggested for the Hoop Fault Complex in NPD (2019).

# 2.6 Uplift Ramifications

Due to extensive Cenozoic uplift and erosion, finding commercial quantities of hydrocarbons in the Barents Sea has been challenging (Ohm et al., 2008). Barents Sea strata have experienced up to 3000m of net erosion, and the Paleogene and almost all of the Neogene strata are missing in the majority of wells (Henriksen et al., 2011a). In the southwestern Barents Sea, an estimated 1000 to 1500 m has been eroded (Baig et al., 2016; Ohm et al., 2008). Estimated exhumation maps of the southwestern Barents Shelf by Baig et al. (2016) are shown in figure 2.9.

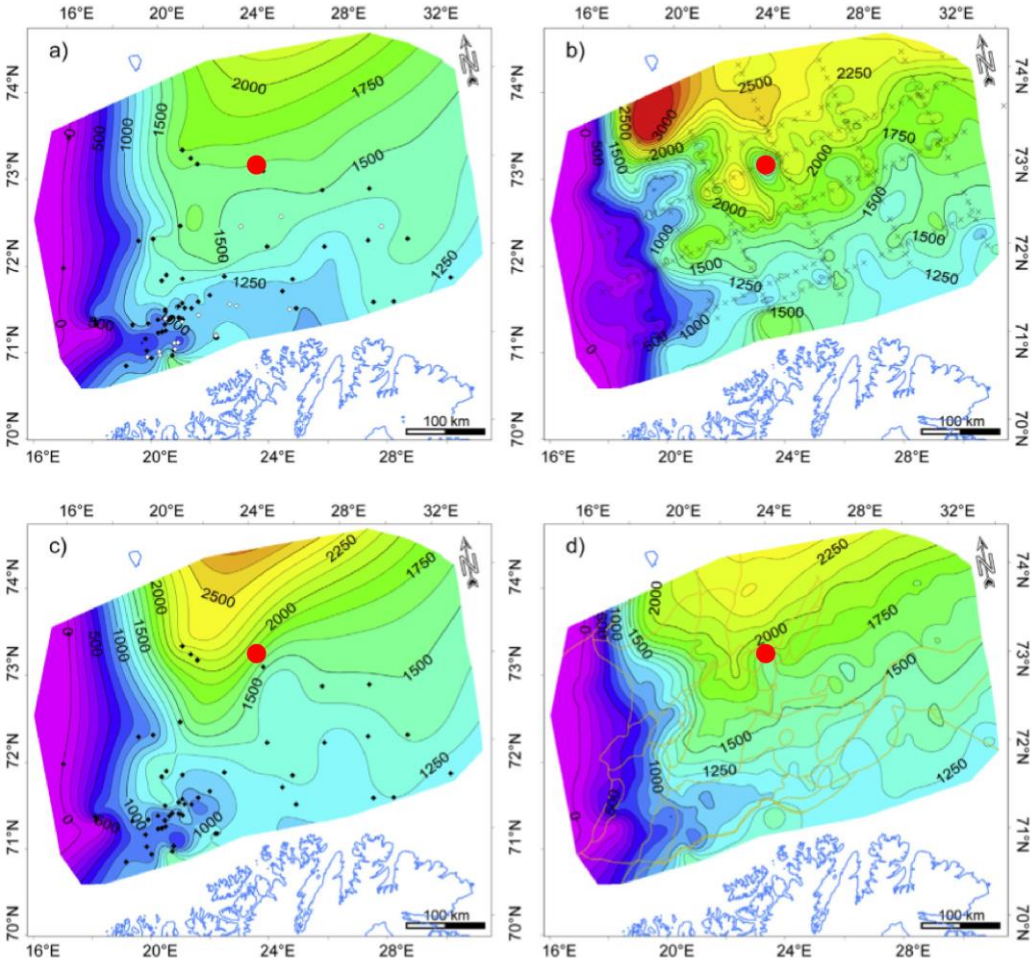


**Figure 2.9:** Estimated exhumation maps from a) sonic logs, b) shot gathers, c) from vitrinite reflectance and d) the arithmetic average net exhumation map of the three data sets from Baig et al. (2016). Data source locations that Baig et al. (2016) used are denoted with the black dots, while the large red dot denotes the approximate location of Wisting Central III.

Primary consequences of uplift include, but are not limited to:

1. The removal of overburden causes pressure release in reservoirs. This results in gas exsolution from the oil as well as gas expansion. This causes the hydrocarbons to be pushed below the spill point of the trap (Henriksen et al., 2011a).
2. The potential tilting of reservoirs during uplift may cause hydrocarbons to be spilled up-dip. It is possible for the spilled hydrocarbons to remigrate and charge traps in more distal locations (Doré and Jensen, 1996).
3. Seals may be cracked during uplift, causing hydrocarbon leakage (Sales, 1993). Stratigraphic or anticlinal traps stand a higher chance to survive uplift as opposed to fault-bounded traps (Henriksen et al., 2011a).
4. Uplifted reservoirs have lower quality than expected for the present burial depth because the reservoir has experienced further mechanical and possibly chemical compaction prior to uplift. Cementation can continue to occur during uplift given the temperature remains above 65-70°C, the threshold temperature for quartz cementation (Bjørlykke and Jahren, 2015).
5. Source rocks are more mature than expected for the present burial depth (Doré and Jensen, 1996).

# Chapter 3: Theoretical Background

## 3.1 Introduction

The most important reservoir properties are porosity and permeability, such that there is capacity to both store and transmit fluids. These properties of sandstone reservoirs are governed by the textural and mineralogical composition, the depositional environment and climate, and the diagenetic processes that occur near the surface and during burial (Bjørlykke and Jahren, 2015).

The starting point for diagenetic processes is the initial sandstone composition. The initial composition is a function of the rocks eroded (provenance), climate, transport and depositional environment (Bjørlykke and Jahren, 2015). Diagenetic models are thus linked to weathering and climate, sediment transport, facies models and sequence stratigraphy (Bjørlykke and Jahren, 2015). Diagenesis encompasses all processes occurring after deposition, which can modify the quality of the reservoir, and are almost completely a function of the initial sediment composition (Bjørlykke & Jahren, 2015). All aforementioned parameters impact the porosity and permeability as seen today, and are thus of interest in this study and further elaborated upon in this chapter.

## 3.2 Sediment Provenance and Depositional Environment

Siliciclastic sediments contain primarily silicate minerals originating from sedimentary, igneous or metamorphic rocks in the hinterland region. All rocks exposed at the Earth's surface are subjected to physical or chemical weathering and are broken down into finer grained sediment (detritus) (Ollier, 1984). Detritus is transported downstream via various transport conductors such as gravity, water, wind or glacial movement from source area to basin. Climatic conditions affect the rate of the weathering and transportation rates. Higher humidity and temperature promote weathering, and the higher rainfall enhances transportation rates of the sediments (Ollier, 1984). As detritus is transported, it is subject to mechanical breakdown, resulting in modifications in grain size, shape, sorting, and mineralogy – ultimately determining the texture and composition of the sediment deposited; additionally, unstable minerals may dissolve (Ollier, 1984). Following deposition, the detritus may be eroded and transported again when flooding or other kinds of eroding events occur. This process is the reworking of detritus, which results in more compositionally stable sediments (Ollier, 1984). The study of sediment source-to-sink systems is important as each process in the system alters the state of sediments, consequently affecting the initial reservoir properties.

## 3.2.1 Detrital Mineralogy

The detrital mineralogy can be used to indicate maturity, provenance, and depositional environment. Sandstones are commonly classified with the use of the three-dimensional QFL ternary diagram, which can indicate provenance and depositional environment using the detrital grain composition (Figure 3.1). This diagram, from Bjørlykke and Jahren (2015), was originally presented by Dott (1964). The diagram portrays the continuous nature of textural variation from mudstone to arenite and from stable to unstable grain composition. The horizontal axis represents textural maturity, while the vertical indicates compositional stability. The three front apices represent end-members of relative physical and chemical durability. The most stable and common end-members are various types of quartz, which occupies the top apex. Feldspar occupies a separate corner at the lower left because of its abundance and intermediate stability. In unstable sands, it is nearly as common as quartz. The most unstable materials are grouped in the lower right corner, which include rock fragments such as ferro-magnesian minerals. (Dott, 1964).

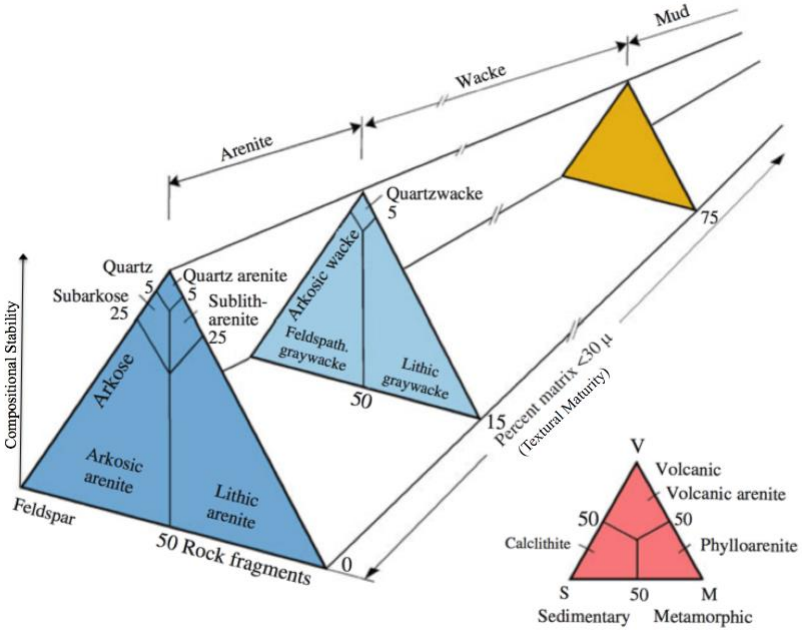


**Figure 3.1:** Classification of sandstones according to Dott (1964) (Modified after Bjørlykke and Jahren, 2015)

The diagram by Dott (1964) subdivides sandstones into quartz arenites, arokoses, and lithic sandstones on the basis of the detrital grain composition (Figure 3.1). Quartz arenites are dominated by quartz and contain less than 5% feldspar and lithic fragments. Such sandstones are compositionally stable, and although they can originate in diverse ways, their purity typically requires a high degree of reworking to remove less stable components (Folk, 1980). Reworking causes unstable minerals such as feldspar and metamorphic rock fragments to break down as well as clay particles to wash out, yielding a high maturity (Folk, 1980). Quartz arenites, especially those of medium to course sand grade, are fastest and most commonly developed directly from plutonic granites or granitic gneisses under humid conditions, if tectonic stability is sufficiently prolonged. Development of quartz arenites is more exceptional in arid climates, requiring a very prolonged period of tectonic stability because the feldspar must be removed

by abrasion alone, unassisted by much chemical decay. Quartz arenites may be derived from metamorphic sources, but this also requires rather prolonged stability to remove all the metamorphic rock fragments. If the source area consists of older sediments, a quartz arenite may be developed at a rapid rate because the source material is already enriched in quartz. Hence, quartz arenites derived from reworked sediments do not require an extensive period of stability (Folk, 1980).

Sandstones constituting over 25% feldspar are classified as arkoses (Dott, 1964). Feldspar is comparatively easier to be decomposed by weathering than quartz. The presence of feldspar at a large percentages therefore indicates special conditions (Folk, 1980). A large feldspar percentage can be attributed to 1) climatic conditions that were too dry or too cold to warrant much weathering, such that the feldspar remained undecomposed, or 2) the source area was uplifted and eroded at such a rapid rate that there was insufficient time for weathering to occur or sediment transport distances were short (Folk, 1980). Consequently it can be an indication for the paleoclimate and depositional setting of the sandstone. However, if feldspars are exposed to a high flux of meteoric water during early burial, the dissolution of feldspar and the precipitation of kaolinite in the intergranular volume may take place.

In lithic arenites, rock fragments are the chief constituent (Dott, 1964). Rock fragments originate typically from metamorphic rocks, fine-grained sedimentary rocks, or basalts and intrusive igneous rocks (Bjørlykke & Jahren, 2015; Folk, 1980). They can serve as indicators for whether the provenance rock was of igneous or metamorphic origin. Rock fragments are characteristically soft and quite susceptible to abrasion. Their abundance in sand therefore varies greatly with environment of deposition, the distance from source, and tectonic activity (Folk, 1980).

## *Quartz*

Quartz is a crystalline variety of $SiO_2$, with a hardness of 7 and lacks any sort of cleavage for practical purposes (Folk, 1980). Because of its hardness and lack of cleavage, it is one of the most durable of the abundant minerals (Folk, 1980). It can be optically discriminated by its uniaxial positive sign, low birefringence grey colour when cut perpendicular to the optic axis, and white to yellow interference colours in parallel sections (Boggs, 2009).

Sources of quartz include igneous rocks, particularly acid plutonic rocks, different types of metamorphic rocks, and sedimentary rocks (Boggs, 2009). Quartz can occur as monocrystalline quartz (single grains) or polycrystalline quartz (composite grains) (Boggs, 2009). Quartz occurs most commonly as monocrystalline quartz in sandstones. Detrital quartz grains have a tendancy to be subangular, with the exception of those which have undergone significant eolian transport or have experienced multiple episodes of deposition and transport (Boggs, 2009).

Monocrystalline quartz exhibits undulatory extinction, to 30 degrees. The majority of quartz grains have inclusions, which consist typically of bubbles or minerals (Boggs, 2009; Folk, 1980).

### Provenance Indicators:

Polycrystalline quartz can be common in some sediments, and its presence can aid in the determination of igneous and metamorphic origin (Young, 1976). Cathode luminescence spectra of quartz has also been used as a provenance indicator (e.g. Matter et al, 1985).

## *Feldspar*

Following quartz, feldspars are the most abundant framework mineral in sandstones (Boggs, 2009). Feldspars are split into two major groups: alkali/K-feldspars and plagioclase feldspars (Boggs, 2009). They exhibit a hardness of 6 and have 3 cleavages. Although feldspars are susceptible to surface weathering they can also be altered post-burial through early diagenesis (Bjørlykke and Jahren, 2015).

Alkali/K- feldspars form a solid solution series from K ($AlSi_3O_8$) (Orthoclase, sanidine, microcline) to Na ($AlSi_3O_8$) (anorthoclase) (Boggs, 2009). **Orthoclase** is monoclinic, has a low birefringence, and can be easily mistaken for quartz in thin section. It has low relief and is commonly untwinned. It can be optically discriminated by an optic sign that is biaxial with a large 2V, which is characteristic of all alkali feldspars (ranging from 40 to 85 as a group, except sanidine) (Boggs, 2009). **Sanidine** is also monoclinic and similar to orthoclase. It may be differentiated by a smaller 2V (0-47 degrees). **Microcline** is a triclinic alkali feldspar that has very characteristic cross hatch lamellae (exhibiting both pericline and albite twins) that form at approximately right angles (Boggs, 2009). **Anorthoclase** is similar to microcline but has finer scale cross hatching, and can be distinguished by a smaller 2V. (Boggs, 2009). It is common in Na-rich volcanic rocks. Extinction angles are generally between 5 and 21 degrees for all alkali feldspars.

Plageoclase feldspars form a solid solution series from $NaAlSi_3O_8$ (albite) to $CaAl_2Si_2O_8$ (anorthite). (Boggs, 2009). Plagioclase minerals are all triclinic. Albite twinning occurs exclusively on triclinic feldspars, especially plagioclase. Carlsbad twinning is also fairly common, while pericline twinning is less common. Albite twinning and the typical absence of pericline twinning can discriminate them from alkali feldspar (Boggs, 2009).

### Provenance Indicators:

Almost all detrital feldspars are igneous or metamorphic in origin. In igneous rocks, feldspar is the dominant mineral and it is not present in such great amounts in sandstones simply due to weathering (Folk, 1980). Much of the mineral originates from granites and gneisses (Folk, 1980), commonly in rifted intracratonic settings (Blatt et al, 2006). K-feldspars are dominant in these rocks, therefore in sedimentary rocks, K-feldspar is the dominant feldspar. When more plagioclase than alkali feldspar is found, a volcanic source is suspect (Folk, 1980), more typical of convergent plate margins (Blatt et al, 2006). Na-rich plagioclase (e.g. albite) is usually from volcanic rocks (Ulmer-Scholle et al., 2014).

Small amounts or zero feldspar is often taken to mean that there was extensive abrasion, reworking, or weathering, but it is important to note that may as well indicate that little to no feldspar was available in the source area (Folk, 1980).

## *Lithic Fragments*

Lithic fragments (also called rock fragments or composite grains) can be derived from a wide variety of lithotypes and typically have source-specific textures and compositions that can be recognized in thin section (Ullmer-Scholle et al., 2014). Because of their multi-crystalline nature, rock fragments are typically more common in courser grain size modes of clastic rocks. Their multi-crystalline nature also causes them to usually more easily yield to the effects of weathering and also later mechanical or chemical diagenesis. However, because the surviving rock fragments can give some of the most direct evidence of contributions from various terranes, it is important that they be accurately identified (Ullmer-Scholle et al., 2014). The provenance rock's areal extent and relief will govern the quantity of lithics; an increase in either will result in more lithic fragments downstream.

## *Allogenic Clay*

The horizontal axis of the QFL diagram in figure 3.1 represents textural maturity. This is given by the content of clay present in the sandstone, or percent matrix that is smaller than 30 microns in size. The type and distribution of clay can be central in determining the diagenesis of sandstones. Clay is a constituent of almost all sandstones and can be deposited simultaneously with framework grains (allogenic) or, can precipitate as a result of mineral alteration (authigenic) (Nichols, 2009). In relation to sandstone classification, the allogenic clay particle percentage will determine if the sandstone is classified as an arenite, wacke or mudstone (Figure 3.1). Clays are diagenetically important because they form easily compressible grains, aiding mechanical compaction and clogging pores (Ali et al., 2010). The size, shape, and distribution of the allogenic clay is controlled by physical and biogenic processes (Wilson and Pittman, 1977). Forms of allogenic clay include dispersed matrix, lamina, sand-sized floccules, and sand- to cobble-sized mud or shale clasts (Figure 3.2). Bioturbation and subsequent infiltration are secondary forms of allogenic clay deposition (Wilson and Pittman, 1977).

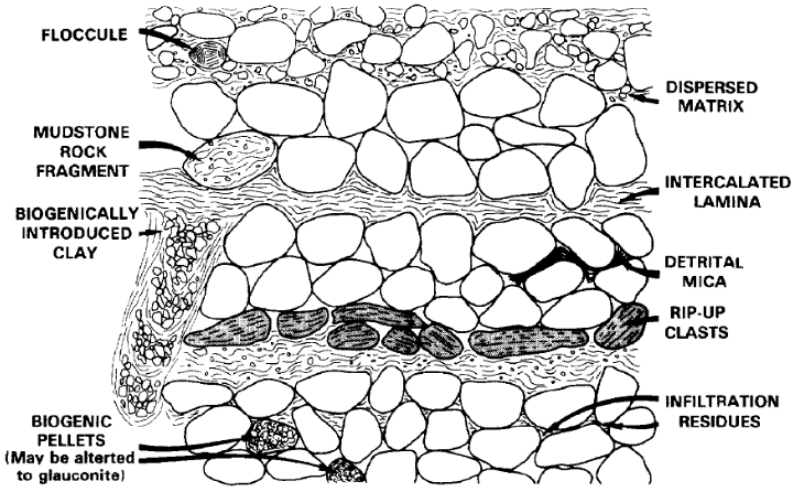


**Figure 3.2:** Allogenic clay found in sandstones (from Wilson and Pittman, 1997).

# 3.3 Diagenesis

Diagenesis encompasses any chemical, physical, or biological change that sediments or existing sedimentary rocks undergo after initial deposition, but below temperatures and pressures necessary for the generation of metamorphic rocks (200-250 C) (Bjørlykke & Jahren, 2015; Burley et al., 1985). Sediments are typically deposited as an assemblage consisting of minerals and dead organic matter which are not in equilibrium with the ambient environment. Diagenesis occurs because the original sedimentary assemblage and the pore water will always react in a way that attempts to reach a state of equilibrium with the environment (Curtis, 1977; Burley et al., 1985). The state of equilibrium is dependent on temperature, pressure, and chemistry. Because these factors change with depth, the equilibrium state continually changes with burial and uplift (Worden & Burley, 2003). Diagenetic processes are therefore continually active as the ambient environment changes during the evolution of the basin (Worden & Burley, 2003). Changes from diagenetic reactions result in differences from the rock's original mineralogy and texture. Three subdivisions of diagenetic processes are distinguished: 'early chemical reactions', 'mechanical compaction', and 'chemical compaction'.

## 3.3.1 Early Diagenetic Reactions

Early diagenetic reactions start to modify the primary sediment composition as soon as sediments are deposited (Bjørlykke and Jahren, 2015). At shallow burial depths, below 1-10 m, sediments are in a chemically open system whereby the atmosphere or water may add or remove dissolved solids by diffusion or advection (Bjørlykke and Jahren, 2015). Because of this, the potential for sediments to change their bulk composition after deposition is much higher at shallow depth than at greater burial (Bjørlykke and Jahren, 2015). Conditions are oxidizing near the surface on land as well as in the uppermost few centimeters of the seabed, while reducing conditions are always present at greater depths in the basin (Bjørlykke and Jahren, 2015). The most important diagenetic processes occurring at shallow burial include (1) meteoric water leaching, (2) early carbonate cementation, and (2) Redox-driven processes on the seafloor (figure 3.3).

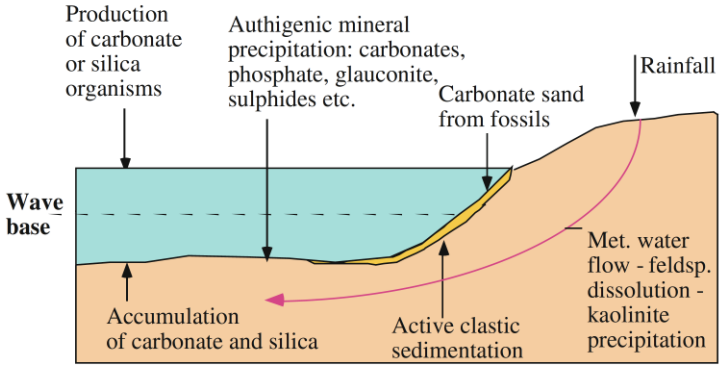


**Figure 3.3:** Several important early diagenetic reactions in shallow marine environments. Sandstones will be flushed by meteoric water flow, causing dissolution of feldspar and micas. Early carbonate cement can be significant in the composition of sandstones. Figure from Bjørlykke and Jahren (2015).

### *3.3.1.1 Meteoric Water Flow*

Meteoric water originates from rainwater that has infiltrated the ground, and is therefore undersaturated with respect to all minerals (Bjørlykke and Jahren, 2015). Rainwater is typically slightly acidic, producing carbonic acid and sulphuric acid from $CO_2$ and $SO_2$ from the air.

Rainwater may seep down to the groundwater. If the water table is above sea level, then this meteoric water will flow along permeable beds into the basin. Because it is undersaturated, it will first dissolve carbonates and thereafter dissolve more unstable minerals, such as feldspar and mica. The dissolution of feldspars and mica give rise to the precipitation of hydrous clay minerals such as kaolinite in the pore space (Bjørlykke, 1998), following the following equations:

**Equation 3.1:** $$2K(Na)AlSi_3 3O_8 + 2H^+ + 9H_2O = Al_2Si_2O_5(OH)_4 + 4H_4SiO_4 + 2K^+(2Na^+)$$

Feldspar Water Kaolinite Silicic acid Dissolved Ions

**Equation 3.2:** $$2KAl_3Si_3O_{10}(OH)_2 + 2H^+ + 3H_2O = 3Al_2Si_2O_5(OH)_4 + 2K^+$$

Muscovite Water Kaolinite Dissolved $K^+$

Such reactions are often referred to as 'subsurface weathering' (Bjørlykke, 1998). Kaolinite is a part of the kaolin-serpentine clay mineral series, and is typically characterized by stacked pseudohexagonal plates in a vermicular form (Worden and Morad, 2003). For the reactions in equations 3.1 and 3.2 to take place, meteoric water must supply H+ ions and remove the silica, K+ and Na+ reaction products. It follows that the K+/H+ ratio must be low for the reaction to transpire. The rate at which feldspars and micas are leached and kaolinite is precipitated is a function of the flux of groundwater flowing through each rock per unit of time. This flux of water must be fairly significant – Bjørlykke (1998) estimated around $10^3$-$10^4$ $m^3/m^2$ to dissolve enough feldspar to precipitate small amounts of kaolinite. This suggests that the degree of feldspar and mica dissolution is a good indicator of the intensity of meteoric flow. Additionally, extensive leaching may occur in conditions of low sedimentation, because these sediments remain within reach of meteoric water for a longer period of time (Bjørlykke, 1998). On the other hand, high sedimentation rates would quickly bury sediments such that they reach a depth at which they are no longer affected by meteoric water flushing faster (Bjørlykke and Jahren, 1995).

With respect to reservoir quality, the dissolution of feldspar and mica produces secondary pore space, but the precipitation of kaolinite results in little net gain in porosity (Bjørlykke and Jahren, 2015). Although there is a minor increase in porosity, the pore filling kaolinite generates a drastic reduction in the permeability, causing an overall decrease in reservoir quality. Additionally, the secondary pore spaces created are often removed during further burial as a consequence of mechanical compaction (Bjørlykke and Jahren, 2015).

### 3.3.1.2 Carbonate Cementation

Most clastic depositional environments have some organisms producing organic matter, of which some part is incorporated into the sediments. Sandstones almost always hold significant quantities of biogenic material from calcareous organisms (Bjørlykke and Jahren, 2015). During shallow burial, marine organisms that are composed of aragonite are dissolved and calcite precipitates, typically as cement in the pore space between grains. Carbonate cement may from layers or concretions, and is in most cases derived biogenically, particularly by the dissolution and precipitation of organisms composed of aragonite. Carbonate concretions may be mistaken for continuous layers of carbonate in cores, but it may be possible to recognize them as concretions (e.g. Walderhaug and Bjørkum, 1998). Because carbonate cemented layers act as barriers to fluid flow, differentiating laterally continuous layers from concretions/nodules is very important.

Because biogenic carbonate is the primary source of calcite cement, the distribution is related to biological productivity relative to the clastic sedimentation rate. Environments with a low clastic sedimentation rates are often found to have a high organic carbonate production (Bjørlykke and Jahren, 2015).

### 3.3.1.3 Redox-Driven Processes on the Seafloor

There is a high gradient in the concentration of oxygen and sulphate across the redox boundary (Bjørlykke and Jahren, 2015). The redox boundary is typically 1-20 cm below the seafloor, and represents an equilibrium between the supply of oxygen through diffusion and its consumption by the oxidation of organic matter (Bjørlykke and Jahren, 2015). As such, the oxygen content decreases rapidly below the water-sediment interface, creating a concentration gradient for downward diffusion of oxygen in to the uppermost sediments (Bjørlykke and Jahren, 2015).

Oxygen may be consumed in the sediments through oxidation, but this is less common in marine environments and more common in terrestrial deposits. In most marine environments, sufficient organic matter is present to serve as reducing agents such that little oxidation takes place. Because of their reduced solubility in the oxidized state, iron and manganese may precipitate on the seafloor as oxides after being transported upwards through the sediments by diffusion (Bjørlykke and Jahren, 2015). Iron may also be precipitated below the redox boundary as sulphides or iron carbonate (siderite). At depths where there is very little free dissolved oxygen in the porewater, sulphates may be reduced by sulphate reducing bacteria, which produces sulphides such as pyrite.

## 3.3.2 Mechanical Compaction

Mechanical compaction is a consequence of increased burial and the associated increase in the effective stress with depth. It includes the re-orientation of grains, sliding of grains, deformation of ductile components, and crushing of brittle grains (Worden and Burley, 2003). Mechanical compaction results in porosity loss. Initial sandstone porosity, as well as porosity loss upon compaction, is a function of the detrital mineralogy (e.g. ductile vs. framework), size, shape, sorting, and burial depth.

Higher quartz content gives higher mechanical stability, such that less compaction occurs. Feldspars are also mechanically very stable. Many lithic fragments, however, have lower mechanical stability and may behave in a ductile manner, such that more compaction occurs (Pittman and Larese, 1991). Thus, the ratio of mechanically stable grains to ductile grains is of importance in porosity loss. Courser grained sandstones have been shown by Chuhan et al. (2003) to result in more mechanical compaction due to grain crushing. This occurs because large grains have on average less grain contacts than smaller grains, on which stresses are distributed (Chuhan et al., 2003). Sandstone with well-rounded grains can carry more load and compact less than sandstones that are angular and have less sphericity, and well sorted sands compact less than poorly sorted sands (Beard and Weyl, 1973).

For well sorted, clean sandstones, starting porosities have been empirically shown to range between 40 and 45% (Boggs, 2009; Bjørlykke and Jahren, 2015). This has been observed to reduce to porosities of 25 to 30% upon experiencing stresses of 20 to 30 MPa, which corresponds to depths of approximately 2 to 4 km when rocks are normally pressured (Bjørlykke and Jahren, 2015). However, many sandstones contain substantial quantities of ductile grains and matrix material, which can be deformed to fill pore spaces to obtain a higher mechanical stability. Furthermore, they reduce friction between rigid grains, promoting further compaction (Worden and Burley, 2003). In these cases, porosity can be reduced to almost zero. Compaction curves (e.g. Mondol, 2009) are often used in the prediction of properties at depth.

Mechanical compaction is governed by effective vertical stress, which is a function of the vertical stress and pore pressure (Bjørlykke et al., 2015). The vertical stress at any point in a basin is given by:

$$\sigma_v = \rho_b g h$$

**Equation 3.3:** Vertical stress $\sigma_v$, where $\rho_b$ is the average sediment bulk density (solids and fluids), $g$ is the acceleration of gravity, and $h$ is the depth. From Bjørlykke et al. (2015).

The effective vertical stress is defined as the difference between the vertical stress and the pore pressure:

$$\sigma_v' = \sigma_v - u$$

**Equation 3.4:** Effective vertical stress $\sigma_v'$, where $\sigma_v$ is the vertical stress (from equation 3.3), and $u$ is the pore pressure (Bjørlykke et al., 2015).

### 3.3.3 Chemical Compaction

Chemical compaction is related to the dissolution and precipitation of minerals as authigenic cements. It is assumed to take place in a chemically closed system where mass balance is obtained, as opposed to early diagenetic reactions. Increasing burial depths correspond to increasing temperatures and pressures, and diagenetic reactions occur because the original sedimentary assemblage is gradually taken out of the state of equilibrium with their environment (Burley et al., 1985). As previously mentioned, the state of equilibrium is dependent on temperature, pressure, and chemistry, which change with burial.

*Quartz Cementation*

Quartz cementation is initiated at 65-70°C, and does not cease until almost all the porosity is lost (Bjørlykke and Jahren, 2015). The initiation of quartz cement marks the transition zone between mechanical and chemical compaction, whereby enough quartz cement is precipitated to carry the grain framework and effectively shut down mechanical compaction (only around 2-3% is needed) (Bjørlykke and Jahren, 2015). It can be recognized in well log data by a jump in p-wave velocities, as velocities in mechanically compacted siliciclastic sediment cannot reach values greater than 3000 m/s (N. Mondol, Personal Communication, January 22nd, 2018). Quartz cement will reduce the IGV. As authigenic quartz and detrital quartz is difficult to distinguish in an optical microscope, this may lead to an underestimation of IGV. Cathode luminescence can help in distinguishing quartz cement.

Quartz cement occurs as a result of pressure dissolution due to higher temperatures and pressures, which increases the surface area of grain contacts and thus distributes the load over a larger area (Bjørlykke and Jahren, 2015). Quartz dissolution is enhanced if mica or clay minerals are present between grain contacts (Bjørkum et al., 1998). Clay-rich lamellae promote the formation of stylolites as a consequence of pressure dissolution. Dissolved silica is precipitated on grain surfaces where it can nucleate (Bjørlykke and Jahren, 2015).

Compaction due to quartz cementation is primarily a function of temperature, but also is a function of time and available surface area for precipitation (Figure 3.4) (Bjørlykke and Jahren, 2015). The rate of quartz cementation increases exponentially with temperature by an estimated factor of 1.7 for every 10°C (Walderhaug, 1996). Quartz cementation and porosity can thus be modelled as an exponential function of the temperature integrated over time, and is proportional with the surface area available for quartz precipitation (Bjørlykke and Jahren, 2015).

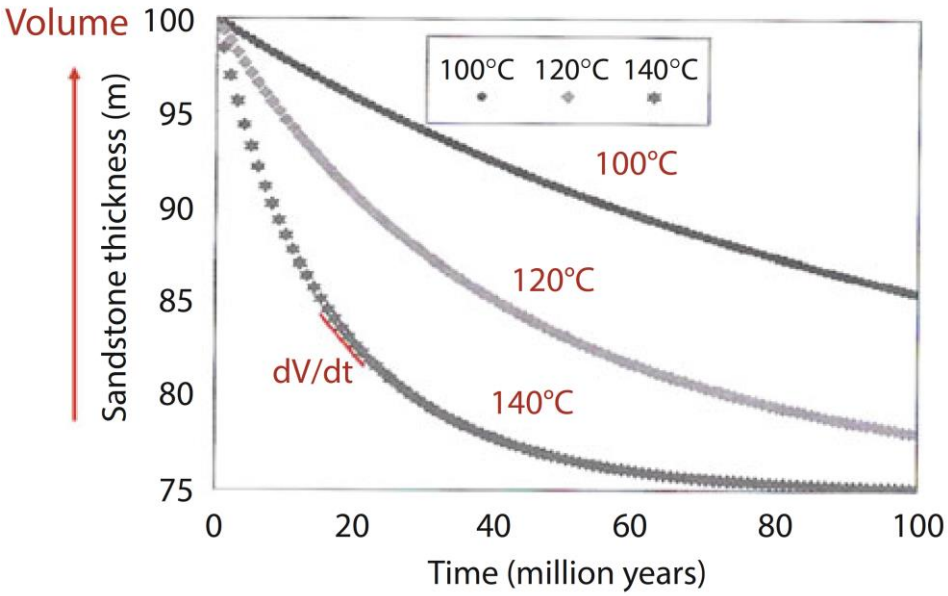


**Figure 3.4:** Model of quartz cementation and compaction due to quartz dissolution as a function of time and temperature. Figure from Bjørlykke and Jahren (2015). Originally produced in Walderhaug et al. (2001). Rate of cementation slows down when porosity is reduced, because the rate-limiting factor is surface area.

The rate-limiting process in quartz cementation has been determined to be the rate of nucleation in the pore space, and is thus surface-controlled (Bjørkum et al., 1998). A consequence of this model is that quartz cementation will continue to precipitate as long as the temperature is above the threshold for growth (65-70°C), and there is still porosity in the sandstone (Bjørlykke and Jahren, 2015). It continues even after being uplifted to shallower depths but is still above the threshold temperature, although at a slower rate (figure 3.5) (Bjørlykke and Jahren, 2015).

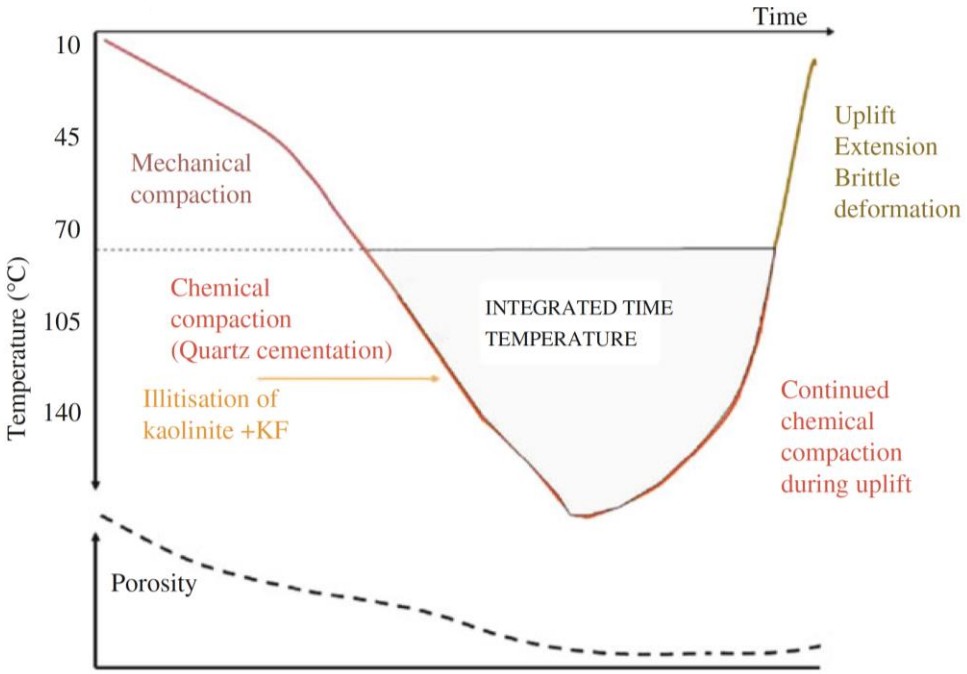


**Figure 3.5:** Quartz cementation as a function of temperature and time. Quartz cementation will continue during uplift as long as the temperature exceeds 65-70°C. From Bjørlykke and Jahren (2015).

### *Authigenic Illite*

Authigenic illite can be formed as an alteration product from smectite or kaolinite and k-feldspar. The reaction of smectite to illite is shown in the simplified equation taken from Boles and Franks (1979):

**Equation 3.5.** $$Smectite + K^+ = Illite + Silica + H_2O$$

This reaction occurs from temperatures of about 70 to 80°C (~ 2 – 2.5 km), and is a progressive process whereby precursor smectite is replaced by illite on a layer-by-layer basis (Worden and Morad, 2003). K-feldspar can be a potential source of potassium. The illite precipitated from equation 3.5 takes on very fibrous morphology that can significantly reduce permeability and also lead to overpressure (Thyberg et al., 2010). Dissolution of smectite and precipitation of quartz and illite will cause a sharp increase in the seismic velocity and rock density, and may thus show up as a horizontal reflector on seismic (Thyberg et al., 2010). Thyberg et al. (2010) documented the presence of microquartz crystals sourced from this reaction in mudstones.

The reaction of kaolinite to illite, from Bjørlykke et al. (1995) is as follows:

**Equation 3.6.** $$Al_2Si_2O_5 + KAlSi_3O_8 = KAl_3Si_3O_{10}(OH)2 + 2SiO_2 + H_2O$$

Kaolinite K-feldspar Illite Silica Water

The reaction in equation 3.6 does not become significant until 120°C (~3.5-4 km). The reaction, like that in equation 3.5, also produces illite that takes on a fibrous shape that is detrimental to reservoir quality. Unlike the smectite to illite reaction, the quartz produced in the kaolinite to illite reaction is not microcrystalline. Instead, it is precipitated around detrital quartz grains in a similar fashion to quartz produced by pressure dissolution (Thyberg et al., 2010).

### *Albitization*

The replacement of K-feldspar or plagioclase by albite is called albitization. It is often observed in sandstones that have undergone temperatures of 90°C or more (Bjørlykke and Jahren, 2015). This occurs because $Na^+$ is normally the dominant cation in porewater at this stage due to the removal of $K^+$ by clay mineral reactions. Although it has an insignificant effect on reservoir quality, it is worth noting – especially in provenance studies.

# Chapter 4: Data and Methods

## 4.1 Introduction

The data and methodology used in evaluating the reservoir quality of sandstones in the Realgrunnen Subgroup in Wisting Central III are presented in this chapter. Three main analyses are conducted in this study: sedimentological analysis, petrographical analysis, and petrophysical analysis.

All sample preparation and results are conducted and obtained by the author, unless otherwise specified in the text. All referred depths are measured depth (MD) unless otherwise stated.

## 4.2 Database

Permission to view and to extract samples from the Wisting Central III drill core was provided by the OMV Norge AS. OMV Norge AS also provided photos of the core and biostratigraphic and core plug data contained in a report by RPS Ichron. Summary of well information is given in appendix A. A core viewing was arranged for sedimentological analysis. At the viewing, samples to be extracted from the core were marked. A summary of the 20 samples along with the petrographical analyses conducted with them is presented in appendix B. Petrophysical well logs are used primarily for uplift estimation. A summary of the available petrophysical logs is presented in appendix C.

## 4.1 Sedimentological Analysis

Sedimentological logging and core sampling of the Fruholmen and Stø formations in well 73247/8-3 (Wisting Central III) was conducted at Weatherford Laboratories AS, Stavanger with the assistance of Lina Hedvig Lina (PhD, UiO) and Eirik Stueland (OMV Norge) on December 20$^{th}$, 2018. Logging was executed at a scale of 1cm: 50cm for optimum qualitative and quantitative purposes. The logged interval totals 95 meters.

The basis for logging and core description encompasses lithology, grain size, bioturbation, and sedimentary structures; however other marked features were noted. The Wentworth (1922) grain size classification chart (figure 4.4 in section 4.2.4.1) was applied in the determination of grain size. A bioturbation intensity chart (figure 4.1) was utilized in assessing the bioturbation index (BI), which relates to the degree of preservation of the primary bedding features. Ichnology atlases (e.g. Knaust, 2017) assisted with the identification of trace fossils. With the use of Adobe Illustrator CS6, the log was then digitalized and condensed to a scale of 1cm: 5m. The logs, together with core photos, biostratigraphic information (used with permission from OMV Norge AS), and reference literature, served as the basis for describing facies, facies associations, and the subsequent interpretation of depositional environments.

The logged sediments are separated into facies based on the grain size, sedimentary structures, bioturbation, lithology, bed thicknesses, and boundaries. A facies can be a bed or bedset which is formed under certain sedimentary conditions, reflecting a specific process (Reading, 1996). The identification of a facies is based purely on descriptive criteria, but are interpreted in a genetic context. Facies that are genetically related to one another were combined into facies associations, reflecting specific sedimentary environments.

The biggest limitation that comes with core logging is the low lateral resolution. This results in an inability to trace facies laterally as well as an incapacity to capture large-scale geological features. This can lead to misinterpretations of structures that may be outside the resolution of the core.

Following the logging procedure, the core to be sampled was marked at Weatherford Laboratories AS., which were extracted by technicians. Twenty samples were then utilized to conduct petrographic analyses, as described in the next section.

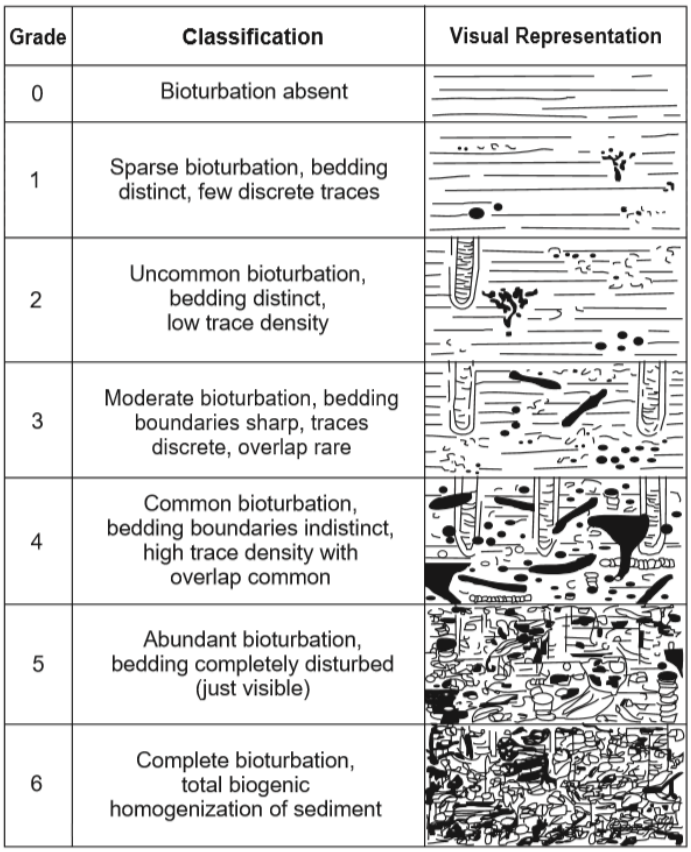


**Figure 4.1:** A bioturbation intensity chart aided in determining the extent of bioturbation during sedimentological logging. From MacEachern et al. (2005).

# 4.2 Petrographic Analysis

The objective of the petrographic analyses are to identify and quantify the mineral content in each sample, describe textural parameters (e.g. grain size, sorting, shape, and contacts), and to assess the intergranular volumes (IGV) (porosity, cements, and matrix). This is accomplished through X-ray diffraction (XRD) analysis, optical microscopy, and scanning electron microscopy (SEM) at the University of Oslo with the guidance of Thanusha Naidoo, Lina Hedvig Line, and Siri Simonsen respectively.

## 4.2.1 X-ray Diffraction (XRD)

X-ray Diffraction (XRD) analysis is a primary method used in the identification and semi-quantification of the minerals present in a prepared sample.

### *Sample Preparation*

A total of 20 samples are prepared for bulk XRD analysis. Because a grain size of approximately 2 microns is necessary to conduct the analysis, several milling steps are executed. Initially each sample is gently crushed using a mortar and pestle. Subsequently, approximately 5 grams of sample is put into a small milling disc, which is placed into a milling machine. The milling machine is run for one minute or until the consistency of flour. This is to reduce the grain size to 0.5 mm.

The grain size is further reduced to 0.05 mm with the use of the McCrone Micronising Mill. Micronization is conducted by placing 2.5 to 3 grams of the milled sample and 7 mL of ethanol in a sealed container along with 48 pieces of agate in the McCrone Micronizing Mill for 10 minutes. The liquidized samples are dried overnight in an oven at a temperature of 50°C.

The dried and powdered samples are then transferred into plastic XRD sample holders. The powder is packed into the shallow pit of the sample holder until it is flushed to the top surface. The edge of a thin section slide is used to pack the sample to prevent preferred orientation (e.g. micas lying flat). The XRD sample holders were loaded into the Bruker D8 Advance XRD machine a with a Lynxeye 1-dimensional position-sensitive detector (PSD) and CuKα radiation ($\lambda = 0.154$ nm) operated at 40mA and 40kV. The randomly oriented whole rock analysis with a step size of 0.01º from 2º to 65º (2θ) at a count time of 0.3 s (2θ) was carried out for about 34 minutes each sample. Exact instrumental analytical parameters used for the machine can be found in appendix D.

### *XRD Analysis*

Upon incidence of a monochromatic X-ray with the sample material, a scattering of X-rays occurs originating from atoms within the sample (Moore and Reynolds, 1997). In crystalline materials, the scattered X-rays undergo constructive and deconstructive interference; this is the process of diffraction. Constructive interference produces peaks on a diffractogram that are unique to the crystal

systems and the distinct lattices that fill the space, which indicate the mineral in question (Moore and Reynolds, 1997). The diffractogram can be further matched up against a large database of structure files. When an X-ray beam hits the sample and is diffracted, the distances between the planes of the atoms that comprise the sample (atomic spacing) can be found using Bragg's Equation (Eq. 4.1), illustrated in figure 4.2.

$$n\lambda=2dsin\theta$$

**Equation 4.1:** Bragg's Equation, where $n$ is a constant, $\lambda$ is the wavelength of the incident X-rays used, $d$ is the characteristic atomic spacing in the mineral lattice and $\theta$ is the angle between the incident rays and the atomic planes (Moore and Reynolds, 1997).

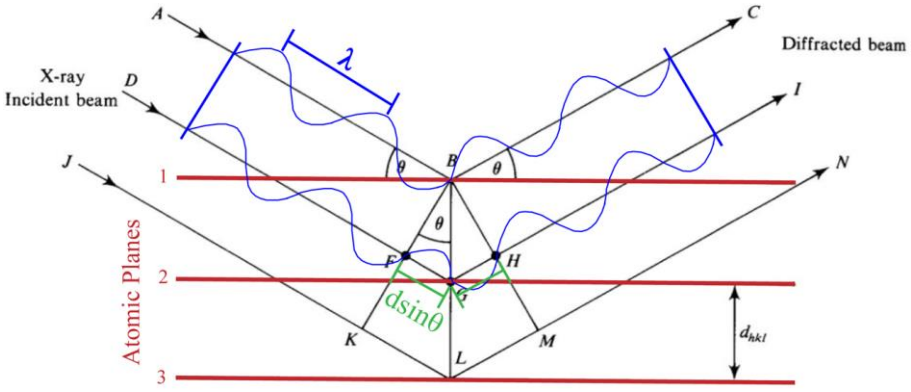


**Figure 4.2:** Illustration of Bragg's Equation, modified by Ilagan (2018) from Zoltai and Stout, (1984).

Bragg's equation is used to compute to the characteristic d-spacing for each atomic plane. A peak in the diffractogram indicates that the atomic planes of a mineral in the sample holds a d-spacing that will generate X-ray reflections for a particular $2\theta$ angle (Moore and Reynolds, 1997). Most materials are not single crystals, such as the sandstones used in this study. Therefore, a powder with randomly oriented crystallites is made from the original material. The powdered samples are scanned through a range of $2\theta$ angles such that all possible diffraction peaks from the powder are detected. The diffractogram contains peaks from all minerals in a given sample. The percentage of a certain mineral in a sample is taken to be proportional to its relative intensity. An X-ray diffractogram acquired in this study is presented in Figure 4.3. The d-spacing of several common minerals is presented in table 4.1. Diffrac Eva is typically used to identify the minerals. This study uses BGMN Profex to semi-quantify the minerals present.

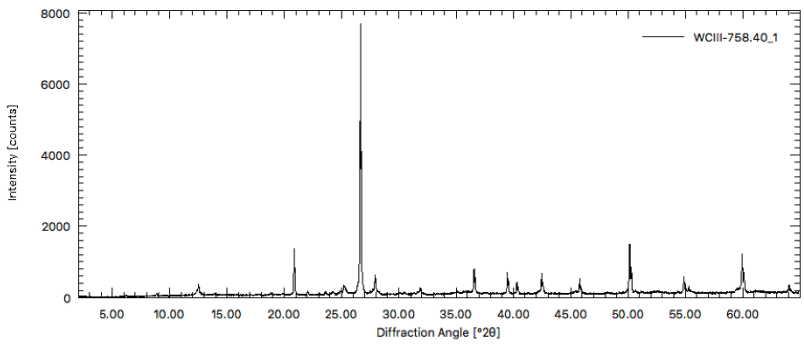


**Figure 4.3:** X-ray powder diffractogram for sample V1 at 758.70 m.

| Mineral | d-spacing (Å) | Mineral | d-spacing (Å) |
|---|---|---|---|
| Quartz | 4.26 | Calcite | 3.03 |
| Plagioclase | 3.19 | Kaolinite | 7.0 / 3.58 |
| K-feldspar | 3.24 | Illite | 10.0 |
| Muscovite | 10.01 | Chlorite | 7.0 / 3.54 |

**Table 4.1:** D-spacing of common minerals used in their identification.

### *Sources of Error and Limitations*

As does most laboratory testing, XRD analysis holds some degree of human error. The most significant source of error during XRD analysis is incorrect or inaccurate sample preparation. When packing the powdered samples into sample holders, it is essential that the sample is not compacted to the point at which a preferred orientation of the grains is reached. This can yield misleading diffractogram readings, especially for micaceous minerals, and the quantitative accuracy of the mineral composition is compromised.

If careful cleaning of the workspace and the equipment is not carried out between samples during the milling process, samples are at risk for contamination. Another source or error relates to the reliability of the software to assign a correct peak-mineral correspondence based on the database employed.

## 4.2.2 Optical Microscopy

Thin sections are 30 micron thin cuts of rock or epoxy impregnated sediment for the purpose of studying in a microscope. Nineteen thin sections were prepared for optical microscopic analysis. A thin section was not made for V15 (see appendix B) due to comprising significant amounts of clay particles, restricting the ability to distinguish between individual minerals during point counting. The thin sections were analyzed using a Nikon optical microscope and a PELCON Automatic Point Counter machine. All samples were analyzed under both plane polarized light (PPL) as well as cross-polarized light (XPL). Optical properties such a relief, colour, opacity, pleochroism, angle of extinction and crystal twinning were used in the identification of minerals.

### *Sample Preparation*

Before making thin sections, it is necessary to extract oil from any oil-saturated samples. Eleven oil-saturated samples were handed over to Head Engineer Kristian Backer-Owe, who carried out the oil extraction process at the University of Oslo. This is conducted by solvent separation using Dichloromethane (DCM+MeOH) with a volume ratio of 93:7 (K. Backer-Owe, Personal Communication, January 30$^{th}$, 2019). The samples were soaked for approximately 24 hours, after which most attainable oil is removed.

Once oil removal was complete, the samples were given to laboratory technician Salahalladin Akhavan, who prepared the thin sections at the University of Oslo. Prior to mounting, rock samples were vacuum-impregnated with blue epoxy to facilitate identification and illustration of features such as porosity that would otherwise be difficult to distinguish. The samples were then cut into 30 μm thin sections and mounted onto 2.5 x 4.5 cm glass slides.

## *Point count analysis*

Point counting is a technique used for determining the quantitative mineralogy of a thin section. Features studied through optical microscopy with respect to the point count analysis include detrital framework grains, cement, matrix, and porosity. These are statistically counted with the use of a PELCON Automatic Point Counter. Point counting is conducted using the methods outlined by Folk (1980). This method involves counting, identifying, and texturally classifying the individual constituents (e.g. framework grains, clays, etc.) that are encountered by the intersection of the cross-hairs along a linear path, with points spaced equidistantly from each other (0.5 mm in this study). The result shows how often each particular constituent was encountered during the analysis, which is automatically calculated as a percentage by the PELCON Automatic Point Counter software. The values obtained are taken to be related to the percent area of the respective constituents present in that thin section.

Three hundred points are counted per sample, which is considered to be representative for the sample under consideration. Identification is conducted according to aforementioned optical properties, using plane or cross-polarized light as appropriate. Visual assessment can be facilitated with the use of textbook examples, e.g. 'A Color Guide to the Petrography of Sandstones, Siltstones, Shales and Associated Rocks' (Ulmer-Scholle et al., 2014) and 'Atlas of Sedimentary Rocks' (Adams et al., 1984). During point-counting it is vital that methodical and consistent measures are fixed at the start and are maintained throughout each sample. On the point counter, eight categories are differentiated; however these are manually subdivided. Quartz is subdivided into monocrystalline and polycrystalline quartz. Feldspars are categorized into plagioclase feldspars, k-feldspars, or unknown. Leaching/alteration of feldspars can make them difficult to distinguish. Subdivisions for rock fragments include, but are not limited to, igneous epiclasts, mud rock fragments, mica, chert, and pseudomorphs. All subdivisions can be found in appendix E.

The results of the point-counted samples are plotted on a QFL ternary diagram (figure 3.1), and intergranular volumes are investigated. (section 5.2).

## *Limitations*

Thin section analysis relies on the level of experience of the interpreter. A common error in point counting is the misidentification of minerals or grains. Minerals that have been heavily altered can be difficult to identify to the untrained eye. Clay minerals are often optically irresolvable, and can only by accurately identified using a clay XRD analysis or SEM.

In addition, a basic assumption of modal analysis is that the slide is representative of the rock, and that the points selected on the slide is a good representation of the entire sample.

## Preservation of Detrital Grains

The degree of preservation of feldspar, lithic grains, and micas is noted during point counting. This is used as an indication of weathering intensity or post-depositional leaching intensity. Feldspars are unstable at surface in conditions where there are large influxes of meteoric water, resulting in feldspar dissolution and kaolinite precipitation. Table 4.2 presents the scale used in the determination of the preservation of a feldspar grain.

| Degree of Preservation | 1 Pristine | 2 High | 3 Intermediate | 4 Low |
|---|---|---|---|---|
| Description | Unweathered with excellent preservation of twins and grain shape. | Some evidence of weathering, however twins are clearly visible. | Grain surfaces are rough and twins are blurry or gone and grains are partially dissolved. | Grain is almost completely dissolved, impeding or almost impeding feldspar identification. |

**Table 4.2:** Scale for determining preservation degree in feldspars.

The degree of preservation of rock fragments is also noted. Table 4.3 was used in this assessment, particularly with micas as they are a good indicator of preservation degree. Similar to feldspar, they are also unstable in meteoric waters, resulting in the precipitation of kaolinite in the pore space.

| Degree of Preservation | 1 Pristine | 2 High | 3 Intermediate | 4 Low |
|---|---|---|---|---|
| Description | Unweathered with no evidence of mechanical deformation. | Some evidence of mechanical deformation. | Grain are deformed and squeezed into the IGV. | Almost completely dissolved and altered; it is recognized by molds. |

**Table 4.3:** Scale for determining preservation degree in rock fragments.

The dissolution of grains creates secondary porosity, which differs from primary porosity since it is a post-depositional process. It is possible to infer the original grain composition using SEM if there are remnants of the original composition. The dissolution of minerals can result in a weakened grain framework, resulting in further mechanical compaction.

### 4.2.3 Scanning Electron Microscopy (SEM)

A scanning electron microscope (SEM) is an instrument that generates high-resolution images by focusing a beam of high energy electrons onto the surface of a solid specimen (Swapp, 2019). The emitted signals convey information about the sample, including the morphology, chemical composition, and crystalline structure (Swapp, 2019). Scanning electron microscopy is conducted on selected samples, primarily to confirm minerals detected through bulk XRD and to help distinguish and identify the optically irresolvable authigenic and detrital clays.

An electron-dispersive X-ray spectrometer (EDS) can be integrated into the SEM. This aids in distinguishing mineral composition by comparing the EDS spectra acquired to previously recorded mineral spectra (Reed, 2005). Elemental mapping can be conducted, whereby an image is created that records the distribution and the intensity of elements present.

Prior to SEM analysis, thin sections are coated with a conductive material, typically carbon, to reduce excess charge from the electron beam. Siri Simonsen from University of Oslo prepared the thin sections for SEM analysis. The prepared thin section is loaded into Hitachi SU5000 FE-SEM (Schottky FEG) with a Bruker XFlash30 EDS at the University of Oslo. Backscatter electron imaging (BEI) and secondary electron imaging (SEI) are used on the samples.

For cathode luminescence (CL) images, a UVD detector was used. This only works in low vacuum conditions, so the pressure was lowered. This is used in order to distinguish between detrital and quartz cement.

## 4.2.4 Textural Analysis

Textural analysis involves the determination of grain size, sorting, roundness, grain contacts, sphericity, intergranular volume (IGV), and porosity. During point counting, each framework grain encountered is classified with respect to roundness, sphericity, and grain contacts. Furthermore, intergranular volume and porosity of each sample is determined though point counting. The determination of grain size and sorting is conducted separately.

### *4.2.4.1 Grain Size and Sorting*

Grain size analysis is conducted by measuring at least 200 random grains per thin section along their long axis. Measurements are exported to Excel and converted to the Phi scale using equation 4.2, in line with the Wentworth grain size classification (figure 4.4).

$$\phi = -\log_2 d$$

**Equation 4.2.** Where $\phi$ relates to grain size as used in the Wentworth (1922) grain size classification scheme, and $d$ is the measurement in mm for the long axis of the grain.

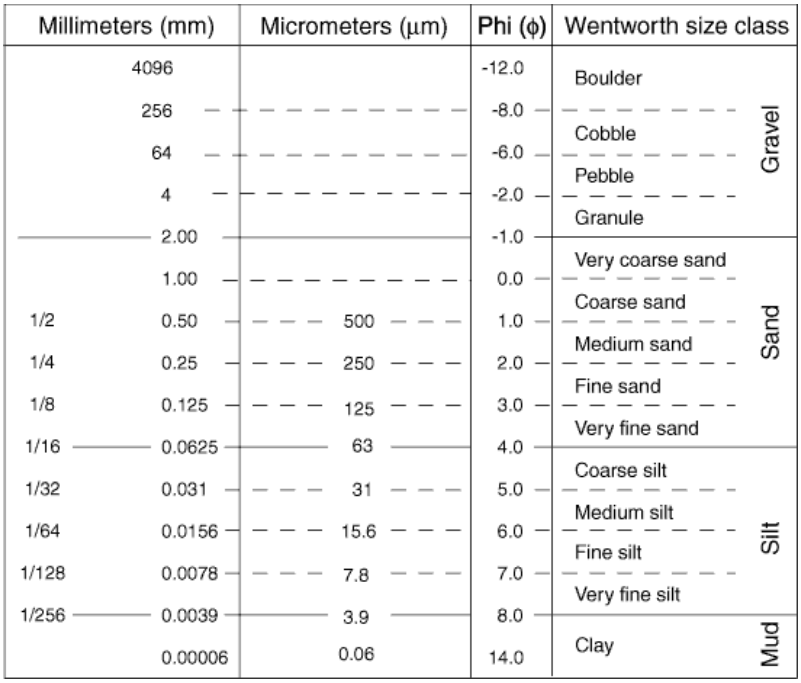


**Figure 4.4.** Definition of sediment grain sizes as defined by Wentworth (1922). Grain sizes were measured in mm along the long axes and converted to Phi values ($\phi$).

The grain sorting can be calculated by taking the standard deviation of the size of all measured grains in a sample (eq. 4.3), which is used together with the classification system in table 4.4. Furthermore, the sorting can be illustrated in a cumulative curve of the grain sizes. A steep curve indicates good sorting, as most grains lay fall in the same class in the Wentworth classification, whereas a more gradual curve indicates poorer sorting (Nichols, 2009). Visual comparators given by Jerram (2001) are presented in figure 4.5, which can be useful in interpretation.

$$Standard\ Deviation = \frac{\Phi_{84} - \Phi_{16}}{4} + \frac{\Phi_{95} - \Phi_{5}}{6.6}$$

**Equation 4.3:** Standard deviation equation used to calculate sorting from phi values from the sample in question, as given by Folk (1980).

| STANDARD DEVIATION (FOLK, 1980) | Φ-VALUE |
|---|---|
| Very well sorted | < 0.35 |
| Well sorted | 0.35 – 0.50 |
| Moderately well sorted | 0.50 – 0.71 |
| Moderately sorted | 0.71 – 1.00 |
| Poorly sorted | 1.00 – 2.00 |
| Very poorly sorted | 2.00 – 4.00 |
| Extremely poorly sorted | > 4.00 |

**Table 4.4:** Verbal terms and corresponding standard deviation values as defined by Folk (1980). Visual comparators for sorting are presented in figure 4.5.

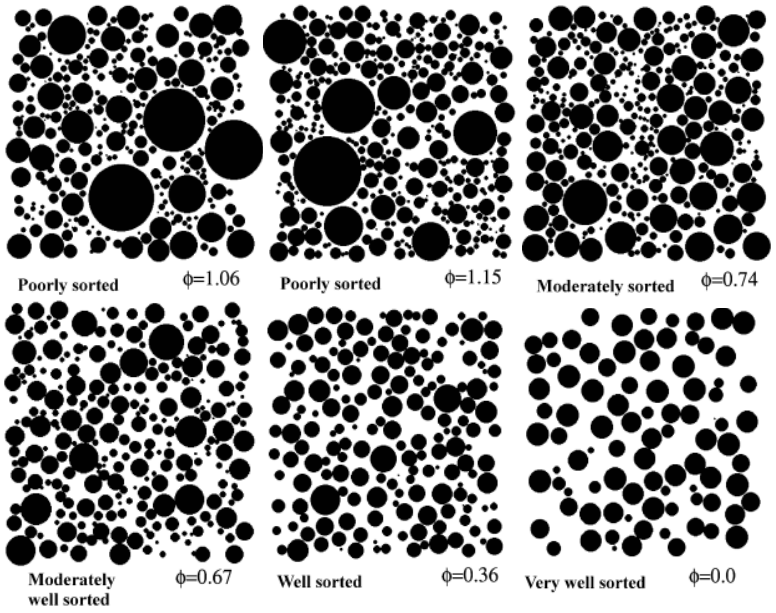


**Figure 4.5:** Grain size sorting visual comparative modified from Jerram (2001) presented with the associated verbal term and standard deviation from Folk (1980), as presented in table 4.4.

### *4.2.4.2 Roundness and Sphericity*

Depending on method of interpretation, grain shapes can be categorized into various subdivisions. Two are used in the analysis in this study: roundness and sphericity. Grain roundness is defined as the description of the relative sharpness of grain corners and edges, whereas sphericity is defined as the degree to which a grain approaches a spherical shape (Boggs, 2009). Although mathematical expressions exist for both (e.g. Wadell, 1932. Sneed and Folk, 1958), visual comparators from Powers (1953) are used in this study when interpreting the sphericity and roundness of grains.

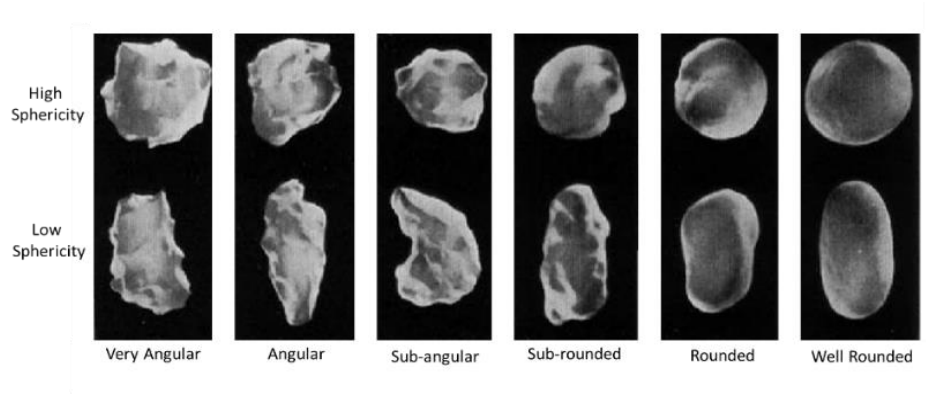


**Figure 4.6:** Visual comparators used when assessing roundness and sphericity. Modified from Powers (1953).

### *4.2.4.3 Grain Contacts*

As sediment is subject to mechanical compaction, a reduction of intergranular volume (IGV) will occur as a result of the reorientation and repacking of grains. Chemical compaction is initiated at temperatures around 65°C, whereby pressure dissolution redistributes the accumulating load over a larger area. With increased compaction, grain contacts typically progress from floating, to tangential, to long, to concavo-convex and finally to sutured as the degree of packing increases and subsequently chemical compaction initiates. These contacts are defined by Taylor (1950) and are illustrated in figure 4.7.

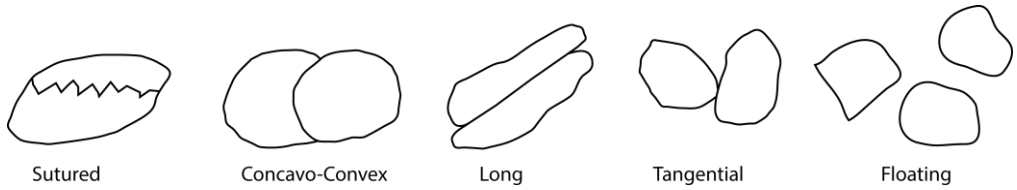


**Figure 4.7:** Schematic diagram showing contacts of grains in sandstones, modified from Tamrakar (2007). Original definitions of contacts are from Taylor (1950).

### *4.2.4.4 Intergranular Volume (IGV) and Porosity*

The intergranular volume (IGV) is the sum of the intergranular porosity, depositional matrix (clay and silt particles between framework grains) and intergranular cement as shown in equation 4.4 from Paxton et al. (2002). In this study and by convention it is measured through point counting thin sections, yielding a percentage value. IGV varies a small amount with sorting, however is not influenced by grain size to a great degree.

$$IGV = V_{porosity} + V_{matrix} + V_{cement}$$

**Equation 4.4**: IGV calculated from volume percentages, from Paxton et al. (2002). The 2D percentage acquired from point counting is taken to translate to respective 3D percentage.

The IGV can be plotted against depth to create an intergranular volume compaction curve. This aids in establishing limits to mechanical compaction, cementation and pressure grain solution. Additionally, equations 4.5 and 4.6 can be applied to compute porosity losses as a result of compaction and cementation, respectively. The computed values can then be plotted in the diagram in figure 4.8 created by Houseknecht (1987). Based on empirical data, most moderate- to well-sorted sands hold approximately 40% porosity at the time of deposition and is thus typically assumed to be the starting or original porosity in equations 4.5 and 4.6 (Bjørlykke and Jahren, 2015). The vertical axis in figure 4.8 represents the percent of original porosity destroyed by compaction as computed by equation 4.5, whereas the horizontal axis represents the percent of original porosity destroyed by cementation as computed by equation 4.6. Lines of equal intergranular porosity plot as straight lines on the diagram, from which intergranular porosity can be estimated.

In the application of the diagram in figure 4.8, it is assumed that porosity loss is independent of grain size but can vary with grain sorting (Houseknecht, 1987). Grain-supported, moderate- to well-sorted samples containing small amounts of matrix (clay-sized particles) are point counted in this study. Because Houseknecht (1987) does not incorporate the depositional matrix in intergranular volume calculations, the diagram as applied in this study will lead to overestimations of porosities. Because matrix material decreases friction between framework grains and deforms in a ductile manner, it plays an important role in filling available pore space and thus aids mechanical compaction. As such, the matrix is included in the Houseknecht (1987) equations 4.5 and 4.6 to calculate intergranular porosity (equation 4.7).

$$Percent\ original\ porosity\ lost\ from\ compaction = \frac{40 - IGV}{40}\ x\ 100$$

**Equation 4.5:** Porosity loss from compaction, result to be used in vertical axis in figure 4.8 (Houseknecht, 1987). Note that 'IGV' includes matrix in this study, contrary to the study by Houseknecht (1987).

$$Percent\ original\ porosity\ lost\ from\ cementation\ = \frac{cement}{40}\ x\ 100$$

**Equation 4.6:** Porosity loss from compaction, result to be used in horizontal axis in figure 4.8 (Houseknecht, 1987).

$$Intergranular\ porosity = intergranular\ volume - (cement + matrix)$$

**Equation 4.7:** Intergranular porosity from Houseknecht (1987), modified to include depositional matrix in accordance with Paxton et al. (2002).

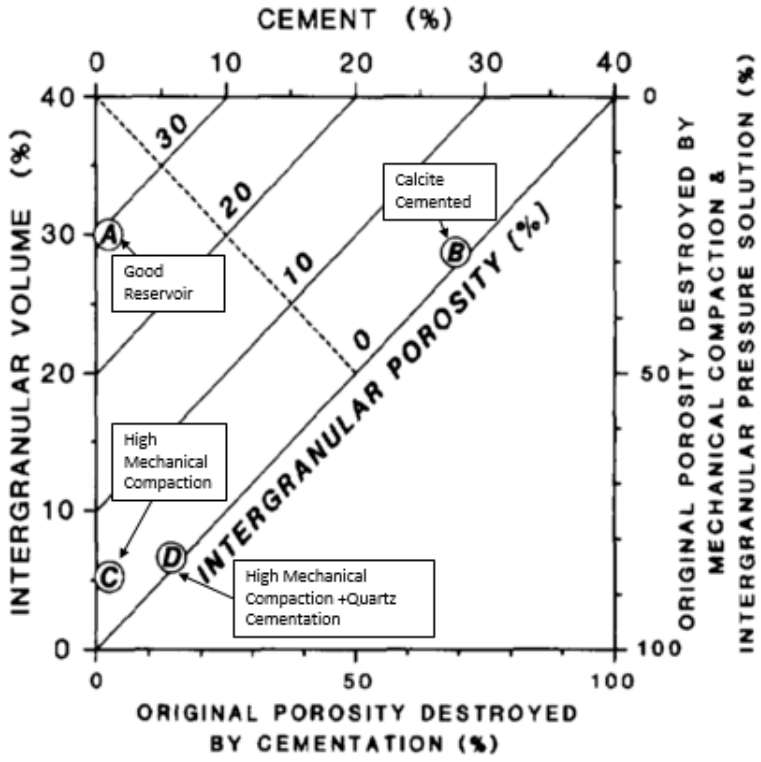


**Figure 4.8:** Diagram modified after Houseknecht (1987) demonstrating porosity loss from mechanical and chemical compaction, with the application of equations 4.5 and 4.6. The diagonal dotted line separates dominating pore-reducing processes. Placement in the upper right area indicates cementation has been the dominant process. Placement in the lower left indicate that mechanical compaction processes dominate.

### *4.2.4.5 Porosity and Permeability*

Porosity and permeability from core plug data are provided by OMV Norge AS. These are the two controlling factors when determining the quality of a sandstone reservoir. Porosity is essential to store hydrocarbons, whereas permeability allows the rock to transmit fluids (Tissot and Welte, 1984). It follows that pore diameters are of importance; if smaller than a minimum size, capillary forces are too high to overcome and fluid flow is then negligible (Bjørlykke and Jahren, 2015). As such, a relationship between porosity and permeability exists whereby fine-grained sandstones are generally less permeable than medium to coarse grained sandstones. Reservoir appraisal cutoff values have been established by Tissot and Welte (1984) and will be used when assessing core plug data (table 4.5).

| Porosity (%) | Permeability (mD) | Appraisal |
|---|---|---|
| 0-5 | - | Negligible |
| 5-10 | - | Poor |
| 10-15 | 1.0-10 | Fair |
| 15-20 | 10-100 | Good |
| 20-25 | 100-1000 | Very Good |

**Table 4.5:** Reservoir appraisal cutoffs as defined by Tissot and Welte (1984).

# 4.3 Petrophysical Analysis

A petrophysical evaluation of Wisting Central III is undertaken based on well log data. The primary target is to estimate uplift and to investigate compaction trends in the whole drilled section. Theoretical equations are applied in estimating the porosity. Analysis was performed with the use of HampsonRussell software and Excel. Stated depths are in measured depth (MD) in meters from the kelly bushing (KB). Well tops were given by OMV Norge AS. Logs utilized are the gamma ray, neutron, density, and sonic logs.

## 4.3.1 Well Logs

### *4.3.1.1 Gamma Ray (GR) Log*

*Principle*

The gamma ray (GR) log measures the total natural gamma radiation from a formation, and is unaffected by the fluid content (Rider, 1986). Gamma radiation stems from naturally-occurring potassium, uranium, and thorium, which emit gamma rays spontaneously. Typical uses for the gamma ray log are (1) lithology discrimination, (2) shale volume estimation, and (3) analysis of facies and depositional environment (Mondol, 2015). The high vertical resolution of the GR log also makes it well-suited for depth matching and fine-scale correlation. The unit of gamma ray log is API (American Petroleum Institute) (Rider et al, 1996).

*Application*

The difference in radioactivity between shales and sandstones/carbonates allows the gamma tool to distinguish between shales and non-shales. Shales show the highest gamma ray values, while evaporites, coal, clean sandstones, and limestone hold the lowest values. Hydrocarbon source rocks create marked responses on the gamma ray log due to higher uranium content than other shales (Mondol, 2015). Although useful in distinguishing lithologies, the GR log cannot uniquely define any lithology. For example, a clean sandstone may contain feldspars, giving the sandstone higher gamma ray values than would be expected from a clean sandstone (Mondol, 2015).

### *4.3.1.2 Neutron Log*

*Principle*

A neutron log records a formation's reaction to bombardment by a neutron source, which sends radiation into the rocks. The measured unit is 'neutron porosity units', which indicates the 'hydrogen index', or the formation's richness in hydrogen (Rider, 1986). The absorption of the neutron radiation is a function of the hydrogen index. Since most of the hydrogen in rocks is present as brine, the neutron log gives an expression of the brine content and therefore the porosity (Mondol, 2015).

*Application*

The neutron log is used to measure porosity. It is an also an exceptional discriminator between gas and oil/water. When the porosity is filled with gas, the neutron log is far too low because gas contains less hydrogen compared to water and oil. This is the 'gas effect'. On the other hand, the neutron log will record higher porosities in mudstones due to the presence of hydrogen in clay minerals. This is the 'shale effect'. Because carbonate minerals contain almost no hydrogen, limestones give reliable values on the neutron log (Mondol, 2015; Rider, 1996). The neutron log is typically combined with the density log, which together offers one of the best lithology indicators available (Rider, 1986)

### *4.3.1.3 Density Log*

*Principle*

The density log records a formation's bulk density in g/cm$^3$. This includes both the solid matrix and the fluid contained in the pore space (Rider, 1986). An induced radiation tool bombards the formation with gamma radiation, and the amount that returns to the sensor is measured. This is affected by the quantity of electrons (Mondol, 2015). A rock with a high bulk density has a large quantity of electrons and therefore attenuates the gamma rays greatly. This results in a low gamma ray count rate that returns to the sensors. A rock with a lower bulk density has a smaller quantity of electrons and therefore attenuates the gamma rays less than a high density formation. This results in a high gamma ray count that return to the sensors.

*Application*

Porosity can be estimated from the density log, and indirectly the hydrocarbon density. It is also used calculating the acoustic impedance (Rider, 1986). It is also a useful lithology indicator, especially when combined with the neutron porosity log (Rider, 1986). The log can also aid in identifying overpressure and fracture porosity (Rider, 1986).

### *4.3.1.3 Sonic Log*

*Principle*

The sonic log provides information on a formation's interval transit time, $\Delta t$. It records the reciprocal of the velocity and is in $\mu$s/ft (Mondol, 2015; Rider, 1996). It is a measure of the capacity of the rock to transmit acoustic waves, which varies primarily with lithology and porosity. A probe on the logging tool sends out acoustic pulses that travel in the formation to the other end of the logging tool, and the time this takes is recorded (Mondol, 2015). Therefore, in a gas or oil filled sand, the travel time is expected to be higher than recorded in a brine filled sand.

*Application*

When solved for the P-wave velocity and multiplied with the density, the acoustic impedance can be found. It can also be used in identifying the transition zone from mechanical to chemical compaction, identifying overpressure zones, determining carbonate intervals, and calculating uplift (Mondol, 2015).

## 4.3.2 Porosity Estimation

Porosity is the ratio of pore volume to bulk volume within the rock. However, this is a simplistic explanation, which may cause problems when it comes to real rocks with water in the pore space. In sandstones, some pore space may be completely isolated, and therefore is not capable of contributing to the transmission of fluid throughout the rock. This leads to two ways of describing porosity: total and effective. Effective porosity encompasses all pore volumes that are capable of transmitting fluid.

There are no logs which measure porosity directly, but it can be estimated from the neutron or density logs as shown here.

### *4.3.2.1 Porosity from Density Log*

As described in section 4.3.1.3, for the density log, the count of gamma rays returning to the sensor is proportional to the electron density of the formation. This is related to formation bulk density through a constant (Mondol, 2015). The bulk density of a formation is a function of matrix density, porosity, and the density of the pore-filling fluid. An estimation of porosity from density can then be calculated using the formula (Rider, 1986):

$$\phi_D = \frac{\rho_{ma} - \rho_b}{\rho_{ma} - \rho_{fl}}$$

**Equation 4.8:** Porosity from density log equation, where $\rho_{ma}$ is the density of the matrix, $\rho_b$ is the density from the density log, and $\rho_{fl}$ is the density of the fluid in the pore space.

Equation 4.8 was used to calculate the 'porosity from density' log, with standard values as dedined in HampsonRussell for brine and matrix used ($\rho_{ma}$= 2.65 g/cm$^3$ and $\rho_{fl}$ = 1.09 g/cm$^3$).

From equation 4.8, it is clear that by choosing different values for the matrix and fluid, the porosity can be easily over- or underestimated. Because of its low density, gas can appreciably affect the porosity log from density, yielding the estimated porosity greater than the true porosity when brine-saturation is assumed. However, the tool measures the invaded zone, so the relevant fluid is the mud filtrate in most circumstances (Mondol, 2015).

### *2.2.6.2 Porosity from Neutron-Density Combination*

A combination of the density and neutron logs is used to estimate porosity that is, to a greater extent, free of lithology effects (Mondol, 2015). Because neutron logs have many sensitivities and rarely measure true porosity, they are almost exclusively used with density logs. Porosity derived from each log (neutron and density) suffers from uncertainties related to the lithology. Thus, by averaging them, the lithological effects can cancel out (Mondol, 2015). The true porosity is estimated by applying equation 4.9.

$$\phi = \sqrt{\frac{{\phi_N}^2 + {\phi_D}^2}{2}}$$

**Equation 4.9:** Equation used to calculate a combined porosity from neutron porosity and porosity from density, where $\phi_N$ is neutron porosity and $\phi_D$ is porosity from density log, as calculated by equation 4.8.

## 4.3.3 Uplift Estimation

### *4.3.3.1 Geothermal Gradient*

The geothermal gradient is calculated in order to estimate the depth at which the transition zone from mechanical to chemical compaction (~65-70℃) occurs at present day. It can give an indication of the maximum temperature the sediments have been exposed to. It is calculated with the use of the bottom hole temperature in the following equation:

$$g_G = \frac{T_{BT} - T_{SF}}{D_{bh} - (D_w + KB)} * 1000$$

**Equation 4.10:** Geothermal gradient, where $T_{BT}$ is the bottom hole temperature, $T_{SF}$ is the seafloor temperature, $D_{bh}$ is the maximum depth of the well (in m TVD), $D_w$ is the depth to the sea floor to sea level, and $KB$ is the height of the kelly bushing above sea level. $T_{SF}$ is taken to be 4℃ because water is the most dense at that temperature.

### *4.3.3.2 Uplift Estimation*

To estimate uplift, the sonic log is converted to P-wave velocity to go from the sonic log unit of µs/ft to the $V_p$ log unit of m/s. This is subsequently plotted against measured depth, along with the 50:50 kaolinite-silt mixture compaction trend from Mondol (2009). This curve is used because it is considered most representative for the succession of rocks the well logs encompass. It is, however, not suitable to use in comparison with clean sandstones – as such, these points should be removed.

The transition zone is interpreted to be where siliciclastic sediments reach velocities of 3000 m/s or more, and a jump to higher velocities is seen in the data. Such high velocities are not found in sediments that have undergone only mechanical compaction (N. Mondol, Personal Communication, January 22nd, 2018). To estimate uplift, the interpreted transition zone is adjusted according to the aforementioned Mondol (2009) reference line. An estimate of uplift can also be given by subtracting the depth of the interpreted transition zone that had formed prior to uplift from the depth of the expected present-day transition zone.

# Chapter 5: Results

This chapter illustrates the results from the sedimentological, petrographic, and petrophysical methods that are presented in Chapter 4. The petrographic results are acquired from 20 samples extracted from the Wisting Central III core, comprising Late Triassic-Early Jurassic sandstones of the Fruholmen, Nordmela, and Stø formations. Note that no samples are available from FA1 (described in section 5.1). Hence, a presentation of the core log of this facies association is given with no further detail.

## 5.1 Sedimentological Analysis

Results from the sedimentological logging of the drill core, conducted as described in section 4.1, are illustrated in this section.

The studied core interval through well Wisting Central III penetrates Mesozoic reservoirs belonging to the Late Triassic to Early Jurassic Realgrunnen Subgroup. In this well, the Fruholmen Formation, Stø Formation, and a possible condensed and/or eroded interval of the Nordmela Formation are present.

The cored interval has been divided into facies based on observations made from logging, which include composition, structures, texture, colour, and biogenic features (see chapter 4). Facies are subsequently grouped into facies associations, from which the interpretation of depositional environments are deduced. Table 5.1 presents the 16 facies that have been recognized, while table 5.2 provides a summary of the 9 facies associations they are grouped into. The facies associations are further elaborated upon in the text. Furthermore, the Brentskardhaugen bed at the transition of the Stø to the Fuglen Formation is discussed briefly. In figure 5.1, the condensed log is presented, following the tables detailing facies and facies associations.

| Lithofacies | Lithology | Structures and Traces | Bed Thickness | Boundaries | Process |
|---|---|---|---|---|---|
| **F1** | Mudstone | Weakly laminated to homogenous | <1 - 20 cm | Normally gradational, occasionally sharp bases. Sharp and occasionally erosional tops. | Hemipelagic suspension fallout and gravity current (fluid muds) |
| **F2** | Siltstone to very fine-grained sandstone | Structureless or planar laminated; occasional ripple lamination | <1 – 10 cm | Sharp or gradational bases and tops | Waxing and waning flow deposition through river-flood periods; possible dilute turbidity currents |
| **F3** | Siltstone to very fine-grained sandstone | Unidirectional ripple lamination | <1 – 10 cm | Sharp erosive base and top | Traction features formed in lower flow regime conditions; asymmetrical current ripples a result of unidirectional flows |
| **F4** | Siltstone to fine-grained sandstone | Wave ripple lamination, low angle cross lamination, ?small scale hummocky cross stratification | <1 – 10 cm | Bed bases are sharp; bed tops are sharp to gradational | Storm and wave generated oscillatory currents |
| **F5** | Fine-grained sandstone | Low angle, swaley, and hummocky cross-stratification | 10 cm – 1 m | Sharp erosive base; erosive or gradational top | Migration of subaqueous bedforms produced by combined flows |
| **F6** | Fine-grained sandstone | Structureless to weakly developed planar stratification | 10 cm – 1 m | Gradational bases and tops | Unidirectional Traction Currents, high energy |
| **F7** | Fine-grained sandstone | Planar Stratification; picked out by concentrations of organic debris and mudstone pebbles | 60 cm – 3 m | Sharp or gradational bases and tops | Unidirectional Traction Currents, intermittent energy |
| **F8** | Heterolithic | Flaser beds; discontinuous drapes of silt and mud alternating with bipolar current ripple laminated sandstones | 30 cm – 1 m | Gradational bases and tops | Alternation of current action and slack-water; high energy |
| **F9** | Heterolithic | Wavy beds; continuous drapes of silt and mud alternating with current bipolar ripple laminated sandstones | 40 cm – 1 m | Gradational bases and tops | Alternation of current action and slack-water; moderate energy |
| **F10** | Heterolithic | Lenticular beds; discontinuous lenses of bipolar current ripple laminated sandstones encased in silt and mud | 5 cm – 1m | Gradational bases and tops | Alternation of current action and slack-water; low energy |
| **F11** | Fine-to medium-grained sandstone | Dune-scale tabular cross bedding, mantled with silt and organic debris | 10 cm – 1 m | Sharp bases and gradational or sharp tops | Migration of tidal dunes |
| **F12** | Fine- to medium-grained sandstone | Pebble grade mud clasts in structureless sandstone matrix | 30 cm – 1 m | Sharp or gradational bases and tops | Moderate to high energy traction cuurents combined with minor cutbank slumping |
| **F13** | Conglomerate | Cobble to boulder grade clasts in a fine-grained structureless sandstone | 50 cm – 1 m | Sharp or gradational bases and tops | Moderate energy traction currents combined with significant cutbank slumping |
| **F14** | Fine- to medium-grained sandstone | Structureless to weakly developed low angle cross-stratification | 30 cm – 1 m | Sharp or gradational bases and tops | Upper plane bed to Swash zone action |
| **F15** | Medium-grained sandstone | Trough cross-stratification | 1 m – 1 m | Sharp or gradational bases and tops | Migration of dunes via unidirectional traction currents |
| **F16** | Conglomerate | Granule to pebble grade clasts in siltstone to medium-sand matrix | 1 cm – 5 cm | Sharp bases and tops | Reworking via transgressive or regressive ravinement |

**Table 5.1:** Summary of facies observed in the drill core. These are grouped into facies associations, as presented in table 5.2.

| Facies Association | Typical Facies | Formation/Member | Depth Interval (m) | Interpretation |
|---|---|---|---|---|
| **FA1** | F1, F2, F3, F4, F5 | Fruholmen/Akkar | 759.00 – 761.65<br>755.00 – 755.70 | Storm-Influenced Prodelta |
| **FA2** | F4, F5, F16 | Fruholmen/Akkar | 755.70 – 759.00 | Storm-Influenced Delta Front |
| **FA3** | F6, F7, F16 | Fruholmen/Reke | 744.50 – 755.00 | Delta Mouth Bar |
| **FA4** | F8, F9, F10, F11 | Fruholmen/Reke | 719.15 – 744.50 | Tidal Flat |
| **FA5** | F4, F12, F13 | Fruholmen/Reke | 699.50 – 719.15 | Multi-Story Meandering Channel |
| **FA6** | F3, F8, F12, F13 | Fruholmen/Reke | 695.80 – 699.50 | Tide-Influenced Distributary Channel |
| **FA7** | F1, F2 | Fruholmen/Reke | 688.00 – 695.80 | Estuarine Mud |
| **FA8** | F8, F11 | Nordmela | 684.75 – 688.00 | Compound Dune Complex |
| **FA9** | F14, F15 | Stø | 666.25 – 684.75 | Upper Shoreface to Foreshore |

**Table 5.2:** Outline of facies associations and respective interpretations of the depositional environment.

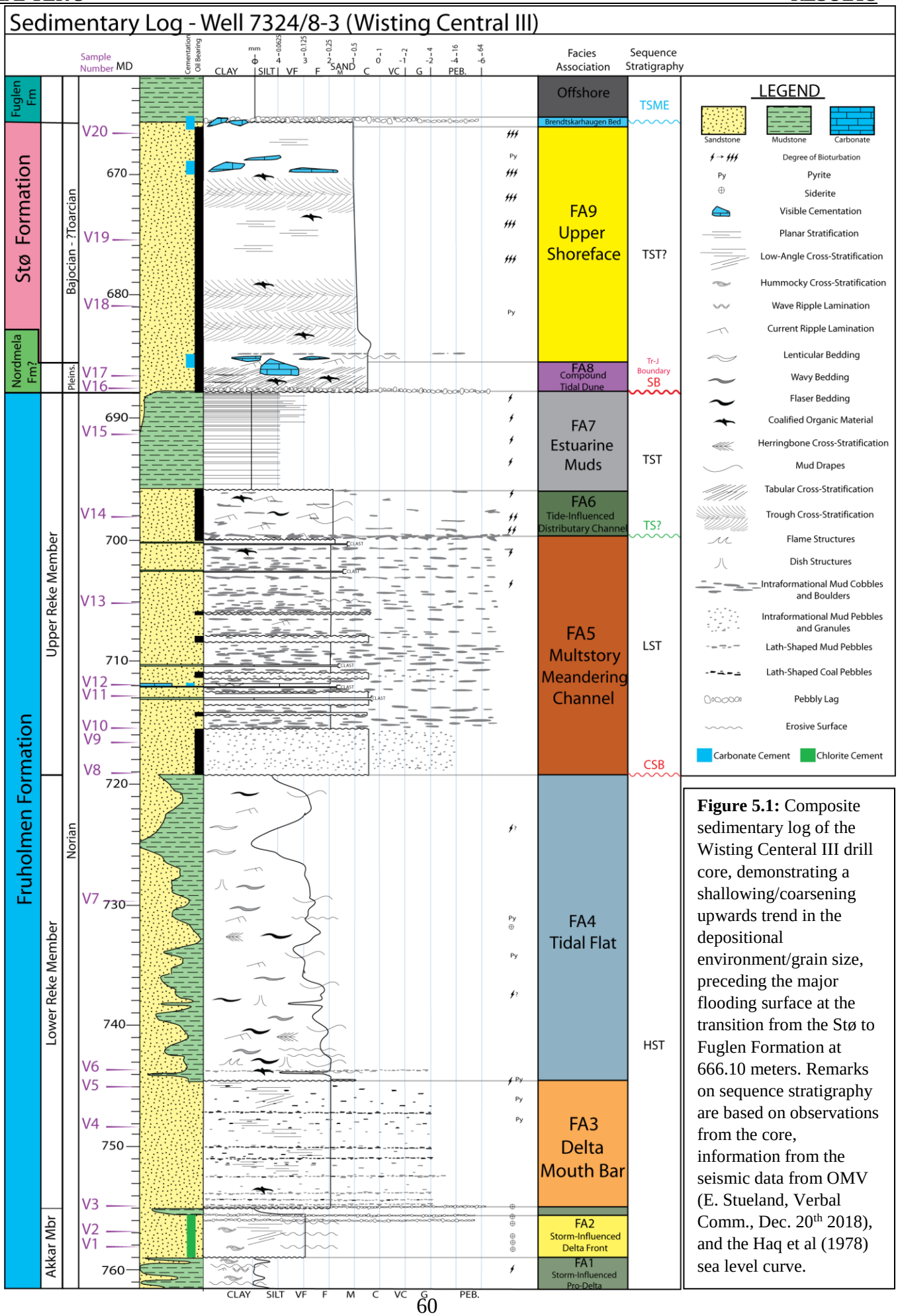


**Figure 5.1:** Composite sedimentary log of the Wisting Centeral III drill core, demonstrating a shallowing/coarsening upwards trend in the depositional environment/grain size, preceding the major flooding surface at the transition from the Stø to Fuglen Formation at 666.10 meters. Remarks on sequence stratigraphy are based on observations from the core, information from the seismic data from OMV (E. Stueland, Verbal Comm., Dec. 20th 2018), and the Haq et al (1978) sea level curve.

## 5.1.1 Fruholmen Formation – Akkar Member

### *FA1 – Storm-Influenced Pro-delta*

*Observations:*

Facies Association 1 (FA1) occurs exclusively in the bottommost portion the cored Akkar member of the Fruholmen Formation at two intervals: 759.00 to 761.65 m and 755.00 to755.70 m, totaling 3.35 meters of the logged succession. FA1 is highly heterolithic throughout, consisting of cm-to decimeter scale beds of homogenous to weakly laminated mudstone (F1), interbedded and alternating with siltstone and sandstone facies. Oscillatory and unidirectional wave ripples and planar lamination, in silt- and very fine-grained sandstones (F3, F4), are the most prevalent structures. Structureless siltstones (F2) also frequently occur. Hummocky cross stratification is present in sparse ~30 cm thick lensoidal sand bodies (F5). Sharp bases together with normal grading from silt or sandstone facies to mudstone facies is common throughout FA1. Wave ripples are often draped with structureless mudstones (F1). Infrequently present bidirectional current lamination and syneresis cracks are observed. FA1 is overall weakly bioturbated (BI 1) with locally moderate bioturbation (BI 2-4). Bioturbation is largely absent in mudstone beds, being confined to the silt- and sandstone beds. Trace fossils identified are *Teichichnus, Rhizocorallium, Planolites,* and *Phycosiphon.* Figure 5.2 presents core photographs to illustrate sedimentary structures and trace fossils common to FA1.

*Interpretation:*

The deposits of FA1 represent a storm-influenced pro-delta setting. The processes yielding the succession are interpreted as (1) hyperpycnal flows originating from riverflood events, forming dilute turbidity currents, together with partial reworking by storm waves, (2) combined flow as a result of storm activity – involving unidirectional geostrophic flow and wave induced oscillatory flow, and (3) interflood background sedimentation from suspension, and/or deposition of fluid mud, formed due to the intense wave action generated by storms, suspending previously deposited mud.

(1) is evidenced by the mudstone facies alternating with the frequently occurring rippled, normally graded silt-and sandstone beds with erosive bases, as well as structureless to planar laminated siltstones beds – typical of deposits from hyperpycnal density underflows initiated at the river mouth during high-discharge floods (Mulder and Syvitski, 1995; Wright et al., 1988). (2) is evidenced by the sparsely occurring lensoidal sandstone bodies containing hummocky cross-stratification, characteristic of products of combined flows generated by storm events (Dumas et al., 2005). Such structures are commonly developed between fair-weather and storm wave base, consistent with the pro-delta interpretation (Dott and Bourgeois, 1982). (3) is evidenced by the numerous intervals of mud, which is often deposited from suspension in low-energy conditions. However, a significant portion of the muds,

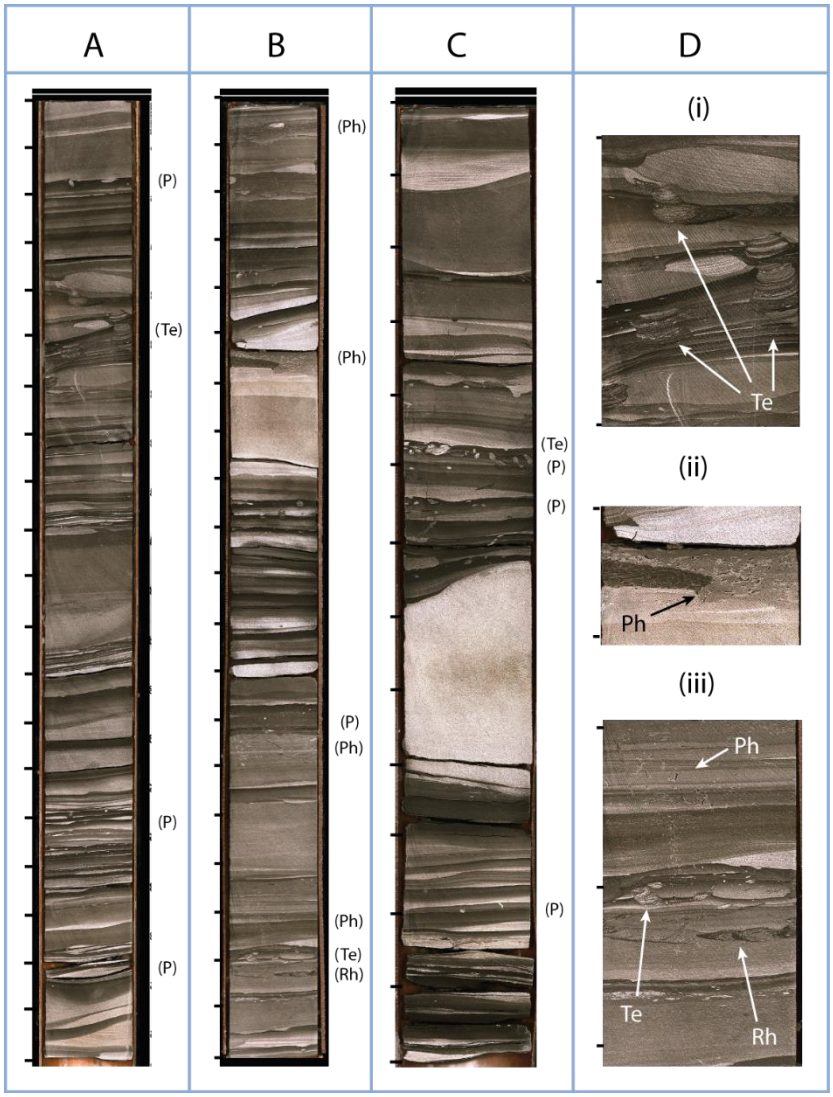


**Figure 5.2:** Core photos showing variety of facies common to FA1. 5 cm are between each tick.

***(A)*** Interval 759-760 m. Sharp based, normally graded siltstone beds frequently containing wave ripple and planar lamination. Homogenous mudstones are present in between. Trace fossils present are *Planolites* (P) and *Teichichnus* (Te). ***(B)*** Interval 760-761 m. Structureless to weak planar laminated silt- to fine grained sandstone with both gradational and sharp bases and tops. Some wave-ripple lamination is extant at the top. A diverse assemblage of trace fossils include *Phycosiphon* (Ar), *Teichichnus, Rhizocorallium* (Rh), and *Planolites.* ***(C)*** Interval 761-761.65. Hummocky-cross stratification is present in prominent lensoidal sandbody at 761.30 to 761.45. ***(D)*** Close up of trace fossils (i) *Teichichnus* (ii) *Phycosiphon* (iii) Proximally spaced *Rhizocorallium, Teichichnus,* and *Phycosiphon.*

especially those that are homogenous and absent of bioturbation, may represent fluid mud deposits. Fluid mud deposits are characterized by cm- to decimeter thick beds with lack of lamination and bioturbation and are interbedded with graded silt- and sandstone beds, such as that found in FA1. (Allison et al., 2000; Kuehl et al., 1986; MacEachern et al., 2005). They may originate from hyperpycnal flows or the resuspension of muds via storms. Sedimentation rates of fluid muds are much higher than by muds from suspension settling; thus likely representing a larger thickness of the muds in the section, but less time (Neill and Allison, 2005). Similarly, the silt- and sandstone bodies in FA1 represent a small fraction of the time muds deposited from settling do, despite constituting over half of the vertical succession of FA1.

The trace fossil assemblage indicate FA1 is of *Cruziana* ichnofacies, typical of mid to distal continental shelf environments above storm wave base, thus in agreement with a pro-delta setting (Benton and Harper, 1997). Synaeresis cracks are related to variable salinity, likely associated with the introduction of fresh water by means of hyperpycnal flows.

## *FA2 – Storm-Influenced Delta Front*

*Observations:*

FA2 is present solely in the Akkar member of the Fruholmen Formation and has one occurrence at the interval 755.70 to 759.00 m, spanning 3.30 meters. FA2 forms a sharp erosional boundary above FA1 and corresponds to an increase in sand content (Figure 5.3Di). It is comprised entirely of amalgamated well sorted silt-to fine grained sandstone, and exhibits large-scale hummocky cross-stratification (F5) which turns to wave ripple lamination (F4) towards the top. Lamination is picked out by dark, thin layers of mica and organic debris which become gradually more prevalent nearing the top (Figure 5.3A and Dii). Sparsely spaced granule to pebble grade siderite nodules are present throughout the succession. Locally reworked lags in the form of ~2 cm thick well-rounded, poorly sorted, granule to pebble grade, clast-supported monomyctic siderite conglomerate (F16) in a fine-grained sandstone matrix, are present on three occurrences in the upper portion of FA2 (Figure 5.3A and Dii). Bioturbation is absent in FA2 (BI 0).

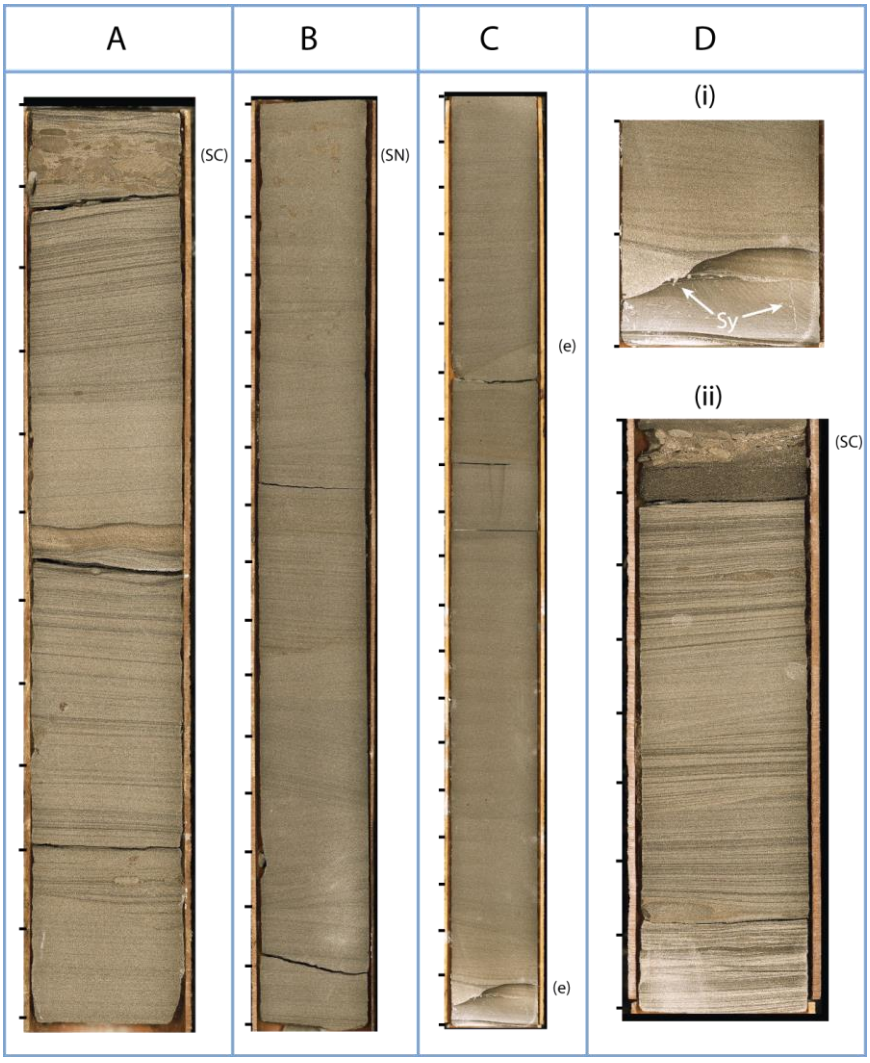


**Figure 5.3:** Core photos showing variety of facies common to FA2. 5 cm are between each tick.

***(A)*** Interval 576 to 576.55. Amalgamated large-scale hummocky cross-stratification accentuated by variations of mica and coaly debris. Siderite conglomerate lag (SC) is present at the top. ***(B)*** Interval 757 to 757.80. Less apparent hummocky-cross stratification due to presence of less mica/organic debris. Siderite nodules/concretions (SN) are found at the top. ***(C)*** Bottom of FA2 interval, demonstrating less mica content and erosive surfaces (e), including the base of FA2. ***(D)*** (i) Close-up of erosive base of FA2, with synaeresis cracks (Sy) in FA1. (ii) Top of FA2, marked with a siderite conglomerate lag (SC).

*Interpretation:*

Deposits of FA2 represent a storm-influenced delta front. The sharp base, wave ripples, and prevalent hummocky cross-stratification of FA2 attest to a strong storm-influence, while the marked increase in sand content with respect to FA1 indicates a proximal shift in environment – all consistent with a storm-influenced delta front setting. This is in agreement with the larger-scale progradational trend observed within the Fruholmen Formation. Hummocky-cross stratification is attributed to the reworking and deposition by storm waves, and is particularly abundant in the delta front environment in connection with floods during major coastal storms (Bourgeois, 1980). The reworked sediment commonly originates during these flood events as low-concentration hyperpycnal flows. These occur where marine water is colder than river outflow, or where the shallow marine setting is brackish, such as occurs at many delta fronts (Bates, 1953). The relationship between the occurrence of hummocky cross stratified sandstone and hyperpycnal flows indicates that storms play a role in both commencing flood events and reworking the hyperpycnal flow deposits from the same storm (Bhattacharya and MacEachern, 2009). Delta-front facies of the Rannoch formation exhibit similar characteristics as FA2 of hummocky cross-stratification in very fine-grained sandstones, which are also attributed to the storm reworking of hyperpycnal flow deposits (Slater et al., 2017). Siderite nodules, reworked sporadically into thin lags, indicate that they form as a result of early diagenetic precipitation shortly following deposition while the sandstone was poorly lithified. This is suggestive of sulphate-poor conditions, typical of low-salinity waters (Curtis and Coleman, 1986). This is in agreement with the delta front setting, which receives a steady influx of river-derived sediments. Furthermore, Bhattacharya and MacEachern, 2009 document that early diagenetic siderite cementation is often present in hyperpycnal sediments. Absence of bioturbation in FA2 records a stressful environment, likely related to fluctuations in salinity.

## 5.1.2 Fruholmen Formation – Reke Member

### *FA3 – Delta Mouth Bar*

*Observations:*

FA3 is present in the Reke member of the Fruholmen Formation and occurs once at the interval 744.50 to 755.00 meters, comprising 10.5 meters of core. FA2 forms a sharp base above FA1 and is composed of fine grained sandstone, with weak- (F6) to well-developed planar stratification (F7), which is accentuated by variations in percentage of lath-shaped granules and pebbles of mudstone and organic debris. Organic debris become more prevalent towards the top, while mudstone clasts are more common in the bottom half. Circle-shaped cm-scale pyrite nodules are scattered throughout. Additionally, local occurrences of siderite nodules are present. Bioturbation is absent throughout FA3 (BI 0). Figure 5.4 presents core photographs illustrating sedimentary structures common to FA3.

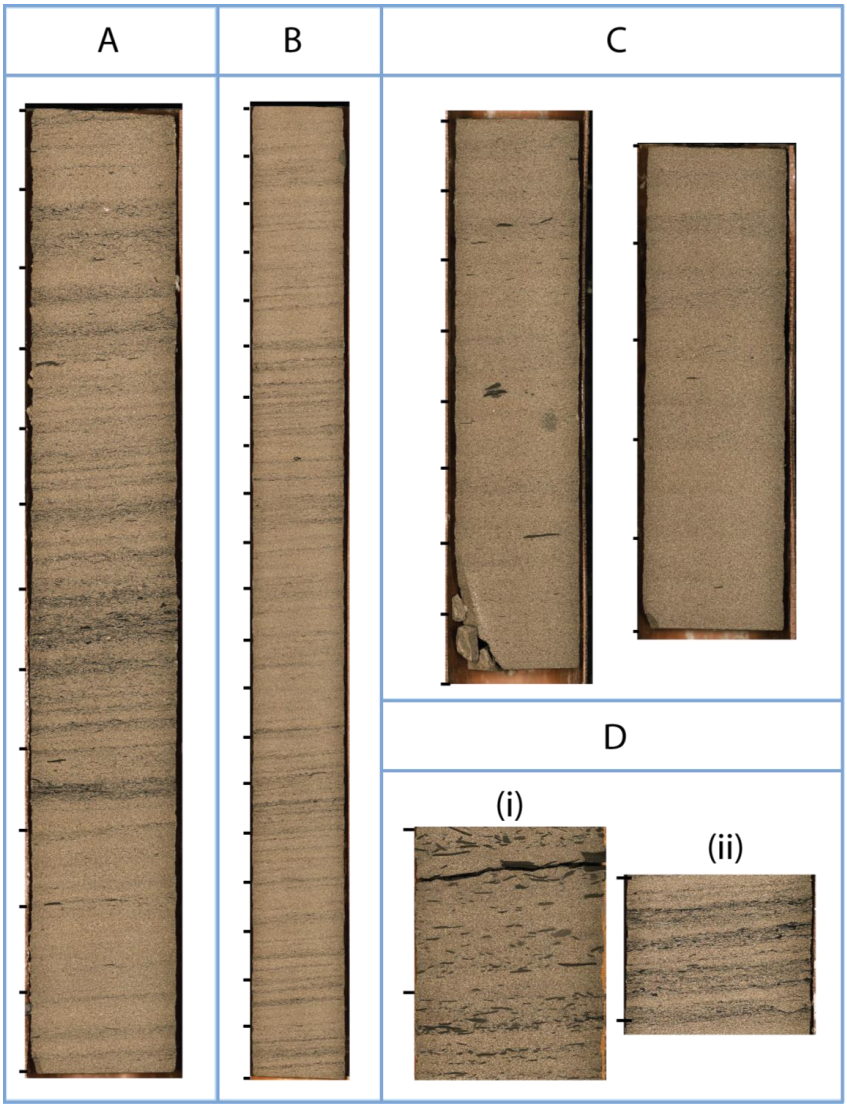


**Figure 5.4:** Core photos showing variety of facies common to FA3. 5 cm are between each tick.

***(A)*** Interval 750 to 750.60. Fine grained sandstone with well-developed planar lamination, picked out by mudstone granules and organic debris (F7). ***(B)*** Interval 751 to 752. More weakly laminated interval of F7. ***(C)*** Intervals 753.45 to 754 (left) and 753-753.30 (right), showing weak to absent planar lamination, with lack of highlighting via mudstone pebbles and organic debris (F6). Mudstone pebbles are scattered on the left. ***(D)*** *(i)* Interval 754.45-754.53. Sub-horizontally aligned pebble mudstone clasts, concentrated as such at various intervals.*(ii)* Interval 750.84-750.90. Well-developed planar stratification highlighted by an abundance of organic debris.

*Interpretation:*

The deposits of FA3 represent deposits of a delta mouth bar, deposited in a subaqueous environment in front of a deltaic distributary mouth in a river-dominated delta setting. The processes producing the interval are interpreted to be as the result of unidirectional traction currents with fluctuations in energy, recorded by the concentrations of mudstone granules and organic debris forming planar lamination. A subaqueous environment on the mouth bar is inferred due to the presence of pyrite nodules and absence of rootlets and nonmarine trace fossils. The dominating presence of unidirectional structures and a lack of tidal and wave signatures (e.g. mud-draped ripples and wave ripple lamination) support the interpretation of a river dominated setting (Dixon et al., 2013). Furthermore, a high amount of wave action would likely result in disintegration of the granules of mudstone found in FA3. Lack of trace fossils is related to a stressed environment, caused probably by high sedimentation rates coupled with the high depositional energy. The large quantity of organic debris indicates proximity to a fluvial system, and the relation of FA3 to the underlying delta front facies FA2 and the overlying delta top/fluvial facies of FA5 and FA6 facies suggests FA3 is positioned at the proximal delta front. While the transition to FA3 could be potentially related to an allogenic progradation induced by a decrease in the creation of accommodation, it is also plausible that it is associated with river avulsion, whereby a new lobe was introduced in this area autogenically. This is deemed to be likely, given that FA3 is seemingly absent in wells in the vicinity, such as in well 7324/8-1 (Wisting Central) and 7324/7-2 (Hanssen), indicating a more local event in space and time (Clark, 2017). An allogenic change in accommodation is more likely to be observed in other wells, as it would hold an influence across the basin.

## *FA4 – Tidal Flat*

*Observations:*

FA3 is present in the Reke member of the Fruholmen Formation and occurs once at the interval 719.15 to 744.50 meters, giving 25.35 meters of thickness. FA1 is pervasively heterolithic and displays large intervals of flaser and wavy bedding (F8 and F9) as well as smaller intervals of lenticular bedding (F10). Sand-rich intervals consist of very fine grained sandstone displaying current ripple lamination along with minor dune-scale cross stratification, with common discontinuous mm-scale drapes of structureless mudstone and organic debris which define flaser bedding (F8 and F11). Flasers are frequently bifurcated, and are more frequently concavely bowed (filling ripple troughs) than convexly bowed (overlying ripple crests), and fail to form continuous layers (Figure 5.5A). Wavy bedding (F9) is displayed as pervasive current ripple lamination with rare wave-ripple lamination in very fine-grained sandstone, alternating at a mm- to cm- scale with highly continuous drapes of structureless mudstone. Drapes both overly ripple crests and fill in ripple troughs (Figure 5.5B). The thicker the mud, the less the form of the ripples is present at the surface of the muds. In intervals dominated by lenticular bedding (F10), mudstone is predominating and the ripple-laminated sandstones form lenses that are highly discontinuous in the vertical, and a majority of the lenses also appear discontinuous in the horizontal -- although lateral resolution is limited (Figure 5.5C). In some cases, the lenses seem to float in the mud. Lenses of sand are typically flat, having a length/height ratio >20. Instances of soft-sediment deformation, such as slump, flame, and dish structures occur sporadically throughout FA4 in cm- to dm- scale intervals (Figure 5.5Eii), as well as pebbles of mudstone. Bioturbation is sparse (BI 1), comprising local occurrences of *Planolites, Arenicolites,* and *fugichnia.*

*Interpretation:*

The FA4 succession is interpreted to belong to deposits of a tidal flat. The dominating structure of current ripples, draped by various thicknesses of mud, attests to a strong tidal influence. The origin of flaser, wavy and lenticular bedding types is directly related to the alternation of current or wave action and slack water (Reineck, 1968). Prevalence of current ripples as opposed to wave ripples further substantiates a tide-dominated setting, with minor wave influence. Local occurrences of dune scale cross bedding are likely produced by small-scale tidal channels. The variation of the content of mud is related to the gradational spectrum from flaser to lenticular bedding, representing an increase in the deposition and preservation of mud. This is a direct reflection of the amount of mud in suspension (Dalrymple, 2010). Additionally, flaser bedding is more commonly occurring in the presence of stronger currents which erode deposited mud from ripple crests, thus recording higher energy (Reineck and Singh, 1980). Because of the low gradient of tidal flats, the wave energy maximum lies near the low-tide level as is the case in figure 5.5. Thus, sand dominates in this area, and the sediment on the tidal flat progressively fines in the landward direction – the intertidal zone can be composed largely of mud (Fan et al., 2004; James and Dalrymple, 2010).

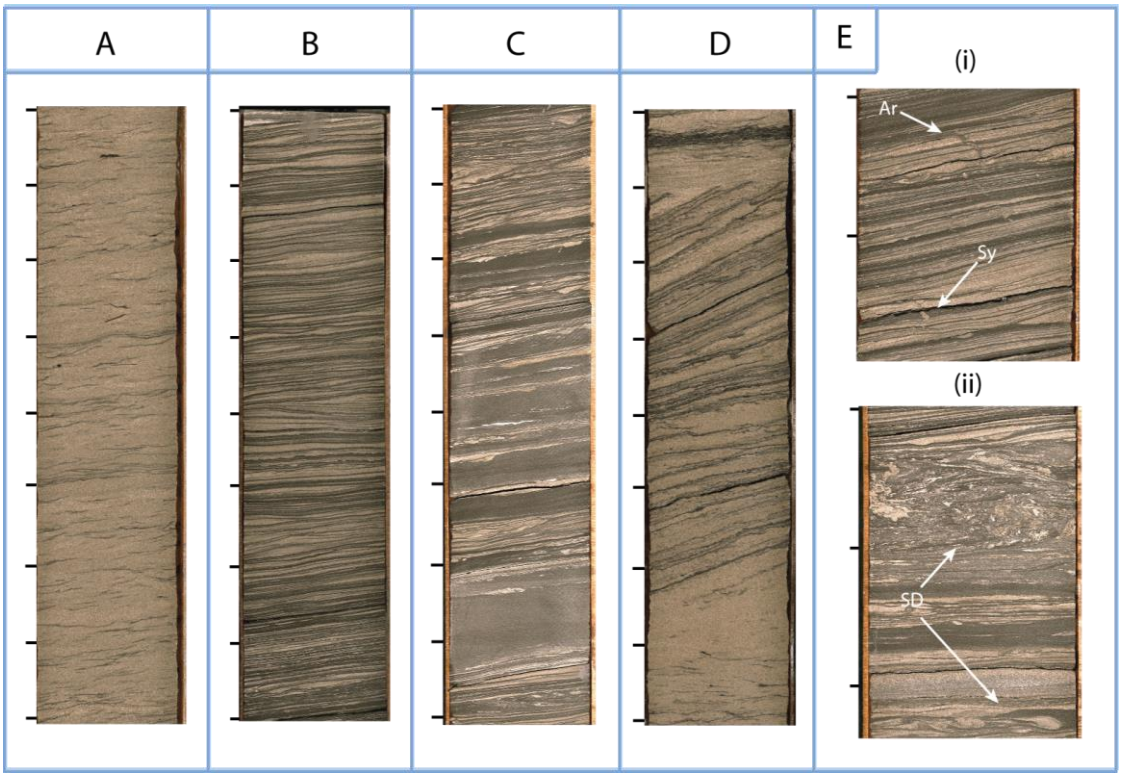


**Figure 5.5:** Core photos showing facies common to FA2. 5 cm are between each tick. ***(A)*** Interval 724.10 to 724.50. Pervasive flaser bedding in deposits interpreted to represent a tidal sand flat. Flasers are discontinuous, displaying bifurcation and are predominantly concave-up, filling ripple troughs. ***(B)*** Interval 736.00 to 736.40. Wavy bedding with laterally continuous flasers and sand lenses, interpreted to be mixed tidal flat deposits. ***(C)*** Interval 723.10 to 723.50. Lenticular bedding, with lenses of sand encased in mudstone, interpreted to be tidal mud flat deposits. ***(D)*** Dune-scale cross stratification, interpreted to represent a minor tidal channel. ***(E)*** *(i)* Sparsely occurring trace fossils include *Arenicolites* (Ar) as pictured. Synaeresis cracks (Sy) document changes in salinity, typical of tidal environments. *(ii)* Soft sediment deformation structures (SD), likely related to slumping.

Areas in FA4 dominated by flaser bedding are related to sand flats (Figure 5.6), which constitute the lower zone of a tidal flat where transport of sand-sized sediments is dominating. Mixed flats, taken to be represented by intervals exhibiting wavy bedding, occurs across the transition between sand flats and mud flats. They are characterized by alternating bedload sedimentation and fallout from suspension (Flemming, 2012). Mud flats, occupying the upper zone of tidal flats, are represented by intervals containing pervasive lenticular bedding. Sedimentation there is dominated by the fallout of suspended sediments (Chang et al., 2007; Flemming, 2012).

The low level of bioturbation is in agreement with a stressed environment brought on by fluctuations in salinity, characteristic of tidal environments. Soft sediment deformation may be present as a result of instability at the margins of minor tidal channels.

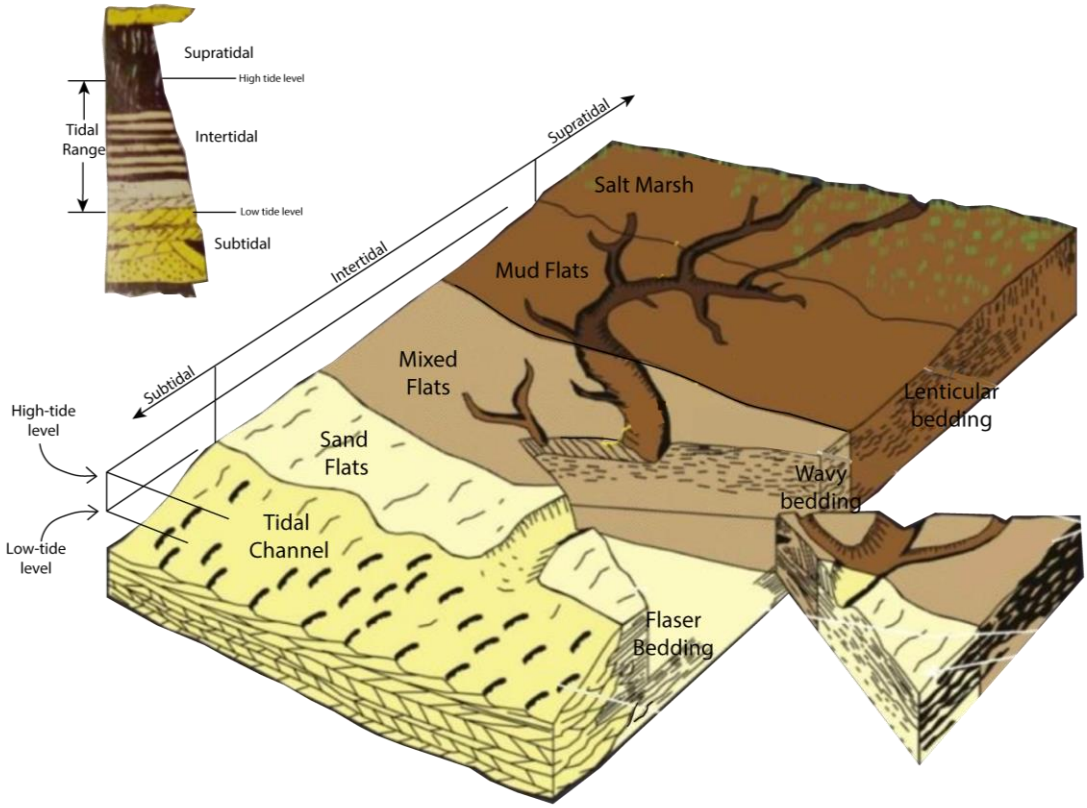


**Figure 5.6:** Tidal flat facies diagram with stratigraphic column demonstrating progradation. Sand flats, mixed flats, mud flats and minor tidal channels are represented in FA4. Sand flats, mud flats, and mixed flats are alternating in no particular order. Modified after Dalrymple (2010).

## *FA5 – Multistory Meandering Channel*

*Observations:*

FA5 is present solely in the Reke member of the Fruholmen Formation at the interval 699.50 to 719.15, totaling 19.65 meters. It consists of erosively based and amalgamated dm- to m-scale beds of structureless fine- to medium-grained sandstone with angular rip-up mudstone clasts ranging from pebble-grade (F12) to cobble- and infrequently boulder-grade (F13). One instance of fining-upwards into wave ripple lamination (F4) is observed. The conglomerates are largely matrix supported, containing highly variable quantities of clasts. Depositional bedding planes are often preserved in mudstone clasts. Although clast composition is primarily mudstone, there are some laminations of silt and fine sandstone within them, sometimes forming lenticular bedding. Clasts tend to be sub-horizontally aligned and are occasionally influenced by soft sediment deformation. No *in-situ* trace fossils were found, however mudstone clasts contain minor *Planolites* burrows. Facies common to FA5 are displayed in core photos in figure 5.7.

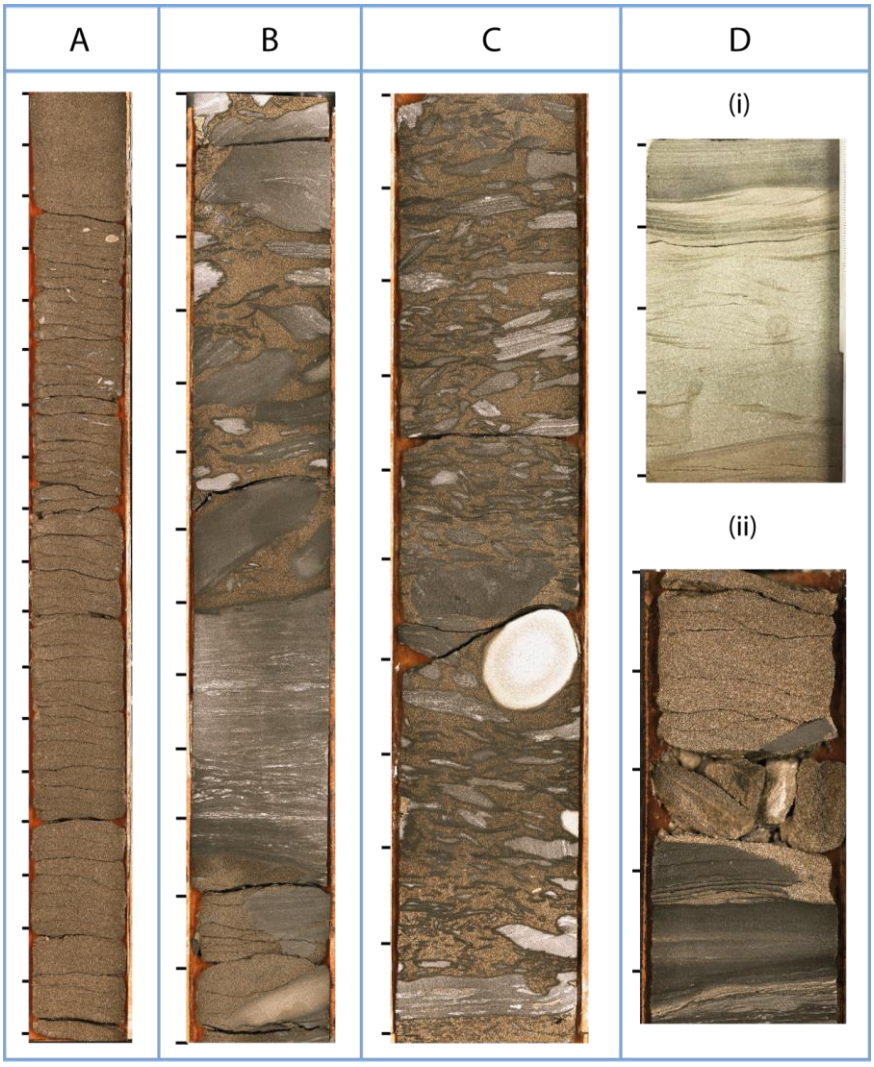


**Figure 5.7:** Core photos showing variety of facies common to FA5. 5 cm are between each tick. ***(A)*** Interval 718.10 to 719.00. Medium-grained sandstone with sparse mudstone pebbles (F12), absent of structures. ***(B)*** Interval 710.00 to 710.65. Intraformational conglomerate pebble, cobble, and boulder sized clasts (F13). Large clast on bottom spans width of core and contains lenticular bedding. ***(C)*** Interval 709.50 to 710.00. Intraformational conglomerate (F13), with angular to subrounded clasts showing soft sediment deformation. Light coloured, well rounded, cobble-sized reworked siderite nodule is present. ***(D)*** *(i)* Interval 711.80 to 712.00. Pebble conglomerate grading into very-fine wave rippled sandstone (F4). *(ii)* Interval 719.00 to 719.20. Incised contact between the lenticular bedded FA4 and FA5. Mudstones in FA4 have been reworked, forming the large angular clasts present.

***NB:*** Parts of FA5 were damaged during drilling; this yielded large horizontal fractures that span the thickness of the core, seen in (A). As such, these were disregarded.

*Interpretation:*

FA5 is interpreted to represent a multistory meandering channel. Although there are no structures such as cross-stratification relating to channel bar development, the incised base as well as the sharp erosional surfaces within FA5 indicate the amalgamation and stacking of channels. Erosion and slumping of unstable floodplain cut-banks create the angular mud clasts, which show soft sediment deformation from travelling as bedload over short distances before their final site of deposition. This interpretation makes these deposits intraformational conglomerates, as the clasts are locally derived from the floodplain and deposited penecontemporaneously with the sandstone matrix. The subordinate instance of wave ripple-laminated silt- and sandstone records deposition during temporary channel abandonment. Typical meandering channel deposits show a fining upwards development, which is largely absent in the interval of FA5. This is posited to be due to frequent avulsion and abandonment episodes in a setting where the rate of creation of accommodation is much less that the rate of sedimentation, likely resulting in the highly amalgamated multistory deposits. This allows units of the intraformational conglomerate facies, most typically occurring at the base of channels, to be juxtaposed and repeated. As such, it is difficult to determine erosive surfaces due to the repeated stacking of the same facies. A similar amalgamation of course-grained meandering river deposits in a low accommodation setting is observed in the Castissent formation in the Tremp Basin in the Spanish Pyrennees. The Castissent sandstone is also present in areas of the basin with more accommodation, where the full fining-upward fluvial development is observed (M. Poyatos More, Personal Communication, October 10$^{th}$, 2018). The occasional occurrence of lenticular bedding in the mudclasts suggests that the channel may have incised into tidal flat sediments.

The base of FA5 documents a basinward shift in facies, with fluvial deposits overlying marginal marine tidal flats. This change is allogenically related to a larger ratio of rate of sedimentation to rate of accommodation creation throughout the basin, as this shift in facies is present in other wells in the vicinity (Clark, 2017). The surface separating FA4 from FA5 may be considered as a sequence boundary, with the falling-stage system tract being related to the incision of the fluvial channel into the tidal mudflats of FA4, which in this case would belong to the highstand system tract of the previous sequence. This is supported by the occurrence of some heterolithic clasts that may have derived from FA4. The deposits of FA5 are thus related to the lowstand systems tract – consistent with the apparently large ratio of rate of sedimentation to rate of accommodation creation characteristic of lowstands. Comparison with the eustatic sea level curve by Haq et al, 1978 throughout the Norian and Rhaetian is in agreement with this interpretation; however, local sea level fluctuations are not factored in.

## *FA6 – Tidally Influenced Distributary Channel/Bayhead Delta*

*Observations:*

FA6 occurs in only the Reke member of the Fruholmen Formation and has one occurrence at the interval 695.80 to 699.50 m, spanning 3.70 meters. FA6 consists primarily of fine-grained sandstones containing current-ripple lamination (F3), which are commonly topped with thin, discontinuous mud drapes, creating flaser bedding (F8). Sporadically throughout FA6 are concentrations of pebble-grade mud clasts, forming an intraformational conglomerate (F12). At the base is a lag of highly deformed cobbles of mudstone clasts (F13). Mudstone clasts are of the same variety as described in FA5, but have been more affected by soft-sediment deformation. Fragments of organic debris occurs infrequently. Bioturbation is generally moderate throughout (BI 2), but is locally high (BI 4) in cm- to dm-scale intervals. Trace fossils include *Cylindrichnus, Rosselia, Palaeophycus, Planolites* and *fugichnia.* Facies common to FA6 are displayed in core photos in figure 5.8.

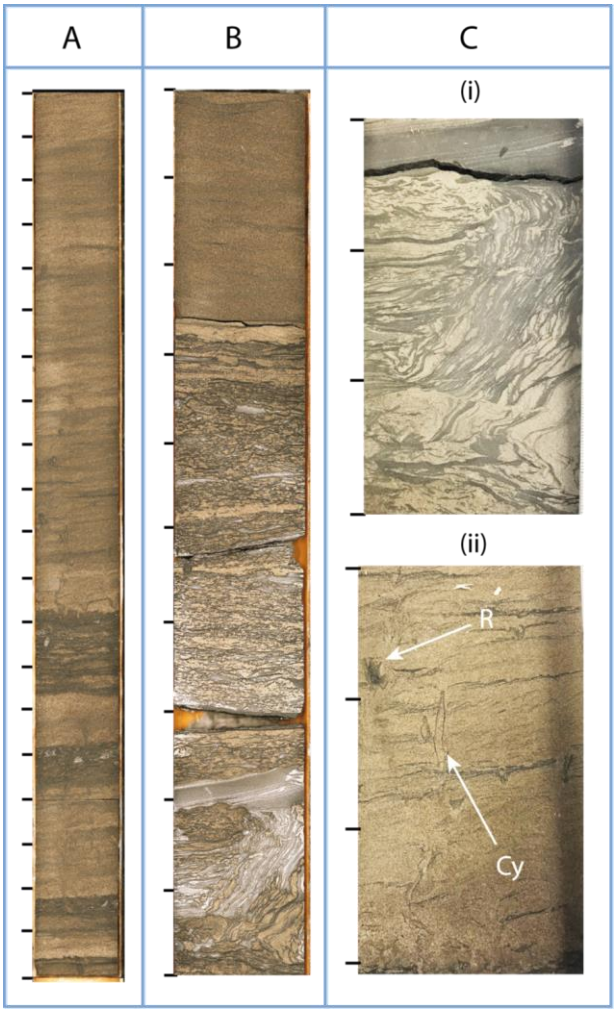


**Figure 5.8:** Core photos showing variety of facies common to FA5. 5 cm are between each tick.

***(A)*** Interval 696.85 to 697.85. Fine-grained sandstone displaying flaser bedding; local concentrations of mudstone pebbles are present. ***(B)*** Interval 689.85 to 699.50. Intraformational conglomerate containing angular mudstone clasts at the base of FA6, representing a possible transgressive surface which may be accompanied by tidal ravinement, forming the conglomerate ***(C)*** *(i)* Interval 699.30 to 699.45. Slumped clast of heterolithic material, likely originating from unlithified tidal-flat deposits existing contemporanously. *(ii)* Interval 697.30 to 697.45. Highly bioturbated interval, including *Cylindrichnus* and *Rosselia.*

*Interpretation:*

FA6 is interpreted to be deposits of a tidally influenced distributary channel. The pervasive flaser bedding records a strong tidal influence, while the intraformational conglomerates and pebbles of organic debris are evidence of the presence of a fluvial channel system. Dominance of current ripple lamination and absence of wave-ripple lamination attest to little to no wave influence. The channel(s) depositing FA6 are interpreted to be the same that deposited FA5, but in a more marginal marine setting; hence, the presence of the many of the same facies (F12 and F13). The differentiating factor between them is the frequently occurring flaser bedding in FA6. The positioning of FA6 above fully fluvial FA5 records a transgression. Given that FA5 is interpreted to comprise a lowstand systems tract, the boundary between the two may represent a transgressive surface – marking the transition from lowstand regression to transgression (Emery and Myers, 2009). Multiple studies have documented that infill successions in incised valleys involve the deposition of estuarine bayhead delta deposits above fluvial sediments (Allen and Posamentier, 1993; Zaitlin and Dalrymple, 1994). It is possible that this is what is seen here, with the distributary channel of FA6 being related to a bayhead delta. This concept is further supported by the positioning of FA7 above FA6. FA7 has been interpreted to be estuarine muds – which typically occur above bayhead delta sediments during the transgression of an incised valley (Allen and Posamentier, 1993; Zaitlin and Dalrymple, 1994). The trace fossil assemblage is in agreement with a marginal-marine setting (Buatois et al., 2012).

## *FA7 – Estuarine Muds*

*Observations:*

FA7 occurs in the uppermost portion of the cored Reke member of the Fruholmen Formation at the interval 688.00 to 695.80 m, comprising 7.8 meters. It is composed of mm-to cm-scale beds of laminated shales (F1) alternating with mm-scale pinstripes of silt- to very fine-grained sandstone. Pinstripes increase in prevalence towards the top, and are isolated in the mud and infrequently display current-ripple lamination (F3) with mud drapes. Sparse mm-to cm-scale pyrite and siderite nodules occur, as well as synaeresis cracks. Bioturbation is weak (BI 1). Traces include *Arenicolutes*, *Planolites*, and possible *Chondrites* and *Gyrolithes*. Facies common to FA7 are shown in figure 5.9.

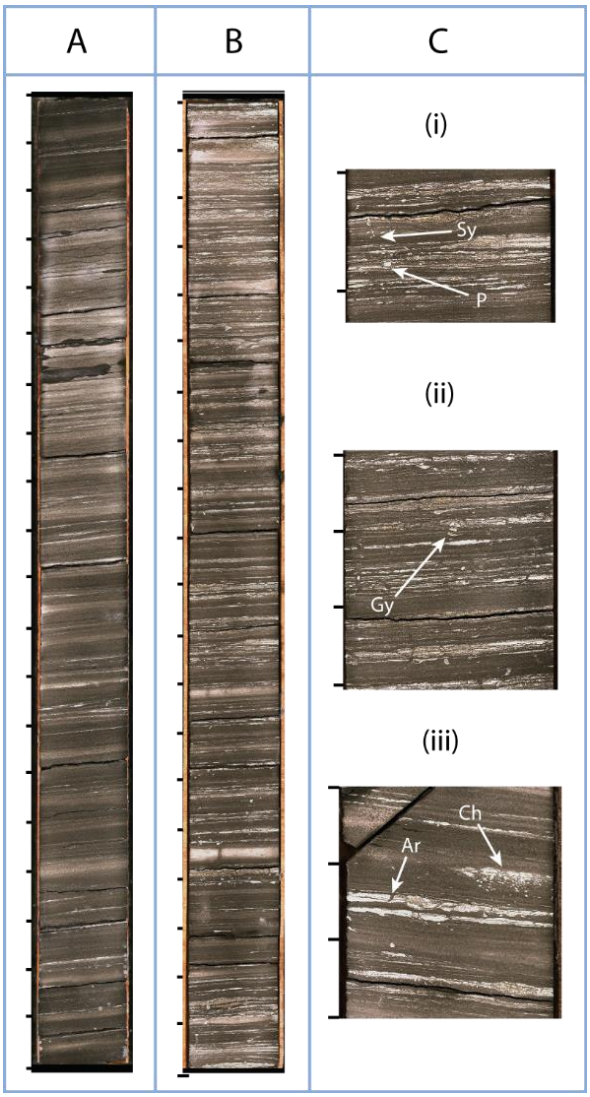


**Figure 5.9:** Core photos showing variety of facies common to FA7. 5 cm are between each tick. ***(A)*** Interval 691.85 to 692.85. Laminated shales with sparse mm-scale pinstripes of sandstone in the bottom half of FA7. ***(B)*** Interval 689.85 to 690.85. More frequently pinstriped FA7 towards the top. ***(C)****(i)* Interval 690.38 to 690.44. Sand-filled synaeresis crack and *Planolites* burrow. *(ii)* Interval 688.95 to 689.10. Example of *Gyrolithes* burrow. *(iii)* Interval 691.35 to 691.50. *Arenicolites* and *Chondrites* burrows.

*Interpretation:*

FA7 is interpreted to represent the deposits of the muddy central basin of an estuary. The occurrence of mud drapes on the infrequently occurring ripple laminations on pinstriped sandstones indicate a moderate degree of tidal influence. The dominance of mudstones suggest a low-energy environment sheltered from fluvial and wave processes, while the trace fossil assemblage suggests marine conditions. Synaeresis cracks document variations in salinity, characteristic of the central basin of an estuary. Seismic data indicates that FA7 fills a channel feature (E. Stueland, Personal Communication, December 20th, 2018), whereby following a transgression, estuarine sediments are deposited into the topography formed by channels. The succession of the multistory meandering channel (F5), tidally influenced distributary channel (F6), overlain by estuarine muds (F7) is typical for the lowstand and subsequent transgression following a sequence boundary, which is interpreted to be the boundary between F4 and F5 (Figure 5.10).

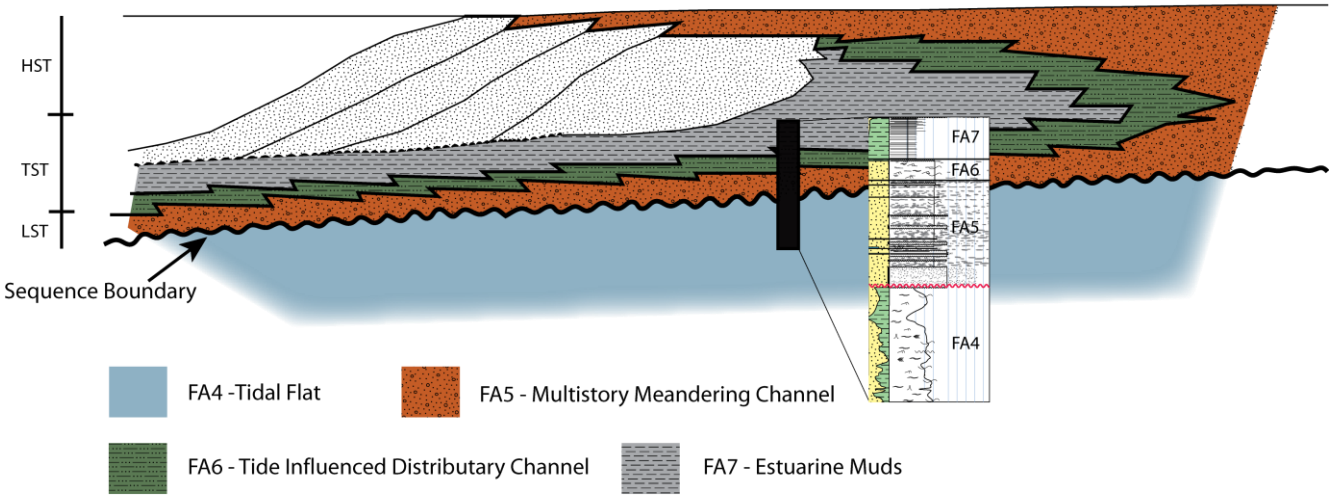


**Figure 5.10**: Distribution of lithofacies resulting from the transgression of an incised valley, followed by estuary filling and progradation. The transgressive component is interpreted to occur from F5 to F7. Modified from Dalrymple et al. (1992).

## 5.1.3 Nordmela Formation

The possible presence of the Nordmela formation is deduced from biostratigraphic data (Biostratigraphic report provided by OMV, acquired by RPS Ichron), indicating Pleinsbachian stage. However, the Stø formation can have these same bugs as the result of reworking of previously deposited sediment. It is reasoned to be part of the Nordmela formation as there are no bugs present in the interval that are confined to times corresponding to the Stø formation. A very small portion, representing the top of the Nordmela Formation, is present.

### *FA8 – Compound Tidal Dune*

*Observations:*

FA8 is the sole facies association in the Nordmela Formation, comprising the interval from 684.75 to 688.00 meters, totaling 3.25 meters. It is composed of amalgamated, 0.3-0.5 meter scale, tabular dune cross-stratified medium grained sandstone (F11). Forsets of dunes are often draped with mud and organic debris and are inclined at approximately the angle of repose; however sparse intervals contain more sub-horizontal forsets which are mantled with current ripples with mud drapes (F8). A pebble grade conglomerate is present at the base (F13), while the top 10 cm of FA8 is highly carbonate cemented. Sparse cm-scale pyrite nodules are present. Bioturbation is absent (BI 0).

*Interpretation:*

FA8 deposits represent a compound tidal dune complex. The frequent mud drapes attest to a strong tidal influence. The amalgamation of large-scale tabular dune cross stratification indicate the migration of subaqueous dunes in sand flats within a high energy shallow marine environment. The development of compound tidal dunes is controlled by asymmetrical currents that produces flow separation at the crests of the dunes, causing an avalanche of gains across the lee side of the dune (Allen, 1980). Preservation of mud drapes occurs during periods of decreased flow (Allen, 1980). Because of the flow asymmetry, the superimposition surfaces and the master bedding plane dip in the same direction as the current, forming a forward-accretion architecture (Olariu et al., 2012).

The highly calcite-cemented interval at the top may be a result of a hiatus in deposition prior to the deposition of the overlying FA9. The pebble lag at the base of the interval is interpreted as a transgressive surface of marine erosion, and defines the boundary between the Fruholmen and Nordmela formations. As such, this marks the Triassic-Jurassic boundary – thus has significant sequence stratigraphic and chronostratigraphic implications. There is a huge gap in time across this boundary, representing at least 20 million years before the introduction of the preserved Nordmela formation, whereby the Tubåen Formation and the Krabbe Member of the Fruholmen Formation are missing. During this gap deposition may have occurred, but was subsequently eroded prior to deposition of FA8.

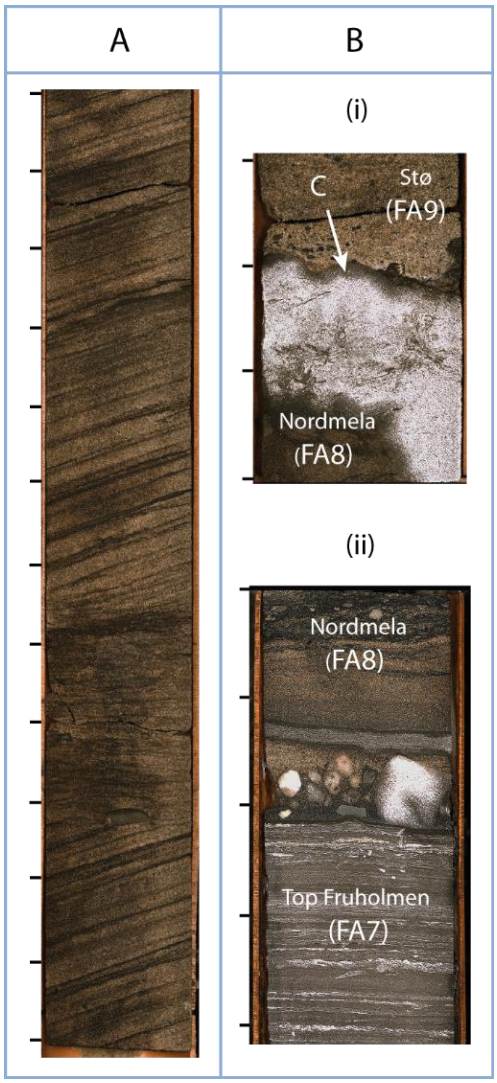


**Figure 5.11:** Core photos showing variety of facies and contacts related to FA8. 5 cm are between each tick.

***(A)*** Interval 686.20 to 686.85 m. Tabular dune scale cross stratification draped with mud and organic debris. ***(B)*** *(i)* Top of FA8, marking the boundary between the Nordmela and Stø Formations. Top Nordmela is highly calcified (C), perhaps indicating a break in sedimentation prior to deposition of the Stø Formation. *(ii)* The Triassic-Jurassic transition separating the Fruholmen and Nordmela Formations, marked with pebbly lithic conglomerate lag placed sharply above FA7.

NB: Sandstones of the Nordmela Formation appear dark and patchy due to presence of oil.

## 5.1.4 Stø Formation

### *FA9 – Upper Shoreface to Foreshore*

*Observations:*

FA9 is the sole facies association present in the cored Stø Formation, represented by the interval from 666.25 to 684.75 m, comprising 18.5 meters of thickness and forming the main reservoir zone. FA9 is composed entirely of medium-grained sandstone with weak trough cross-stratification (F14) and structureless to weakly developed low-angle cross- and planar stratification (F13). There is an overall very slight fining upward trend throughout the succession. Organic debris is sparsely present throughout. Structureless areas have been highly bioturbated such that bedding planes are lost, and to such a degree that even outlines of individual traces are lost (BI 6). This is deduced due to an abundance of fecal pellets. Sparse coal-rich drapes are present towards the bottom of FA10. Facies common to FA9 are displayed in core photos in figure 5.12.

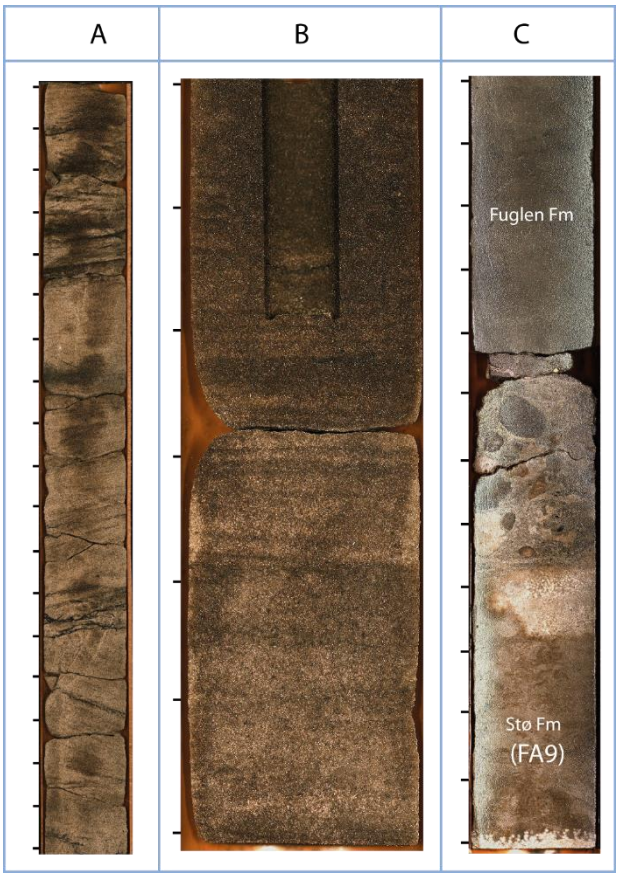


**Figure 5.12:** Core photos showing variety of facies and contacts related to FA8. 5 cm are between each tick.

***(A)*** Interval 678.85 to 679.75. Faint trough cross-stratified sandstone with occasional organic debris ***(B)*** Interval 673.40 to 673.70. Planar to low angle lamination. ***(C)*** Interval 665.40 to 666.00. Transition from Stø to the overlying Fuglen Formation, marked by a highly calcified and possibly glauconitic condensed section, equivalent to the Brentskardhaugen bed on Svalbard.

NB: Sandstones of the Stø Formation appear dark and patchy due to presence of oil.

*Interpretation:*

Deposits of FA9 are interpreted reflect an upper shoreface to foreshore environment. This is evidenced by the presence of trough cross stratified sandstone and low-angle to planar cross lamination (Figure 5.12). The high textural and mineralogical maturity and visual porosity attests to a shoreface

environment as well. Coalified material was likely sourced from the backshore environment which existed coevally.

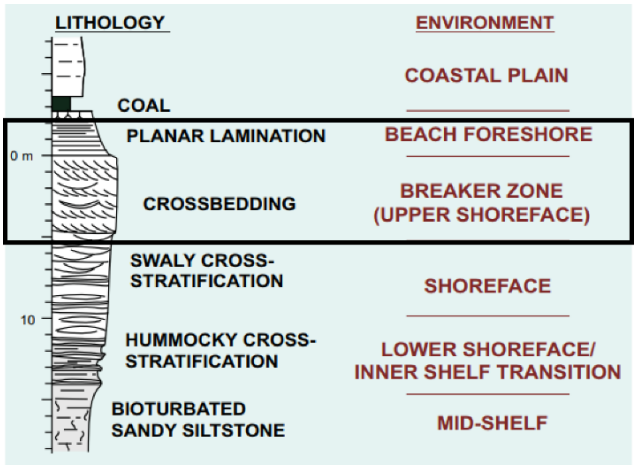


**Figure 5.12:** Shallowing-up shoreface succession in facies model of Walker and Plint (1992). Boxed in black are facies interpreted to exists in the cored Stø Formation.

## *Condensed Section – Brentskardhaugen Equivalent*

A condensed section of approximately 1 m in thickness is present between the Stø and Fuglen formation (figure 5.12C). In addition to logging at Weatherford, additional description and interpretation of the condensed section was conducted with the assistance of Vilde Bjørnebye at University of Oslo. Because the focus of this thesis is to characterize reservoir sandstones, emphasis is not given to this unit beyond this short description. Further information with respect to the characterization, formation, and spatial distribution of this section can be found in Bjørnebye (*in prep*).

*Observations:*

The interval consists of a largely calcite cemented conglomerate. Clasts are well rounded and poorly sorted, and are found to be up to 5 cm in size. The composition of the clasts encompasses a wide variety of constituents, but predominantly comprises quartz granules, siderite nodules, shell fragments, and possible phosphate nodules. Sand-grade green grains and ooids are present, suggesting the possible presence of glauconite.

*Interpretation:*

This is a transgressive lag deposit, originating from the transgression of the shelf in late Bathonian times. Bjørnebye (*in prep*) found that the many variety of clast types present can originate from different periods of time due to the reworking of material of various ages. This results in the highly mixed clast composition observed. Phosphate nodules are found in XRD analyses by Bjørnebye (*in prep*) to consist predominantly of fluorapatite, which is an early diagenetic cement. These nodules have been often found to contain a fossil at their center. Abundant glauconite and diagenetic siderite are likely consequences of low sedimentation rates. Klausen et al. (2018) and Bjørnebye (*in prep*) relate this bed to the Brentskardhaugen bed on Svalbard.

# 5.2 Petrographic Analysis

This section presents the results obtained from the petrographic methods described in section 4.2, namely XRD analysis, point counting, SEM, and textural analysis. Many parameters are displayed in diagrams with average values for each facies. Individual sample results for these parameters can be found in appendix E.

## 5.2.1 Mineralogy from Bulk XRD

Bulk XRD results for each sample are presented in figure 5.13 alongside the sedimentary log in their respective locations. Sylvite present in some samples are interpreted to have precipitated from the drilling mud, and are thus subtracted in the normalized XRD data.

Most notable is the strong compositional difference between the Fruholmen Formation and the overlying Stø and Nordmela formations. In the Stø and Nordmela formations, quartz is clearly the dominating mineral with minimal proportions of feldspar and other minerals. This is as opposed to the Fruholmen Formation, which shows a markedly higher mineral diversity. To observe differences between depositional environments, figure 5.14 shows XRD results when averaged with respect to facies association. Mineralogy given by XRD is summarized on a formation-by-formation basis, with constituents listed in order of decreasing abundance.

### *Fruholmen Formation*

Bulk XRD results show that **quartz** is the dominating mineral for all facies in the Fruholmen Formation, having an average value of 56 percent throughout. A significant portion of feldspar is detected, most of which is plagioclase feldspar. Bulk XRD is particularly useful in readily differentiating between plagioclase and K-feldspars – due to grain dissolution, they can be often hard to identify via optical microscopy. The **plagioclase feldspar** averages 15 percent of the Fruholmen Formation samples. The proportion of **K-feldspar** is small, averaging 6 percent. However, K-feldspar is seen to steadily increase throughout the Fruholmen Formation, being at 3 percent in FA2 and going up to 10 percent in FA6, as seen in figure 5.15. Plagioclase feldspar remains relatively constant, although decreasing slightly. A diverse assemblage of additional minerals are detected. **Muscovite/Illite** is detected in all samples and consistently consists of about 8 percent of the sample; however the sample from FA7 - estuarine mud deposits, comprises of 21 percent muscovite/illite. Because illite and muscovite have almost matching structure files, bulk XRD analyses are not capable of accurately separating them. **Kaolin** is present in all samples, at slightly smaller percentages, averaging about 6 percent. Again, FA7 – estuarine muds, contains a higher proportion at 25 percent. **Chlorite** is present in yet lower average proportions, averaging 5 percent but remains detected in all samples, with the exception of V12 of FA5, which is

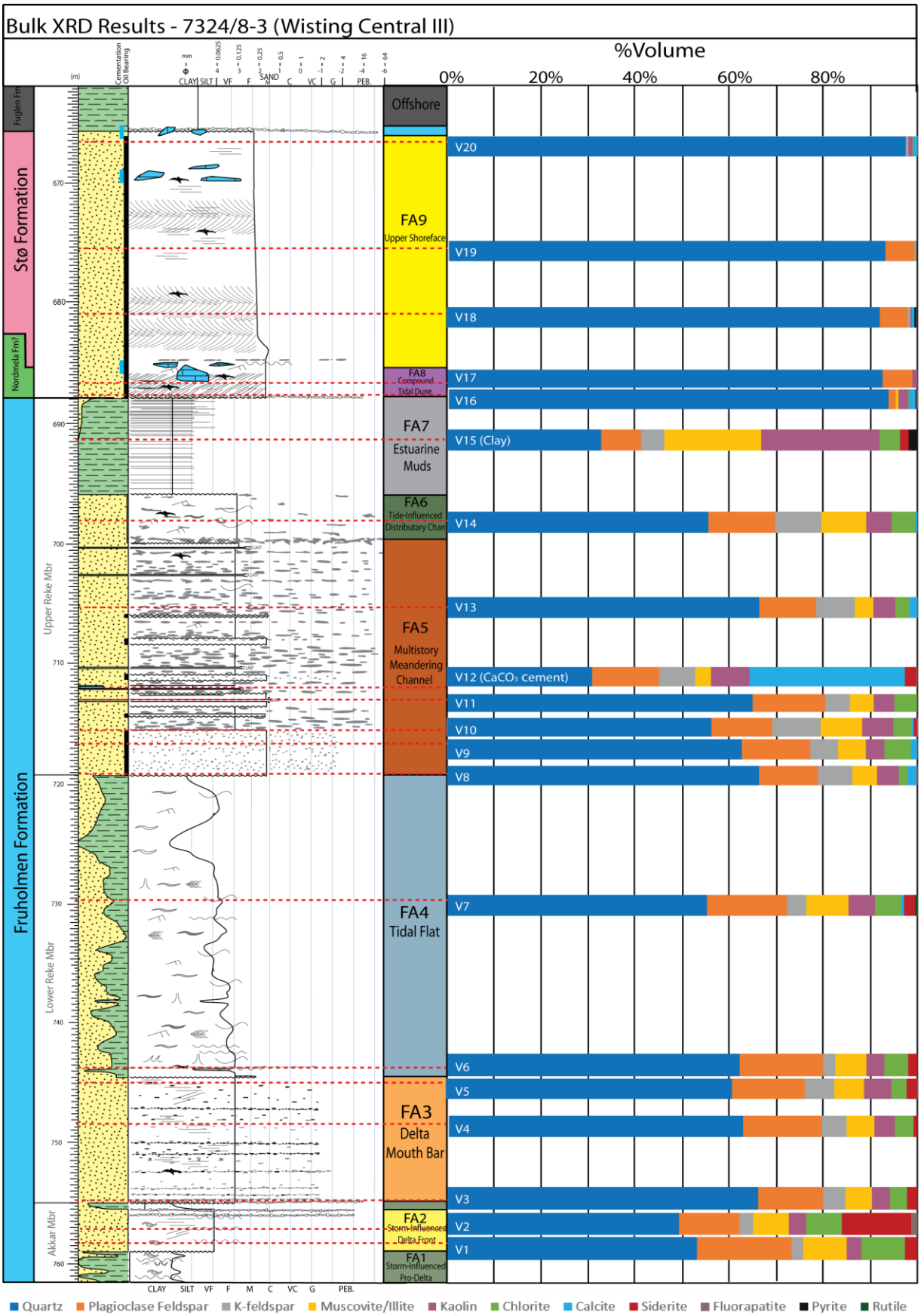


**Figure 5.13:** Bulk XRD results for each sample fromWisting Central III, alongside the sedimentary log. Samples are displayed alongside their respective locations on the log. Legend for log in figure 5.1 holds.

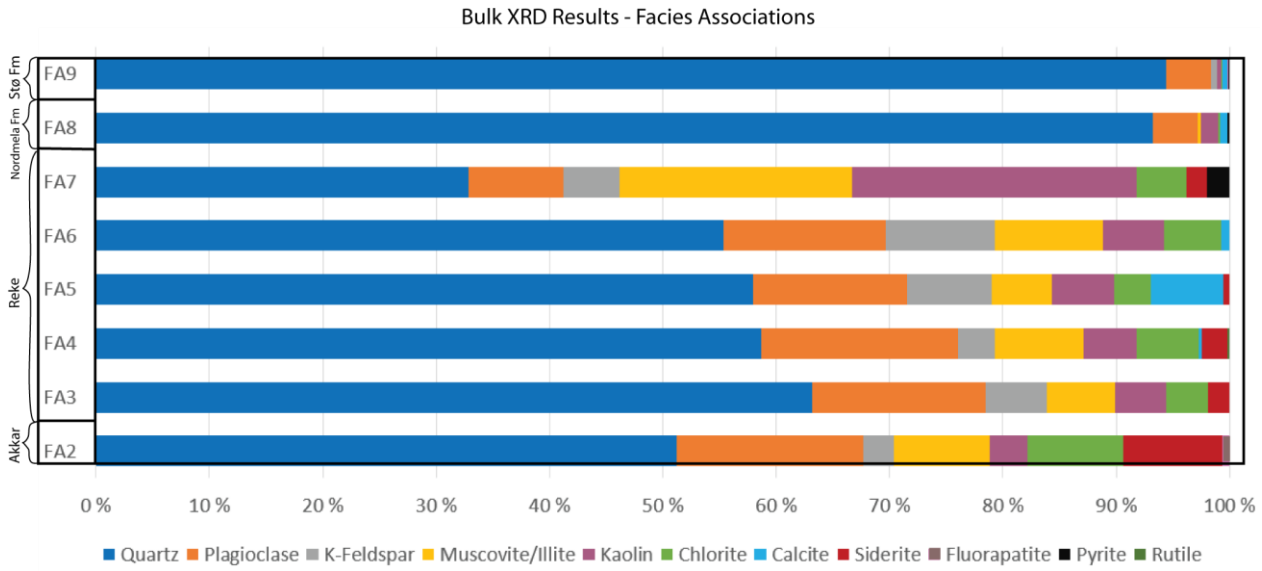


**Figure 5.14:** Bulk XRD results averaged with respect to facies association to observe differences between depositional environments.

calcite cemented. Chlorite holds particularly high percentages in samples from FA2 – storm influenced delta front deposits. **Calcite** is not frequently detected; when present, it typically makes up less than 2 percent. The exception is the calcite cemented sample, V12 from FA5, containing 33 percent calcite, thereby skewing the average for FA5 as seen in figure 5.14. **Siderite** is common to the majority of samples in small percentages, typically at approximately 2 percent. An exception is sample V2 from FA2 – storm influenced delta front deposits, holding 15 percent siderite. Sample V2 also holds the only instance of **fluorapatite** detected, at less than 1 percent. Although observed when logging the core in FA3 and FA4 (delta mouth bar and tidal flat) of the Fruholmen Formation, **pyrite** only shows up in the XRD results in sample V15 of FA7 – estuarine muds deposits, at 2 percent. V7 of FA4, tidal flat deposits, holds the only instance of **rutile**, at 0.4 percent.

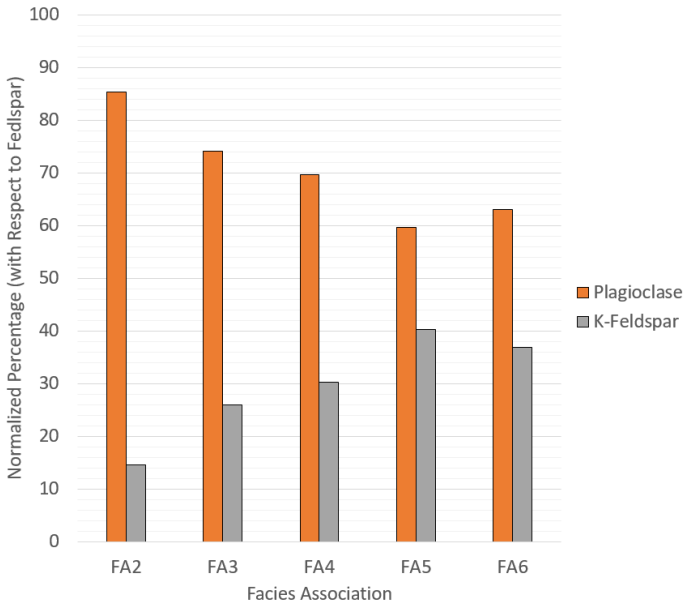


**Figure 5.15:** Feldspar distribution according to XRD results, normalized with respect to feldspars and averaged for each facies association in the Fruholmen Formation. Plagioclase is consistently dominating but a steady increase in the percentage of K-feldspar is observed stratigraphically up section.

## *Nordmela Formation*

**Quartz** is the obviously dominating mineral given by the XRD results for the Nordmela Formation, comprising an average of 93 percent. **Plagioclase** feldspar follows quartz in quantity, having an average value of only 4 percent. K-feldspar is not detected in any of the samples from the Nordmela Formation. **Kaolin** occurs in small percentages, averaging 2 percent. Chlorite, Calcite, Pyrite, and Muscovite/Illite all occur in samples from the Nordmela Formation at percentages less than 1 percent.

## *Stø Formation*

Much like the Nordmela Formation, **quartz** is the clearly dominating mineral, with XRD results showing quartz to comprise 94 percent. Again, **plagioclase feldspar** is the next most abundant mineral, with an average percentage of 4 percent, similar to the Nordmela Formation. **K-Feldspar** is present in all samples from the Stø Formation, in percentages less than 1 percent. Kaolin, chlorite, calcite, and pyrite occur in percentages also less than 1 percent in all or the majority of samples. Fluorapatite is detected in sample V18, at 0.1 percent.

## 5.2.2 Point Counting and SEM

The mineralogical constituents from point counting and SEM for the Fruholmen, Nordmela, and Stø formations in Wisting Central III are presented in this section on a formation-by-formation basis. From point counting results, the framework grain quantities presented in the next sections (quartz, feldspar, and rock fragments) are recalculated to represent 100% of each sample and their relative quantities are plotted on a ternary diagram, shown in figure 5.16. As previously mentioned, samples with high clay content were not made into thin sections because the ability to distinguish individual minerals is restricted; as such, FA1 and FA7 are not represented.

Each respective formation shows similar trends in the in the point counting results with respect to the XRD results presented in the last section. Although similarities are seen between bulk XRD results and point counting results, advantages in point counting are in the distinctions made when encountering quartz (mono- or poly-crystalline), lithic fragments (e.g. volcanic, metamorphic), matrix (allogenic vs. authigenic), cement (e.g. quartz, chlorite) and various degrees of alteration of minerals. Additionally, porosity and IGV estimations are acquired from point counting. As such, results are not directly comparable to bulk XRD analysis results. Full point-counting results can be found in appendix E.

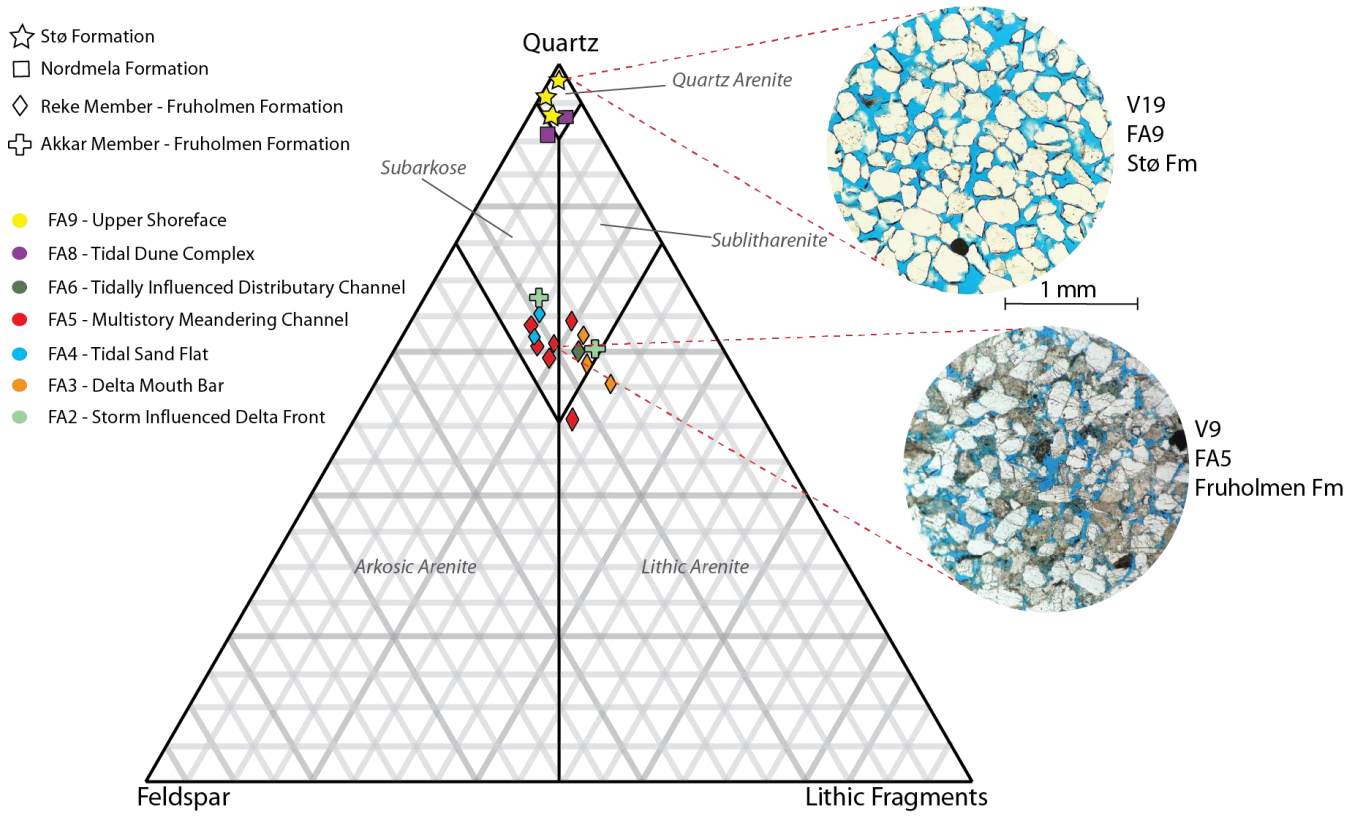


**Figure 5.16:** Quartz, feldspar, and rock-fragment proportions of sandstones in Wisting Central III. Classification is based on Dott (1964). Thin sections under PPL, V19 from the Stø Formation and V9 from FA5 of the Reke Member of the Fruholmen Formation, are shown. Thin sections demonstrate a far higher diversity of grains in the Fruholmen Formation, whereas the grains of the Stø Formation are unvaried in appearance due to comprising almost exclusively of quartz..

## *Fruholmen Formation*

Thin section analyses were conducted on fourteen samples from the Fruholmen Formation – two from the Akkar Member, and twelve from the Reke Member. Based on the relative proportions of quartz, feldspar, rock fragments, and matrix, seven samples were classified as subarkosic arenites, five as sublithic arenites, and two as lithic arenites (figure 5.16). Although the samples plot in three classes on the ternary diagram, compositional differences are comparatively minor, with all plotting just above the middle of the QFL diagram.

The following mineral/grain tabulations include detrital mineralogy and authigenic mineralogy. Detrital mineralogy includes framework grains and allogenic matrix, and authigenic mineralogy includes cements and authigenic clays. Constituents are ordered in terms of decreasing abundance.

### Detrital Mineralogy

#### Framework Grains

*Quartz*

Quartz is the dominating mineral seen throughout the Fruholmen Formation. Point counting results show that it comprises a range of 31% to 51%, with an average of 45% in the Fruholmen Formation (appendix E). A clear predominance of monocrystalline quartz over polycrystalline quartz (at a range of 1-5%) is also demonstrated by the point counting results. When quartz, feldspar, and rock fragment quantities from point counting are recalculated to represent 100% to plot on the ternary diagram, quartz comprises a range of 51% to 67%, with an average of 61% (figure 5.16, appendix E). Quartz grains commonly contain micro-scale fluid inclusions and infrequent heavy mineral inclusions (figure 5.17). The detrital quartz grains are also frequently lined with quartz cement, giving grain edges sharp corners and smooth surfaces.

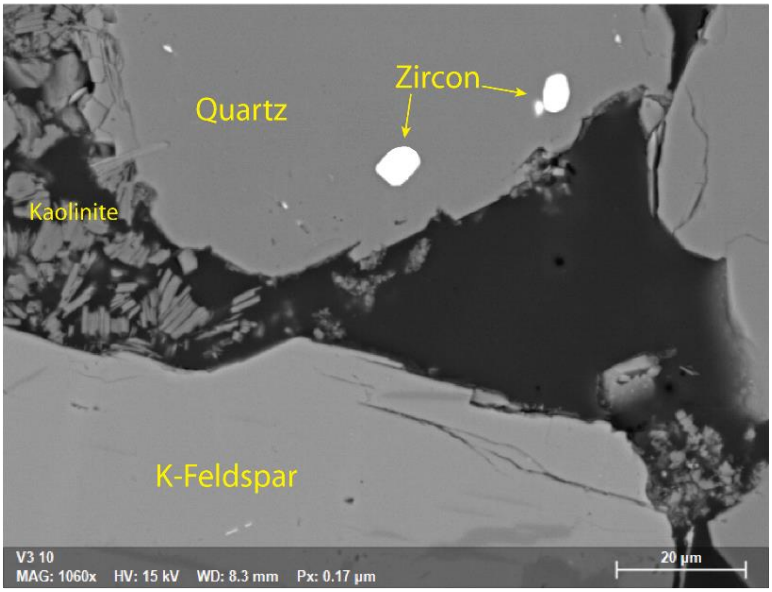


**Figure 5.17:** Zircon inclusions within quartz from sample V11 of FA5 – meandering channel deposits.

*Feldspar*

As stated in section 4.2, feldspar grains are subcategorized during point counting as K-feldspar, plagioclase, or altered/unidentifiable as shown in appendix E, with 'unidentifiable' meaning that feldspars could not be accurately identified through microscopic analysis. Feldspars were point counted to comprise a range of 11% to 16%, with an average of 14% (appendix E). When recalculated to plot in the ternary diagram, feldspar comprises a range of 17% to 24%, with an average of 19 % (figure 5.15; appendix E). Feldspar grains are variably dissolved, ranging from pristine to skeletal. Plagioclase grains display lamellar twinning, which microcline grains display characteristic tartan twinning. A strong predominance of plagioclase feldspars is documented throughout the Fruholmen Formation. An increase in the proportion of K-feldspars is registered stratigraphically up-section, agreeing with XRD results (figure 5.15). Figure 5.18 shows a SEM elemental map, demonstrating the predominance of plagioclase feldspars.

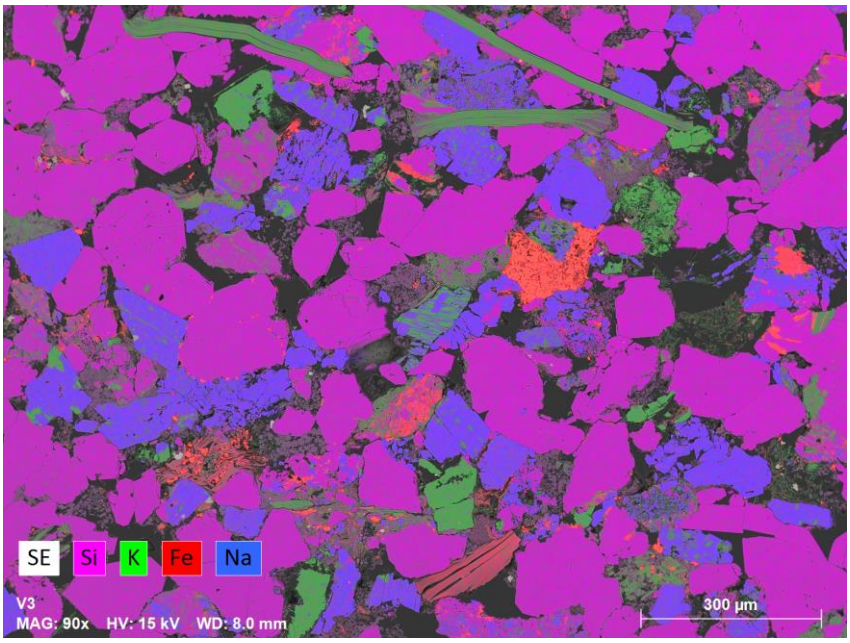


**Figure 5.18:** SEM elemental map from sample V3 of FA3, with Si, K, Fe,and Na highlighted with pink, green, red, and blue, respectively. Plagioclase (Albite), coloured in dark blue/violet due to sodium content, is observed to be the dominating feldspar. K-feldspars appear green due to potassium content. Mica laths are also green, but are easily differentiated by their long, thin shape with obvious perfect basal cleavage. Quartz, in pink, is the clear dominating mineral.

*Rock Fragments*

The relative abundance of various rock fragments in the Fruholmen Formation is presented in figure 5.19. Point counting results show that rock fragments comprise a range of 11% to 23%, averaging 18% in the Fruholmen Formation (appendix E). When recalculated to plot on the ternary diagram, rock fragments comprise a range of 15% to 28%, averaging 20% (figure 5.16; appendix E). The rock fragment assemblage comprises primarily of **igneous rock fragments** (figure 5.19). The igneous assemblage includes volcanic grains as well as composite plutonic grains consisting of quartz, feldspar, and mica. Many of the volcanic grains are partially dissolved, and are often found to be replaced with chlorite (figure 5.20). Some igneous rock fragments are heavily degraded and mechanically squeezed into intergranular areas, often chocking pore throats. When degraded to such a degree that their original identity cannot be determined and the grains are so deformed that they clog pore throats, they may be

mistaken for matrix. Subordinate metamorphic grains are observed but are uncommon, and are included within the igneous rock fragment assembly in figure 5.19. These grains are composed of polycrystalline quartz with mica and display a schistose texture. High quantities of **mud rock fragments** are found, particularly in FA3 – mouth bar and FA5 – meandering channel deposits. These are observed to be altered to authigenic illite and microcrystalline quartz. These grains are interpreted to be syn-sedimentary. They often compact in a ductile manner, sometimes blocking pore throats. **Mica** laths are present throughout the Fruholmen Formation, seen as pristine to weakly altered. Alteration to authigenic kaolinite is often seen between cleavage planes. Mica grains are identified by their high birefringence colours and perfect basal cleavage, and may be weakly deformed by surrounding, more rigid grains. **Organic debris** are amorphous and behave in a ductile manner similar to mud rock fragments. **Pseudomorphous replacements** are most often picked out by authigenic phyllosilicate minerals that take the shape of a grain. Commonly seen are chlorite pseudomorphs. Because it is difficult to determine what mineral they replace, these grains are assumed to originate from the dissolution of highly unstable components and are classified as rock fragments. Minor amounts of **chert** was counted in several samples. Other rock fragments include particles of siderite, as well as opaque minerals and minerals that could not be identified but are present in trace amounts. Heavy minerals comprise garnet, apatite, rutile, zircon, monazite, xenotime, and sphalerite; these grain particles were identified through SEM and are considered to be present in trace amounts.

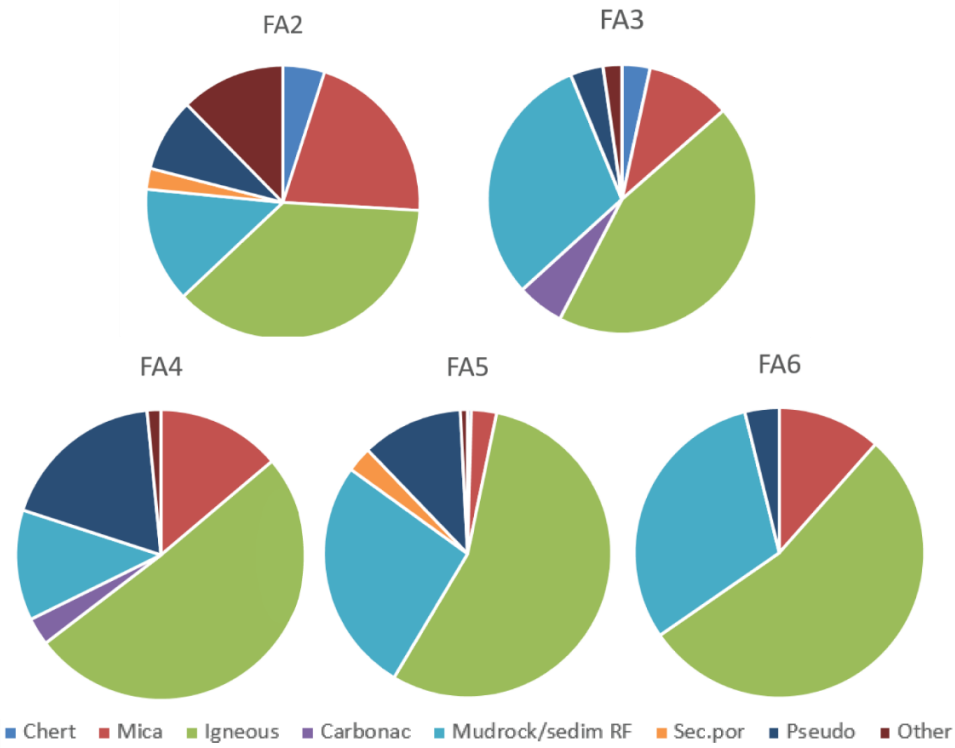


**Figure 5.19:** Relative abundance of rock fragment components, averaged for each sampled facies in the Fruholmen Formation. Igneous rock fragments are consistently dominating, followed by mudrock fragments.

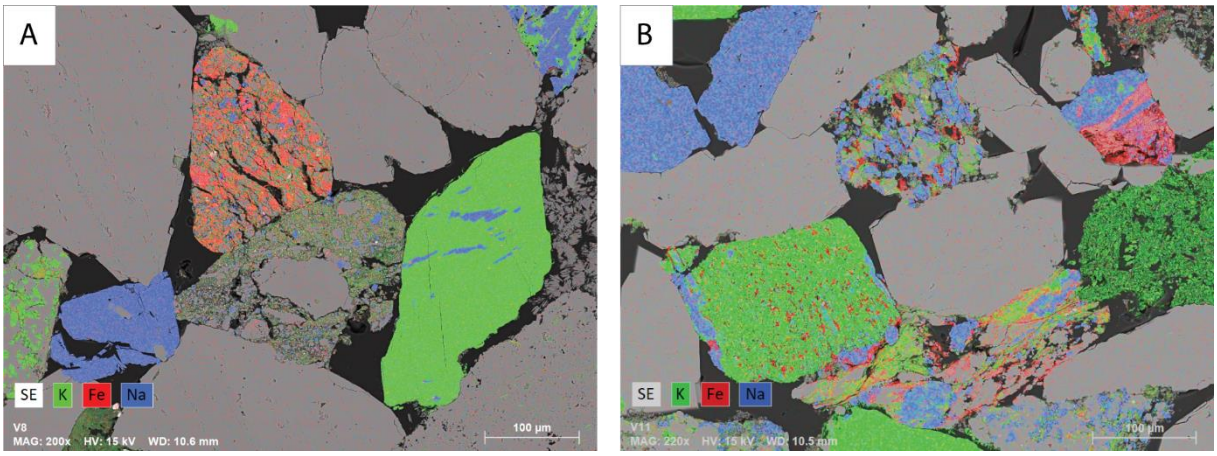


**Figure 5.20:** ***(A)*** Several rock fragments from sample V8, with potassium, iron, and sodium highlighted green, red, and blue respectively. Grains are partly degraded but have acted as rigid grains during compaction. High iron concentrations in the upper fragment are from chlorite. ***(B)*** Rock fragments from sample V11. Blue and green areas highlight albite and k-feldspar, respectively. Red marks areas of chlorite. Lithic rock fragments are again degraded.

### Allogenic Matrix

The matrix clays are not resolvable in optical microscopy. Results from point counting show a range from 1% to 18%, with an average of 6%. Detrital clays occurs most commonly as dispersed matrix, but also as infiltration residual. Intercalated laminae are common in FA4 – tidal flats. SEM analysis identified the detrital clays as illite. Heavily deformed and altered igneous and mud rock fragments (pseudomatrix) may at times have been mistaken for allogenic matrix during point counting.

## Authigenic Mineralogy

The identification of authigenic minerals, such as kaolinite, illite, and microcrystalline quartz is challenging through optical microscopy. From bulk XRD, an estimation of some authigenic minerals is given (figure 5.13). For confirmation, SEM analysis was conducted on selected samples to see the dominating authigenic mineralogy. Although quartz cement is approximated by point counting, it is much better illustrated with cathode luminescence (CL). Selected samples were analyzed with CL to accentuate the extent of quartz cementation. Authigenic minerals found are presented in order of decreasing abundance.

#### *Kaolin*

Kaolin (kaolinite and dickite) is present in all samples in the Fruholmen Formation, with point counted quantities averaging 3%. However, this is likely an underestimation given that kaolin can be difficult to discern via optical microscopy, especially in sandstones with small grain sizes. In SEM, kaolin is often observed to have a booklet morphology and frequently takes on a vermicular appearance, filling both primary and secondary pore space. Kaolin is found filling pores and chocking pore throats, typically in combination with altered feldspars and micas. Because kaolinite becomes thermodynamically unstable at temperatures exceeding 90°C, it recrystallizes to either illite or dickite. The recrystallization product is determined by the availability of potassium and the ambient temperature. Dickite holds the same

chemical composition as kaolinite, although crystals are thicker. Bulk XRD analysis is not sufficient to capture the structural differences between them, which would require a clay fraction XRD analysis. Pore-filling kaolinite and possible dickite is shown in SEM images in figure 5.21. However, given the estimated maximum burial temperatures of 70-80°C (section 5.5.3), the presence of dickite is not supported.

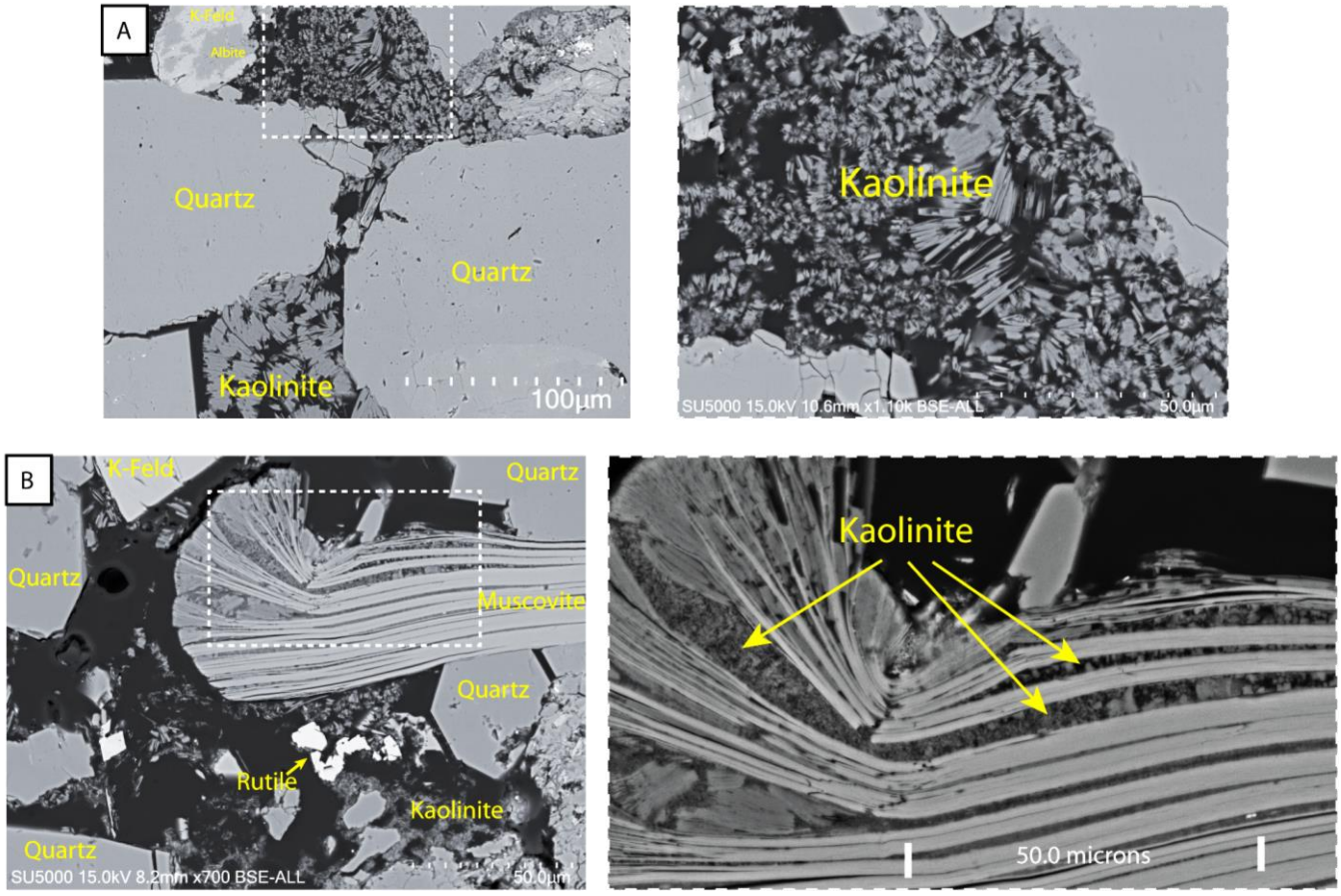


**Figure 5.21:** ***(A) (Left)*** Kaolinite found in the pore space between quartz and feldspar grains. From sample V8 of FA5 meandering channel deposits. ***(A)(Right)*** Close-up of boxed section in (A) (left), showing a combination of thicker crystals and very thin crystals, possibly documenting the presence of dickite crystals. ***(B)(i)*** Muscovite grain expanding along cleavage planes due to replacement with kaolinite. From sample V3 of FA3 – delta mouth bar. ***(B)(Left)*** Close-up of boxed area in (B) (right).

### *Quartz Overgrowths*

Through point counting, quartz overgrowths amounted to a minor percentage, averaging about 1%. However, following CL analysis, this percentage is concluded to be higher than can be seen via optical microscopy. A numerical estimate has not been made, but based on observations in CL, it stands to reason that it is one of the most significant authigenic minerals, following kaolin. Figure 5.22 displays images of the same quartz grain as seen with SEM, CL, and then both overlapping. In SEM-backscattered light (figure 5.22A), the quartz grain appears to be quite homogenous with no evidence of filled fractures. With CL (figure 5.22B), the quartz overgrowth appears darker, and quartz cemented veins are illuminated. When the two images are overlapped, the quartz overgrowth is evident, demonstrating how it may be challenging to point count quartz cement under an optical microscope.

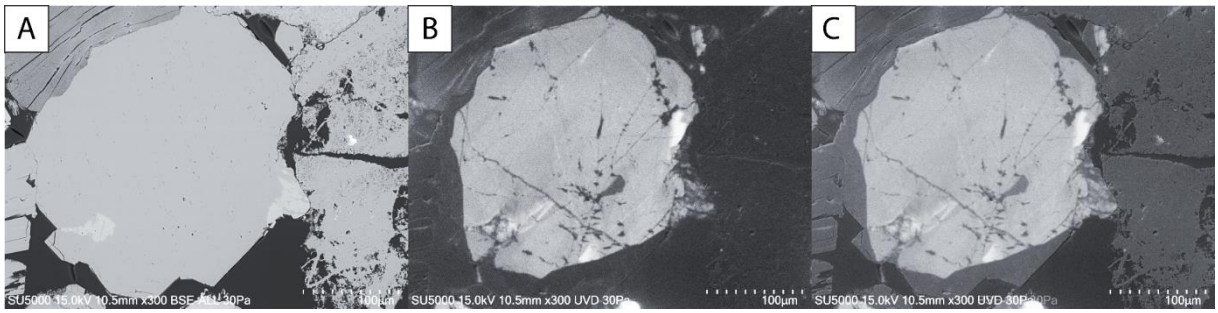


**Figure 5.22:** ***(A)*** Quartz grain taken with SEM, showing an opaque appearance, with sharp corners and smooth surfaces forming the boundary of the grain. ***(B)*** The same grain taken with CL, illuminating the original quartz grain. Quartz overgrowths appear darker. ***(C)*** Images A and B overlapped to illustrate the extent of the quartz cement around the grain as well as the fractures that are filled in. Image is from sample V8 of FA5.

### *Chlorite*

Authigenic chlorite is present in the Fruholmen Formation in variable amounts. Point counting results yield a range of 0% to 10%, with an average of 3%. Chlorite is often seen as a pseudomorph after unstable grains and also is found to replace minerals in volcanic rock fragments, likely ferromagnesian minerals (e.g. figure 5.20A). Although recorded in most samples, chlorite is particularly abundant in the FA2 delta front deposits. In FA2, the chlorite coats grains, presumably obstructing precipitation of authigenic quartz cement.

### *Illite*

When authigenic, illite is most commonly associated with mud rock fragments and found with microcrystalline quartz. Figure 5.23 demonstrates authigenic illite that has in part replaced a mud rock fragment. It is often found in combination with small authigenic quartz crystals.

### *Microcrystalline Quartz*

Microcrystalline quartz was identified though SEM analysis. It is observed within mud rock fragments in combination with authigenic illite. Figure 5.23 shows microcrystalline quartz that has in part replaced a mud rock fragment.

### *Siderite and Pyrite*

Siderite occurs as individual or clustered crystals, both within primary pore spaces and as displacive cements in grains. Siderite crystals often show zoning, with centers appearing darker in SEM, recording a higher abundance of manganese (figure 5.24Aii).

Pyrite is present in trace amounts, as framboidal or blocky cements which precipitate in primary porosity. Pyrite is also found to replace grains and amorphous organic matter. Examples of siderite and pyrite in the Fruholmen Formation are shown in figure 5.24.

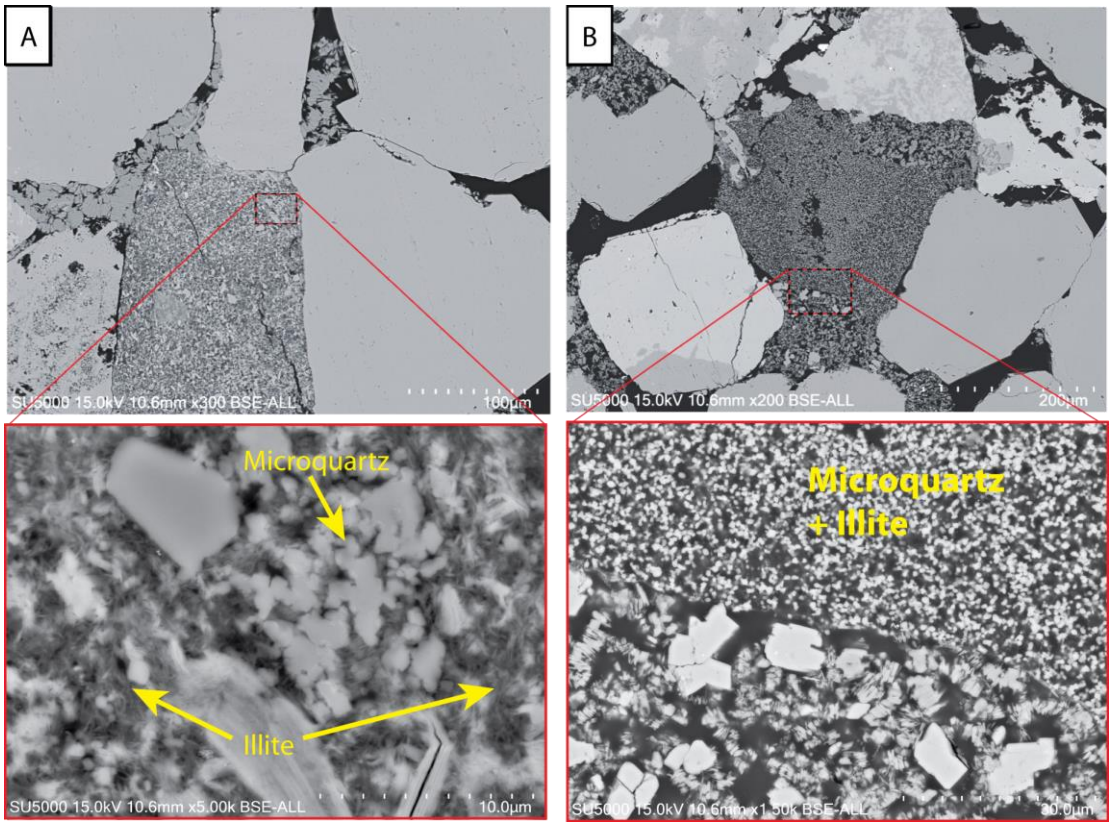


**Figure 5.23:** Images of (A) a mud rock fragment from sample V8 of FA5 meandering channel deposits, which has been largely replaced by microcrystalline quartz and illite. Illite takes on a fibrous/hairy appearance. (B) A mud rock fragment, also replaced with quartz and subordinate illite.

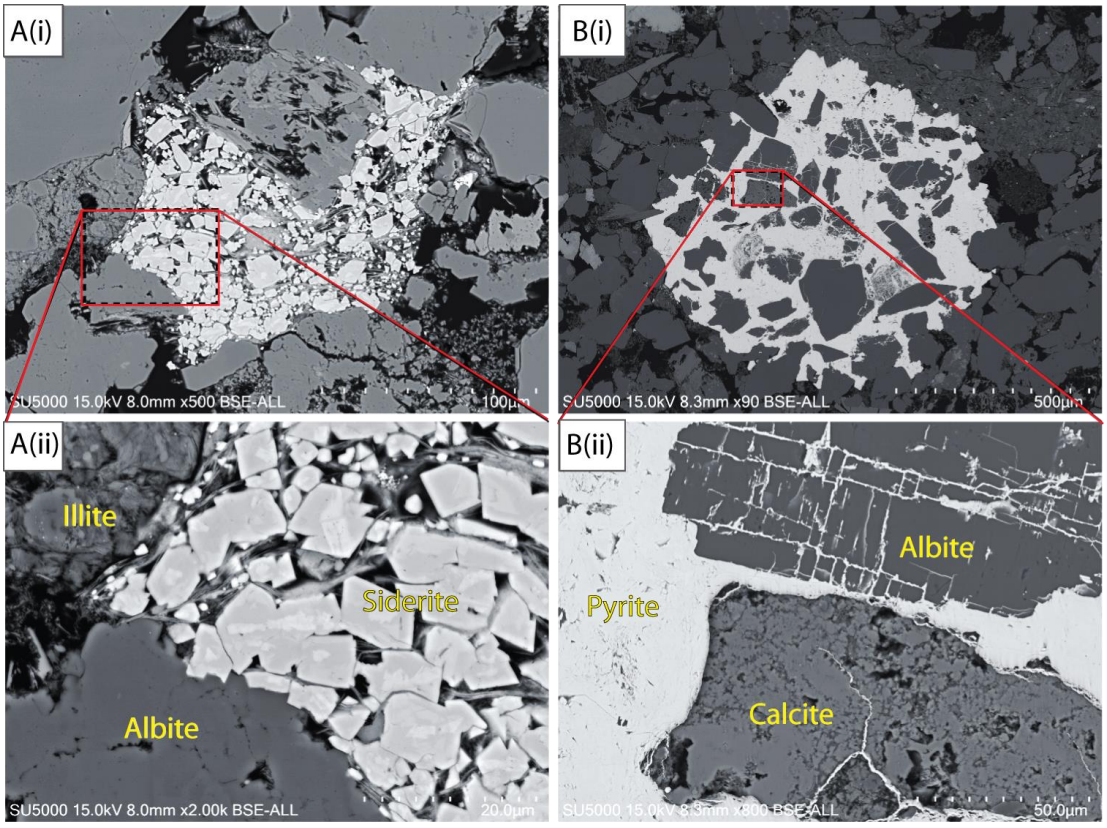


**Figure 5.24: (**A*)(i)* Cluster of zoned siderite crystals forming in between laths of chlorite in sample V3 in FA3 delta mouth bar deposits. (ii) close up, showing distinct zoning; the dark centers contain more manganese. *(B)* Pyrite, infilling primary porosity and filling in cracks (i) close up shown in (ii).

*Calcite Cement*

Calcite cement is insignificant in most samples from the Fruholmen Formation, comprising typically less than 1%. It is distributed in a patchy fashion in primary pores. However, sample V12 of FA6 – meandering channel deposits, is completely calcite cemented, having a calcite percentage of 32 percent from point counting. The cement largely fills the available pore space, yielding a negligible primary porosity. Throughout the core, cemented sections are noted, and they seem to occur irregularly, with a random distribution. V12 is the only sample from a cemented zone, and holds the highest IGV of 38% (these zones are marked on the composite log in figure 5.1). An image of sample V12 in XPL is shown in appendix G to demonstrate calcite cementation.

## *Nordmela Formation*

Thin section analysis were conducted on the two samples from the Nordmela Formation. Based on the relative proportions of quartz, feldspar, rock fragments, and matrix, sample V16 classified as a quartz arenite and V17 as a subarkosic arenite. As stated, only one facies association, FA7 – compound tidal dune, comprises the Nordmela Formation. Although the two samples from the formation classify differently, their compositional differences are minor, with both plotting at the top of the QFL diagram. The following tabulations again include detrital mineralogy (framework grains and matrix) and authigenic mineralogy (cements and authigenic clays). Constituents are ordered in terms of decreasing abundance.

### Detrital Mineralogy

#### Framework Grains

*Quartz*

Quartz is point counted to constitute about 66% of the samples from the Nordmela Formation. When recalculated to plot on the QFL ternary diagram, it constitutes an average of 91%. Similar to the Fruholmen Formation, there is a predominance of monocrystalline quartz as opposed polycrystalline quartz, which constitutes 3-4% of samples. Quartz grains are seen to commonly contain micro-scale fluid inclusion and occasionally heavy mineral inclusions. The SEM elemental map in figure 5.25 demonstrates the dominance of quartz in the Nordmela Formation.

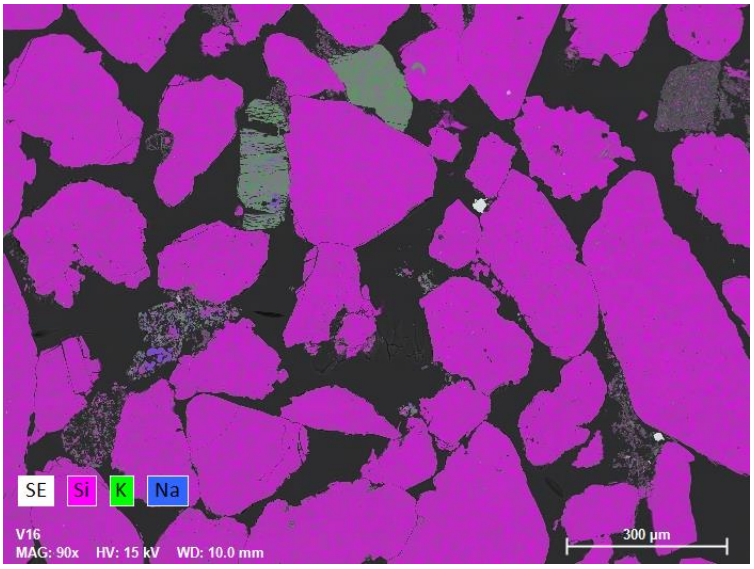


**Figure 5.25:** SEM elemental map of sample V16 of FA8 of the Nordmela Formation, highlighting Si, K, and Na. The dominance of quartz is demonstrated. Several decayed rock fragments are observed, and K-feldspar is picked out by the green colour.

*Feldspar*

Feldspar comprises only an average of 3% in the Nordmela Formation. When recalculated to plot on the QFL ternary diagram, it constitutes an average of 4%. Feldspar grains are variably dissolved, ranging from pristine to skeletal. Both point counting and XRD results show there to be a dominance of plagioclase feldspars. No K-feldspars were point counted or were detected by XRD, but trace amounts were found through SEM (figure 5.25).

*Rock Fragments*

Rock fragments in the Nordmela Formation are challenging to recognize due to high degrees of alteration. They comprise an average of 3 percent of the samples. Most rock fragments encountered are of igneous or metamorphic origin. Heavy minerals encountered include apatite, garnet, rutile, tourmaline, and zircon. Examples of rock fragments found in the Nordmela Formation are shown in figure 5.26.

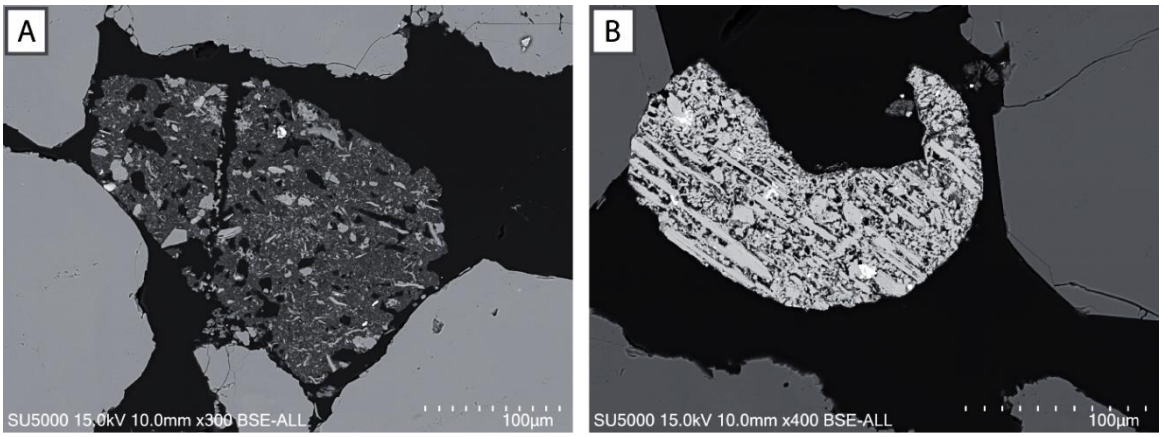


**Formation 5.26:** Examples of rock fragments encountered in the Nordmela Formation. ***(A)*** Mud rock fragment from sample V16 in the Nordmela Formation, partly degraded and composed of small grains of K-feldspar, quartz, muscovite, zircon, and rutile in a matrix of illite ***(B)*** Partly degraded and dissolved detrital rutile grain from sample V16 of the Nordmela formation; the intergrown mineral was likely another titanium-rich mineral such as ilmenite. Small zircon crystals are found within it.

### Allogenic Matrix

The allogenic matrix is largely formed of illite. Allogenic clay is rare in samples from the Nordmela formation, with point counting yielding an average of 0.16%. In SEM, authigenic clays are sometimes seen to coat detrital grains. As with the Fruholmen Formation, rock fragments degraded beyond recognition may be counted as matrix if there is no way to properly identify them as rock fragments.

## Authigenic Mineralogy

*Quartz overgrowths*

Quartz overgrowths constituted a minor percentage from point counting, averaging 2 percent. Cathode luminescence was not performed on either of the samples from the Nordmela Formation, however the frequently occurring sharp corners and smooth surfaces of quartz grain boundaries indicate that it is the most significant authigenic mineral. CL performed on Fruholmen and Stø Formation samples both indicated higher percentages of quartz cement than tabulated during point counting. The same likely holds true for the Nordmela Formation, as it is easy to underestimate quartz cement under an optical microscope.

*Kaolin*

Kaolin is point counted to comprise 0.33 % on both samples from the Nordmela Formation. SEM analysis shows that kaolin is present in trace amounts. Where present, it fills pores and is sometimes in mud rock fragments. It occurs as booklets and vermicules, similar to figure 5.21 of the Fruholmen Formation but to a far smaller extent.

*Pyrite*

Pyrite is present in both samples from the Nordmela Formation in percentages less than 1%. Pyrite is framboidal and is found in primary pores and often is replacive in decayed grains.

## *Stø Formation*

Thin section analyses were conducted on three samples from the Stø Formation. Based on the relative proportions of quartz, feldspar, rock fragments, and matrix, all three samples from the Stø Formation are classified as quartz arenites (figure 5.16). Compositional differences between the three samples are minor, with all samples plotting at the top of the QFL diagram.

The following mineral/grain tabulations include framework grains, matrix, cements, and authigenic clays. Constituents from each category are ordered in terms of decreasing abundance.

### Detrital Mineralogy

#### Framework grains

*Quartz*

**Quartz** grains are the obviously dominating framework grain (figure 5.16) with point counting results displaying an average of 69% (appendix E). Point counting results show a marked predominance of monocrystalline quartz as opposed to polycrystalline quartz (below 5%). When recalculated to plot on the ternary diagram, quartz comprises an average of 94% (figure 5.16; appendix E). Quartz grains frequently contain micro-scale fluid inclusions and heavy mineral inclusions. Figure 5.27 demonstrates the predominance of quartz in the Stø Formation.

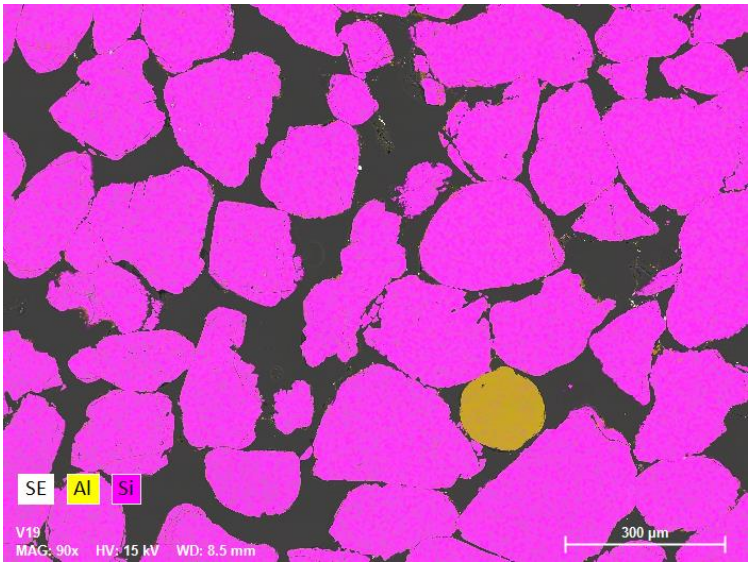


**Figure 5.27:** SEM elemental map of sample V19 from the Stø Formation, with Si and Al highlighted pink and yellow, respectively. The clear dominance of quartz is demonstrated, as well as the high porosity. The highly spherical aluminum bearing grain is tourmaline.

*Feldspar*

Feldspars make up a minor percentage of the Stø Formation, averaging 3%, much like the Nordmela Formation (appendix E). When recalculated to plot on the ternary diagram, feldspar comprises an average of 3.5%. (figure 5.16, appendix E). Feldspar grains are variably dissolved, ranging from pristine to skeletal. Both point counting and XRD results show there to be a general dominance of plagioclase feldspars.

*Rock Fragments*

Rock fragments in the Stø Formation are challenging to recognize due to high degrees of alteration. They comprise an average of only 1% of the samples. Heavy minerals encountered include apatite, garnet, rutile, tourmaline, and zircon. Examples of various rock fragments are shown in figure 5.28.

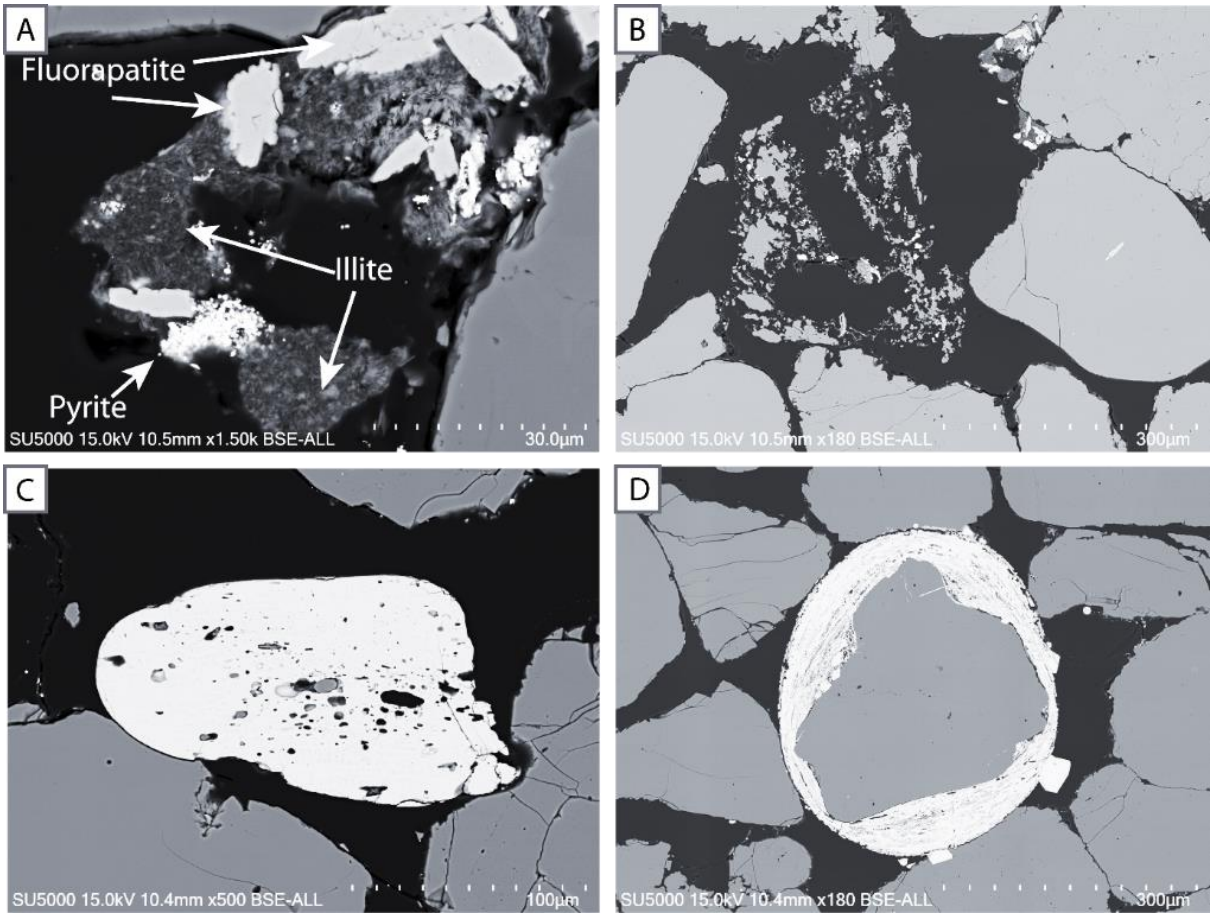


**Figure 5.28:** Examples of rock fragments encountered in the Stø Formation. ***(A)*** Rock fragment from V18 of the Stø Formation, showing small fragments of fluorapatite with illite ***(B)*** Largely dissolved rock fragment ***(C)*** Well- rounded detrital rutile grain, containing inclusions which have been dissolved. A quartz inclusion remains. ***(D)*** Well-rounded detrital concentric layers surrounding a detrital quartz nucleus, forming an ooid. Found in sample V18 of the Stø Formation. The original layers have recrystallized into pyrite.

*Allogenic Matrix*

The allogenic matrix is largely formed of illite. Allogenic clay is rare in samples from the Stø Formation, with point counting yielding 0% in all samples but one, which amounted to 0.33%. Allogenic clays are often seen as infiltration residuals, acting as grain coatings (figure 5.29).

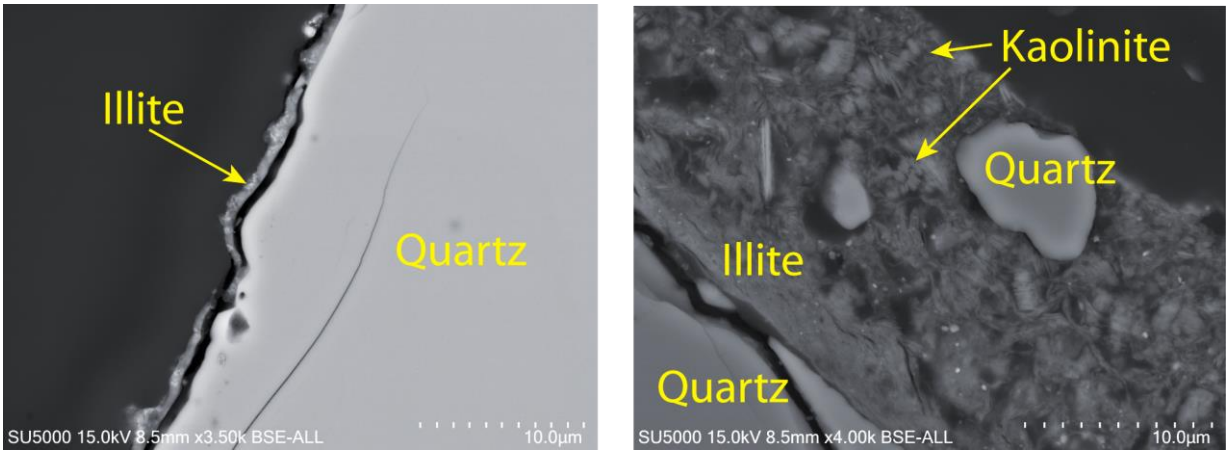


**Figure 5.29.** Allogenic clay coating on detrital quartz grain from sample V18 of FA9 of the Stø Formation.

## Authigenic Mineralogy

*Quartz Overgrowths*

Quartz overgrowths amounted to a minor percentage when point counting, from 1% to 2.00%. However following CL analysis, this percentage is concluded to be higher than as determined via optical microscopy in the Stø Formation. Based on these observations, it stands to reason that it is the most significant authigenic mineral in the Stø Formations as it occurs frequently on the quartz grains. Figure 5.30 demonstrates how it is easy to underestimate the percentage of quartz cement when point counting. Some quartz cement appears to have corroded, no longer showing the sharp corners (figure 5.30). Quartz overgrowths in the Stø Formation have also often been seen to have jagged edges as opposed to straight edges – quite uncharacteristic for quartz cement. This may relate to the illite coatings in figure 5.29.

**Figure 5.30:** Quartz overgrowths demonstrated with two overlapping images from SEM and CL from sample V18 from the Stø Formation. The overgrowths are seen to line the detrital quartz grains and fill in fractures. Overgrowths and fracture fill may represent two different events at different times. Boxed in red is a possible corroded quartz overgrowth, which may be evidence for reworking.

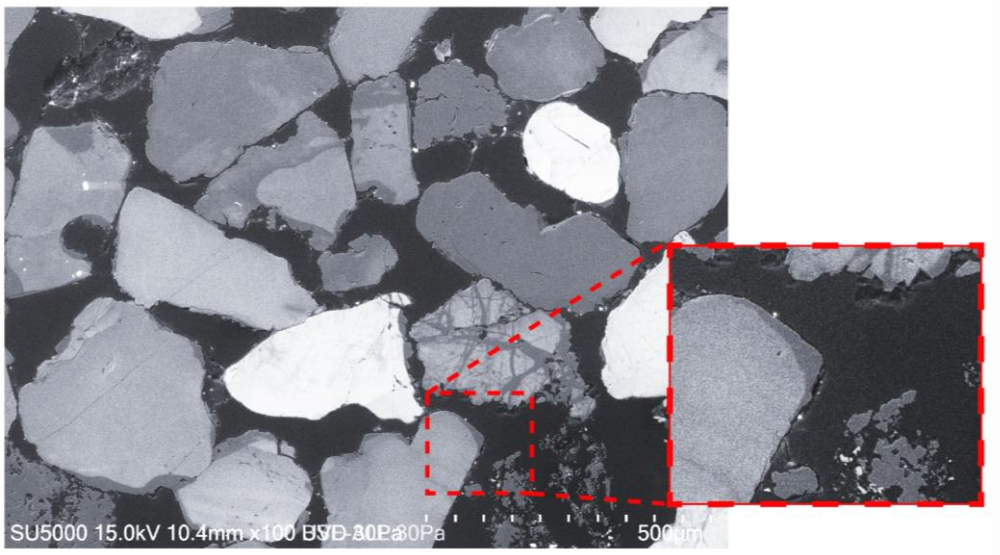

*Kaolin*

Kaolin minerals (kaolinite and dickite) are recorded by point counting to be absent in the Stø Formation, while SEM analysis shows that they are present in trace amounts. SEM analysis shows that kaolinite fills pores as well as replaces rock fragments and occurs as booklets and vermicules, much like those in figure 5.21 of the Fruholmen Formation, but to a far smaller extent.

*Pyrite*

Pyrite was not counted in point counting but are observed through SEM. Pyrite occurs as framboidal or blocky and is found in primary pores, often replacing decayed grains.

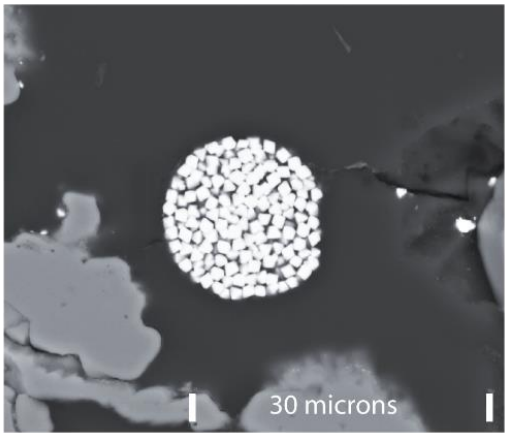


**Figure 5.31:** Framboidal pyrite found in sample V18 of FA9 of the Stø Formation in the primary pore space.

## 5.2.3 Textural Analysis

Textural analysis was conducted as described in section 4.2 on all sandstone samples.

### *Grain Size and Sorting*

Grain size and sorting are presented by facies association in figure 5.32, which shows cumulative grain size distribution plots on the left and histograms showing sorting of the samples on the right. Sorting is calculated using the standard deviation (equation 4.3) from Folk (1980). The inclination of the curves on the cumulative grain size distributions gives indication to the degree of sorting, while the values as calculated with equation 4.3 show more clear and objective results. Both are presented to allow maximum possibility of comparison with similar studies (e.g. Clark, 2017; Ilagan, 2018).

#### Fruholmen Formation

FA2 demonstrates a sharp positively skewed curve, with both samples showing the sharpest increase between Phi values of 4 and 5, classifying the samples as course silt. Both are computed to be well-sorted.

FA3 also demonstrates a sharp positively skewed curve, although not quite as sharp as that of FA2. All three samples show the sharpest increase between Phi values of 3 and 4, classifying them as very fine sand. Two samples are computed to be well sorted, while one is moderately well sorted.

FA4 shows a more normally distributed curve which shows for both samples the sharpest increase from Phi values 3 to 4, classifying them as very fine sand. Both samples are moderately well sorted.

FA5 shows the broadest range of curves, with the majority being sharp and positively skewed. The largest deviation is sample V12, which is the only calcite cemented sample. The large majority of samples within FA5 show the sharpest increase between Phi values of 2 and 3, thus classifying them as a fine sand. Sorting is predominantly well-sorted to moderately-well sorted.

The sole FA6 sample has a sharp curve, with most grains being between Phi values of 3 and 4, thus classifying as very fine sand. The sample is computed to be very well sorted.

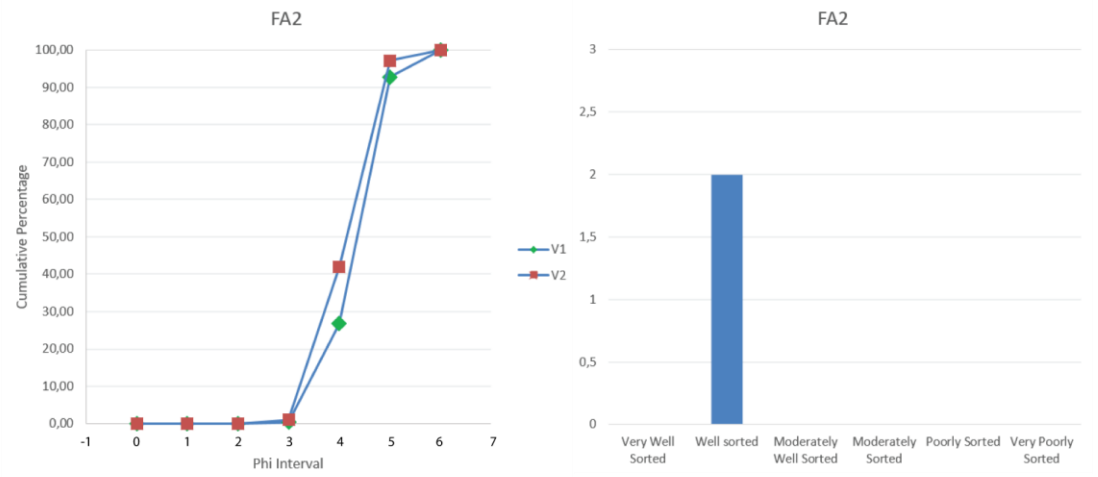
FA2
Cumulative Percentage
Phi Interval
V1
V2
FA2
Very Well Sorted
Well sorted
Moderately Well Sorted
Moderately Sorted
Poorly Sorted
Very Poorly Sorted

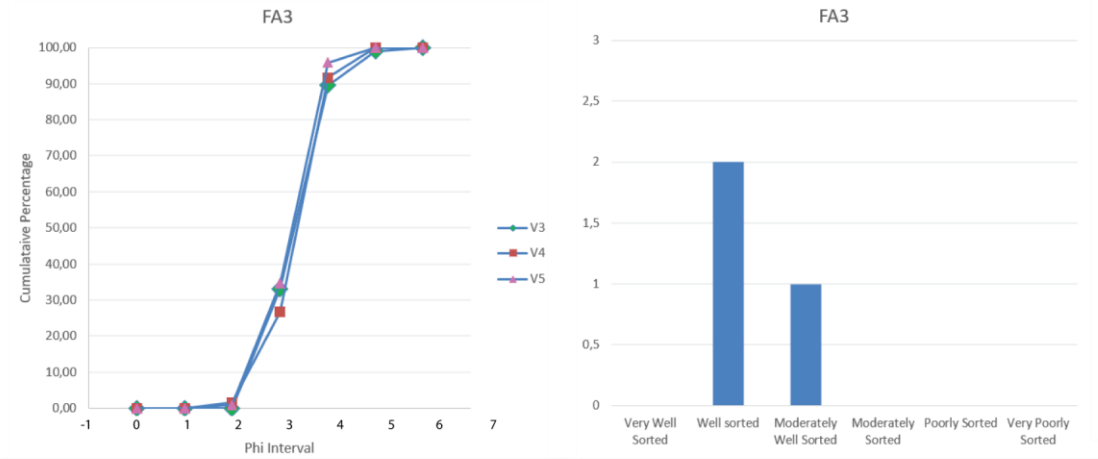
FA3
Cumulataive Percentage
Phi Interval
V3
V4
V5
FA3
Very Well Sorted
Well sorted
Moderately Well Sorted
Moderately Sorted
Poorly Sorted
Very Poorly Sorted

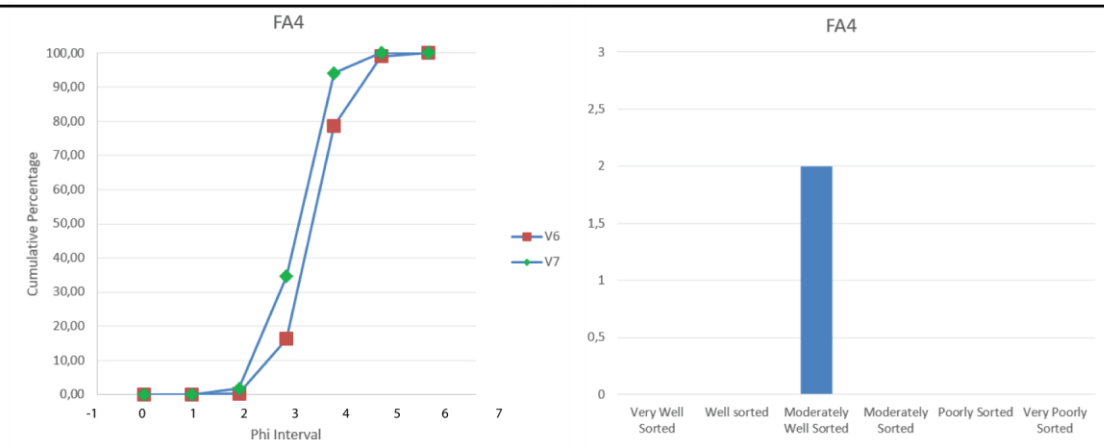
FA4
Cumulative Percentage
Phi Interval
V6
V7
FA4
Very Well Sorted
Well sorted
Moderately Well Sorted
Moderately Sorted
Poorly Sorted
Very Poorly Sorted

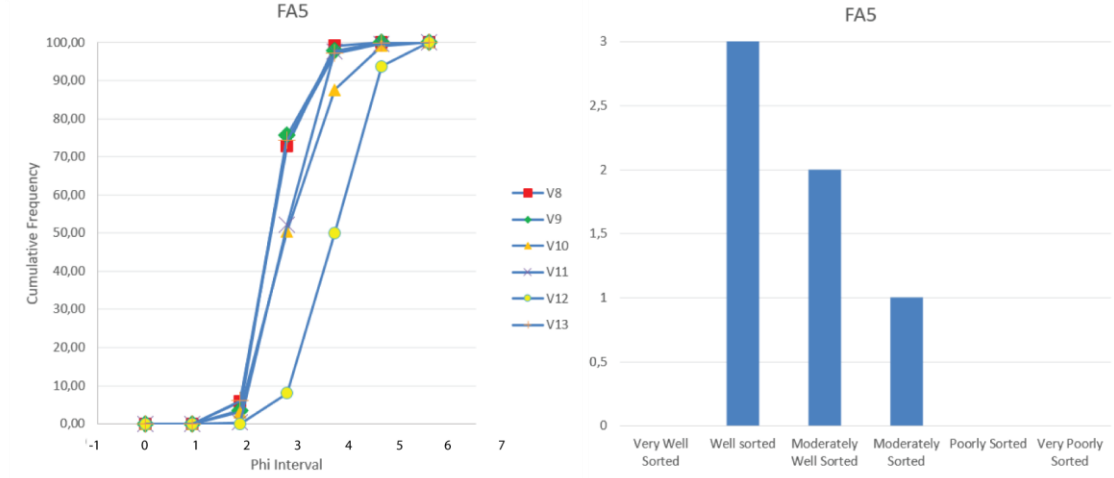
FA5
Cumulative Frequency
Phi Interval
V8
V9
V10
V11
V12
V13
FA5
Very Well Sorted
Well sorted
Moderately Well Sorted
Moderately Sorted
Poorly Sorted
Very Poorly Sorted

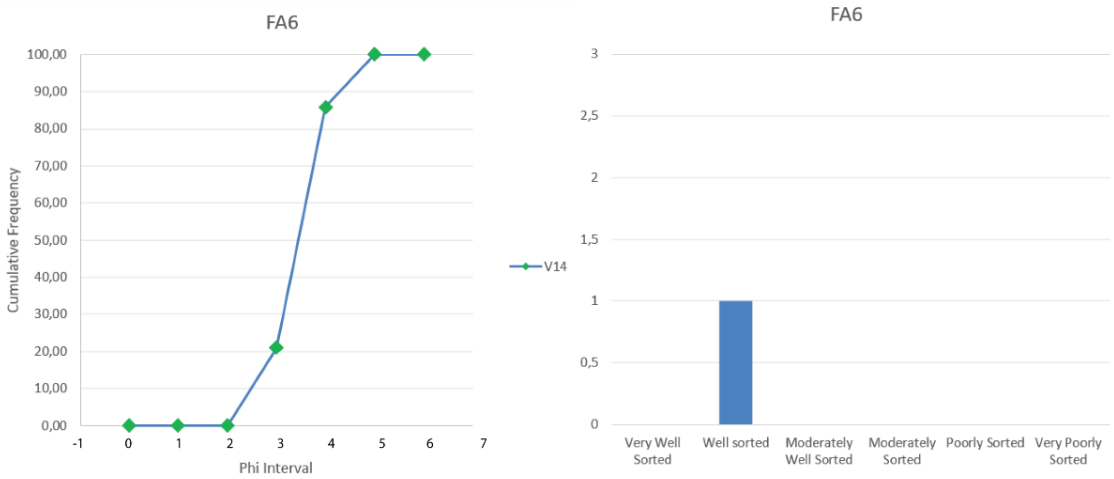


**Figure 5.32:** Cumulative grain size distribution plots for each facies association. Sorting is signified by the inclination of the curve. Histograms hold sorting for samples as calculated via the standard deviation (equation 4.3).

## Nordmela Formation

Grain size and sorting for FA8 and FA9 are presented in figure 5.33 in the same format as those for the Fruholmen Formation.

FA8, comprising the Nordmela Formation, shows a positively skewed curve exhibiting a sharp increase between the Phi values 1 and 3, signifying fine to medium grained sand. Both samples are well sorted.

## Stø Formation

FA9, comprising the Stø Formation, shows a positively skewed curve with a sharp increase between Phi values 2 and 3, signifying fine sand. Samples are very well- to well-sorted.

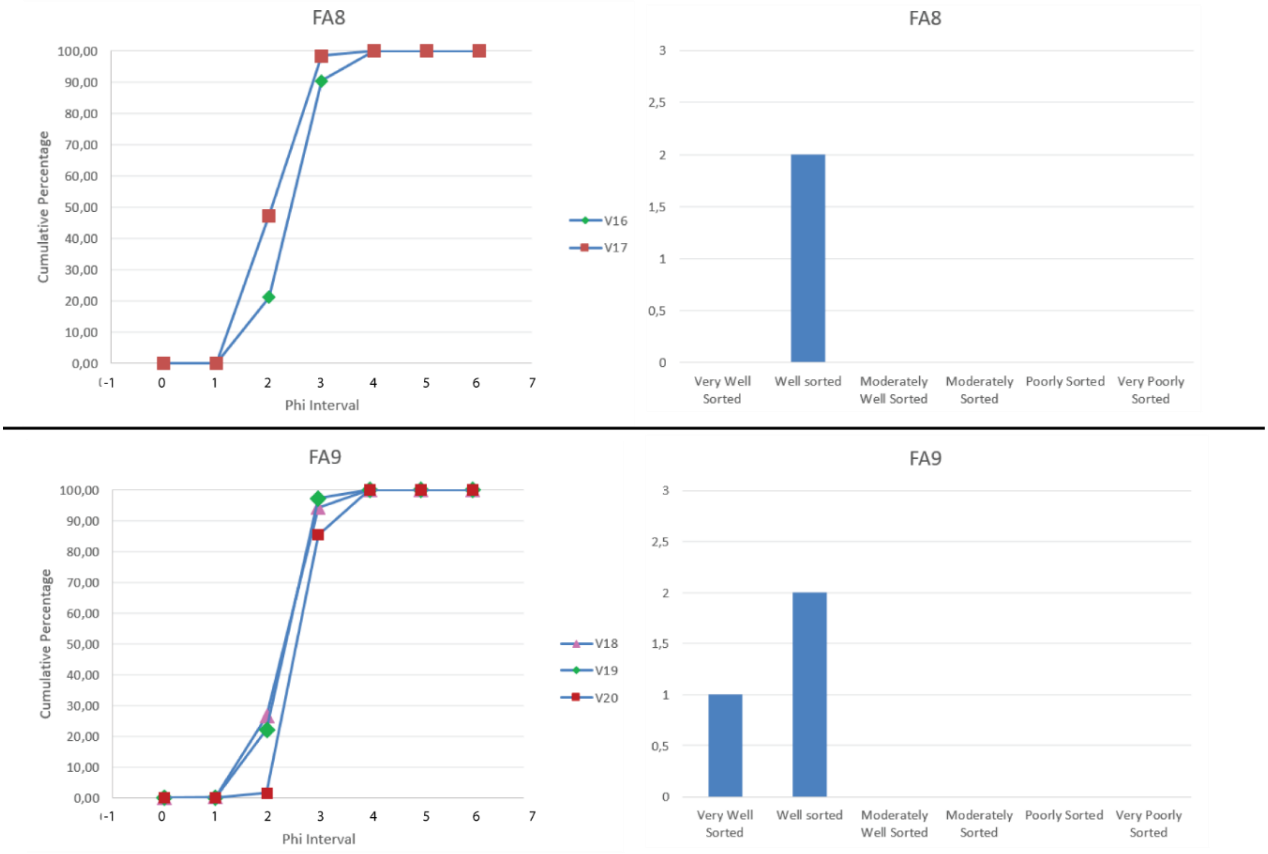


**Figure 5.33:** For the Nordmela (FA8) and Stø (FA9) Formations, cumulative grain size distribution plots on the left and histograms showing sorting of the samples on the right, calculated using the standard deviation (equation 4.3) from Folk (1980).

### 5.2.3.2 Grain Contact Analysis

Figure 5.34 shows the distribution of types of grain contacts, which are averaged with respect to facies association.

Long grain contacts are shown to be the dominant contact throughout the Fruholmen Formation (FA2-FA6). The calcite-cemented sample (V12 in FA5) contains an abundance of floating and tangential contacts, thus skewing the results of FA5.

In the Stø (FA9) and Nordmela (FA8) Formations, tangential contacts are shown to be the most prevalent, followed closely by long grain contacts.

As previously mentioned, there is difficulty in detecting quartz cement during point counting. Because quartz cementation can obscure the boundaries of the original detrital grain, the contacts can be difficult to discern. Because the quartz cement welds grains together, it can be easy to overestimate long or concavo-convex contacts, leading to slightly skewed results.


**Figure 5.34:** Distribution of floating, tangential, long, and concavo-convex contacts, averaged for each facies association.

### *5.2.3.3 Grain Shapes*

Distribution of grain roundness and sphericity, averaged with respect to facies association, are shown in figure 5.35 and 5.36 respectively.

#### Fruholmen Formation

FA2, FA3, and FA4 of the Fruholmen Formation all show a dominance of sub-angular grains. Stratigraphically up section, there is an overall slight increase in sub-rounded grains with an overall gradual decrease in angular and sub-angular grains. In FA5 and FA6, sub-rounded grains are shown to be dominating.

The entirety of the Fruholmen Formation shows a prevalence of grains with low sphericity. FA2-FA4 show a clear dominance of low-sphericity grains, whereas and FA5 and FA6 show higher percentages of high sphericity grains, but still maintain a dominance of low-sphericity grains.

#### Stø and Nordmela Formations

In FA8 (Nordmela) and FA9 (Stø), high proportions of rounded and sub-rounded grains occur. The Stø and Nordmela Formations (FA9 and FA8) show also larger percentages of high-sphericity grains.

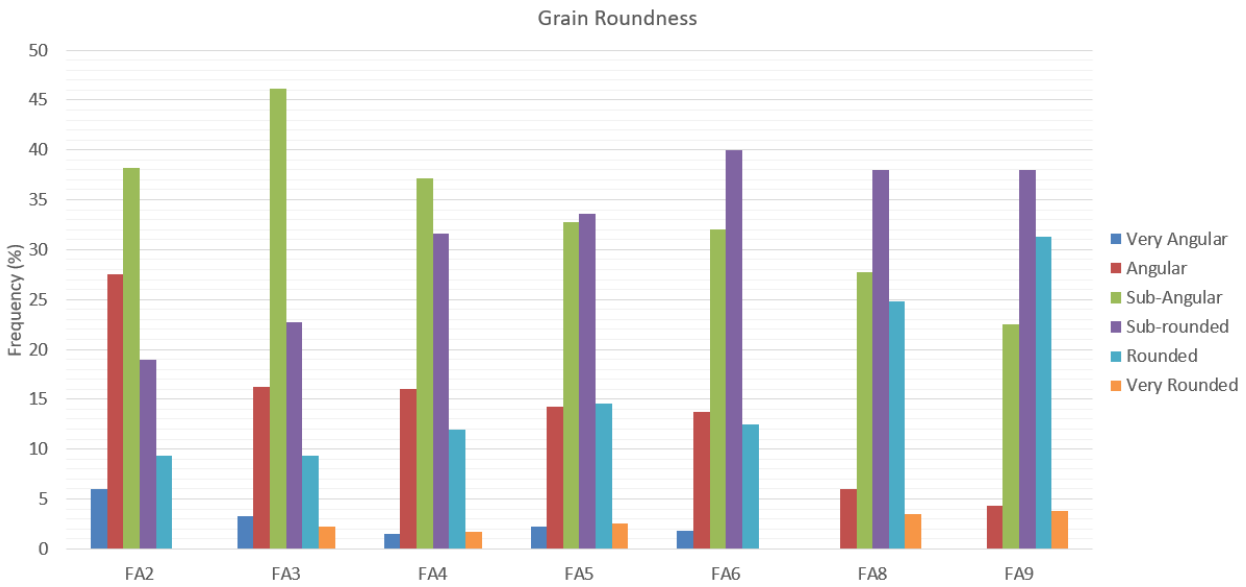


**Figure 5.35:** Grain roundness distribution averaged with respect to facies association.

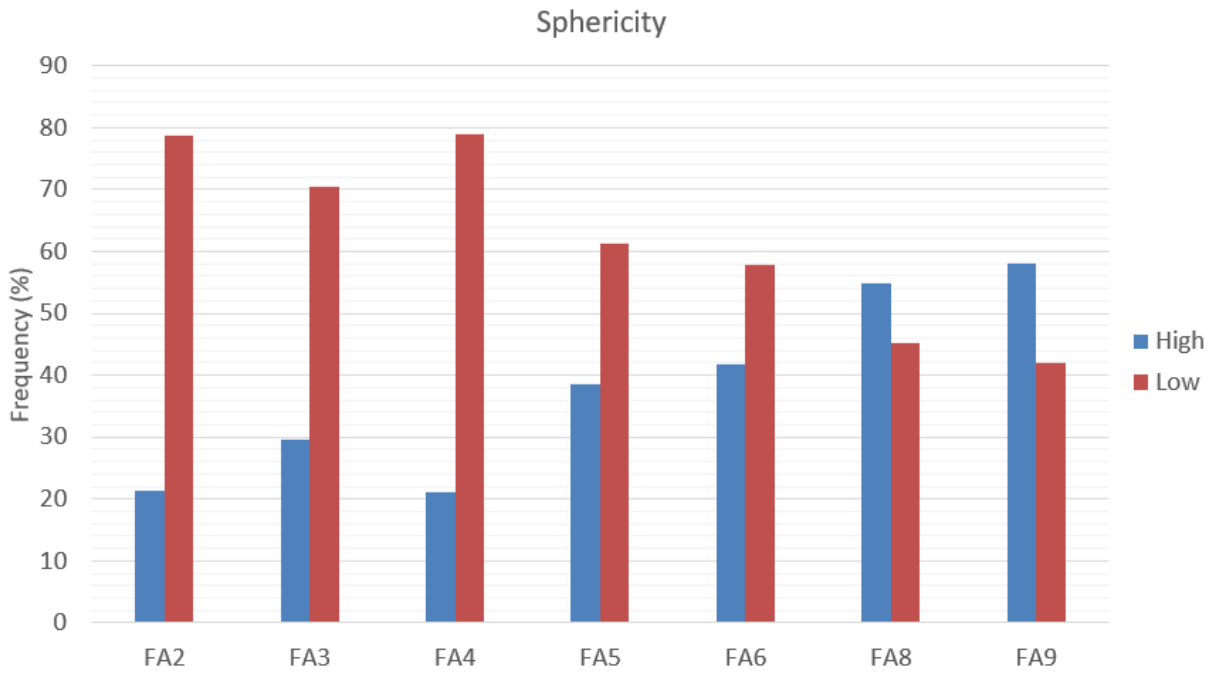


**Figure 5.36:** Sphericity distribution averaged with respect to facies association.

Previously noted challenges are met also in the determination of grain shapes. Quartz cement, difficult to distinguish in the optical microscope, may result in a misrepresentation of the grain shape and can possibly lead to biased results.

### *5.2.3.4 Intergranular Volume (IGV)*

The IGV of each sample is derived from point counting. Results are shown in figure 5.37 alongside the sedimentary log. The diagram shows the proportions of primary porosity, matrix, and cement in each sample. Intergranular cements accounted for in the diagram are calcite, chlorite, siderite, and quartz as well as authigenic pore filling minerals such as kaolinite. IGV averaged with respect to facies association is presented in figure 5.38.

#### Fruholmen Formation

Intergranular volume values range from 20% to 38% in the Fruholmen formation, averaging 27%. The calcite cemented sample, V12, represents the highest intergranular volume recorded. Matrix and cement make up a significant amount of the intergranular volume in the Fruholmen Formation, as stated in section 5.2.2, averaging 6 % and 8%, respectively.

The FA2 delta front deposits on average contain the highest percentages of cement, holding comparatively large proportions of both chlorite and siderite, at 9% and 3%, respectively. FA2 also shows some of the highest IGVs recorded. FA3 – mouth bar deposits on average have the lowest IGV, at about 21%. FA4 on average holds by far the largest quantities of matrix, at 15%. FA5 – meandering channel deposits includes one calcite cemented sample (V12), skewing results slightly; otherwise constituents are of similar proportions as FA3. FA5 has the highest average primary porosity in the Fruholmen Formation, at 13%. FA6 –tide influenced distributary channel deposits have relatively high proportions of matrix at 10%, but is otherwise similar to the underlying FA5 with the exception of the calcite cemented sample.

#### Nordmela Formation

FA8 – compound tidal dune deposits, comprising the Nordmela Formation, show an average IGV of 28%. The Nordmela Formation contains a virtually absent proportion of matrix, averaging 0.2%, and very small proportions of cement, averaging 3%. This is a stark contrast to the Fruholmen Formation. Authigenic mineralogy is dominated by quartz cement. A high primary porosity is recorded, averaging 25%.

#### Stø Formation

FA9 – upper shoreface deposits, comprising the Stø Formation, displays an average IGV of 26%. The Stø Formation, similar to the Nordmela Formation, contains yet smaller proportions of matrix and cement, on average 0.1% and 2% respectively. Quartz is again the dominating authigenic cement. A high primary porosity of 23% is recorded.

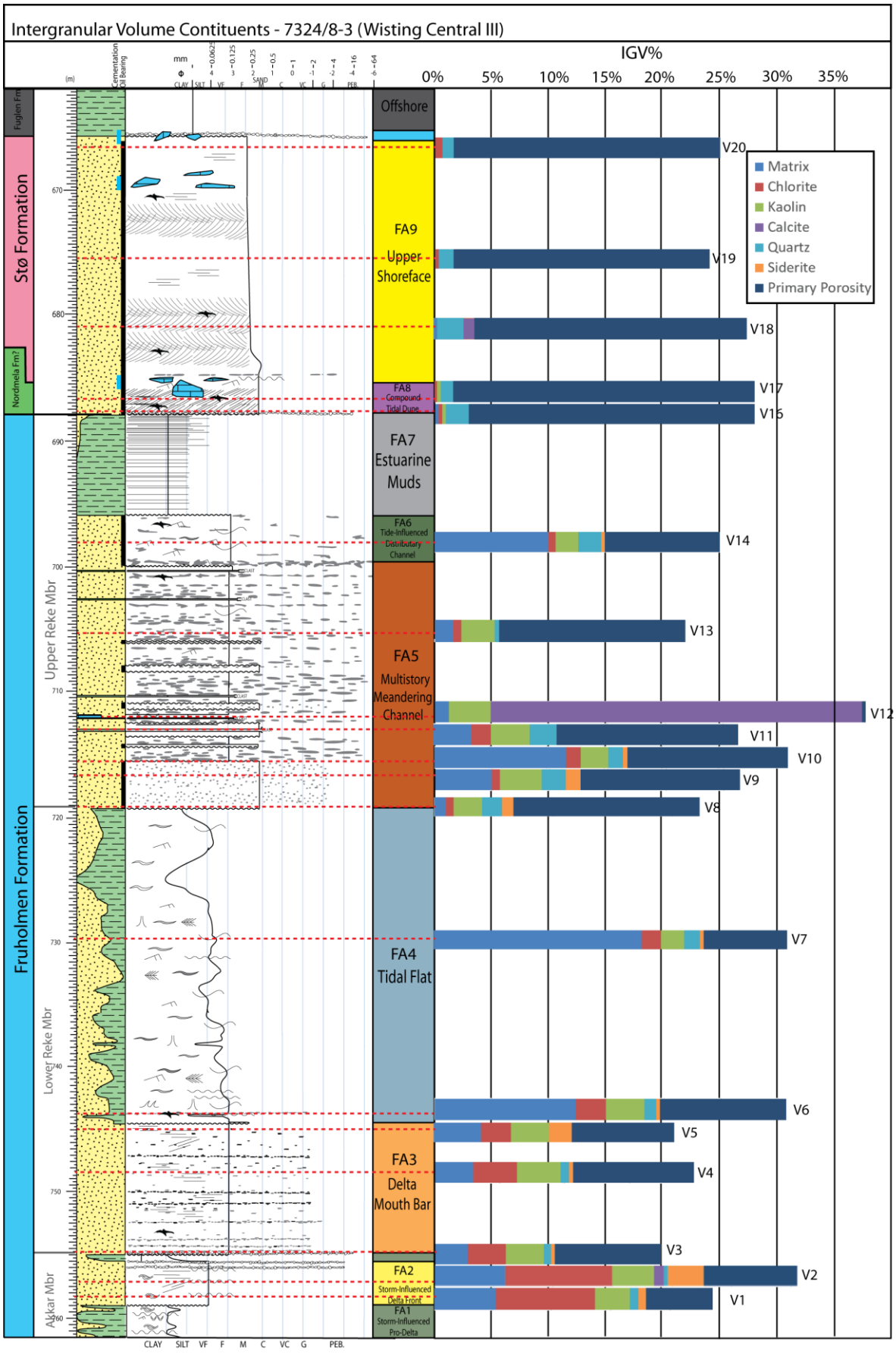


**Figure 5.37:** Intergranular volumes as determined by point counting. Legend for sedimentary log remains as in figure 5.1. High proportions of matrix and cement are found in the Fruholmen Formation.

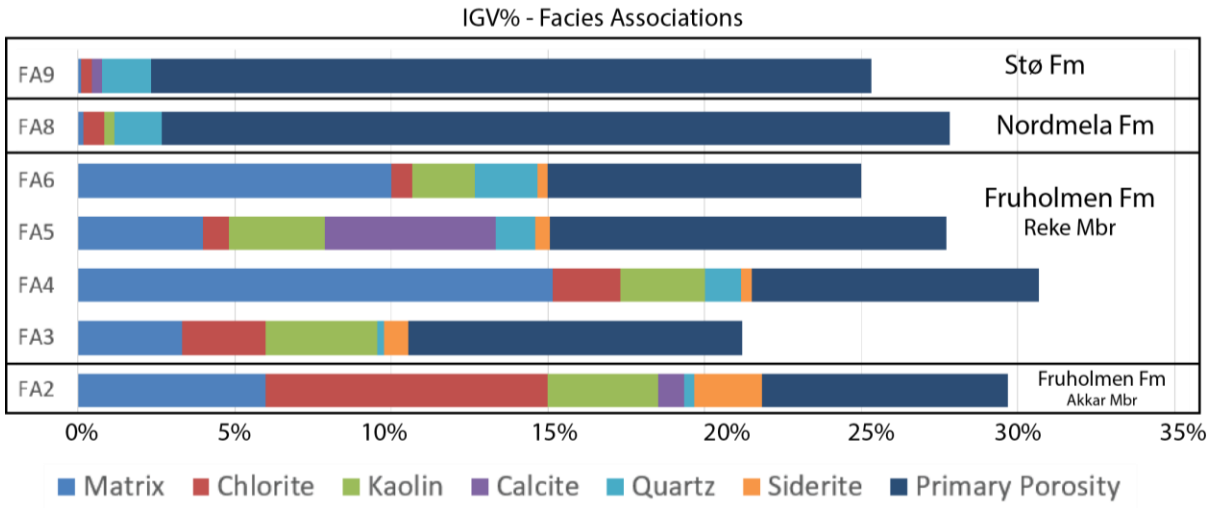


**Figure 5.38:** Intergranular volumes averaged with respect to facies association. High proportions of matrix and cement are found throughout the Fruholmen Formation, which are nearly absent in the Nordmela and Stø Formations.

### *5.2.3.5 Porosity and Permeability*

Porosity and permeability have been assessed using core plug data provided by OMV Norge. The helium porosity is plotted against the horizontal permeability in figure 5.39, along with cut-off values with respect to reservoir quality as defined in Tissot and Welte (1984). Core plug values that are nearest to the sample depths are displayed using coloured points for comparison with the petrographic results in this study (figure 5.39). Note that although these points are close to the sample depths, facies can vary a great deal over small lengths. Points besides these are plotted with black points in the same graph, coded by shape to represent facies association.

The Fruholmen Formation shows very variable porosity and permeability values. Although many points show ‘very good’ porosity values, almost none show permeability values that exceed the ‘very good’ cutoff. The FA5 and FA6 deposits show the most promising values, while FA4 and FA3 also show potential. FA1 and FA2 are less promising.

Samples from the Nordmela and Stø formations all show ‘very good’ porosity and permeability; this can be connected with the IGV results in section 5.2.3.4, which showed these formations to have high porosity and near negligible amounts of authigenic minerals and allogenic matrix.

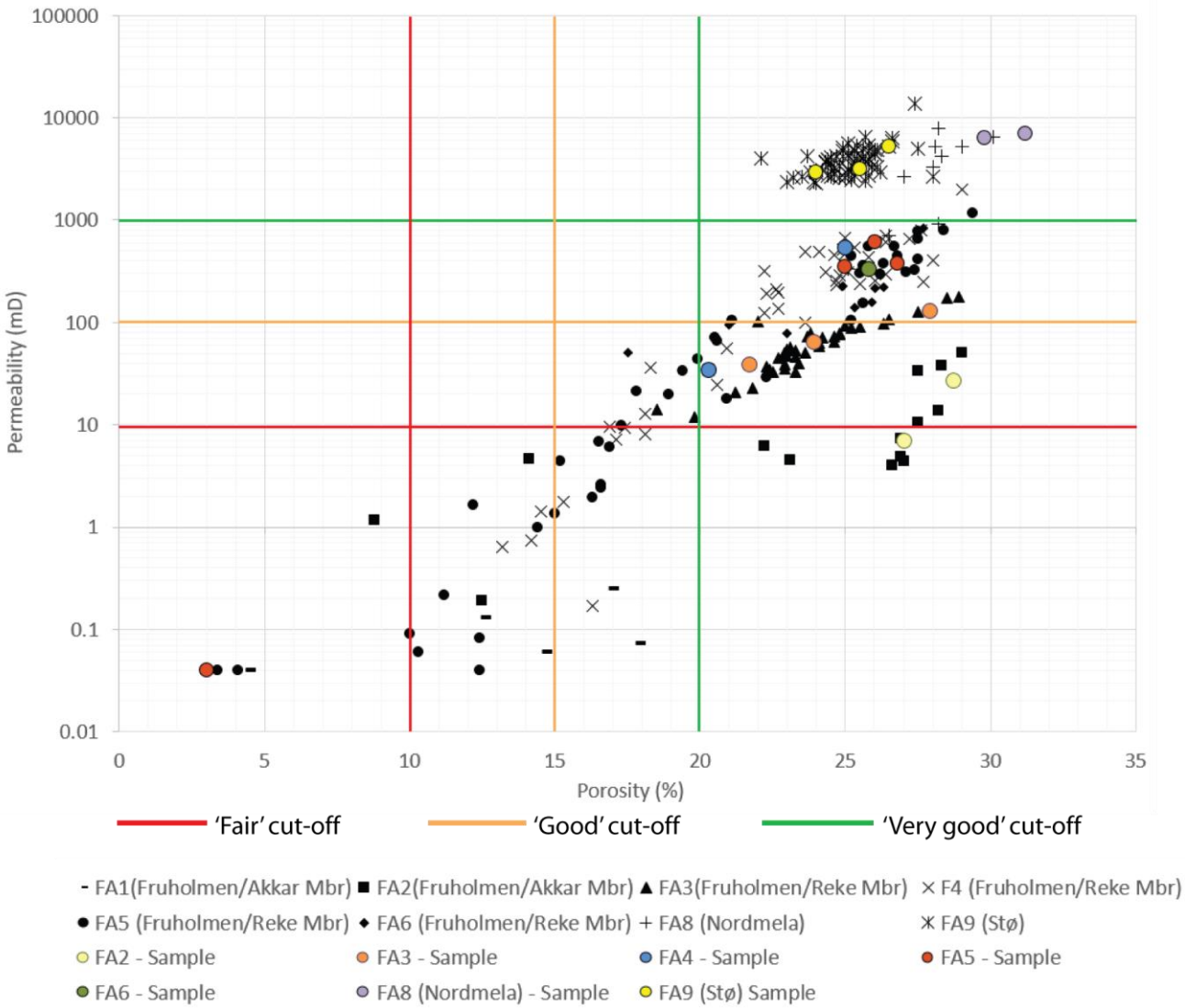


**Figure 5.39:** Helium porosity vs. horizontal permeability. Coloured points are values selected that are closest in proximity to the sampled depths in this study. No points were found in proximity to V10 and V11 from FA5, thus these are excluded. The black points are the 'background trend' of each facies association, utilizing all available measurements. The Stø and Nordmela formations are shown to exhibit 'very good' porosity and horizontal permeability. A majority of points from the Fruholmen Formation show 'very good' porosities. However, permeabilities assume a broad range, where FA5 meandering channel and FA6 distributary deposits appear the most promising. Sand flat facies of FA4 show promise, however the regular alternation with tidal mud flats of FA4 present vertical flow barriers. Cut off values are as defined in Tissot and Welte (1984).

# 5.3 Petrophysical Analysis

As discussed in section 2.6, the SW Barents Sea has experienced a significant amount of uplift. Petrophysical data is used in this study primarily to give an estimation for the depths at which sediments have been buried. Secondary aims of the petrophysical analysis include assessing porosity and evaluating depositional environments.

Figure 5.40 displays the logged interval alongside the gamma ray, neutron-density, p-wave velocity, and three porosity logs with the purpose of comparing the petrophysical data with the results from the sedimentological and petrographical analyses. The porosity logs include the neutron porosity log, the porosity log computed from density, and the combined neutron-density porosity. As previously noted in section 4.3.2, the combined porosity is often considered ideal because both the neutron porosity and the porosity from density log suffer from uncertainties related to the lithology; thus, by averaging them, the lithological effects can cancel out. The entirety of the sonic (calculated for velocity), bulk density, gamma, and neutron porosity logs are displayed in figure 5.40 for the purpose of uplift estimation.

The gamma ray log displays an overall cleaning-upward trend from the Fruholmen to the Stø Formation, indicating a decrease in clay content.

## 5.3.1 Fruholmen Formation

The Fruholmen Formation exhibits a varied gamma ray response, suggesting frequent changes in depositional energy. The repeated alternation between a positive and negative separation in the neutron-density log also attests to a mixed energy depositional regime throughout the Fruholmen Formation.

As FA1 has a large shale content, the positive separation as seen in the neutron-density log is expected. However its shaliness is not so apparent from the gamma ray log, having as similar response as FA2, a fine grained sandstone. Porosity values are shown to be comparatively lower, as expected.

FA2 is not easily separable with the GR log, but can be detected with the neutron-density log as it exhibits lower bulk density values and higher neutron porosity values than the surrounding clay-dominated FA1. Additionally, the porosity in FA2 is shown to be higher than the surroundings, and the velocity lower.

FA3 is not easily distinguished from other facies associations with the GR log. However, GR readings do not fluctuate so much throughout this interval as opposed to the rest of the Fruholmen Formation. The neutron-density log registers it because FA3 exhibits a slight but consistent negative separation throughout the interval.

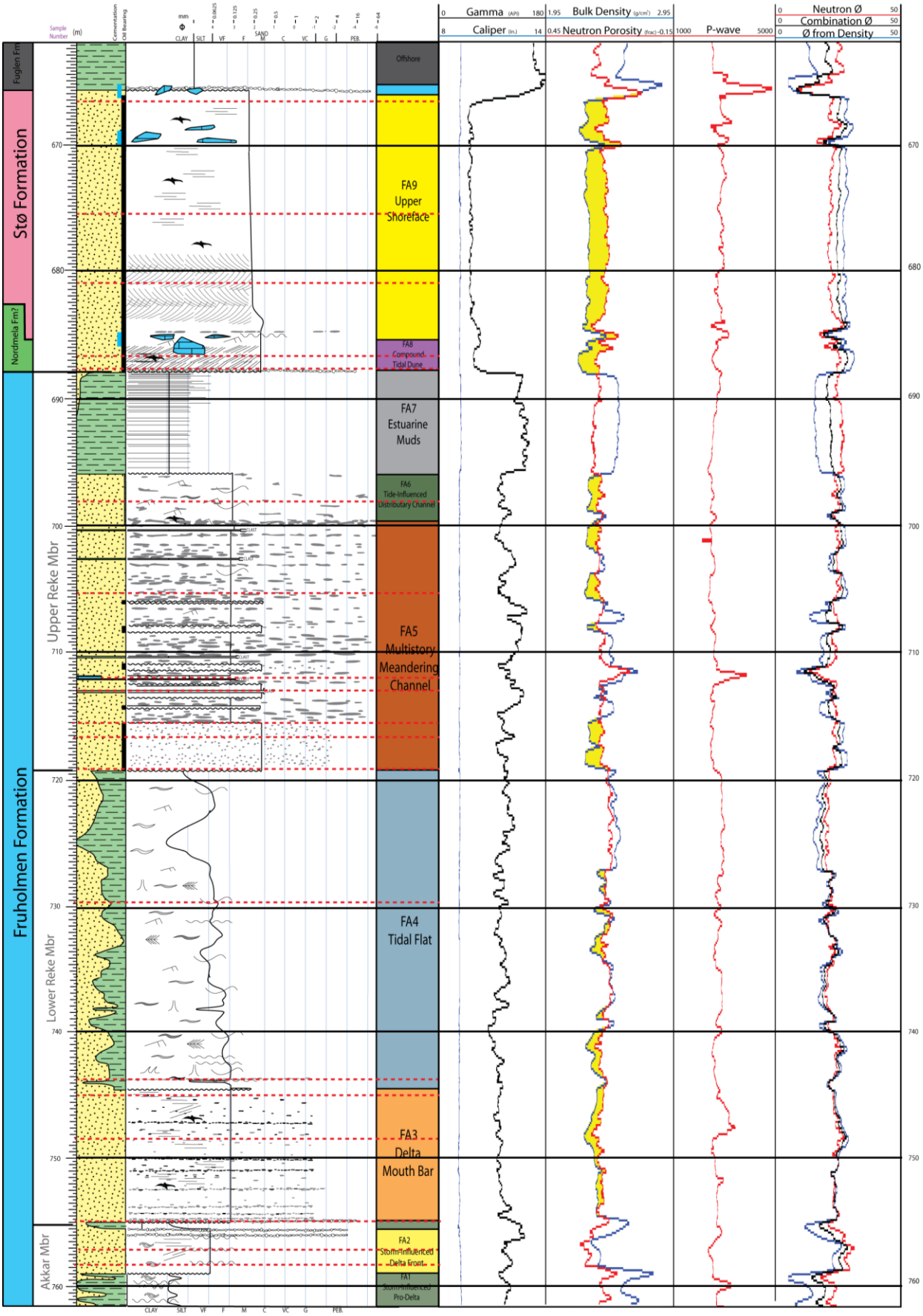


**Figure 5.40:** Sedimentary log alongside petrophysical logs, from left to right: Track (1) gamma, (2) neutron-density, (3) p-wave, (4) porosity from neutron (red), from density (blue) and combination (black).

FA4 has regularly fluctuating GR responses, agreeing with the large variations in sand content seen throughout the interval. As described in section 5.1.2, these relate to the alteration between tidal sand, mud, and mixed flats. Furthermore, the neutron-porosity log also shows alternations between a slight positive and slight negative separation.

FA5 shows many intervals with large negative separation in the neutron-density log, and some intervals with a small positive separation. Intervals of positive separation are related to areas with a high density of large intraformational mud clasts. These clasts also cause a variation in the gamma ray response. A small interval that is carbonate cemented shows a prominent peak in the P-wave velocity log and an abrupt decrease in porosity; this is accompanied by a sharp increase in density. Sample V12 was sourced from this interval.

The gamma ray response of FA6 is separated from that of the underlying FA5 by its higher consistency. There is relatively high negative separation throughout the interval in the neutron-porosity log.

FA7 shows consistently high gamma ray values, accordant with its high shale content. Furthermore, a large positive separation is shown in the neutron-porosity log. The porosity logs behave as expected when encountering a shale -- the neutron porosity log shows unreasonably high values due to the shale effect, the density log shows very low values, and the combined log is placed in between.

## 5.3.2 Stø and Nordmela Formations

Together, the Stø and Nordmela Formations take on a cylindrical shape, appearing as an even block of very low GR with a sharp top and base. This corresponds with petrographic results, which showed that these formations consisted of quartz-rich sandstone with negligible clay content. Overall, the entire interval shows a large negative separation, with the exception of intervals that bear calcite cement; these areas are shown in the sedimentary log and can be picked out in the well logs by fluctuations in the p-wave and porosity, as well as bulk density.

The transition from the Stø to the Fuglen Formation is marked by a cemented transgressive lag, which creates a pronounced spike in the p-wave velocity, accompanied by sharp decreases in porosity and an increase in density.

## 5.3.3 Compaction and Uplift

Figure 5.41 displays the P-wave velocity, neutron porosity, gamma ray, and density logs for the entire well, colour coded by formation. These graphs illustrate compaction trends, with the P-wave velocity steadily increasing while the neutron porosity decreases. The presence of oil bears seemingly little effect on the P-velocity in the Stø Formation, evidencing that the interval has undergone chemical compaction, serving to heighten the velocities. The Stø Formation is particularly conspicuous in the gamma ray log, comprising a very clean interval – additionally it holds lower density values compared with all other

formations measured. This is in agreement with observations made in the petrographic analysis, whereby negligible amounts of detrital material was documented and a high porosity, which had held low-density oil, was recorded.

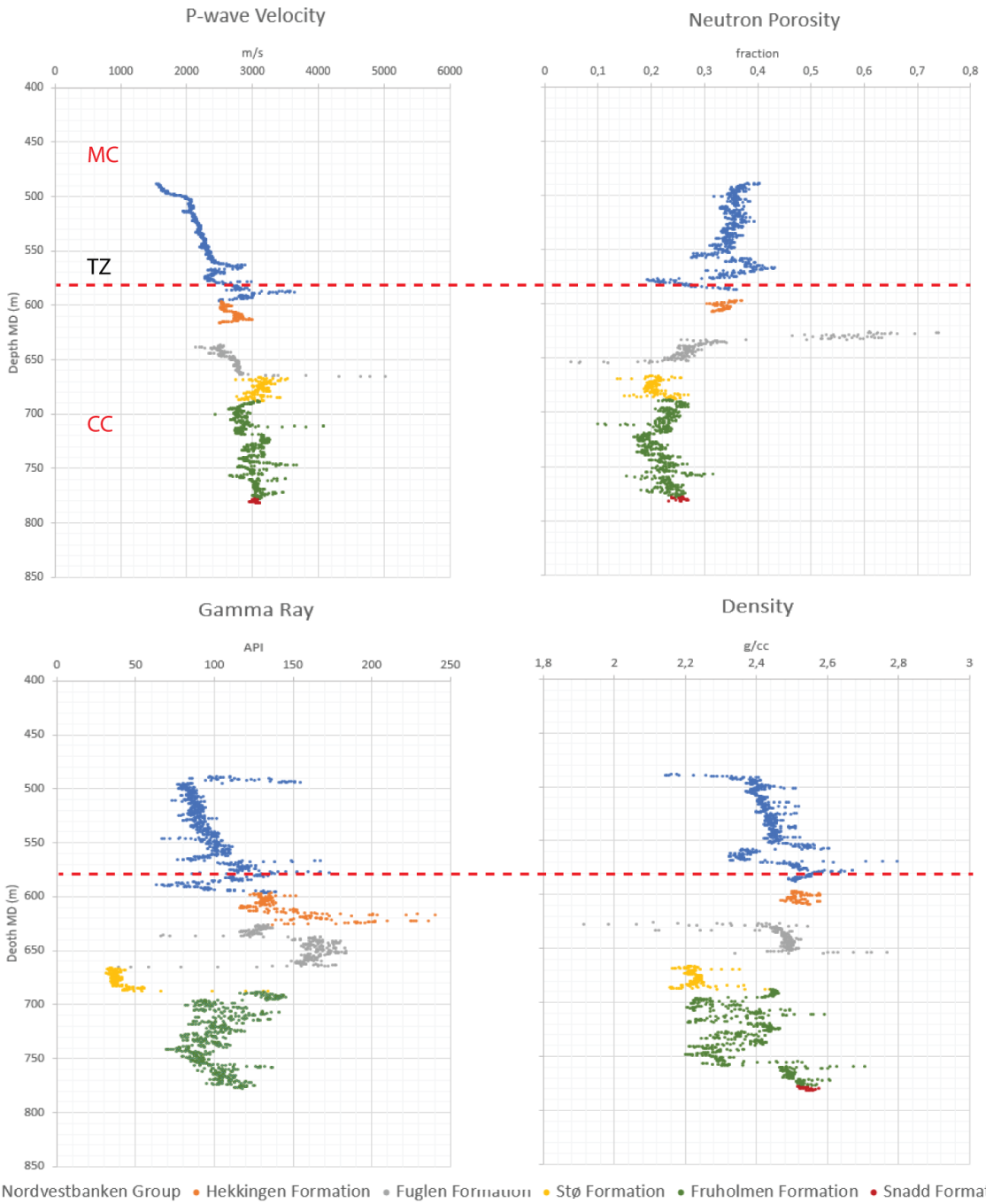


**Figure 5.41:** Velocity, neutron porosity, gamma, and density logs for well 7324/8-3. Typical compaction trends are observed, with a steady increase in P-wave velocity with depth and a decrease in neutron porosity. Density is more variable however an overall increase in density is seen. The red dotted line marks the interpreted transition zone from mechanical to chemical compaction. This can often be picked out where velocities exceed values of 3000 m/s; in the absence of compaction, this is not possible in sandstones or shales. One must, however, be wary of the presence of carbonates as they hold high velocities regardless of depth.

## *Uplift Estimation*

A shale-dominated trend was segregated from the p-wave velocity data using a gamma ray cut-off of 80 API. The p-wave velocity of the shale trend was used to estimate uplift, with the Mondol (2009) empirical 50:50 silt and kaolinite mixture compaction trend used as the reference line to which the interpreted transition zone was adjusted. This particular curve is chosen because it is assumed to best fit the overall shale lithology of the succession. The shale data is initially plotted at its current depth (figure 5.42: dark blue). The transition zone is then identified and is subsequently adjusted (figure 5.42: light blue) to best fit the compaction curve (figure 5.42: solid black line). The estimated uplift is estimated to be 1480 meters.

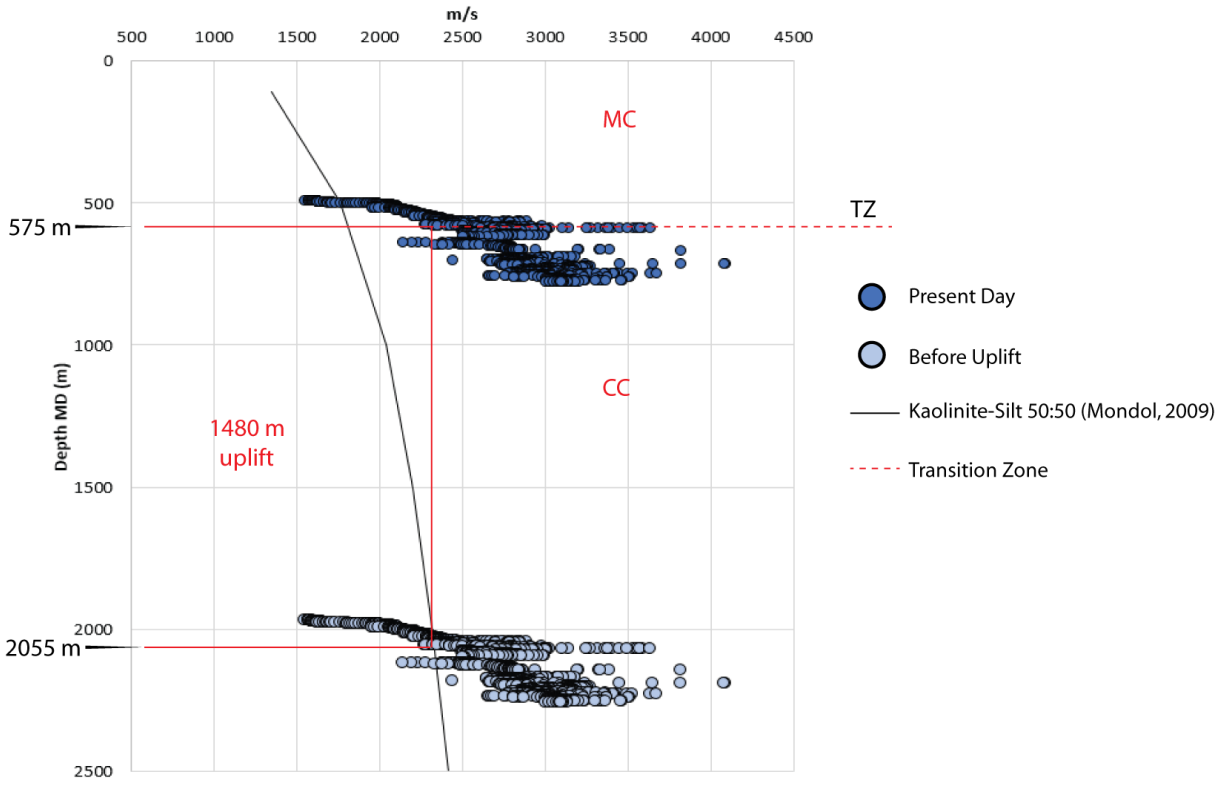


**Figure 5.42:** Uplift estimate based on empirically tested data (Mondol, 2009 50:50 Kaolinite:Silt curve). The interpreted transition zone is adjusted according to this curve- Additionally, the geothermal gradient can be used to determine where the transition zone had existed prior to uplift. The present day transition zone is then adjusted to this depth. Both methods give a similar result of approximately 1480 meters.

## *Geothermal Gradient Estimation*

The geothermal gradient was calculated using equation 4.10 with the bottom hole temperature of 17 °C, sea bottom temperature of 4°C, bottom hole depth of 805 m, water depth of 400 m, and Kelly bushing of 23 m. It has been computed to be 34.0 °C/km. This result fits with the Smelror (2009) estimated average geothermal gradient of the SW Barents Sea of approximately 31 to 38 °C.

$$Gg = \frac{17°C - 4°C}{805m - (400m + 23m)} * 1000m = 34.0°C/km$$

With the computed geothermal gradient, temperatures at the maximum burial depths of the cored intervals can be deduced. The present depths of the cored interval are 650 to 762 meters. Thus, at present the temperature interval calculated to be is 22.1 °C to 25.9 °C. Because an estimated 1480 meters of uplift have taken place, at maximum burial depth these sediments were present at the approximately the interval of 2130 to 2240 m. This corresponds to a computed temperature interval of 72.4 to 76.2 °C, with the use of the computed geothermal gradient. These are simply values attained through plugging the bottomhole temperature into the equation and utilizing the uplift determined in the previous section. This method comes with uncertainties, especially given that the well penetrates very shallow depths (deepest depth is only 805 meters). This also yields fewer data points to work with and a greater difficulty in determining the transition of mechanical to chemical compaction. As such, estimated temperature values are heretofore said to be 70-80°C.

# Chapter 6: Discussion

## 6.1 Introduction

The primary objective of this thesis is to characterize the reservoir properties of sandstones from the Fruholmen, Nordmela, and Stø formations from the Wisting Central III drill core from the southwestern Barents Shelf. Reservoir properties currently observed are a function of climate, provenance, depositional environment, and diagenesis. Results obtained from the sedimentological, petrographic, and petrophysical analyses are thus discussed with respect to these factors and are further evaluated in combination with published literature. An additional aim for this study is the evaluation of the reservoir quality of the sandstone units.

Lateral and temporal changes in mineralogy and texture are briefly compared and discussed, in particular in relation to Gemini North (7325/4-1)(section 6.3.1). A detailed characterization of reservoir sandstones in the Realgrunnen Subgroup of Gemini North (7325/4-1) can be found in Skretting (*in prep*).

## 6.2 Reservoir Quality Controls

Factors determining the initial sandstone composition are climatic changes, changes in palaeodrainage direction and thereby provenance, depositional environment, or changes in subsidence rates; a combination of these factors may be at play. The initial sandstone composition controls the diagenetic reactions that transpire at depth. The succeeding paragraph summarizes key observations found in Wisting Central III. These parameters are then sequentially discussed with respect to observations found in published literature.

The most pronounced vertical change shown in the results is across the Triassic-Jurassic boundary, between the Fruholmen and Nordmela Formations. This boundary represents some ~20-30 million missing years, whereby the Krabbe Member of the Fruholmen Formation and the Tubåen Formation are completely absent. This change is most clearly reflected in the framework grain constituents (figure 5.16), whereby the Fruholmen Formation classified as relatively immature, with all samples exhibiting a moderate quantity of feldspar (primarily plagioclase) and lithic rock fragments. The Jurassic Nordmela and Stø formations displays a markedly higher maturity, with samples plotting almost exclusively as quartz arenites on the QFL diagram. The constituents of the intergranular volume also show a significant change across this boundary, with the Fruholmen Formation consistently showing much higher amounts of matrix and authigenic clays and cements, whereas the overlying Jurassic succession exhibits much higher proportions of primary porosity in lieu of these constituents (figure 5.37). Additionally, a large increase in textural maturity of the sandstones is evident across the boundary (figure 5.35 and 5.36). XRD results follow suit, having a significantly higher mineralogical diversity detected in the Fruholmen

Formation than the Stø (figure 5.13). Particularly, Mg- and Fe- rich constituents (e.g. Chlorite and Siderite) are present in the Fruholmen Formation, which are nearly completely absent in the Jurassic Nordmela and Stø Formations.

Parameters that may give rise to these observations are discussed chronological order from climate to provenance and depositional environments to burial diagenesis.

### 6.2.1 Paleoclimate

Paleoclimate is of major importance in the development of different mineral assemblages because of its influence on weathering and impact on early diagenesis and mineral dissolution. A humid climate involves a higher annual precipitation, leading to higher fluvial discharge and increased river capacity. Additional effects of a more humid climate include an increase in the production of organic matter, a rise in the level of the water table, and subsequently a higher meteoric water flow rate. The primary consequence of a humid climate on the mineralogy is the pronounced leaching of feldspars and micas, which occurs due to meteoric flushing (section 3.3.1). This early diagenetic reaction yields pore-filling kaolinite.

Bergan and Knarud (1993) suggest a change in climate from semi-arid to humid conditions from the Mid to Late Triassic to Early Jurassic. As such, if it is assumed that the Fruholmen, Nordmela, and Stø Formations all held the same composition at deposition, a higher quantity of leached feldspars and precipitated kaolinite would be found stratigraphically up-section. Clearly, this is not the case for the results from Wisting Central III – a prominent decrease in feldspar and mica content is seen across the Triassic-Jurassic boundary. Bergan and Knarud (1993) explain that increases in mineralogical maturity are attributed to decreased subsidence rates, allowing intense reworking of sand, whereby unstable components are removed and the precipitated kaolinite is eliminated. Meanwhile, the humid climate would allow transport of sediment with greater caliber, as seen in the Stø and Nordmela formations. While a change from arid to more humid climates may be accurate for many European basins, more recent paleoclimate reconstructions by Hochuli and Vigran (2010) and Mueller et al (2016) indicate that humid conditions were already present in the Barents Sea area from the Late Carnian stage. As such, the primary change in climate appears to pre-date the turnaround in mineralogy. However, the onset of the Jurassic may have brought yet further, but not as marked, increases in humidity (Hochuli and Vigran, 2010). Sparse ooids in the Stø Formation (figure 5.28D) attest to a warm climate in the Early Jurassic (Van Houten and Purucker, 1984).

Although a change in climate is inferred, its relationship to the distinct change in mineralogy is gauged to be small in relation to changes in provenance and accommodation space – especially so when considering that the mineralogical composition varies laterally throughout the Fruholmen Formation (see section 6.2.2). Additionally, a shift from immature to mature provenance area (discussed in section 6.2.2) may obscure the climatic maturity effect across the boundary. However, increased humidity in the Jurassic in the Barents Sea likely played a role in enabling transport of sediments of a larger caliber, giving increased grain sizes. Furthermore, the leaching of feldspars combined with many cycles of reworking would lead to the eventual elimination of feldspar and therefore kaolinite, giving the highly mature sandstones observed.

### 6.2.2 Provenance

Primary provenance areas during Late Triassic to Early Jurassic times are shown on a modern-day map in figure 6.1, colour coded according to the orogeny they relate to. A schematic paleogeographic map based on Omma et al. (2011) is shown in the bottom right-hand corner. Key provenance areas include the easterly Uralian orogeny, the more westerly Caledonian orogeny, and sediments from the westerly Fennoscandia Shield, which originate from the Sveconorwegian orogeny and Svecofennian orogeny, as well as Paleoproterozoic and Archean complexes. Several studies have utilized detrital zircon ages to constrain provenance areas in the Late Triassic-Early Jurassic successions of the Barents Sea (e.g. Fleming et al, 2016, Klausen et al., 2017; Pozer Bue and Andresen, 2014). The ages of the detrital zircons indicate the source area, as according to the age of the orogenies as shown in the time-scale in figure 6.1. Mørk (1999) and Bergan and Knarud (1993) have additionally conducted petrographic provenance studies over areas in the Barents Sea. Aforementioned studies with other supporting literature will be used with results from this study to evaluate the provenance of the Triassic-Jurassic sandstones of the Fruholmen, Nordmela, and Stø Formations in Wisting Central III. Petrographic changes relating to provenance are discussed with respect to two surfaces: The Early Norian maximum flooding surface (MFS), which separates the Snadd and Fruholmen Formations, and the Triassic-Jurassic transition, which separates the Fruholmen and Nordmela Formation in Wisting Central III.

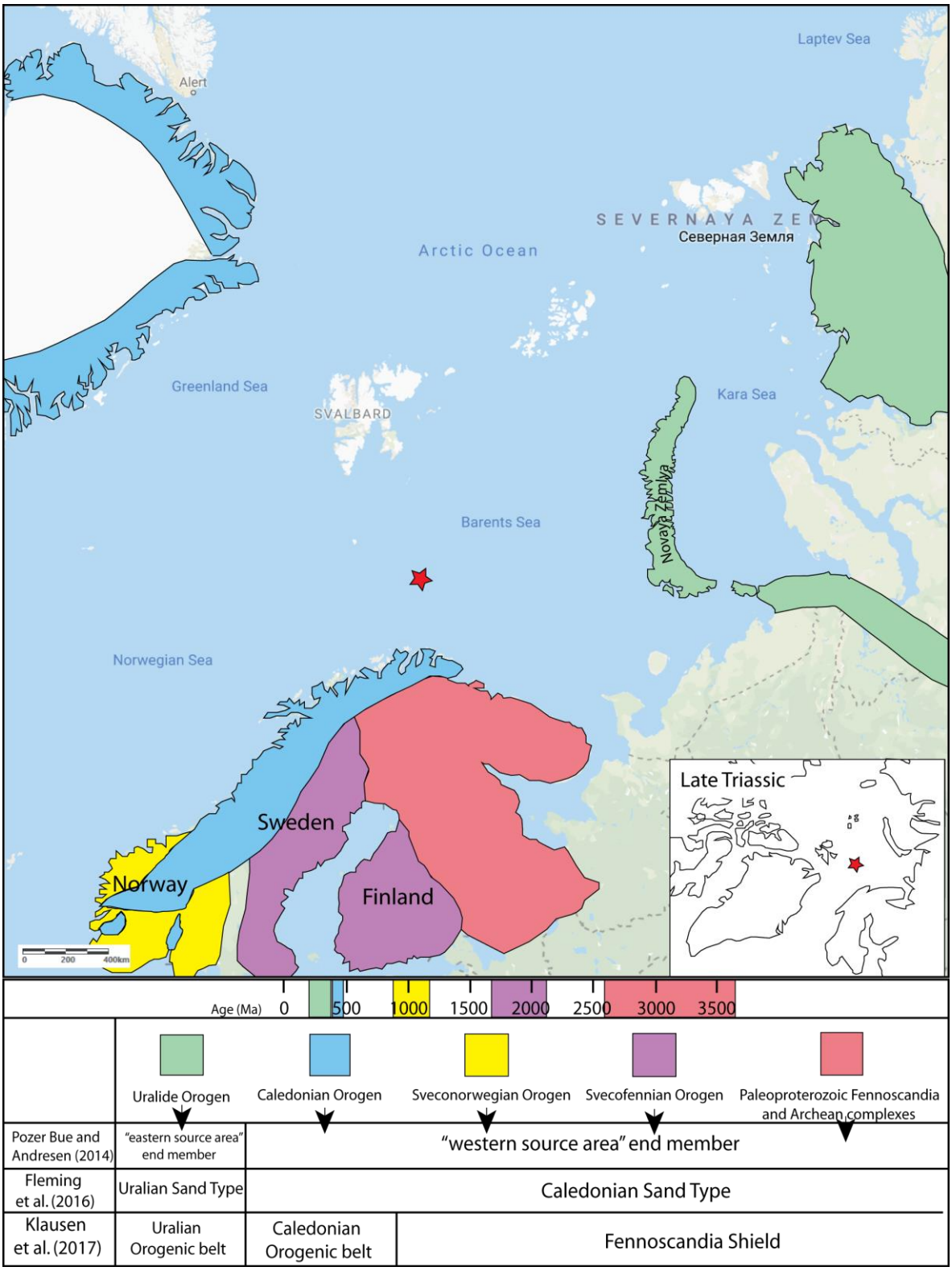


**Figure 6.1:** Main provenance areas during Late Triassic to Early Jurassic times on a modern map, with a schematic paleogeographic map in the bottom right corner modified from Omma et al., (2011). Map and time scale are colour coded with the respective orogenies. These are further related to provenance areas as defined by Pozer Bue and Andresen (2014), Fleming et al. (2016), and Klausen et al. (2017). Map modified from Google (n.d.)

### *6.2.2.1 Changes Across the Early Norian MFS*

Petrographic results for the Fruholmen Formation from this study are displayed on a QFL diagram in figure 6.2, in combination with the results from the Fruholmen Formation and the underlying Snadd Formation from previous master's theses from the University of Oslo and Norwegian University of Science and Technology (NTNU). The boundary between the Snadd and Fruholmen Formations is marked by the Early Norian MFS.

Results from this study, combined with the recent works of Klausen et al. (2017) and Fleming et al., (2016), dispute the previously widely accepted conclusion from Bergan and Knarud (1993) and Ryseth (2014, p. 208) that the petrographic change across the Early Norian MFS "is the most distinct and regionally important petrographic turn-around in the Arctic region." Bergan and Knarud (1993) utilized XRD and microscope petrography to record a dramatic change in mineral assemblage, from a more immature to a very mature composition, across the early Norian MFS. Other studies (e.g. Mørk et al., 1982; Pozer Bue and Andresen, 2014; Ryseth, 2014) relate their findings or record similar petrographic results at this surface or at the time equivalents on Svalbard. These petrographic changes have been related to hinterland rejuvenation, whereby the Caledonian/Fennoscandian source area became more important than the easterly Uralian source (e.g. Ryseth, 2014). These works are, however, biased towards sediments from basin margin areas (e.g. Hammerfest Basin, Nysleppen Fault Complex). Instead, results from this study favor a more gradual petrographic change at the turn of the Norian in the basin interior, particularly in the Hoop area, contrasting to the stark changes seen at the southern margin.

As shown in figure 6.2, in the Hammerfest basin and adjacent areas in the south, the dramatic petrographic change referred to by Bergan and Knarud (1993) and Ryseth (2014) is observed. However in the basin interior, which includes the results from Wisting Central III, this petrographic change is relatively subtle or overlapping. Provenance studies conducted by Fleming et al. (2016) show that there are large geographic variations in the detrital zircon signature from the Fruholmen Formation (figure 6.3). In the south, a Caledonian/Fennoscandian signature dominates, whereas in the basin interior, very young detrital zircon ages are found, corresponding to a Uralian provenance area, possibly Novaya Zemlya (Klausen et al., 2017)(figure 6.1). This agrees with the more immature petrographic character of the Fruholmen Formation recorded in this study, because Uralian sourced sands have been found to classify as being more compositionally immature than Caledonian/Fennoscandian sourced sands (Fleming et al., 2016). As previously stated, change in mineralogy at the turn of Fruholmen times has been related to hinterland rejuvenation, bringing in more compositionally mature sediment from the Fennoscandian Shield (e.g. Ryseth, 2014). However, results from this study imply that this change is not as immediately or strongly reflected in areas in the basin interior, likely due to larger distances from

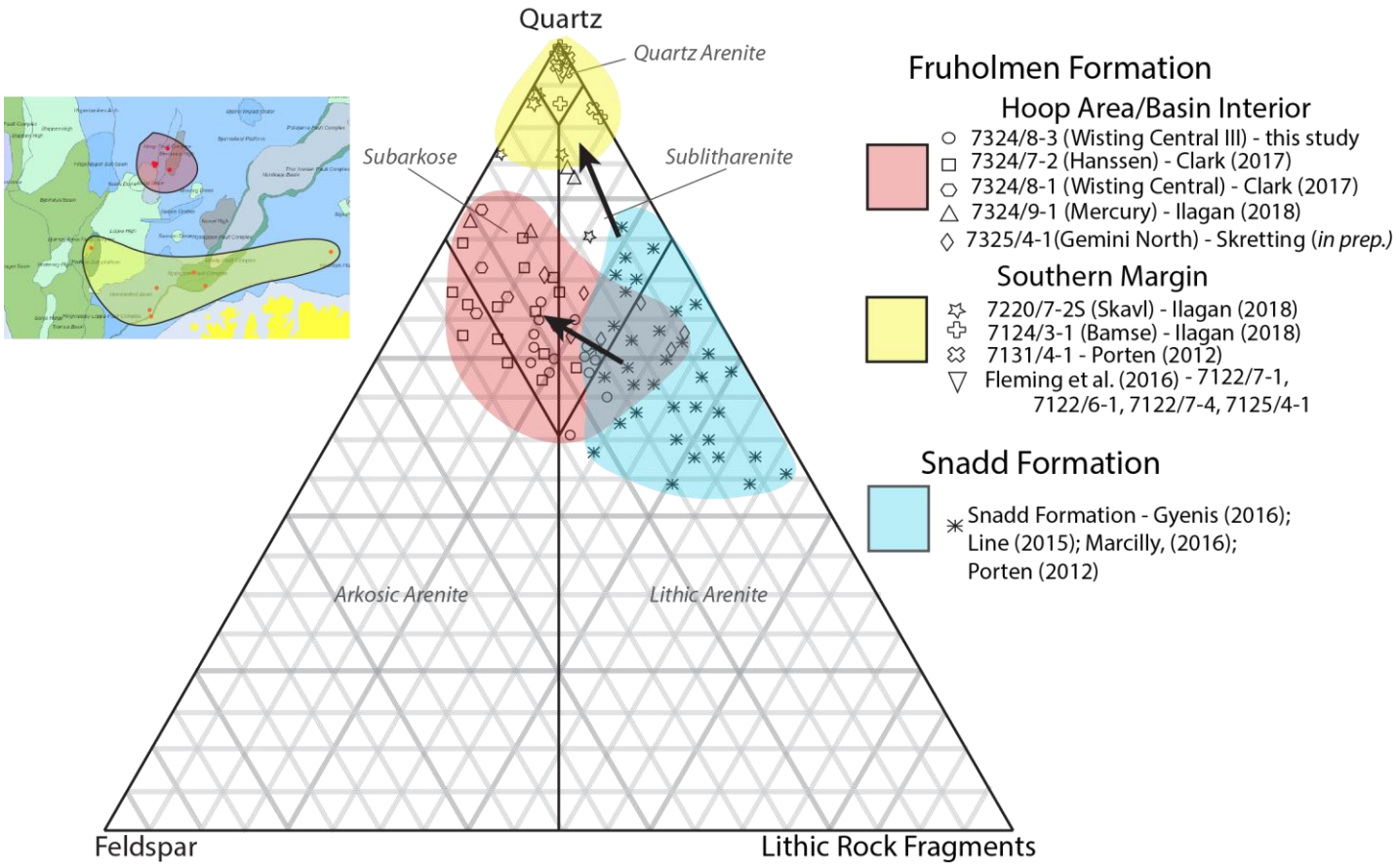


**Figure 6.2:** Petrographic results from this study for the Fruholmen Formation, together with results for the Fruholmen Formation and Snadd Formation from previous studies. Altogether, the results demonstrate that a drastic petrographic change occurs at the early Norian MFS in southern margin areas, proximal to the Fennoscandian Shield. Wells in this southern margin area are included in the yellow cloud on the map and the diagram. A more subtle change in petrographic character is seen in the Hoop area of the basin interior. Wells included in the basin interior are represented by the red cloud on the map and ternary diagram. Geographic distinctions are not made for the Snadd Formation because it is observed to be more petrographically similar across the basin. Map is from NPD (2019). Dott (1964) sandstone classification is used.

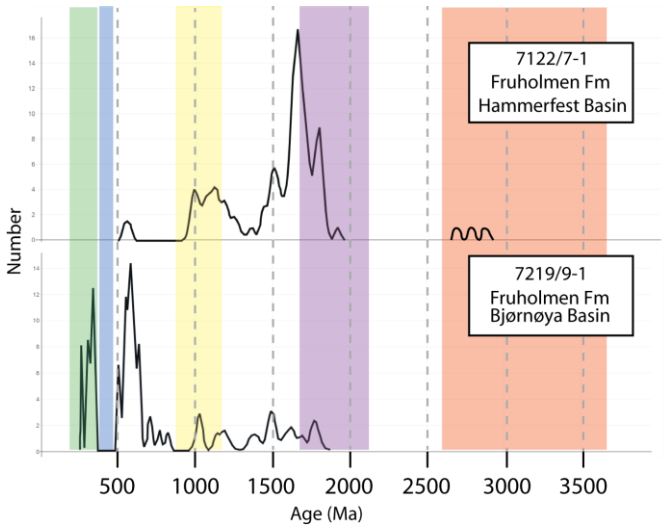


**Figure 6.3:** Zircon data from the Fruholmen Formation in the Hammerfest Basin (southern margin) and the Bjørnøya Basin (basin interior), modified from Fleming et al. (2016). In the Hammerfest basin, the Fruholmen Formation is of Caledonian /Fennoscandian provenance. In the Bjørnøya Basin, a dominantly easterly provenance signature is found, indicating continued influence of the Uralian Orogeny in the basin interior. Another possibility is the reworking of underlying Uralian sourced sediments, or mixing of the two provenance areas.

Colour scheme in figure 6.1 holds.

the southern Caledoanian/Fennoscandian provenance area. This indicates that the Fruholmen Formation may represent the initial stages of a new basin configuration that became pronounced at the turn of the Jurassic, whereby there are vast geographical variations in petrographic character.

Provenance indicators found in the Fruholmen Formation in Wisting Central III include the lithic fragments (section 5.2.2), which predominantly comprise chloritized volcanic fragments (figure 5.20) and mud rock fragments (figure 5.23). Many of the mud rock fragments have been determined to have originally composed of smectite (see section 6.2.3.3). The dominance of plagioclase feldspars relative to k-feldspars can also provide an indication of provenance (figure 5.15). Plagioclase is typically the least stable of the feldspars (Busenberg and Clemency, 1976), thus the strong presence of plagioclase combined with significantly less K-feldspar must have an explanation other than diagenetic reasons (section 5.2.1).

Overall, the provenance indicators from the Fruholemen Formation strongly suggest an easterly source area, likely located in the orogenic belt of Novaya Zemlya/Urals. This concurs with findings from Klausen et al. (2017). Basalt extrusions, which produce plagioclase-rich sediments upon erosion, are recorded to have taken place in these areas during the early Triassic (Heafford, 1988), potentially giving the high plagioclase content observed. Uplift from the Novaya Zemlya protrusion has furthermore exposed basalts and greenschists that have been found in the area (Ronkina et al., 1985), which contain unstable mafic minerals that are rich in iron and magnesium. This can explain the presence of diagenetic chlorite found throughout the Fruholmen Formation, which is particularly prevalent in the Akkar Member (figure 5.37 and figure 5.38). The presence of mud rock fragments initially composed of smectite also attests to an easterly provenance area. Although smectite is typically characteristic for areas of low precipitation or poor drainage, it also forms from volcanic rocks such as basalt in more humid conditions (Bjørlykke, 2015). The precursor to the grain coating chlorite found in FA2 may also have been smectite. Mørk (1999) has additionally related lithic fragments and more mafic-rich components in Barents Sea sediments to a Uralian source area. These results are in contrast to earlier studies (e.g. Bergan and Knarud, 1993; Ryseth, 2014) suggesting that the Caledonian/Fennoscandian provenance area was ubiquitously dominant at the start of Fruholmen times.

Had the provenance area for the Fruholmen Formation in Wisting Central III been predominantly Caledonian/Fennoscandian, the erosion of metamorphic basement rocks, plutonic rocks, as well as the reworked Proterozoic quartzites resting on the Fennoscandian Precambrian basement would lead to sandstones of much high maturity and larger proportions of K-feldspar (Olaussen et al., 1984; Mørk, 1999; Harrison et al., 2011). However, slightly higher compositional maturities than the underlying Snadd Formation are extant in the Fruholmen Formation in Wisting Central III, perhaps suggesting that mixing or reworking has occurred.

Detrital zircon studies by Klausen et al. (2017) included the Fruholmen Formation from Wisting Central (7324/8-1) (Figure 6.4). Because this well is approximately 2 km away from Wisting Central III, the results are assumed to be comparable. Exceptionally young zircon ages almost equivalent to the Norian age of deposition are recorded by Klausen et al (2017), indicating a magmatically active provenance area while, or shortly before, these formations were deposited. Klausen et al. (2017) postulates these to originate from the protrusion of the Novaya Zemlya fold and thrust belt in the east. Novaya Zemlya is considered a structural continuation of the Urals, but with the main orogeny occurring later than in the Urals, in the early Kimmerian (Triassic–Middle Jurassic) (Polkin 1974). Because this compressional event may have uplifted previously deposited sediments in that area, a possible source for sediment could have been the Lower Triassic sediments from Novaya Zemlya, which have been petrographically studied by Mørk (1999). Mørk (1999) observed that Lower Triassic sandstones from Novaya Zemlya also had very high plagioclase/k-feldspar ratios as well as chloritized volcanic rock fragments, similar to the results from this study. Transport and reworking processes to the final site of deposition at the Hoop area may have rendered these sandstones more mature, yielding the Fruholmen Formation sandstones observed in Wisting Central III as illustrated in figure 6.5.

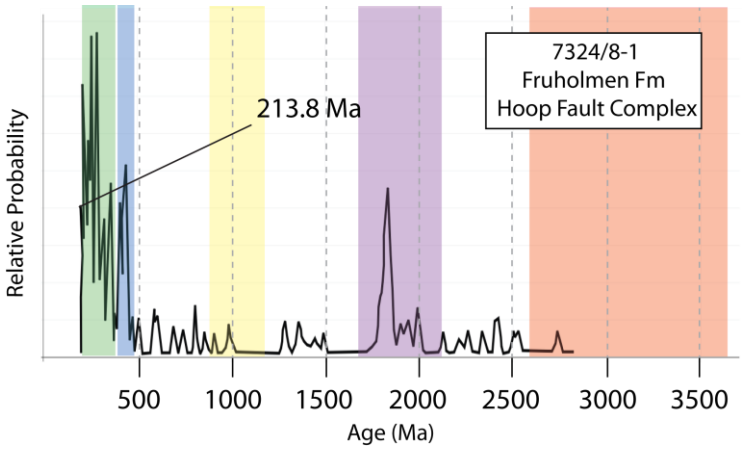


**Figure 6.4:** Zircon data for the Fruholmen Formation from Wisting Central (7324/8-1), showing a dominant Uralian signature with minor Fennoscandian and Caledonian input. Modified after Klausen et al. (2017). Exceptionally young zircon ages are observed, with the youngest being 213.8 Ma.

Colour scheme in figure 6.1 holds.

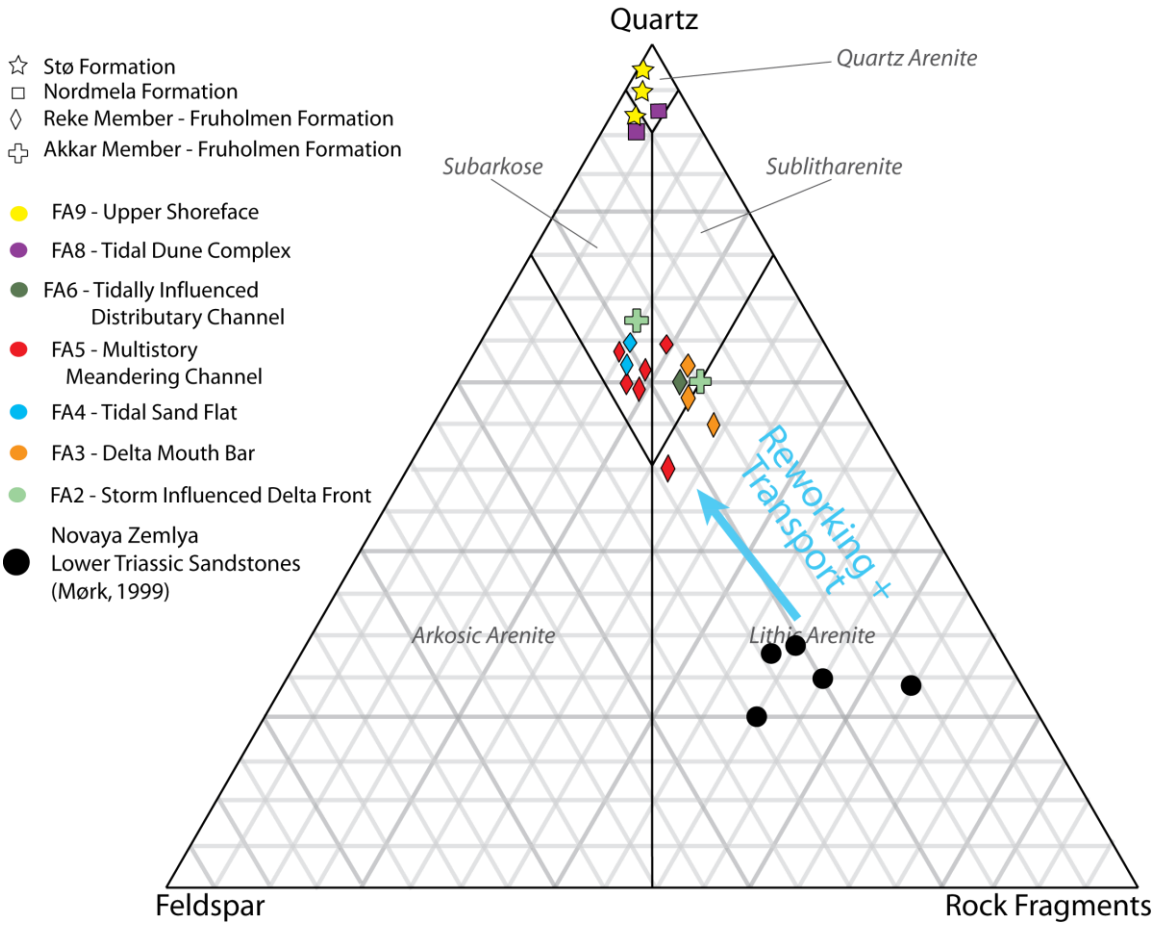


**Figure 6.5:** Fruholmen sandstones in this study may have originated from the protrusion of Novaya Zemlya, which would have uplifted previously deposited sediments – potentially lower Triassic sandstones. Such sandstones were petrographically studied by Mørk (1999). The rock fragment assemblage described for Novaya Zemlya sandstones is similar to that found in the Fruholmen Formation in Wisting Central III. The transport from Novaya Zemlya to their site of deposition in the Hoop Fault Complex area may have led to the increase in maturity as represented in the figure. Novaya Zemlya data points were extracted from Mørk (1999). Dott (1964) sandstone classification is used.

It is possible that the Caledoanian/Fennoscandian provenance area became more important stratigraphically up-section throughout the Fruholmen Formation. This may be evidenced by the steadily increasing proportions of K-feldspar (figure 5.15). Clark (2017) also recorded increasing proportions of k-feldspar throughout the Fruholmen Formation in the Hanssen (7324/7-2) and Wisting Central (7324/8-1) wells. Additionally, the Akkar Member is found to contain much more chlorite (figure 5.37 and appendix E), possibly suggesting a greater influence from the east than the overlying Reke Member. Textural maturity and grain size are also shown to increase up section throughout the Fruholmen Formation (section 5.2.3). However this may be a function of depositional environment and/or less available accommodation, allowing re-working (Ryseth, 2014). However, the relative immaturity of the Fruholmen Formation sandstones and seemingly high preservation of early diagenetic kaolinite indicate that first-generation sediments are observed. Had significant reworking taken place, much of the authigenic kaolinite would likely be eliminated – but this is not the case. Results from Klausen et al. (2017) are in agreement with a greater influence of the Caledonian/Fennoscandian provenance area up-

section, with these zircon signatures becoming more prominent upward in stratigraphy in the Fruholmen Formation.

Altogether, the Fruholmen Formation shows complex geographic variation with respect to provenance area and subsequently petrographic character. Results from this study in combination with current literature indicate that the Fruholmen Formation in Wisting Central III area had primarily an eastern Uralide provenance area, likely with some influence from the Novaya Zemlya protrusion. This demonstrates that eastern provenance areas continued to supply sediments at least until the Norian in the Hoop area. This is contrary to previous assumptions that a ubiquitous change to a primarily Caledonian/Fennoscandian provenance occurred over the entirety of the western Barents Sea across the Early Norian MFS (Bergan and Knarud, 1993; Ryseth, 2014).

#### *6.2.2.2 Changes Across the Triassic-Jurassic Boundary*

Basin reorganization that had commenced during Fruholmen times culminated by the turn of the Jurassic. This corresponds with an abrupt increase in petrographic maturity in Wisting Central III. Relatively few provenance indicators from the petrographic results of this study are present in the Jurassic Nordmela and Stø formations. Furthermore, distinguishing between source areas on the basis of mineralogy in the condensed Nordmela and Stø Formations is uncertain due to the polycyclic nature of the deposits and pervasive weathering of provenance regions (Dypvik, 1979; Ryseth, 2014). This is compounded by low rates of erosion and sedimentation (Klausen et al., 2018). However, their high textural and compositional maturity (figure 5.35 and 5.36) as well as the presence of rounded tourmaline grains (figure 5.27) indicates extensive reworking. This is in agreement with the low accommodation present during the Pleinsbachian to Bajocian, likely driven by forebulge uplift occurring in the Hoop area related to the Novaya Zemlya fold and thrust belt (Müller et al., 2019).

Detrital zircon analyses were conducted on samples from the Nordmela (Klausen et al., 2017) and Stø formations (Klausen et al., 2018) in Wisting Central (7324/8-1) (figure 6.6). Due to the proximity of this well to Wisting Central III, results are assumed to be comparable. Results show that young detrital zircons characteristic of eastern sources continued across the Triassic-Jurassic boundary into the overlying Nordmela Formation in well 7324/8-1 (Wisting Central). However the signature on this sample is mixed, with Caledonian ages also well represented. A similar signature is found in the Stø Formation, however the Caledonian/Fennoscandian signature is overall higher. This mixing of signatures probably indicates recycling of the underlying Triassic strata (the Fruholmen Formation, likely the Krabbe Member, as this is not preserved) that contained Uralian provenance signatures. Meanwhile, the primary provenance area during Nordmela and Stø times was likely Caledonian/Fennoscandian. This interpretation is supported by evidence for a high level of reworking in the Stø and Nordmela formations, including the high textural maturity (high sphericity and roundness) as opposed to the underlying sediments. The rounded tourmaline grains, documented to almost

exclusively occur in highly reworked sediment, also support this interpretation (Feo-Codecido, 1956). Other evidence for reworking includes corroded quartz overgrowths. A candidate for this is identified in figure 5.30, while more convincing evidence can be found in a Stø Formation sample from Gemini North (7435/4-1), featured in Skretting (*in prep*). The thin Nordmela Formation in Wisting Central III, coupled with the absence of the Tubåen Formation and the relatively thin Fruholmen Formation show the potential for reworking in the area.

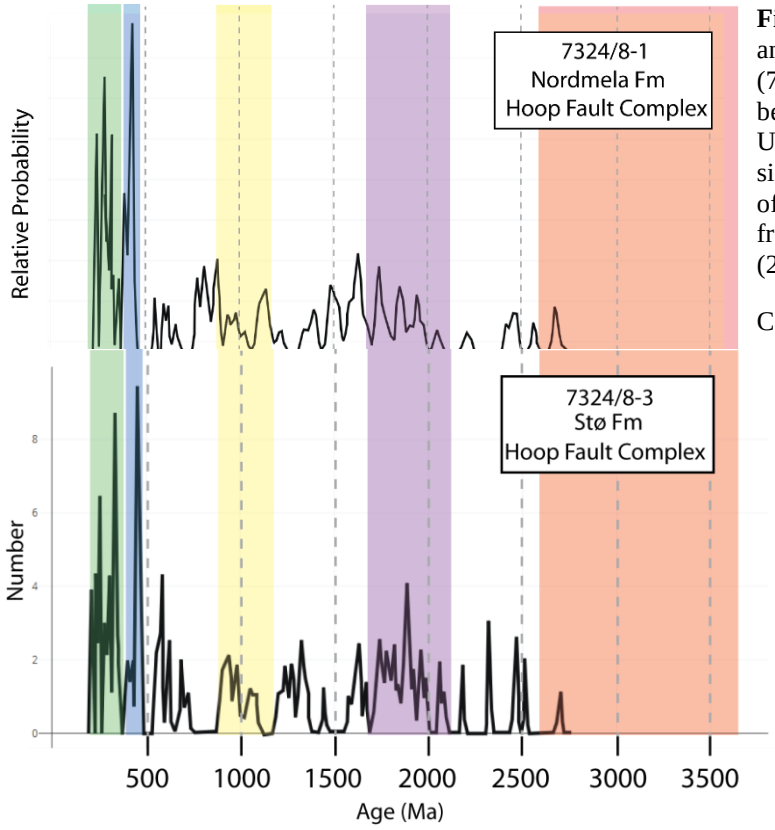


**Figure 6.6:** Zircon data for the Nordmela and Stø Formations from Wisting Central (7324/8-1), showing a relatively even mix between Caledonian, Fennoscandian, and Uralian source signatures. The Uralian signature is taken to result from reworking of underlying Triassic deposits. Modified from Klausen et al. (2017) and Klausen et al. (2018).

Colour scheme in figure 6.1 holds.

## 6.2.2 Depositional Model and Stratigraphic Development

The facies associations described and interpreted in section 5.1 in Wisting Central III record a range of shallow marine to coastal depositional environments. Based on observations, seismic data, and literature, the studied succession has been interpreted in a sequence-stratigraphic context (See figure 5.1). These interpretations record relatively low order base-level fluctuations in an overall regressive and low-accommodation regime, possibly initiated by forebulge uplift from the protrusion of Novaya Zemlya in the east (Müller et al., 2019).

The core interval is interpreted to record the development of an overall regressive deltaic-shoreline system. Data from wireline logs as shown in figure 5.40 (GR, NPHI, RHOB) is in agreement with a general coarsening/shallowing-upward development. Results corresponds with type sections as well as other wells cored in the subsurface of the Barents Sea, which record that the Late Triassic (Norian) Fruholmen Formation represents the transition from open marine sediments of the Akkar Member to coastal deposits of the Reke Member, and the Nordmela and Stø Formation record a variety of clastic coast lithofacies (Clark, 2017, Dalland et al., 1988; NPD, 2019)

### *6.2.2.1 Triassic Lithostratigraphy*

FA1-4 are interpreted to record the overall coarsening-upward progradational development of a deltaic system, characteristic for a highstand system tract (HST). Figure 6.7A displays the depositional model, with observed facies associations represented as well as those that likely existed contemporaneously. In accordance with literature, this shoreline was likely oriented in a NE-SW direction (e.g. Anell et al., 2014a). The cored interval passes down into uncored mudrocks similar in wireline log character to FA1. This may record either continued FA1 or offshore mud deposition, likely into the Maud Basin at the start of the Norian. The HST holds intervals dominated by fluvial (FA3), tidal (FA4), and wave influences (FA1 and 2), implying a division into areas dominated by these different processes. The delta itself is interpreted to be fluvial dominated due to the nature of the mouth bar (FA3) – the presence of mudrock fragments indicates little to no wave-reworking, and no tidal signatures are found. Lack of bioturbation may indicate fast deposition. The influence of the storms evidenced in FA1 and FA2 were likely infrequent enough as to have a minor effect on deposits above fair-weather wave base. Tidal flats traversed by minor tidal channels (FA4) developed in tide-dominated areas away from significant river output. Longshore drift likely supplied sand from this delta system further along the coast to the tidal flat areas.

The incised erosional surface between FA4 (tidal flat) and FA5 (multistory meandering channel) is proposed as a candidate sequence boundary (CSB), and is the boundary between the Lower and Upper Reke Members. A schematic for the development of this sequence boundary is shown in figure 6.7B. Some of the intraformational mud clasts are heterolithic in nature, pervaded by lenticular and flaser

bedding, attesting to derivation from the incision into the underlying tidal flat deposits of FA4 as base level decreased.

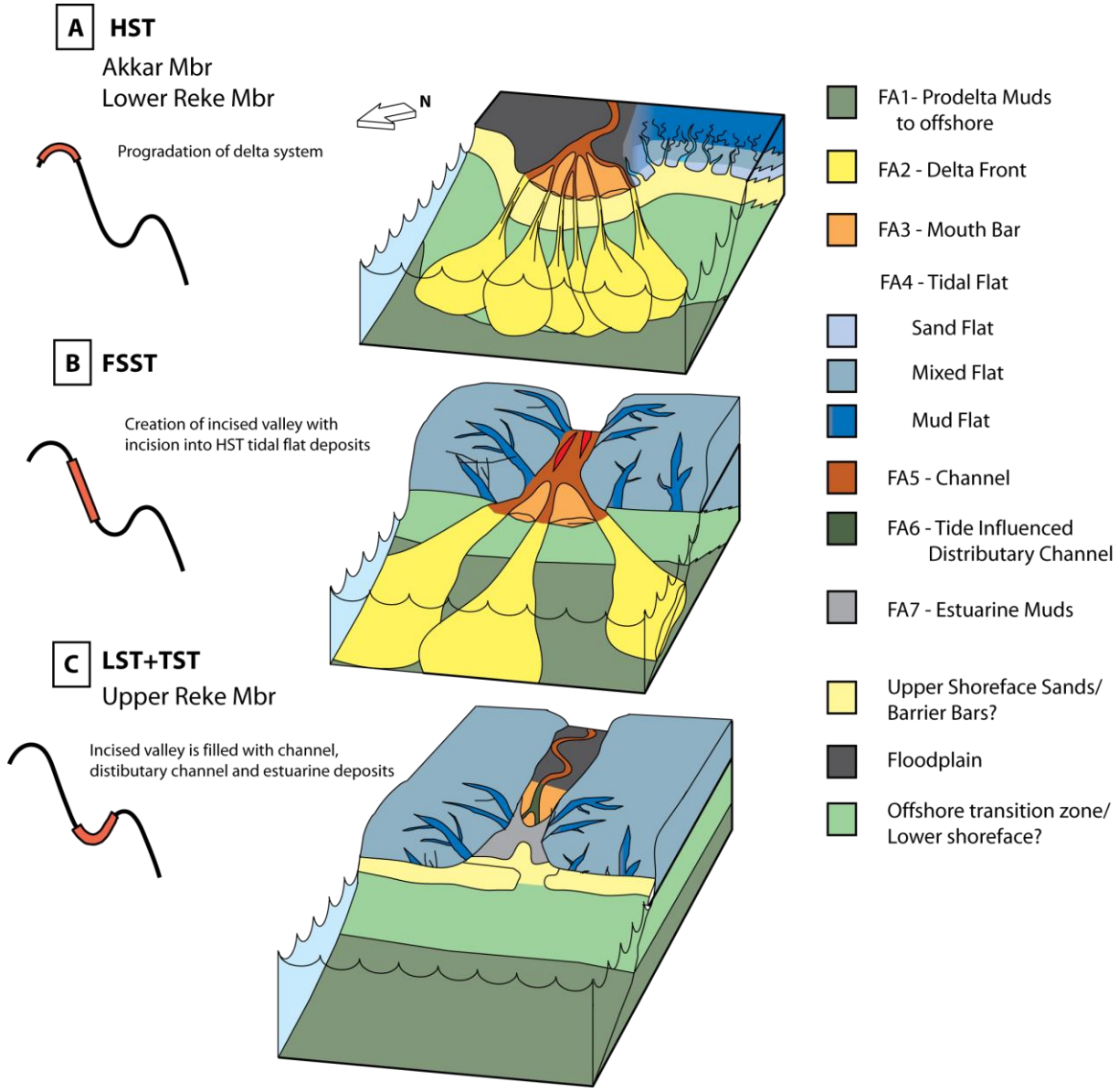


**Figure 6.7:** Development of the Fruholmen Formation as function of changes in base level. ***(A)*** Facies model for the highstand system tract, comprising the Akkar Member and Lower Reke Member (FA1-4). ***(B)*** 'Falling stage' system tract, associated with incised valley development, with incision into FA4 highstand deposits. No sediments from the FSST are interpreted in the core, due to erosion and bypass as base level fell. ***(C)*** When accommodation allows it, the FA5 meandering fluvial sediments are deposited in the incised valley created, representing the lowstand system tract. As the valley is transgressed, FA6 (tide influenced distributary channel) and FA7 (estuarine muds) are sequentially deposited. The transgressive surface may be located within FA5 or at the boundary between FA5 and FA6.

The amalgamated fluvial deposits of FA5 are interpreted to indicate progradation in low accommodation settings, indicating a lowstand system tract (LST). The tidally influenced distributary channel and estuarine deposits of FA6 and FA7 above represent the initiation of a transgressive system tract; seismic data shows them to infill a channel feature, interpreted to be an incised valley (E. Stueland, Personal Communication, May 13th, 2019). Figure 6.7C shows a schematic of the infilling of the incised valley

with FA5, FA6, and FA7. Environments thought to exist contemporaneously are also represented. The infilling of the valley is also demonstrated in figure 5.10.

Most sequence stratigraphic studies conducted in the SW Barents Sea have a strong focus on the Triassic successions (Anell et al., 2014a; Glørstad-Clark et al., 2010; Klausen et al., 2015). However they are primarily confined to the Induan (Havert Formation) to Carnian (Snadd Formation) successions, and exclude the Norian-Rhaetian Fruholmen Formation. The reasoning for this is twofold: (1) Forebulge uplift during the Late Triassic-Early Jurassic resulted in significant erosion of the Fruholmen Formation, and (2) Clinoformal geometries have not been/are difficult to identify in the Fruholmen Formation. Absence of clinoformal geolmetries is due to the aforementioned erosion and potentially less accommodation present during the Norian-Rhaetian. Accommodation during deposition of the Fruholmen Formation is debated. The maximum thickness of the Fruholmen Formation is about 600 m, which is deposited over 26 million years (Norian-Rhaetian), while the Snadd Formation reaches thicknesses over 2000 m in 15 million years (Ladinian-Carnian) (Halland et al., 2014; Klausen et al., 2017), suggesting lower accommodation in the Norian-Rhaetian. The stacked channel deposits of FA5, with an absence of floodplain deposits, also indicate low accommodation.

No published studies discuss sequences in the Fruholmen Formation in detail. However, the sequence recorded in the Fruholmen Formation in this study may possibly be part of the 3rd order sequence referred to as 'N2' in Klausen et al. (2015) (figure 6.8), which was not a target of their study.

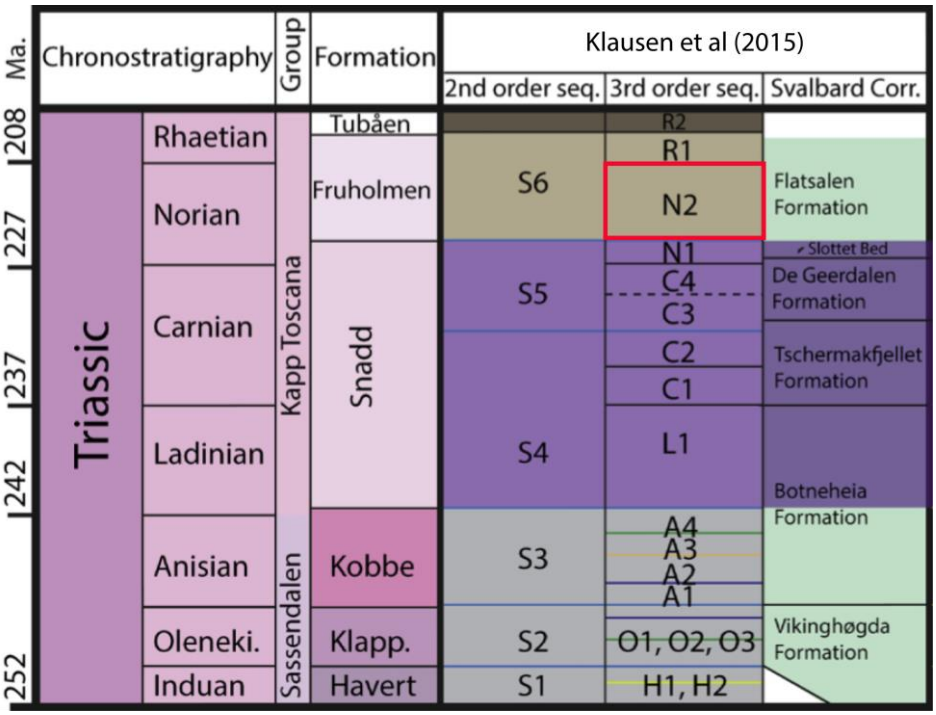


**Figure 6.8:** Sequence subdivisions of Triassic stratigraphy in the Barents Sea from Klausen et al. (2015). The sequence interpreted in this study may relate to the third order 'N2' sequence proposed by Klausen et al. (2015).

### 6.2.2.2 Triassic-Jurassic Boundary

A significant depositional hiatus is seen across the Triassic-Jurassic boundary in Wisting Central III (from the Fruholmen to Nordmela Formation). This hiatus is marked by a distinct angular unconformity between Upper Triassic strata and Lower Jurassic strata within the basin, and large parts are shown by Müller et al. (2019) to have formed topographic highs. Müller et al. (2019) has linked these unconformities to compression-induced uplift induced by the Novaya Zemlya Fold and Thrust Belt. This caused an important change in basin configuration, inducing uplift in the foreland bulge area (including the Hoop area) and creating foreland basins in the east (Ritzmann and Faleide, 2009). In the Hoop area, this uplift is exacerbated by Lower Permian salt movement during the Late Triassic to Early Jurassic, explaining the abrupt decreases in thicknesses of these strata as well as absence of the Tubåen Formation altogether in Wisting Central III (Müller et al., 2019).

### 6.2.2.3 Jurassic Lithostratigraphy

The Nordmela Formation (FA8) occurs as a small interval documenting the migration of a tidal dune complex. A period of non-deposition is inferred prior to the deposition of the Stø Formation (see section 5.1.3). The condensed nature and hiatus is likely related to the aforementioned uplift and salt tectonism occurring at the time.

Persistent low-accommodation settings since the early Jurassic resulted in a highly condensed succession, whereby the Stø Formation was deposited, reworked, and eroded over approximately 14 million years (Klausen et al., 2018), preserving only 18.5 meters in Wisting Central III. An upper shoreface interpretation is given to the Stø Formation in Wisting Central III due to the textural and compositional maturity and trough cross stratification (section 5.2.3). Sparse grains of fluorapatite found through SEM (figure 5.28A) support low sedimentation rates as well as reworking. Fluorapatite is an early diagenetic cement formed typically in low-sedimentation regimes (Bjørlykke, 2015). Subsequent to precipitation, the cement was likely reworked such that fluorapatite grains were formed. Sparse occurrence of ooids, indicating shallow, highly agitated marine water, are in agreement with a shoreface environment (Van Houten and Purucker, 1984). Additionally, such ooids are in many cases associated with hiatuses – in agreement with the low sedimentation rates characterizing the Stø Formation (Kordi et al., 2011).

Klausen et al. (2018) splits the Stø Formation into three depositional sequences. Based on their descriptions, two are found in Wisting Central III: SIIa, forming the entire sandstone interval of the Stø Formation (FA9 – upper shoreface deposits), and SIII, occurring as a highly condensed transgressive lag conglomerate on top of the sandy Stø Formation (likely Brentskardhaugen bed equivalent). The upper shoreface deposits are seen to be highly amalgamated, in line with the description of SIIa by Klausen et al. (2018). The condensed nature indicates that palaeowaterdepth was restricted, and Klausen

et al. (2018) gives an estimate of 40 m. The depositional model put forward by Klausen et al. (2018) for SIIa is shown in figure 6.9.

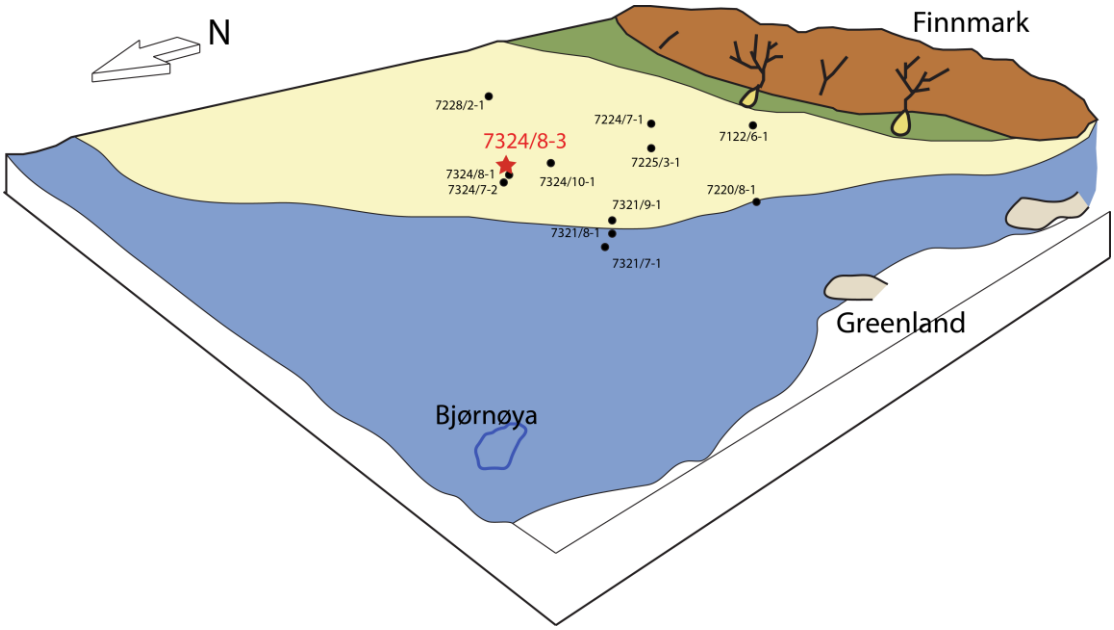


**Figure 6.9:** Depositional model for the Stø Formation, as a linear clastic coast in an overall transgressive and low-accommodation regime. Figure modified from Klausen et al. (2018).

## 6.2.3 Diagenesis

Diagenetic processes alter original reservoir properties such as porosity and permeability. Processes include early chemical reactions, mechanical compaction, and chemical compaction. The effects of these diagenetic processes are observed in the sandstones analysed petrographically from Wisting Central III, and can give an indication of the temperature the sediments have been exposed to. A summary of the primary diagenetic reactions observed can be found in appendix F.

### *6.2.3.1 Early Diagenesis*

Early diagenesis occurs in a chemically open system, where sediments may react with the atmosphere and water (see section 3.3.1). Therefore, these reactions are limited to sediments within 10m from the surface (Bjørlykke and Jahren, 2015). Kaolinite precipitation and carbonate cementation are the primary early diagenetic processes observed. Redox-driven processes on the sea floor may also lead to a suite of reactions, including the generation of pyrite, which is seen in some samples (figure 5.24 and 5.31).

*Kaolinitization*

Kaolinite precipitation is the most frequently observed early diagenetic process, seen pervasively throughout the Fruholmen Formation samples (figure 5.21 and 6.10). Kaolinite only occurs in trace amounts in the Nordmela and Stø formations (figure 6.10). Authigenic kaolinite originates from the leaching of feldspars and muscovite, and precipitates in the primary pore space (equations 3.1 and 3.2). The reaction reduces the reservoir quality, diminishing both primary porosity and permeability. For these reactions to take place, feldspar and muscovite must be in the initial mineral assemblage and be exposed to a sufficient flux of meteoric water. Continuous meteoric water flushing supplies hydrogen ions and removes cations produced from the reaction, such as Na+, K+ and silica out of the system, thereby allowing further kaolinite precipitation (Bjørlykke, 1998). These conditions are typically met in humid fluvial and shallow marine environments, aligning with the depositional models put forward in this study. The relatively high quantities of kaolinite in the Fruholmen Formation indicate meteoric leaching has occurred prior to deeper burial, in agreement with the high percentage of feldspars classified as altered during point counting (appendix E). Only trace amounts of kaolinite are observed across the Triassic-Jurassic boundary in the Stø and Nordmela formations. However, the Jurassic formations may have experienced extensive leaching as well, due to the low feldspar content present. The intense reworking the Stø and Nordmela formations have undergone would likely have washed out any precipitated kaolinite. The very limited accommodation and low burial rates in the Early-Middle Jurassic infer that the total flow of water through the sediments is higher as the sediments remain longer at a shallow depth. This may lead to almost complete leaching of the feldspars, while the high degree of reworking would remove any/most of the precipitated kaolinite (figure 6.10). The result would be the currently observed texturally and compositionally mature sandstones. Because accommodation was

higher in the Norian, this extensive reworking did not occur during the deposition of the Fruholmen Formation and first generation sediments were likely preserved.

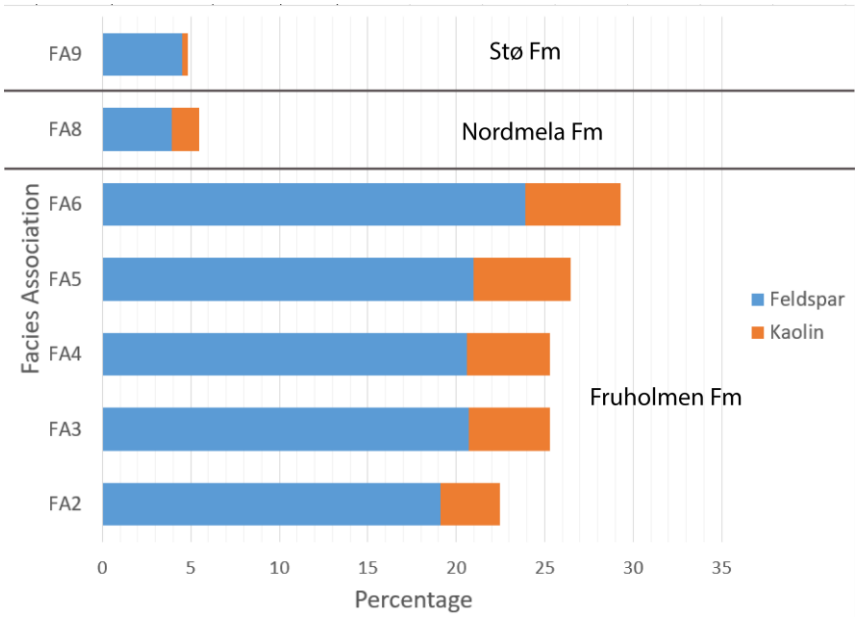


**Figure 6.10:** XRD results for feldspars and kaolin, averaged with respect to facies association. The extent of feldspar alteration and kaolinite precipitation are signs of early diagenetic meteoric water flushing. The Fruholmen Formation (FA2-6) show higher values than the Nordmela (FA8) and especially the Stø (FA9) Formations.

Increased kaolinitization has also been shown to be related to falling base level and thus sequence boundaries. The uplift occurring at the Triassic-Jurassic transition due to the protrusion of Novaya Zemlya resulted in a massive reduction of base level, producing the large hiatus observed (Müller et al., 2019). A fall in base level results in an increase in hydrodynamic head and creates a basinward shift in the meteoric water zone, promoting the leaching of feldspars and precipitation of kaolinite (Kordi et al., 2011). The two interpreted sequence boundaries can contribute in explaining the kaolinite present in the Fruholmen Formation. On the other hand, during relative sea-level rise, there is an invasion of marine water into the sandstones as a consequence of landward migration of the shoreline, as well as low sedimentation rates (Kordi et al., 2011). This is possibly evidenced by the the sparse fluorapatite and ooids in the Stø and Nordmela Formations (Van Houten and Purucker, 1984; Kordi et al., 2011).

### *Carbonate Cementation*

Calcite cement is observed in one sample in FA5 (V12), and as thin intervals and nodules in FA8 (Nordmela Formation) and FA9 (Stø Formation). Siderite cement is observed in FA2 (V2 and V3).

The calcite-cemented intervals/nodules occur randomly throughout facies. As such, no direct trends are inferred. However, the pervasive calcite cementation observed at the top 10 cm of the Nordmela Formation may have been formed from a hiatus prior to the deposition of the Stø Formation. Intervals of carbonate cementation are derived from the dissolution and reprecipitation of biogenic carbonate or early aragonite cement (Bjørlykke and Jahren, 2015).

Textural differences are observed within the calcite cemented thin section (V12), particularly with the grain contacts – far more grains exhibit floating or tangential contacts than all the other samples, which

are not calcite cemented. Calcite cemented V12 also holds the highest IGV observed, at 38%. These observations demonstrate that calcite cementation is the result of early diagenetic reactions and fills pore space prior to mechanical compaction, preventing the crushing and reorganization of grains. Carbonate cementation almost completely dispenses primary porosity and permeability, such that reservoir quality is negligible.

Siderite cement is found in the thin sections of FA2 – the storm influenced delta front deposits. Additionally, siderite nodules, reworked sporadically into thin lags, are found in FA2 (see section 5.1.1). The reworking indicates that they originate from early diagenetic precipitation while the sandstone was poorly lithified. This is suggestive of sulphate-poor conditions, typical of low-salinity waters (Curtis and Coleman, 1986). This coincides with a delta front setting, as a steady influx of river-derived sediments is supplied. Bhattacharya and MacEachern, (2009) also document that early diagenetic siderite cementation is often present in hyperpycnal sediments. As with calcite cement, areas of the thin sections that are siderite cemented contain higher quantities of tangential and floating contacts, attesting to being a product of early diagenesis.

*Pyrite*

During shallow burial, sulfate-reducing bacteria degrade organic matter, producing hydrogen sulfide. The hydrogen sulfide will precipitate dissolved iron in the form of iron monosulfides, which will further react to form the framboidal and blocky pyrite (Berner, 1984; Wilkin and Barnes, 1997). Blocky pyrite is more commonly observed, in agreement with the observation by Wilkin and Barnes (1997), where blocky pyrite cements are more common in sandy rocks as opposed to fine-grained rocks. Pyrite does not influence reservoir quality to a large extent, thus is not of focus in this study.

### *6.2.3.2 IGV and Mechanical Compaction*

The intergranular volume is the volume of pore space, cement, and depositional matrix in grain-supported sandstones (Paxton et al., 2002). A combination of compactional and cementation processes determines the intergranular volume present. The relative effect of these processes on the resultant intergranular volume can be estimated with the use of equations by Houseknecht (1987) and Paxton et al. (2002) when plotted onto the diagram in figure 6.11 (see section 4.2.4.4). Starting depositional porosity is assumed to be 38% (as opposed to 40% stated in equations 4.5 and 4.6), equivalent to the IGV of the fully calcite cemented sample (V12). Furthermore, this diagram may act as a useful comparator with respect to similar studies (e.g. Clark, 2017). Point counted cements include calcite, quartz and authigenic pore-filling minerals such as kaolinite and chlorite. Houseknecht (1987) utilized sandstones that were moderately- to well-sorted and grain-supported. As all samples in this study fit that description, it is deemed appropriate to represent them on the diagram. Note that authigenic cements (e.g. quartz cement) can be difficult to distinguish via optical microscopy. As such, porosity loss from chemical processes may be slightly underestimated.

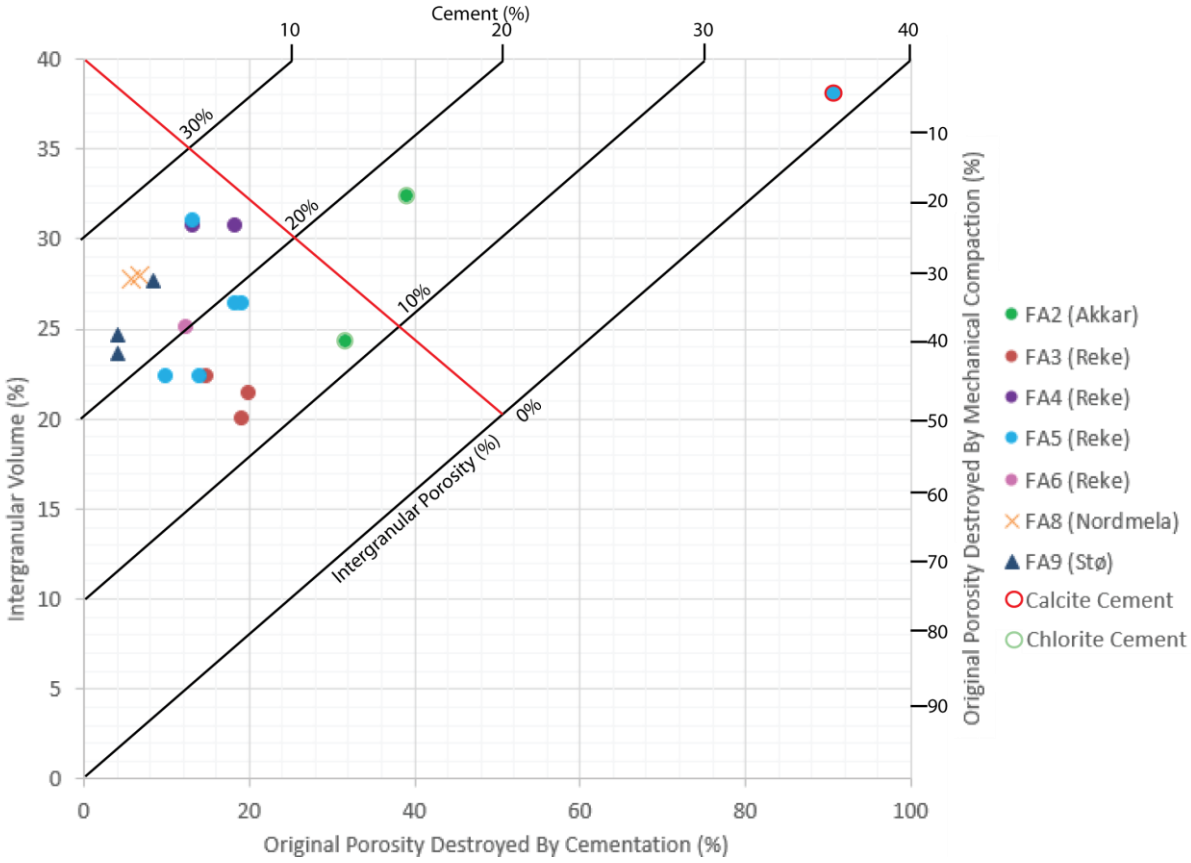


**Figure 6.11:** Cementation vs intergranular volume data from applying equations 4.5 and 4.6. Plotted points show that mechanical compaction is the primary cause of porosity reduction.

As seen in figure 6.11, almost all of the samples plot in the lower left side of the red line, signifying that mechanical compaction is the primary pore reducing mechanism. Additional evidence supporting mechanical compaction as the dominant pore reducing mechanism is found in the textural analysis, where the majority of grains are seen to either long or tangential, followed by concavo-convex (section 5.2.3.2). As samples in Houseknecht (1987) contained negligible matrix amounts, matrix was not accounted for in equations for intergranular volume of that study. Because this study includes the allogenic matrix in the determination of the IGV, results for those samples with substantial matrix may be skewed upwards and to the left, indicating an unrepresentative higher porosity on the diagram. Such may be the case for the samples of FA4, which contain the most matrix material (figure 5.38). Samples plotting on the upper right side of the red line signify that cementation is the dominant pore reducing mechanism. Only two samples plot in this area: V2 and V12, of which are chlorite and calcite cemented, respectively. Only 4.5% of the IGV is estimated to have been lost as a result of mechanical compaction in the calcite-cemented sample, as opposed to 20% of the IGV in the chlorite cemented sample. Calcite cement can therefore be assumed to have developed during early diagenesis as this would impede mechanical compaction by counteracting vertical stress.

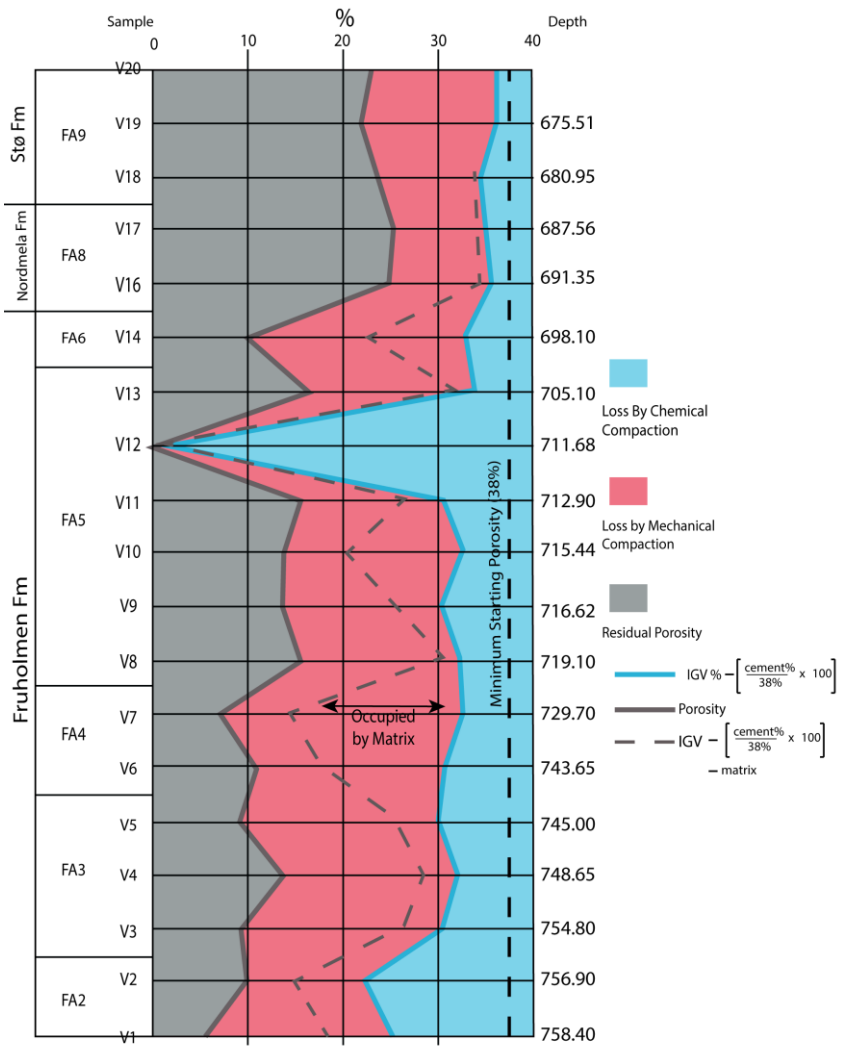


**Figure 6.12:**

Estimated loss by mechanical and chemical compaction regimes vs. sample number, as according to Houseknecht (1987). Minimum initial porosity is defined as 38%.

The Fruholmen Formation is clearly shown to have undergone far more mechanical compaction. This may be related to the presence of more ductile grains and matrix, as well as more angular grain shapes. FA4 shows greatest influence by mechanical compaction. FA4 also has the highest amount of matrix as well as poorest sorting (appendix E) of the analyzed samples. Nordmela and Stø Formation samples show less mechanical compaction, possibly related to virtual absence of ductile grains and matrix, as well as more rounded grains.

Figure 6.12 shows the estimated porosity losses due to mechanical and chemical processes vs sample number. Maximum estimated burial of the cored interval is computed to be between 2130 to 2240 m (section 5.3.3), which equates to approximately 21-22 MPa. Matrix and ductile grains exacerbate mechanical compaction by filling pore spaces when compressed and thus reduce porosity further. When point counting it is therefore important to differentiate between ductile deformation and depositional matrix. The currently observed porosity in the Fruholmen Formation, which holds a moderate portion of matrix and ductile grains (typically igneous and mud rock fragments), is expectedly reduced due to more mechanical compaction. Additionally, Fruholmen Formation samples show greater proportions of angular and sub-angular grains, as well as low sphericities, rendering the rocks more mechanically compressible. The Nordmela and Stø formations, on the other hand, comprise clean, fine- to medium-grained, mature sandstone, where ductile rock fragments are virtually absent. These formations accordingly show higher porosity values following burial, associated with less mechanical compaction. Higher quantities of sub-rounded and rounded grains as well as a larger proportion of more spherical grains additionally render these sandstones less compressible.

*Allogenic Clays*

Allogenic clays are primarily seen in the Fruholmen Formation, and are characterized by dispersed matrix, clay laminae, or infiltration residuals. Clay laminae can be correlated to depositional environments, with FA4 – tidal flat deposits containing the highest percentages (figure 5.38). Mud rock fragments initially composed of smectite (see section 6.2.3.3) are found through SEM in FA3 – delta mouth bar and FA5 –meandering channel deposits. The Stø Formation has trace amounts of allogenic clays, occurring as infiltration residuals acting as grain coatings (figure 5.29).

Results indicate that detrital clay infiltration is the most common source of the pore-filling illite observed throughout the samples. The original infiltrated clay was most likely illite, but possibly includes minor smectite which has been diagenetically altered to illite. No smectite was detected through XRD or SEM, but the fibrous textures sometimes seen in illite imply that it may have authigenically altered from smectite, given that this reaction occurs at approximately 70°C.

Grain-coating allogenic illite is found frequently in the Stø Formation (figure 5.29). Coatings are observed through SEM to be fairly thin (2 microns) and to partially to completely coat grains. Hansen et al. (2017) studied the illite coatings in the Stø Formation, and their results showed that Stø Formation samples with coatings had significantly lower amounts of quartz cement than those without coatings, but smaller IGVs because the presence of clays at grain contacts promotes pressure dissolution. The presence of illite coating may prevent quartz cementation by limiting the surfaces available for quartz to nucleate (Bjørlykke and Jahren, 2015). The illitic clay coatings have thus played a role in preserving porosity in the Stø Formation.

Grain coatings likely formed via infiltration processes, and were later subjected to varying degrees of reworking (Wilson, 1992; Hansen et al., 2017). Matlack et al. (1989) found that four criteria are favourable in clay emplacement by infiltration: 1) coarse sediment, 2) high concentrations of clay in suspension, 3) fluctuating water levels and 4) little sediment reworking. In situ sands in the vadose zone after clay infiltration have grain coatings and meniscus shaped bridges of clay at grain contacts (Matlack, 1989). Reworking would remove the grain bridging clays, while grain coats are more likely to persist. The Stø Formation, however, is interpreted to have undergone a high degree of reworking, evidenced by results (section 5.2.3) and documented by literature (e.g. Klausen, 2018). The preservation of grain coating illite could relate to the number of reworking cycles. For example, perhaps coatings survive two rounds of reworking but are not as pronounced after three or more. Because clay coating is unlikely to survive such extensive reworking, it is also possible that clay infiltration may have taken place subsequent to reworking, thereby increasing preservation potential. Because only two samples from the Stø Formation were analysed in SEM, it is not known whether these coatings are continuous throughout the Stø Formation in Wisting Central III.

### *6.2.3.3 Chemical Compaction*

As opposed to early diagenesis, chemical reactions taking place at deeper burial depths occur in a closed system, driven thermodynamically (Bjørlykke, 1998). Evidence of quartz cementation is observed in all three formations. Authigenic illite is often found in combination with quartz in the Fruholmen Formation. Authigenic chlorite is also found in the Fruholmen Formation, and appears to dominate the authigenic mineralogy in the Akkar Member, where it coats detrital grains of FA2 – storm influenced delta front deposits.

*Quartz Cementation*

Quartz cement occurs as apparent single-crystal overgrowths on the surfaces of detrital quartz grains. Quartz overgrowth typically initiates at temperatures above 60°C, with maximum formation commonly occurring in the temperature range of 90-160°C (Bjørlykke and Egeberg, 1993). The volume of quartz cement precipitated is determined by the sandstones' temperature history and amount of quartz surface area where quartz overgrowth can form (Bjørlykke & Jahren, 2015). Only about 3% quartz cement is sufficient to strengthen the grain framework to counteract porosity loss caused by mechanical compaction (Bjørlykke and Jahren, 2015). Based on observations made with cathode luminescence, enough quartz cementation has precipitated to significantly reduce further mechanical compaction in the sandstones studied. This is supported by the maximum burial temperature estimates of 70-80°C.

Quartz cementation increases exponentially with temperature and is proportional to the surface area available for precipitation. As available surface area is reduced, the chemical compaction process slows down (Bjørlykke and Jahren, 2015). Variation in quartz cement is related to the presence of illitic coatings (figure 5.29; see section 6.2.3.2), and the unknown time the sediments have been exposed to temperatures necessary for the development of quartz cement.

Dissolution of quartz can be enhanced by mica and clay minerals present at grain contacts (Bjørkum, 1996). The Fruholmen Formation holds substantial quantities of these constituents. This may lead to an increase in the precipitation of quartz cement, but this cannot be confirmed because accurate estimates of the quantities of quartz cement present have not been made.

*Illitization*

Authigenic illite has been found replacively in combination with microcrystalline quartz in mud rock fragments in the Fruholmen Formation (figure 5.23 and 6.13). Several reactions occur at depth that result in the precipitation of illite.

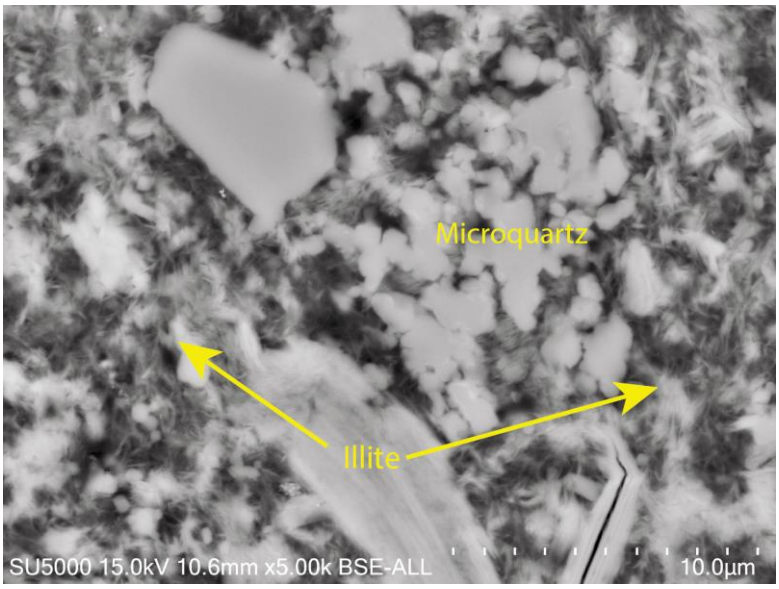


**Figure 6.13:** Close up of mud rock fragment pictured in figure 5.23A, illustrating microquartz and the hair-like textures formed by authigenic illite.

Smectite will react with potassium and aluminium ions to create mixed layer minerals, illite, and quartz (equation 3.5). This reaction starts at around 70°C (Bjørlykke et al., 1995; McKinley et al., 2003) and forms fibrous textures that are detrimental to reservoir permeability (figure 6.13). The dissolution of metastable smectite minerals creates a high silica concentration relative to quartz saturation in the pore water (e.g., Egeberg and Aagaard, 1989; Bjørlykke and Aagaard, 1992; Abercrombie et al., 1994). The high silica concentrations result in the formation of microquartz, which is the only possible form of quartz cementation in confined silica super-saturated systems due to slow growth rates of quartz at low temperatures (around 60–80°C) (e.g., Williams et al., 1985; Bjørlykke and Egeberg, 1993; Jahren et al., 2000). The local formation of microquartz within mud rock fragments is consistent with closed system diagenesis and suggests a low mobility of silica (Thyberg et al., 2010). This shows that the growth rate of quartz and diffusion of silica is not high enough in sandstones to prevent micro-quartz formation (Jahren et al., 2000). The microquartz crystals nucleate on substrates like earlier formed micro-quartz crystals and on illite– smectite and authigenic illite, and can lead to formation of micro-quartz networks (Thyberg et al., 2010).

As previously mentioned in section 6.2.1, the climate in the area has been documented to be humid, which is not conducive to the formation of smectite. However, as discussed in section 6.2.2 on provenance, an eastern source area containing basalt and greenschist rocks has been deduced. Although smectite is more typical of arid environments, it is commonly seen to form in humid conditions in the presence basalt and volcanic ash (Bjørlykke, 2015). This is a potential source of the smectite that had composed the rock fragments in the Fruholmen Formation. Upon erosion in the Uralian hinterland, the

smectite was probably transported in suspension in rivers. Crevasse splays would then spill over the smectite such that it becomes part of the flood plain deposits. Cut bank erosion and avulsion would then break off mud rock fragments of smectite, which are subsequently deposited as part of the Fruholmen Formation.

If the original composition of allogenic clays is illitic, then no further chemical reactions occur during diagenesis. It is possible to differentiate authigenic from allogenic illite based on the appearance – authigenic illite forms hairy/fibrous textures. This is particularly evident on grain coatings, whereby allogenic illite is tangential to the grain surface, whereas authigenic illite would form at high angles to the grain surface.

Authigenic illite also forms as an alteration product of kaolinite (equation 3.6), but this reaction is not favoured before temperatures of 120-140℃ are reached. Because maximum burial temperature estimates are significantly lower than 120℃, this diagenetic reaction is not expected to have occurred. Observations from SEM are in agreement, with relatively high quantities of kaolinite with absence of alteration found in the Fruholmen Formation.

*Chloritization*

Chlorite is often seen to form pseudomorphic replacements throughout the Fruholmen Formation. In FA2 – storm influenced delta front, authigenic chlorite coatings are present.

Chlorite occurs as grain replacements often as a result of breakdown of volcanoclastic grains and Fe-Mg rich detrital minerals such as amphibole, pyroxene, and biotite (De Ros et al., 1994; Worden and Morad, 2003). The presence of these minerals in the detrital mineralogy of the sandstone suggests the presence of mafic rocks – likely basalt – in the source area. This is in agreement with findings by Mørk (1999) as well as with a Uralian source area.

Chlorite coatings are typically produced through the chloritization of grain coating berthierine-odinite or smectite (Morad et al., 2000). The transformation of precursor clay minerals to chlorite occurs at temperatures higher than 80°C (Ehrenberg, 1993; Jahren and Aagaard, 1989). This suggests that the rocks observed have at least undergone these temperatures. Emplacement of the precursor clays is likely via infiltration, as described for the allogenic illite coatings (section 6.2.3.2).

The chlorite coatings present in FA2 – storm influence delta front deposits likely retard the precipitation of quartz overgrowths, and thus prevent porosity loss from chemical compaction. However, extensive chlorite cementation can block pore throats and thus reduce the permeability (Worden and Morad, 2003).

# 6.3 Reservoir Quality Analysis

The previously discussed parameters of climate, provenance, depositional environment, and diagenesis determine the presently observed porosity and permeability, and therefore reservoir quality. Based on sedimentological logging, thin section analyses, and core plug data, FA1, FA2, FA4, and FA7 have been discarded with respect to reservoir quality. The prodelta FA1 and estuarine FA7 are discarded due to consisting largely of mudstone. FA2 is appraised to have negligible to poor permeability values when applying cutoffs by Tissot and Welte (1987). Although core plug data and thin section analysis show that the tidal flat FA4 may be promising, exclusively sandstone samples (from sand flat deposits) were selected for analysis from FA4, rendering them unrepresentative for the entire facies association. The regular 0.5-1 m alterations between sand flats, mixed flats, and mud flats as well as extensive occurrence of mud drapes present vertical flow barriers.

FA3, FA5, and FA6, of the Fruholmen Formation and FA8 and FA9 of respectively the Nordmela and Stø Formations exhibit varying reservoir properties, which will be discussed and characterized in this section. When assessing the reservoir quality, it is vital to be aware that a small fraction of rock is assumed to represent properties of the entire facies association. Additionally, discrepancies between core plug and point counted porosities may be attributed to the micro-porosities overlooked within the clay minerals present in the matrix and numerous mud rock fragments. Core plug data measures in 3D, while point counting is determined with a 2D section, also leading to porosity underestimations in point counting. Observations made when logging the core can contribute in the assessment and variation in quality. Table 6.1 sums up primary factors influencing reservoir quality and provides an evaluation for each selected facies association.

## 6.3.1 Fruholmen Formation

### *FA3 – Delta Mouth Bar*

Reservoir appraisal values from Tissot & Welte (1984) characterize the FA3 reservoir as ‘fair’. FA3 consists of a well-sorted, very fine-grained sandstone (see section 5.2.3), and is relatively clean with an average of about 3% matrix. Point counting results show an average porosity of about 11%, whereas core plug data shows an average of about 18%. Core plug data show a relatively narrow range in permeability throughout the succession, averaging 65.54 mD. Mechanical compaction has been determined to be the dominant porosity reducing mechanism (see section 6.2.3.2). High quantities of ductile grains (e.g. mud rock fragments, mica, and some igneous rock fragments), authigenic clays, and matrix exacerbate the effect of mechanical compaction. These constituents comprise an average of about 26%. The dominance of long grain contacts attests to the dominance of mechanical compaction as well as the relatively high quantities of ductile grains. More angular grains (figure 5.35) also promote more mechanical compaction. Although the primary pore reducing factor is mechanical compaction, enough

quartz cement is estimated to have been produced (~3%) to stabilize the grain framework. Presence of partially dissolved feldspars combined with observations through SEM suggest that kaolinite may be significant in diminishing reservoir quality.

## *FA5 – Multistory Meandering Channel*

Reservoir quality analysis for FA5 excludes the calcite cemented sample (V12) because it has negligible reservoir properties. However the potential presence of a laterally continuous calcite-cemented sandstone layer is essential to take note of.

Reservoir appraisal values from Tissot & Welte (1984) characterize samples from FA5 as 'good'. It is important to recognize that samples were exclusively sourced from the sandstone matrix of FA5. In some intervals, large mudstone rip-up clasts pervade FA5 (figure 5.7), whereas they are not as numerous in other stratigraphic sections. Clearly the presence of these clasts would diminish the reservoir quality. Although samples analyzed classify as 'good' in reservoir quality, reservoir quality as a whole, especially in the intervals pervaded by mudstone clasts, is obviously significantly poorer. The remaining description is in respect to the analyzed thin sections and core plug data, and thus only yields properties of the sandstone matrix.

FA5 predominantly consists of well-sorted, fine-grained sandstones, and is relatively clean with an average of about 4% percentage of matrix. Point counting results show an average porosity of 16%. Core plug data shows an average porosity of 20%. Huge variations in permeability exist throughout FA5 – from values nearing zero mD to over 1000 mD. Values average at about 197 mD, again excluding the calcite cemented interval. Mechanical compaction has been determined to be the dominant porosity reducing mechanism (see section 6.2.3.2), with the exception of the small calcite cemented interval. Ductile grains and matrix, comprising an average of 22%, as well as high quantities of angular to sub-angular grains, exacerbate mechanical compaction. The dominance of long grain contacts also attests to the dominance of mechanical compaction. The occurrence of partially dissolved feldspars combined with observations through SEM suggest that kaolinite may be significant in diminishing reservoir quality.

## *FA6 – Tide Influenced Distributary Channel*

Reservoir appraisal values from Tissot & Welte (1984) characterize the sample from FA6 as 'good'. While FA6 has some mudstone rip-up clasts similar to those of FA5, they are not nearly as pervasive as in FA5 and most of the interval occupied by FA6 is free of them.

FA5 predominantly consists of well-sorted, fine-grained sandstones. It holds a relatively high proportion of matrix at 10%, probably due to tidal influence. The point counted sample shows a porosity of 10%. Core plug data shows an average porosity of 23%. This discrepancy is attributed to the location of the sample, where flaser bedding was prominent, likely holding more clay than typical for FA6.

Permeability varies throughout FA6 but not extensively as does FA5. The average permeability is about 295 mD. Mechanical compaction has been determined to be the dominant porosity reducing mechanism (see section 6.2.3.2). Again, relatively high quantities of ductile grains and matrix, at 29%, exacerbate mechanical compaction. The presence of partially dissolved feldspars and observations through SEM suggest that kaolinite plays a role in diminishing reservoir quality. The lack of intraformational rip-up clasts promotes the quality of the reservoir in relation to FA5.

## 6.3.2 Nordmela Formation

### *FA8 – Compound Tidal Dune Complex*

Reservoir appraisal values from Tissot & Welte (1984) characterize FA8 as 'very good'. FA8 consists of well-sorted, fine- to medium-grained sandstones, and is exceptionally clean with only trace quantities of matrix. Point counting results show an average porosity about 25%. Core plug data shows an average porosity of 28%. Permeability is consistently high, averaging 4237 mD. Mechanical compaction has been determined to be the dominant porosity reducing mechanism (see section 6.2.3.2). Low proportions of ductile grains and matrix renders FA8 capable of retarding more significant amounts of mechanical compaction, on contrast to facies associations belonging to the Fruholmen Formation. The higher proportions of sub-rounded and rounded grains (figure 5.35) also renders FA8 less compressible. Curtailed levels of mechanical compaction probably results in the greater proportions of tangential contacts observed in the Nordmela Formation (figure 5.34). The top 10 cm of the Nordmela Formation is calcite cemented, diminishing quality in this interval. The lateral extent of the calcite cementation cannot be ascertained.

## 6.3.3 Stø Formation

### *FA9 – Upper Shoreface*

Reservoir appraisal values from Tissot & Welte (1984) characterize FA9 as 'very good'. FA9 consists of well-sorted, fine-grained sandstones, and is exceptionally clean with only trace quantities of matrix. Point counting results show an average porosity about 23%. Core plug data shows an average porosity of 25%. Permeability is consistently high, averaging 3930 mD. Mechanical compaction has been determined to be the dominant porosity reducing mechanism (see section 6.2.3.2). Illite coatings (see section 6.2.3.2) have likely inhibited quartz cementation, thereby preserving porosity. Like FA8, the low proportions of ductile grains and matrix renders FA8 capable of retarding more significant amounts of mechanical compaction. The higher proportions of sub-rounded and rounded grains (figure 5.35) also renders FA8 less compressible. Smaller levels of mechanical compaction probably results in the greater proportions of tangential contacts observed in the Stø Formation (figure 5.34). Sparse calcite cemented nodules are present throughout, but never are large enough to extend beyond the width of the core. Their lack of both vertical and horizontal continuity suggest they do not play a large role in the overall quality of FA9.

| | Property | FA3 | FA5 | FA6 | FA8 | FA9 | Effect on Reservoir Quality |
|---|---|---|---|---|---|---|---|
| **Initial Composition** | Quartz % | 41.78 | 42.93 | 42.67 | 62.17 | 70.11 | • Framework Grain |
| | Feldspar % | 13.11 | 15.20 | 12.66 | 3.17 | 2.67 | • Framework Grain<br>• Early diagenetic leaching and precipitation of kaolinite |
| | Lithic Fragments % | 19.67 | 14.60 | 17.33 | 3.00 | 1.00 | • Often ductile behavior, facilitating mechanical compaction |
| | Allogenic Clay % | 3.33 | 3.87 | 10.00 | Trace, Coats Grains | Trace, Coats Grains | • Facilitates mechanical compaction by reducing friction between framework grains<br>• Reduce primary porosity<br>• When coating grains, can inhibit quartz cementation |
| **Authigenic Composition** | Kaolinite* | >3.55 | >3.00 | >2.00 | trace | trace | • Fills pores and clogs throats, reducing both porosity and permeability |
| | Calcite | none | One horizon ? | none | Minor nodules | Minor nodules | • Expends both porosity and permeability<br>• Potential vertical flow barriers |
| | Quartz* % | >0.33 | >1.53 | >2.00 | >1.50 | >1.55 | • Reduces porosity<br>• 3% can terminate mechanical compaction |
| | Illite* | In mud RFs | In mud RFs | In mud RFs | Absent | Absent | • Hair-like fibers reduce permeability |
| **Textural Properties** | Grain Size | Very Fine | Very Fine to Fine | Very Fine | Fine to Medium | Fine | • Small grain sizes decrease compressibility of the rock due to high number of contacts |
| | Sorting | Well-sorted | Mod-erate to Well | Well-sorted | Well-sorted | Well-sorted | • Better sorting results in less mechanical compaction |
| | Dominant Shape | Sub-angular | Sub-rounded | Sub-rounded | Sub-rounded | Sub-rounded | • More rounded grains results in less mechanical compaction |
| | Avg. IGV | 21.22 | 25.66 | 25.00 | 27.84 | 25.34 | • Volume between framework grains |
| | Porosity – Point Counting | 10.67 | 15.14 | 10.00 | 25.16 | 23.00 | • Available space to store hydrocarbons |
| | Porosity – Core Plug | 18.43 | 19.60 | 23.20 | 28.10 | 25.10 | |
| | Permeability | 65.54 | 197 | 295.2 | 4237 | 3930 | • Ability to transmit hydrocarbons |
| | ***Reservoir Quality*** | ***Fair*** | ***Poor** to Good*** | ***Good*** | ***Very Good*** | ***Very Good*** | |

**Table 6.1:** Mineralogical composition and textural properties with the resultant reservoir quality for each analyzed facies.

*: These components are likely underestimated due to difficulty to distinguish via optical microscopy.

**: Lower reservoir quality inferred for FA5 than based on petrographic and core plug data, due to mud clasts.

### 6.3.1 Wisting Central III (7424/8-3) and Gemini North (7325/4-1): Results Comparison

This study was conducted alongside a similar study which applies the same analytical methods on Realgrunnen Subgroup sandstones from Gemini North (7325/4-1). For the detailed results and discussion entailing this study, refer to Skretting (*in prep).* Gemini North contains the Fruholmen, Stø, and possibly the Nordmela Formation. Skretting *(in prep)* indicates the Nordmela Formation is absent in Gemini North., although Skretting (*in prep*) notes the possibility of its existence. Therefore, in this section the Nordmela and Stø formations will be grouped and referred to as 'Jurassic sandstones'. Brief comparisons with respect to reservoir quality are made in this section primarily with the use of XRD and point counting results, in addition to core plug data from the respective wells. Figure 6.14 displays the locations of the two wells under consideration.

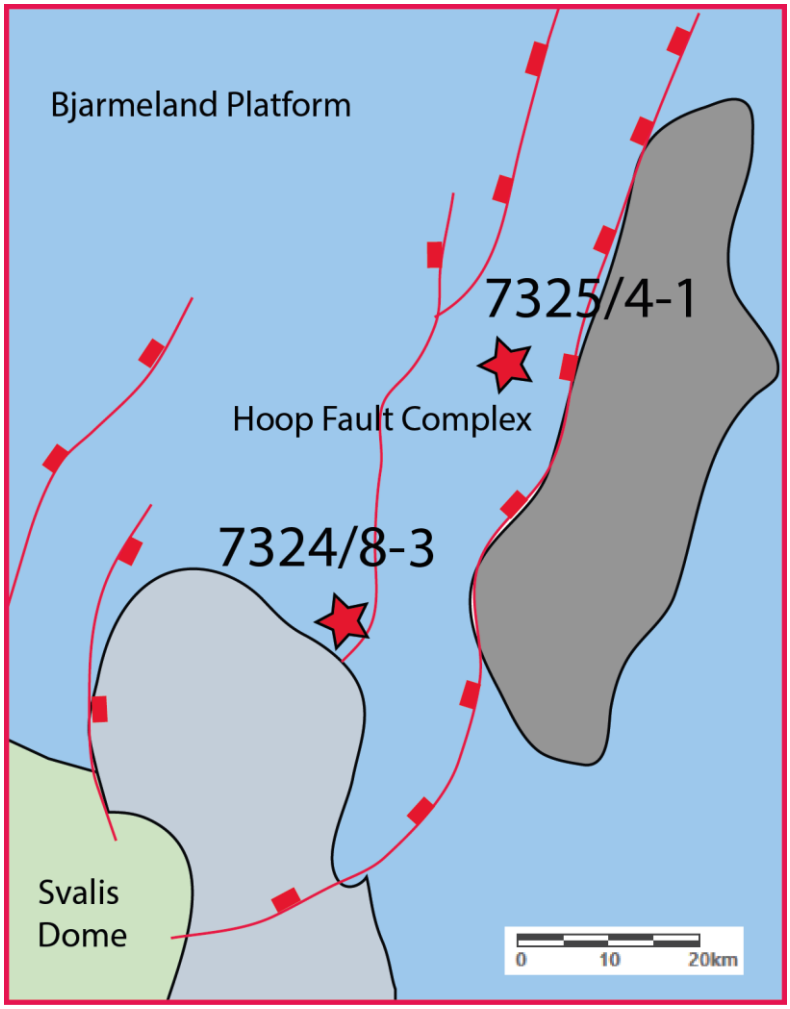


**Figure 6.14:** Locations of the wells discussed in this section. Gemini North (7425/4-1) is approximately 35 km to the northeast of Wisting Central III (7324/8-3).

### 6.3.1.1 XRD Comparison

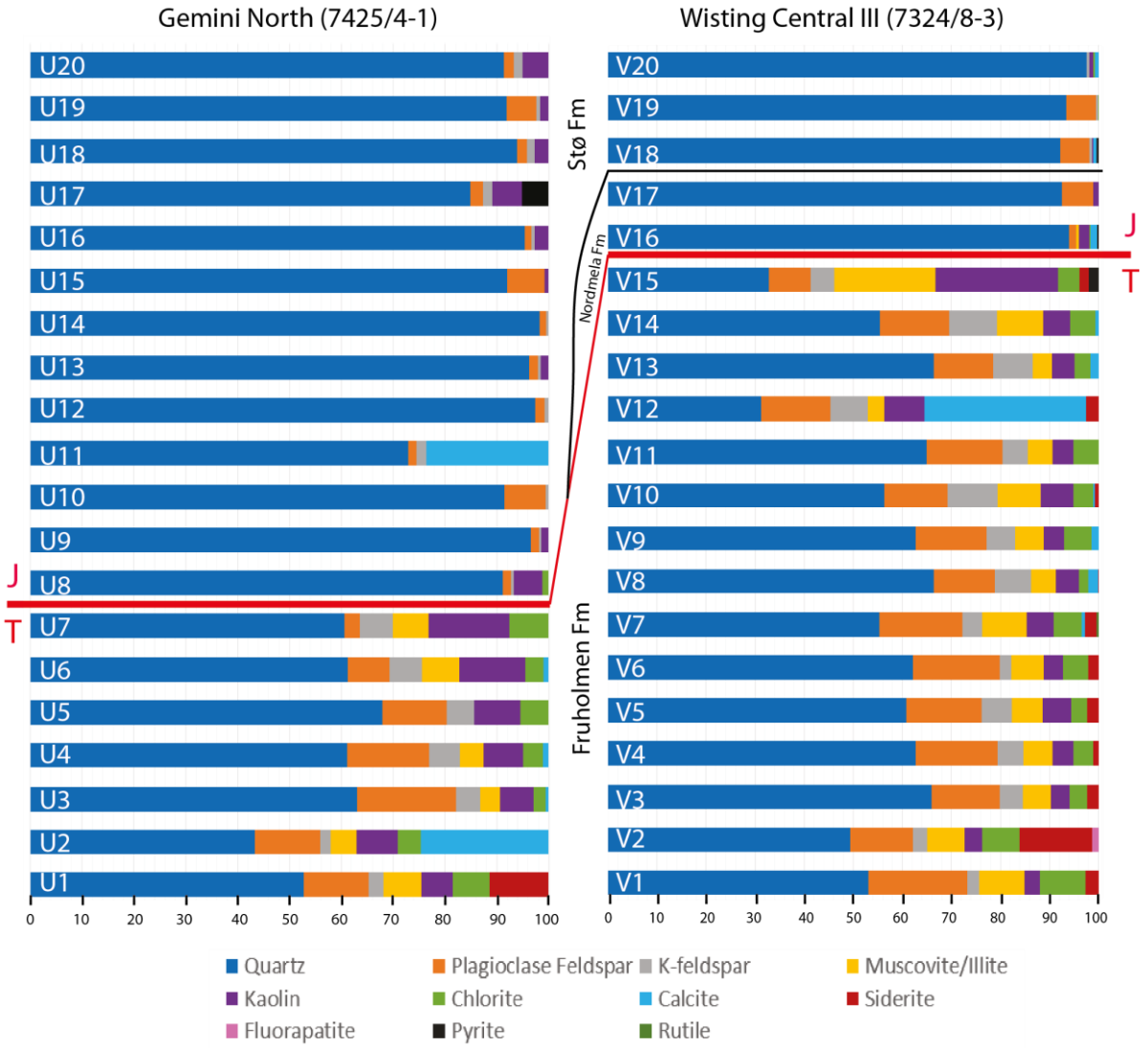


**Figure 6.15:** XRD results for both wells placed side-by-side. Triassic-Jurassic transition in marked in red. Higher proportions of kaolinite are seen in the Fruholmen Formation in Gemini North, as well as in the Stø Formation. Note that V15 from Wisting Central III is a clay sample.

XRD results from both Wisting Central III and Gemini North show the same abrupt change in mineralogy that has been noted previously across the Triassic Jurassic transition, associated with a decrease in mineralogical diversity and a loss in Mg- and Fe-rich components (figure 6.15). Formation specific comparisons are discussed in chronological order.

*Fruholmen Formation*

The trend of increasing relative proportions of K-feldspar with respect to plagioclase feldspar as observed in Wisting Central III (7324/8-3; this study), Hanssen (7324/7-2), and Wisting Central (7324/8-1)(Clark, 2017) is also observed in Gemini North (7325/4-1). Figure 6.16 demonstrates this more clearly.

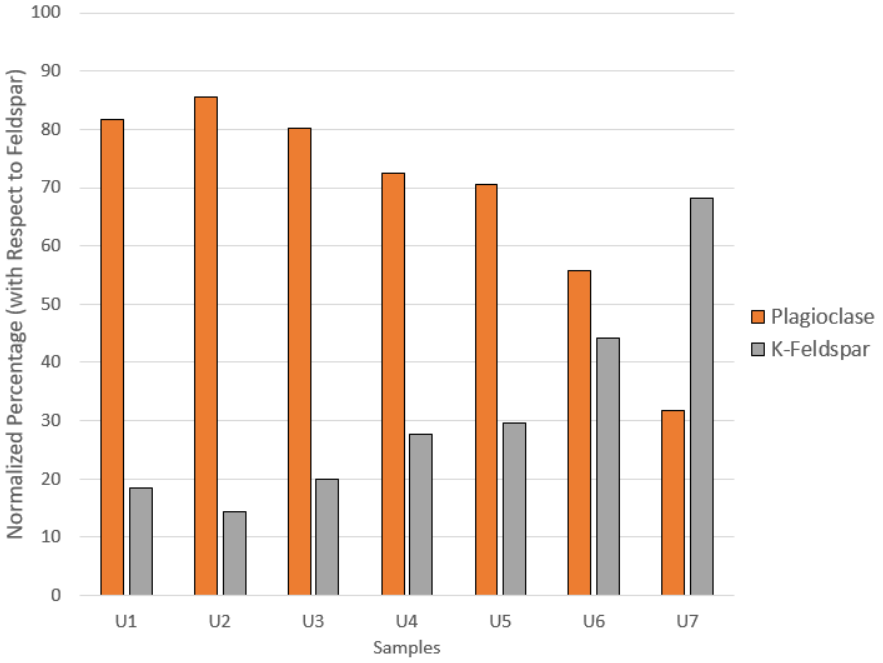


**Figure 6.16:** Increasing relative proportions of k-feldspar throughout the Fruholmen Formation samples in Gemini North (7325/4-1). This same trend is seen in Wisting Central III (7324/8-1) – see figure 5.15. The same trend is also demonstrated in Hanssen (7324/7-2) and Wisting Central (7324/8-1) (shown in Clark, 2017).

As mentioned in section 6.2.2, this trend could record the increasing importance of input from a Caledonian source through time.

Another remark on Fruholmen Formation XRD results is the overall much larger percentages of kaolin in Gemini North (7325/4-1). Note that the V15 sample is composed primarily of clay, so should be removed from consideration. The higher percentages could be due to greater meteoric water flow, resulting in the leaching of more feldspars. A potential reason for increased water flow Gemini North (7325/4-1) may be in slower deposition and burial rates. If deposition is slow, the sediments are under the influence of meteoric water flow for a longer period of time. This reasoning is supported by differences in thicknesses of the Fruholmen Formation between the two wells – the Lower Reke Member in Wisting Central III is 36 meters thick, whereas in Gemini North it is only 12 meters thick. This implies more accommodation and/or higher sediment input in Wisting Central III, whereby burial rates are higher and thus are buried to a depth at which sediments are out of the reach of meteoric water flow at a faster rate. Slower burial rates in Gemini North suggest that the sediments underwent more time under the influence of meteoric leaching, reflected by the increase in kaolinite content. A figure demonstrating higher proportions of kaolin to feldspar in Gemini North compared to Wisting Central III can be found in appendix H.

*Jurassic Sandstones*

The only notable difference in the XRD results of the Jurassic Sandstones is the presence of sizable percentages of kaolin in multiple samples in Gemini North (7325/4-1), which is almost completely absent in samples from Wisting Central III. Given that the Stø Formation was deposited in an overall transgressive regime characterized by extensive reworking, the presence of kaolinite or lack thereof may indicate the extent of reworking. High degrees of reworking would lead to the elimination of kaolinite. As such, it is possible that the area of Gemini North (7325/4-1) was less prone to reworking during Stø times. This is also reflected in the grain shapes, as will be shown in section 6.3.1.2.

Overall, greater percentages of kaolinite in both the Fruholmen Formations and the Jurassic sandstones in Gemini North result in poorer reservoir quality (see section 6.3.1.3).

### *6.3.1.2 Point Counting Comparison*

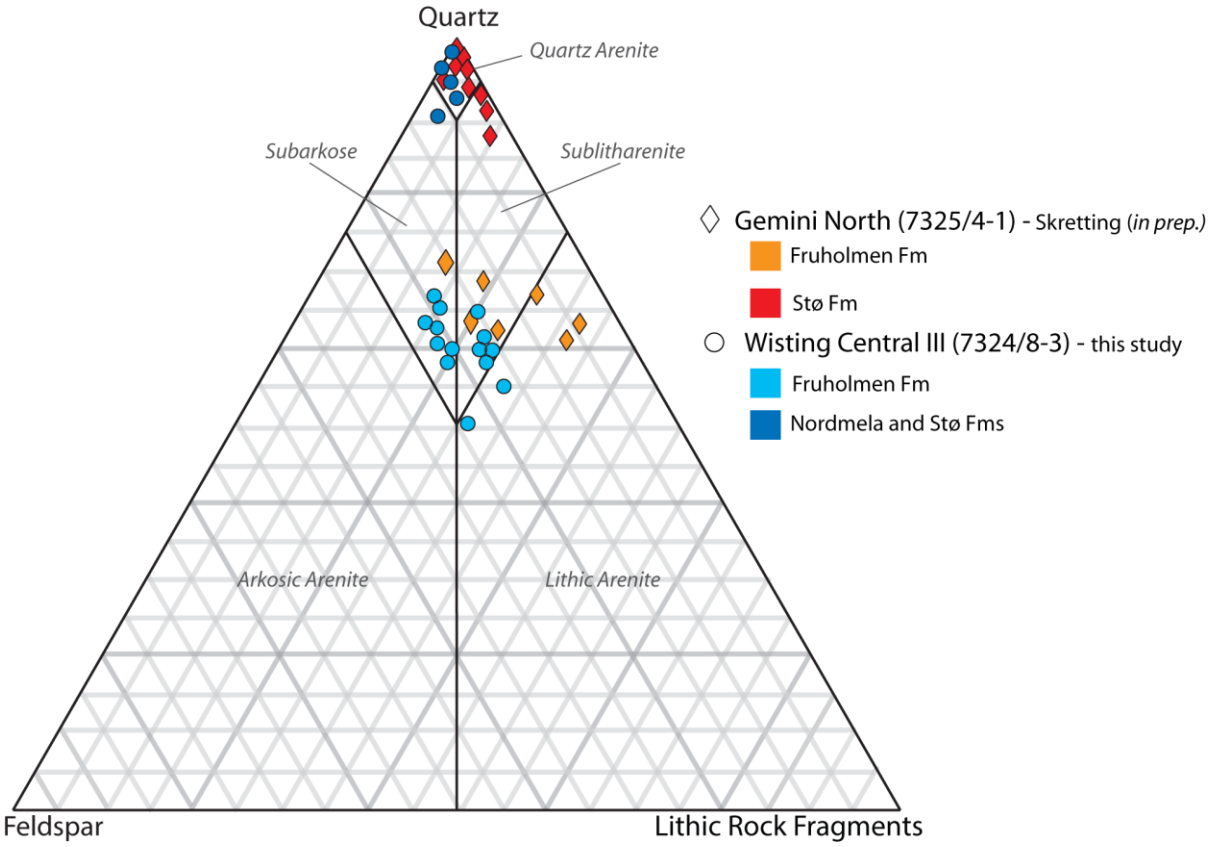


**Figure 6.17:** QFL ternary diagram with results from both wells. The Triassic Fruholmen and Jurassic Stø and Nordmela Formations from both wells plot similarly, respectively. Gemini North is found to contain a higher proportion of lithic rock fragments, with more plotting as lithic arenites. Because lithic rock fragments are more likely to behave in a ductile manner, this may promote mechanical compaction in Gemini North. However, it is also important to note that discrepancies may arise due to subjective differences in the interpreter.

Results from both Wisting Central III and Gemini North (7325/4-1) plot at relatively similar positions in the Dott (1964) QFL diagram with respect to formation (figure 6.17). The main difference in the Fruholmen Formation lies in the generally larger proportions of lithic rock fragments in Gemini North

(7324/4-1). Skretting (*in prep*) documents these to be primarily igneous epiclasts. Although not observed first-hand, results in this study show that these grains are weak and have a tendency to deform in a ductile manner. If this holds true in Gemini North (7325/4-1), these grains would promote mechanical compaction and reduce reservoir quality.

Skretting (*in prep*) also tabulated slightly more lithic rock fragments in the Stø Formation, however compositional differences are minor and they are unlikely to play a significant role in aiding mechanical compaction.

Textural results also support more extensive reworking of the Stø Formation in Wisting Central III. Across the Triassic-Jurassic transition, sandstones in Gemini North (7325/4-1) show little change in angularity, remaining dominantly sub-angular in shape. In contrast, in Wisting Central III, a distinct change from being dominated by angular grains in the Fruholmen Formation to rounded grains in the Stø Formation is observed. Significant reworking leads to the presence of more rounded grains. In turn, these sandstones suffer less from mechanical compaction, offering more promising reservoir qualities.

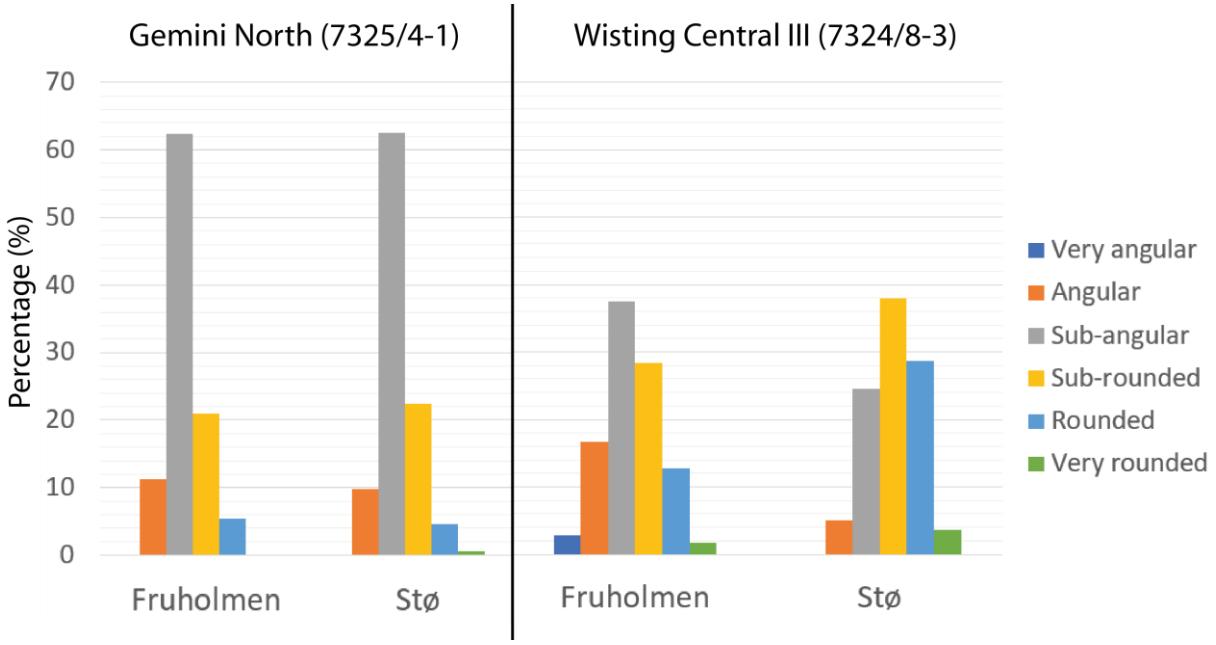


**Figure 6.18:** Grain shape percentages in both wells from the Fruholmen and Stø Formations. While some discrepancy can be subjective due to the difference in the interpreter, there is nonetheless very little change across the Triassic-Jurassic transition in Gemini North, with sub-angular grains dominating in both the Fruholmen and Stø Formations. On the other hand, in Wisting Central III there is a shift towards more sub-rounded and rounded grains from the Fruholmen to the Stø Formation.

### *6.3.1.3 Porosity and Permeability*

A porosity and permeability plot using core plug data for both wells is plotted in figure 6.19.

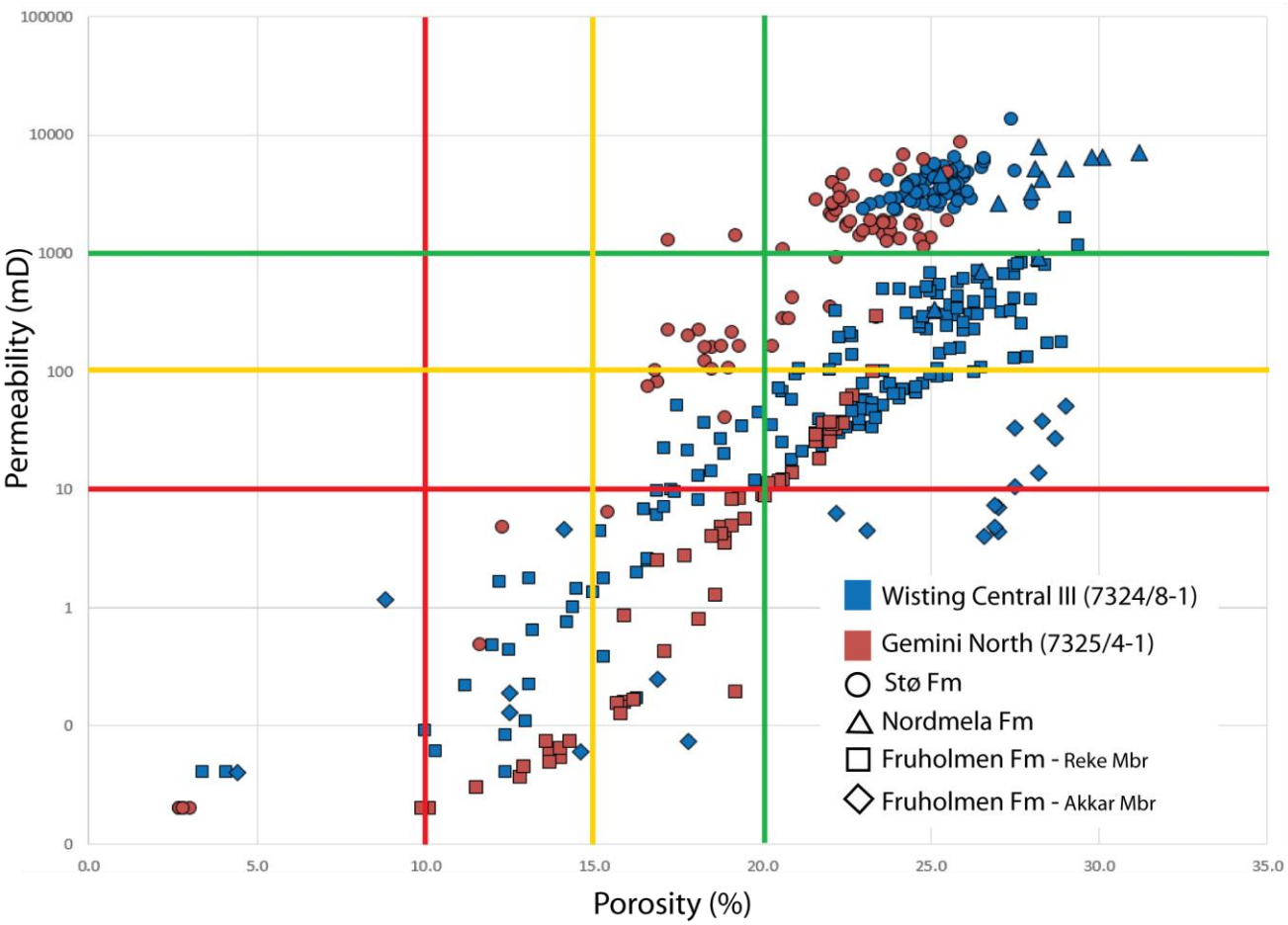


**Figure 6.19:** Porosity vs permeability from core plug data for both wells. Lines are porosity and permeability cutoff values as established by Tissot and Welte (1987), with red being 'fair', yellow being 'good' and green being 'very good'. Wisting Central III is shown to have typically more promising reservoir properties, with the majority of the Fruholmen Formation having 'very good' porosity values and 'good' permeability values. The Fruholmen Formation in Gemini North, although showing some 'very good' porosity values, typically shows permeability values that are no more than 'fair'. This is attributed to higher percentages of pore-filling kaolinite. Similar observations are seen in the Stø Formation. In Wisting Central III, the Stø exclusively plots at 'very good' porosities and permeabilities. Gemini North has many points that also plot in this region; however a spread of values extending into only 'fair' porosities and permeabilities are seen.

*Fruholmen Formation*

Note that a much thicker expanse of the Fruholmen Formation exists in Wisting Central III, where the Reke member is 67 meters thick. In Gemini North (7325/4-1) it is only 27 meters thick, thus holding fewer measurements. Additionally, in Wisting Central III the Fruholmen Formation records several depositional environments that are not present/not interpreted in Gemini North (see Skretting, *in prep.*). This contributes to the greater variance of values seen in the Fruholmen Formation in Wisting Central III.

Wisting Central III shows higher porosities and permeabilities than core plug samples from Gemini North. Generally, the Fruholmen Formation of Wisting Central III has 'very good' porosities and 'good' permeabilities when utilizing cutoffs established by Tissot & Welte (1984). The majority of samples in Gemini North assume 'very good' porosities, however only 'fair' permeabilities. The shortcomings in reservoir quality of sandstones from Gemini North (7325/4-1) have been alluded to in the previous sections. More kaolin, higher quantities of igneous lithic rock fragments, and more angular grains (especially in the Stø Formation) may play a role in the generally lower quality. Larger proportions of pore-filling kaolin in Gemini North is probably the primary factor decreasing the permeability.

*Jurassic Sandstones*

In Wisting Central III, the reservoir quality is exclusively 'very good' in relation to both porosity and permeability, and values are tightly packed. While many of the measurements from Gemini North also show 'very good' reservoir quality, there is a much larger spread of measurements, extending towards only 'fair' porosities and permeabilities. This is attributed to higher amounts of kaolinite, as detected by XRD in section 6.3.1.1, in the Stø Formation of Gemini North.

# Chapter 7: Conclusions

The aim of this study is to describe reservoir properties and to characterize the quality of sandstones of the Realgrunnen Subgroup from Wisting Central III. Lateral and temporal changes in mineralogy and texture are examined, particularly in relation to Gemini North (7325/4-1). These aims are achieved through sedimentological, petrographical, and petrophysical analyses.

XRD analysis was conducted to determine the mineralogy present within the samples. Point counting yielded information on the proportions of various grain types as well as constituents comprising the intergranular volume (IGV). Several samples were selected for SEM and CL-analyses, to confirm mineralogy detected through bulk XRD as well as to observe authigenic minerals difficult to distinguish through optical microscopy (e.g. kaolin, quartz cement). The primary purpose of the petrophysical logs was to estimate uplift and thereby maximum burial depth and temperature.

Reservoir quality is a function of porosity and permeability, of which are governed by climate, provenance, depositional environment, and burial diagenesis. As such, these parameters play important roles when characterizing reservoir potential that may be found in the vicinity of the drill core, and have thus formed the foundation for the discussion in this thesis.

The following conclusions have been derived from the results of this study:

- Vast petrographic differences are found across the Triassic-Jurassic boundary in Wisting Central III, where the Late Triassic Fruholmen Formation has been found to be significantly more mineralogically immature than the Early Jurassic Nordmela and Stø formations. Authigenic minerals, such as kaolinite, chlorite, and siderite are relatively abundant in the Fruholmen Formation. These are absent or present in only trace amounts in the Nordmela and Stø Formations.
- The far fewer amounts of feldspars, micas, and kaolin present in the Early Jurassic sandstones than the Triassic sandstones is not in accordance with a more humid paleoclimate at the turn of the Jurassic. Climatic effects are obscured by change in provenance combined with the reworking of sediments.
- Provenance indicators in the Fruholmen Formation in Wisting Central III are in favour of an eastern source area. This is in agreement with recent findings by Klausen et al. (2017), who suggested the Novaya Zemlya protrusion as a potential provenance area. This conclusion is, however, at odds with previous works that suggest a Caledonian/Fennoscandian for the Fruholmen Formation throughout the SW Barents Sea. These works, however, had focus on sediments in the southern basin margin area.
- Petrographic results from Jurassic Nordmela and Stø formations in Wisting Central III yield few provenance indicators. However, the high textural and compositional maturity indicates extensive reworking. The high compositional maturity is more in line with a

Caledonian/Fennoscandian source. Detrital zircon studies show that a mix of provenance signatures are found. The primary source at this time is interpreted to be Caledonian/Fennoscandian, while other signatures are mixed in as a result of reworking of underlying sediment.

- Depositional environments are of great significance as they determine the grain size and sorting found, thereby playing a large role in dictating the reservoir quality observed. The facies associations observed in the Wisting Central III drill core record a range of shallow marine to coastal depositional environments. The Fruholmen Formation is interpreted to represent the overall progradation of a delta system, with a low-order transgressive occurrence at the top. A transgressive lag marks the Triassic-Jurassic boundary, representing 10s of millions of years of missing time. The Nordmela Formation records the migration of a tidal dune complex, whereas the Stø Formation is interpreted to be upper shoreface deposits, reflected in its markedly clean character.
- The primary pore reducing factor is determined to be mechanical compaction. Mechanical compaction has been more significant in the Fruholmen Formation, probably due to higher quantities of ductile grains and matrix, as well as holding more angular grains with less sphericity as opposed to the Nordmela and Stø formations.
- The secondary reducing reservoir quality factor is early diagenesis, specifically kaolinite precipitation and calcite cementation. Kaolinite is particularly abundant throughout the Fruholmen Formation, diminishing reservoir quality.
- Estimated geothermal gradient combined with the uplift estimation of 1480 m in Wisting Central III suggests that Realgrunnen Subgroup sandstones have a maximum burial temperature of 70-80℃. However, presence of chlorite cement ascertains that temperatures reached at least 80℃. Results show the interval has been in the chemical compaction domain. Petrographic results and CL analysis show quartz cementation, which is estimated to not exceed 5%. The smectite to illite reaction had also initiated, seen in fibrous textures and microquartz within the mud rock fragments.
- Evaluation of reservoir properties with petrographic results and core plug data show that the Jurassic Nordmela and Stø Formations have ‘very good’ reservoir quality.
- Evaluation of reservoir properties with petrographic results and core plug data show that the Late Triassic Fruholmen Formation has ‘poor’ to ‘good’ reservoir properties, with dependence on depositional environment. ‘Poor’ qualities seen in FA1, FA4 and FA7 are attributed primarily to high quantities of depositional clay. The ‘Poor’ quality in FA2 is due to low permeability values, which are not seen to commonly surpass the ‘fair’ cutoff. FA3, FA5, and FA6 class as ‘fair’, ‘poor’ to ‘good’, and ‘good’ respectively.
- In general, reservoir quality in Wisting Central III is shown to be better than in Gemini North.

# Chapter 8: Further Work

Several areas of improvement, with the use of data acquired as well as with additional analyses, are recommended to improve the characterization of the Realgrunnen Subgroup and to understand lateral variations in the vicinity of the Wisting field.

With acquired dataset:

- Great potential remains in the comparison of the results from Wisting Central III and Gemini North. Ideally all textural and mineralogical parameters would be compared and further related to the resultant porosity and permeability. Moreover, comparison across the entirety of the Wisting field would be advantageous. Petrographic data is available from Wisting Central (7324/8-1), Hanssen (7324/7-2), and Mercury (7324/9-1). The most natural next step in this study would be to compare core plug data and the textural and mineralogical parameters between all these datasets.
- SEM analysis of a sample from the Akkar Member would be useful to observe chlorite coating.

Other analyses:

- Heavy mineral analyses (e.g. zircon) to increase understanding of provenance and paleodrainage patterns.
- Clay XRD analysis for accurately differentiating and quantifying clays
- Fluid inclusions found in quartz grains may be utilized to estimate precipitation rates of quartz cement and for establishing detailed thermal histories of rocks (fluid inclusion geothermometry)
- A more extensive cathode luminescence analysis with emphasis on quartz cement may aid in more precisely determining intergranular volumes. Point counted values underestimate quartz cement due to difficulties in distinguishing between detrital quartz grains and cement in optical microscopy.
- TEM analysis may be used to determine the precursor clay mineral to the chlorite coating (speculated to be smectite)

# References

Abercrombie, H. J., Hutcheon, I. E., Bloch, J. D., & Caritat, P. D. (1994). Silica activity and the smectite-illite reaction. *Geology*, *22*(6), 539-542.

Adams, A., MacKenzie, W., & Guilford, C. (1984). *Atlas of sedimentary rocks under the microscope*. Harlow: Longman.

Ali, S.A., Clark, W.J., Moore, W.R., & Dribus, J.R. (2010). Diagenesis and Reservoir Quality. *Oilfield Review*, *22* (2), 14-27.

Allen, J. R. L. (1980). Sand waves: a model of origin and internal structure. *Sedimentary Geology*, *26*(4), 281-328.

Allen, G. P., & Posamentier, H. W. (1993). Sequence stratigraphy and facies model of an incised valley fill; the Gironde Estuary, France. *Journal of Sedimentary Research*, *63*(3), 378-391.

Allison, M.A., Kineke, G.C., Gordon, E. S., & Goni, M.A. (2000). Development and reworking of a seasonal flood deposit on the inner continental shelf off the Atchafalaya River. *Continental Shelf Research*, *20*(16), 2267-2294.

Anell, I., Midtkandal, I., & Braathen, A. (2014a). Trajectory analysis and inferences on geometric relationships of an Early Triassic prograding clinoform succession on the northern Barents Shelf. *Marine and Petroleum Geology*, *54*, 167-179.

Anell, I. M., Braathen, A., & Olaussen, S. (2014b). The Triassic–Early Jurassic of the northern Barents Shelf: a regional understanding of the Longyearbyen CO2 reservoir. *Norsk Geologisk Tidsskrift*, *94*, 83-98.

Baig, I., Faleide, J.I., Jahren, J.S., & Mondol, N.H. (2016). Cenozoic exhumation on the southwestern Barents Shelf: Estimates and uncertainties constrained from compaction and thermal maturity analyses. *Marine and Petroleum Geology*, *73*(C), 105-130.

Bates, C. C. (1953). Rational theory of delta formation. *AAPG Bulletin*, *37*(9), 2119-2162.

Beard, D. C., & Weyl, P. K. (1973). Influence of texture on porosity and permeability of unconsolidated sand. *AAPG bulletin*, *57*(2), 349-369.

Benton, M., & Harper, D. (1997). *Basic palaeontology*. Harlow: Longman.

Bergan, M., & Knarud, R. (1993). Apparent changes in clastic mineralogy of the Triassic–Jurassic succession, Norwegian Barents Sea: Possible implications for palaeodrainage and subsidence. In *Norwegian Petroleum Society Special Publications* (Vol. 2, pp. 481-493).

Berner, R. A. (1984). Sedimentary pyrite formation: an update. *Geochimica et cosmochimica Acta*, *48*(4), 605-615.

Bhattacharya, J. P., & MacEachern, J. A. (2009). Hyperpycnal rivers and prodeltaic shelves in the Cretaceous seaway of North America. *Journal of Sedimentary Research*, *79*(4), 184-209.

Blatt, H., Tracy, R., & Owens, B. (2006). *Petrology: igneous, sedimentary, and metamorphic*. New York, NY: Freeman.

Bjørkum, P. A. (1996). How important is pressure in causing dissolution of quartz in sandstones? *Journal of Sedimentary Research*, *66*(1), 147-154.

Bjørkum, P. A., Oelkers, E. H., Nadeau, P. H., Walderhaug, O., & Murphy, W. M. (1998). Porosity prediction in quartzose sandstones as a function of time, temperature, depth, stylolite frequency, and hydrocarbon saturation. *AAPG bulletin*, *82*(4), 637-648.

Bjørlykke, K., & Aagaard, P. (1992). Clay minerals in North Sea sandstones. In Houseknecht, D. & Pittman, E. (Eds), *Origin, Diagenesis, and Petrophysics of Clay Minerals in Sandstones.* Tulsa, OK: Society for Sedimentary Geology.

Bjørlykke, K., & Egeberg, P. K. (1993). Quartz cementation in sedimentary basins. *AAPG bulletin*, *77*(9), 1538-1548.

Bjørlykke, K., Aagaard, P., Egeberg, P. K., & Simmons, S. P. (1995). Geochemical constraints from formation water analyses from the North Sea and the Gulf Coast Basins on quartz, feldspar and illite precipitation in reservoir rocks. *Geological Society, London, Special Publications*, *86*(1), 33-50.

Bjørlykke, K. (1998). Clay mineral diagenesis in sedimentary basins—a key to the prediction of rock properties. Examples from the North Sea Basin. *Clay minerals*, *33*(1), 15-34.

Bjørlykke, K. (2015). Sedimentary Geochemistry: How sediments are produced. In Bjørlykke, K. (Ed.), *Petroleum Geoscience: From Sedimentary Environments to Rock Physics* (2nd Ed.) (pp. 301-318). Berlin: Springer

Bjørlykke, K. H., Høeg, K., & Mondol, N. (2015). Introduction to geomechanics: Stress and strain in sedimentary basins. In Bjørlykke, K. (Ed.), *Petroleum Geoscience: From Sedimentary Environments to Rock Physics* (2nd Ed.) (pp. 301-318). Berlin: Springer

Bjørlykke, K., & Jahren, J. (2015). Sandstones and Sandstone Reservoirs. In Bjørlykke, K. (Ed), *Petroleum Geoscience: From Sedimentary Environments to Rock Physics* (2nd Ed.) (pp. 119-149). Berlin: Springer

Bjørnebye, V. (*in prep*) *Characterization of a Jurassic Transgressive Lag Deposit in the SW Barents Sea* (Master's thesis)

Boggs Jr, S., & Boggs, S. (2009). *Petrology of sedimentary rocks*. Cambridge university press.

Boles, J. R., & Franks, S. G. (1979). Clay diagenesis in Wilcox sandstones of Southwest Texas; implications of smectite diagenesis on sandstone cementation. *Journal of Sedimentary Research*, *49*(1), 55-70.

Bourgeois, J. (1980). A transgressive shelf sequence exhibiting hummocky stratification; the Cape Sebastian Sandstone (Upper Cretaceous), southwestern Oregon. *Journal of Sedimentary Research*, *50*(3), 681-702.

Breivik, A.J., Faleide, J.I., & Gudlaugsson, S.T., (1998). *Crustal structure and development of the SW Barents Sea and the adjacent continental margin.* Doctor Scientiarum Thesis, University of Oslo, Norway.

Buatois, L. A., Santiago, N., Herrera, M., Plink-Bjorklund, P., Steel, R., Espin, M., & Parra, K. (2012). Sedimentological and ichnological signatures of changes in wave, river and tidal influence along a Neogene tropical deltaic shoreline. *Sedimentology*, *59*(5), 1568-1612.

Bue, E. P., & Andresen, A. (2014). Constraining depositional models in the Barents Sea region using detrital zircon U–Pb data from Mesozoic sediments in Svalbard. *Geological Society, London, Special Publications*, *386*(1), 261-279.

Burley, S.D., Kantorowicz, J.D. and Waugh, B., 1985. Clastic diagenesis. *Geological Society, London, Special Publications*, *18*(1), pp.189-226.

Busenberg, E., & Clemency, C. V. (1976). The dissolution kinetics of feldspars at 25 C and 1 atm CO2 partial pressure. *Geochimica et Cosmochimica Acta*, *40*(1), 41-49.

Chang, T. S., Flemming, B. W., & Bartholomä, A. (2007). Distinction between sortable silts and aggregated particles in muddy intertidal sediments of the East Frisian Wadden Sea, southern North Sea. Sedimentary Geology, 202(3), 453-463.

Chuhan, F. A., Kjeldstad, A., Bjørlykke, K., & Høeg, K. (2003). Experimental compression of loose sands: relevance to porosity reduction during burial in sedimentary basins. *Canadian Geotechnical Journal*, *40*(5), 995-1011.

Clark, A. F. (2017). *Reservoir characterization of the Fruholmen and Stø Formations in the Hoop Fault Complex, SW Barents Sea* (Master's thesis).

Curtis, C. D. (1977). Geochemistry: Sedimentary geochemistry: environments and processes dominated by involvement of an aqueous phase. *Philosophical Transactions of the Royal Society of London. Series A, Mathematical and Physical Sciences*, *286*(1336), 353-372.

Curtis, C. D., & Coleman, M. L. (1986). Controls on the precipitation of early diagenetic calcite, dolomite and siderite concretions in complex depositional sequences. In Gautier, D. L. (Ed.), *Roles of Organic Matter in Sediment Diagenesis: Based on a symposium sponsored by the Society of Economic Paleontologists and Mineralogists, 38* (pp. 23-33.) Tulsa, OK: Society of Economic Paleontologists and Mineralogists.

Dalland, A., Worsley, D., and Ofstad, K. (1988). A lithostratigraphic scheme for the Mesozoic and Cenozoic succession offshore mid- and northern Norway. *NPD Bulletin, 4.*

Dalrymple, R. W., Zaitlin, B. A., & Boyd, R. (1992). Estuarine facies models; conceptual basis and stratigraphic implications. *Journal of Sedimentary Research*, *62*(6), 1130-1146.

Dalrymple, R. (2010) Tidal Depositional Systems. In: James, N, Dalrymple R. (Eds.) *Facies Models 4* (pp. 201-231). St. John's: Geological Society of Canada.

De Ros, L. F., Anjos, S. M., & Morad, S. (1994). Authigenesis of amphibole and its relationship to the diagenetic evolution of Lower Cretaceous sandstones of the Potiguar rift basin, northeastern Brazil. *Sedimentary Geology*, *88*(3-4), 253-266.

Dixon, J. F., Steel, R. J., & Olariu, C. (2013). A model for cutting and healing of deltaic mouth bars at the shelf edge: mechanism for basin-margin accretion. *Journal of Sedimentary Research*, *83*(3), 284-299.

Dott, R. H. (1964). Wacke, graywacke and matrix; what approach to immature sandstone classification?. *Journal of Sedimentary Research*, *34*(3), 625-632.

Dott Jr, R. H., & Bourgeois, J. (1982). Hummocky stratification: significance of its variable bedding sequences. *Geological Society of America Bulletin*, *93*(8), 663-680.

Doré, A. G. (1995). Barents Sea Geology, Petroleum Resources and Commercial Potential. *Arctic*, 207-221.

Doré, A. G., & Jensen, L. N. (1996). The impact of late Cenozoic uplift and erosion on hydrocarbon exploration: offshore Norway and some other uplifted basins. *Global and Planetary Change*, *12*(1-4), 415-436.

Dumas, S., Arnott, R. W. C., & Southard, J. B. (2005). Experiments on oscillatory-flow and combined-flow bed forms: implications for interpreting parts of the shallow-marine sedimentary record. *Journal of Sedimentary research*, *75*(3), 501-513.

Dypvik, H. (1979). Mineralogy and geochemistry of the Mesozoic sediments of Andøya, Northern Norway. *Sedimentary Geology*, *24*(1-2), 45-67.

Egeberg, P. K., & Aagaard, P. (1989). Origin and evolution of formation waters from oil fields on the Norwegian shelf. *Applied Geochemistry*, *4*(2), 131-142.

Ehrenberg, S. N. (1993). Preservation of anomalously high porosity in deeply buried sandstones by grain-coating chlorite: examples from the Norwegian continental shelf. *AAPG Bulletin*, *77*(7), 1260-1286.

Ehrenberg, S. N., Nielsen, E. B., Svånå, T. A. & Stemmerik, L. 1998a. Depositional evolution of the Finnmark carbonate platform, Barents Sea: results from wells 7128/6-1 and 7128/4-1. *Norwegian Journal of Geology*, 78, 185–224.

Emery, D., & Myers, K. (Eds.). (2009). *Sequence stratigraphy*. Malden, MA: Blackwell Publishing.

Faleide, J. I., Gudlaugsson, S. T., & Jacquart, G. (1984). Evolution of the western Barents Sea. *Marine and Petroleum Geology*, *1*(2), 123-150.

Faleide, J. I., Vågnes, E., & Gudlaugsson, S. T. (1993). Late Mesozoic-Cenozoic evolution of the south-western Barents Sea in a regional rift-shear tectonic setting. *Marine and Petroleum Geology*, 10(3), 186-214.

Faleide, J., Tsikalas, F., Breivik, A., Mjelde, R., Ritzmann, O., Engen, O., Wilson, J., Eldholm, O. (2008). Structure and evolution of the continental margin off Norway and Barents Sea. *Episodes*, *31*(1), 82-91.

Faleide, J.I., Bjørlykke, K. & Gabrielsen, R.H. (2015). Geology of the Norwegian Continental Shelf. In Bjørlykke, K. (Ed), *Petroleum Geoscience: From Sedimentary Environments to Rock Physics* (2nd Ed.) (pp.603-635). Berlin: Springer

Fan, D., Li, C., Wang, D., Wang, P., Archer, A. W., & Greb, S. F. (2004). Morphology and sedimentation on open-coast intertidal flats of the Changjiang Delta, China. *Journal of Coastal Research*, 23-35.

Feo-Codecido, G. (1956). Heavy-mineral techniques and their application to Venezuelan stratigraphy. *AAPG Bulletin*, *40*(5), 984-1000.

Fleming, E. J., Flowerdew, M. J., Smyth, H. R., Scott, R. A., Morton, A. C., Omma, J. E., Frei, D. & Whitehouse, M. J. (2016). Provenance of Triassic sandstones on the southwest Barents Shelf and the implication for sediment dispersal patterns in northwest Pangaea. *Marine and Petroleum Geology*, *78*, 516-535.

Flemming B.W. (2012). Siliciclastic Back-Barrier Tidal Flats. In Davis Jr., R., Dalrymple, R. (Eds.) *Principles of Tidal Sedimentology*. Dordrecht: Springer

Folk, R. L. (1980). *Petrology of sedimentary rocks*. Austin, TX: Hemphill

Gabrielsen, R.H., Færseth, R.B., Jensen, L.N., Kalheim, J.E. & Riis, F. (1990). Structural elements of the Norwegian continental shelf. Part I: The Barents Sea Region, *Norwegian Petroleum Directorate Bulletin No 6*. 5-32

Gabrielsen, R. H., Sokoutis, D., Willingshofer, E., & Faleide, J. I. (2016). Fault linkage across weak layers during extension: an experimental approach with reference to the Hoop Fault Complex of the SW Barents Sea. *Petroleum Geoscience*, *22*(2), 123-135.

Gernigon, L., & Brönner, M. (2012). Late Palaeozoic architecture and evolution of the southwestern Barents Sea: insights from a new generation of aeromagnetic data. *Journal of the Geological Society*, *169*(4), 449-459.

Gernigon, L., Brönner, M., Roberts, D., Olesen, O., Nasuti, A. & Yamasaki, T. (2014). Crustal and basin evolution of the southwestern Barents Sea: From Caledonian orogeny to continental breakup. *Tectonics*, 33(4), pp. 347–373. doi: 10.1002/2013TC003439.

Gjelberg, J., Dreyer, T., Høie, A., Tjelland, T., Lilleng, T., Brooks, J., & Glennie, K. (1987). Late Triassic to Mid-Jurassic Sandbody development on the Barents and Mid-Norwegian shelf. *Petroleum Geology of North West Europe*, 1105-1129

Glørstad-Clark, E., Faleide, J.I., Lundschien, B.A. & Nystuen, J.P. 2010. Triassic seismic sequence stratigraphy and paleogeography of the western Barents Sea Area. *Marine and Petroleum Geology*, 27(7), 1448-1475.

Google. (n.d.). Barents Sea. Retrieved May 10, 2019 from https://www.google.com/maps/place/Barents+Sea/@71.8923521,19.8790861,4z/data=!3m1!4b1!4m5!3m4!1s0x4454b138bab4d2d1:0x8826e47cd19038f0!8m2!3d74.9883921!4d37.1063683

Google Earth, ed. (May 10, 2019).

Gudlaugsson, S.T., Faleide, J.I., Johansen, S.E. & Breivik, A.J. 1998. Late Palaeozoic structural development of the south-western Barents Sea. *Marine and Petroleum Geology*. 15, 73-102.

Gyenis, T. (2016). *Reservoir Quality of the Triassic Snadd and Kobbe Formations in the Barents Sea* (Master's thesis).

Halland, E. K., Mujezinovic, J., and Riis, F. (2014). CO2 Storage Atlas: Norwegian Continental Shelf, *Norwegian Petroleum Directorate.*

Hansen, H. N., Løvstad, K., Müller, R. & Jahren, J.S. (2017). Clay coating preserving high porosities in deeply buried intervals of the Stø Formation. *Marine and Petroleum Geology, 88*, 648-658.

Harrison, C., & St-Onge, M. R. (2008). *Geological map of the Arctic*. Geological Survey of Canada, Map 2159A, scale 1:5000000.

Haq, B. U., Hardenbol, J., & Vail, P. R. (1987). Chronology of fluctuating sea levels since the Triassic. *Science*, *235*(4793), 1156-1167.

Heafford, A.P., (1988). Carboniferous through Triassic stratigraphy of the Barents Shelf. In W.B. Harland and E.K. Dowdeswell (Eds.), *Geological Evolution of the Barents Shelf Region.* Graham and Trotman, London, pp. 89-108.

Heald, M. T., & Larese, R. E. (1974). Influence of coatings on quartz cementation. *Journal of Sedimentary Research*, *44*(4), 1269-1274.

Henriksen, E., Bjørnseth, H. M., Hals, T. K., Heide, T., Kiryukhina, T., Kløvjan, O. S., Larssen, G. B., Ryseth, A. E., Rønning, K., Sollid, K., and Stoupakova, A. (2011a). Uplift and erosion of the greater Barents Sea: impact on prospectivity and petroleum systems. *Geological Society of London: Memoirs*, 35(1), 271-281.

Henriksen, E., Ryseth, A. E., Larssen, G. B., Heide, T., Rønning, K., Sollid, K., and Stoupakova, A. V. (2011b). Tectonostratigraphy of the greater Barents Sea: implications for petroleum systems. *Geological Society of London: Memoirs*, 35(1), 163-195.

Hochuli, P. A., & Vigran, J. O. (2010). Climate variations in the Boreal Triassic—inferred from palynological records from the Barents Sea. *Palaeogeography, Palaeoclimatology, Palaeoecology*, *290*(1-4), 20-42.

Houseknecht, D. W. (1987). Assessing the relative importance of compaction processes and cementation to reduction of porosity in sandstones. *AAPG bulletin*, *71*(6), 633-642.

Ilagan, T.G. (2018). *Reservoir characterization of the Realgrunnen Subgroup in Wells 7124/3-1, 7220/7-2S and 7324/9-1 in SW Barents* (Master's thesis).

Indrevær, K., Gabrielsen, R. H., & Faleide, J. I. (2017). Early Cretaceous synrift uplift and tectonic inversion in the Loppa High area, southwestern Barents Sea, Norwegian shelf. *Journal of the Geological Society, 174*(2), 242-254.

James, N. P., & Dalrymple, R. W. (Eds.). (2010). *Facies models 4.* Canada: Geological association of Canada.

Jakobsson, M., Mayer, L.A., Coakley, B., Dowdeswell, J.A., Forbes, S., Fridman, B., Hodnesdal H., Noormets, R., Pedersen, R., M. Rebesco, Schenke, H.W., Zarayskaya, Y., Accettella, A.D., Armstrong, A., Anderson, R.M., Bienhoff, P., Camerlenghi, A, Church, I., Edwards, M., Gardner, J.V., Hall, J. K., Hell, B. ,Hestvik, O.B., Kristoffersen, Y., Marcussen, C., Mohammad, R., Mosher, D., Nghiem, S.V., Pedrosa, M.T., Travaglini, P.G., & Weatherall, P. (2012). The International Bathymetric Chart of the Arctic Ocean (IBCAO) Version 3.0, *Geophysical Research*

*Letters*, doi: *10.1029/2012GL052219*.
[*Auxiliary Material*]

Jahren, J. S., & Aagaard, P. (1989). Compositional variations in diagenetic chlorites and illites, and relationships with formation-water chemistry. *Clay Minerals*, *24*(2), 157-170.

Jahren, J., Ramm, M., Worden, R. H., & Morad, S. (2000). The porosity-preserving effects of microcrystalline quartz coatings in arenitic sandstones: Examples from the Norwegian continental shelf. In Worden, R.H & Morad, S. (Eds), *Quartz Cementation in Sandstones* (pp. 271-280) Oxfrod, UK: Blackwell Publishing

Jerram, D. A. (2001). Visual comparators for degree of grain-size sorting in two and three-dimensions. *Computers and geosciences*, *4*(27), 485-492.

Klausen, T. G., Ryseth, A. E., Helland-Hansen, W., Gawthorpe, R., & Laursen, I. (2015). Regional development and sequence stratigraphy of the Middle to Late Triassic Snadd formation, Norwegian Barents Sea. *Marine and Petroleum Geology*, *62*, 102-122.

Klausen, T. G., Müller, R., Sláma, J., & Helland-Hansen, W. (2017). Evidence for Late Triassic provenance areas and Early Jurassic sediment supply turnover in the Barents Sea Basin of northern Pangea. *Lithosphere*, *9*(1), 14-28.

Klausen, T. G., Müller, R., Sláma, J., Olaussen, S., Rismyhr, B., & Helland-Hansen, W. (2018). Depositional history of a condensed shallow marine reservoir succession: stratigraphy and detrital zircon geochronology of the Jurassic Stø Formation, Barents Sea. *Journal of the Geological Society*, *175*(1), 130-145.

Knaust, D. (2017). *Atlas of trace fossils in well core: appearance, taxonomy and interpretation*. Cham: Springer.

Koevoets, M. J., Hammer, Ø. Olaussen, S., Senger, K., & Smelror, M. (2018). Integrating subsurface and outcrop data of the middle Jurassic to Lower Cretaceous Agardhfjellet formation in central Spitsbergen. *Norwegian Journal of Geology*, *98*(4), 1-34.

Kordi, M., Turner, B., & Salem, A. M. (2011). Linking diagenesis to sequence stratigraphy in fluvial and shallow marine sandstones: Evidence from the Cambrian–Ordovician lower sandstone unit in southwestern Sinai, Egypt. *Marine and Petroleum Geology*, *28*(8), 1554-1571.

Kuehl, S. A., DeMaster, D. J., & Nittrouer, C. A. (1986). Nature of sediment accumulation on the Amazon continental shelf. *Continental Shelf Research*, *6* (1-2), 209-225.

Larsen, R. M., Fjaeran, T., and Skarpnes, O. (1993). Hydrocarbon potential of the Norwegian Barents Sea based on recent well results. *Norwegian Petroleum Society Special Publications*, 321-331.

Larssen, G. B., Elvebakk, G., Henriksen, L. B., Kristensen, S. E., Nilsson, I., Samuelsberg, T. J., Svånå, L., Stemmerik, L., & Worsley, D. (2002). Upper Palaeozoic Lithostratigraphy of the Southern Norwegian Barents Sea. *Norwegian Petroleum Directorate Bulletin*, 9, 76.

Line, L.H. (2015) *Reservoir Characterization of the Middle-Upper Triassic Kobbe and Snadd Formations in the southwestern Barents Sea* (Master's thesis).

MacEachern, J. A., Bann, K. L., Bhattacharya, J. P., & Howell Jr, C. D. (2005). Ichnology of deltas: organism responses to the dynamic interplay of rivers, waves, storms, and tides. In Gioson, L., Bhattacharya, J.P. (Eds.), *River Deltas: Concepts Models and Examples* (pp. 49-85). SEPM Special Publications, vol. 83. Tulsa, OK: SEPM.

Mahajan, A., Gabrielsen, R. H., & Faleide, J. I. (2014). Structural Evolution Using 3D Seismic of Hoop Fault Complex, SW Barents Sea Norway. In *Conference Arctic Energy Tromso, Vol. NGF Abstr. Proc. 2014* (Vol. 2).

Marcilly, C. F. M. (2016). *Reservoir characterization of the Upper Triassic Snadd Formation in the southwestern Barents Sea* (Master's thesis).

Matlack, K. S., Houseknecht, D. W., & Applin, K. R. (1989). Emplacement of clay into sand by infiltration. *Journal of Sedimentary Research*, *59*(1), 77-87.

Matter, A., & Ramseyer, K. (1985). Cathodoluminescence microscopy as a tool for provenance studies of sandstones. In *Provenance of arenites* (pp. 191-211). Dordrecht:Springer

McKinley, J. M., Worden, R. H., Ruffell, A. H., & Morad, S. (2003). Smectite in sandstones: a review of the controls on occurrence and behaviour during diagenesis. In Worden, R. H. & Morad, S. (Eds.) *Clay Mineral Cements in Sandstones* (Vol. 34, pp. 109-128). Malden, MA: Blackwell Publishing.

Mondol, N. H. (2009). Porosity and permeability development in mechanically compacted silt-kaolinite mixtures. In *SEG Technical Program Expanded Abstracts 2009* (pp. 2139-2143). Society of Exploration Geophysicists.

Mondol, N. H. (2015). Well logging: Principles, Applications and Uncertainties. In Bjørlykke, K. (Ed), *Petroleum Geoscience: From Sedimentary Environments to Rock Physics* (2nd Ed). Berlin: Springer.

Moore, D. M., & Reynolds, R. C. (1989). *X-ray Diffraction and the Identification and Analysis of Clay Minerals* (Vol. 322, p. 321). Oxford: Oxford University Press.

Mørk, A., Knarud, R. and Worsley, D. (1982). Depositional and diagenetic environments of the Triassic and Lower Jurassic succession of Svalbard. In Embry, A.F. and Balkwill, H. R. (Eds.), *Arctic Geology and Geophysics* (pp. 371-398) Calgary: Canadian Society of Petroleum Geologists.

Mørk, M. B. E. (1999). Compositional variations and provenance of Triassic sandstones from the Barents Shelf. *Journal of Sedimentary Research*, *69*(3), 690-710.

Mueller, S., Hounslow, M. W., & Kürschner, W. M. (2016). Integrated stratigraphy and palaeoclimate history of the Carnian Pluvial Event in the Boreal realm; new data from the Upper Triassic Kapp Toscana Group in central Spitsbergen (Norway). *Journal of the Geological Society*, *173*(1), 186-202.

Mulder, T., & Syvitski, J. P. (1995). Turbidity currents generated at river mouths during exceptional discharges to the world oceans. *The Journal of Geology*, *103*(3), 285-299.

Müller, R., Klausen, T. G., Faleide, J. I., Olaussen, S., Eide, C. H., & Suslova, A. (2019). Linking regional unconformities in the Barents Sea to compression-induced forebulge uplift at the Triassic-Jurassic transition. *Tectonophysics*.

Mulrooney, M. J., Rismyhr, B., Yenwongfai, H. D., Leutscher, J., Olaussen, S., & Braathen, A. (2018). Impacts of small-scale faults on continental to coastal plain deposition: Evidence from the Realgrunnen Subgroup in the Goliat field, southwest Barents Sea, Norway. *Marine and Petroleum Geology*, *95*, 276-302.

Neill, C. F., & Allison, M. A. (2005). Subaqueous deltaic formation on the Atchafalaya Shelf, Louisiana. *Marine Geology*, *214*(4), 411-430.

Nichols, G. (2009). *Sedimentology and stratigraphy* (2nd Ed.). Chichester: Wiley-Blackwell.

Nøttvedt, A., Cecchi, M., Gjelberg, J. G., Kristensen, S. E., Lønøy, A., Rasmussen, A., Rasmussen, P.H., Skott, P.M., & Van Veen, P. M. (1993). Svalbard-Barents Sea correlation: a short review. In *Norwegian Petroleum Society Special Publications* (Vol. 2, pp. 363-375). Elsevier.

NPD (2019). FactPages. Norwegian Petroleum Directorate. Available from: http://factpages.npd.no/FactPages/Default.aspx?culture=en [Accessed 20.02.2019].

Ohm, S. E., Karlsen, D. A., & Austin, T. J. F. (2008). Geochemically driven exploration models in uplifted areas: Examples from the Norwegian Barents Sea. *AAPG Bulletin*, *92*(9), 1191-1223.

Olariu, C., Steel, R. J., Dalrymple, R. W., & Gingras, M. K. (2012). Tidal dunes versus tidal bars: The sedimentological and architectural characteristics of compound dunes in a tidal seaway, the lower Baronia Sandstone (Lower Eocene), Ager Basin, Spain. *Sedimentary Geology*, *279*, 134-155.

Olaussen, S., Dalland, A., Gloppen, T. G., & Johannessen, E. (1984). Depositional environment and diagenesis of Jurassic reservoir sandstones in the eastern part of Troms I area. In *Petroleum Geology of the North European Margin* (pp. 61-79). Springer, Dordrecht.

Ollier, C.D., (1983). *Weathering* (2nd Ed.). London: Longman.

OMV. (2019a). Wisting. Available from: https://www.omv.no/en-no/aktiviteter/wisting-discovery [Accessed 25.02.2019].

OMV. (2019b). Increased Wisting Volumes. Available from: https://www.omv.com/en/news/190114-increased-wisting-volumes [Accessed 25.02.2019].

Omma, J. E., Pease, V., & Scott, R. A. (2011). U–Pb SIMS zircon geochronology of Triassic and Jurassic sandstones on northwestern Axel Heiberg Island, northern Sverdrup Basin, Arctic Canada. *Geological Society of London, Memoirs*, *35*(1), 559-566.

Paxton, S. T., Szabo, J. O., Ajdukiewicz, J. M., & Klimentidis, R. E. (2002). Construction of an intergranular volume compaction curve for evaluating and predicting compaction and porosity loss in rigid-grain sandstone reservoirs. *AAPG bulletin*, *86*(12), 2047-2067.

Pettijohn, F. J., Potter, P. E., & Siever, R. (2012). *Sand and sandstone*. Springer Science & Business Media.

Pittman, E. D., & Larese, R. E. (1991). Compaction of lithic sands: experimental results and applications (1). *AAPG Bulletin*, *75*(8), 1279-1299.

Polkin, Y. I. (1974). Novaya Zemlya-Pay-Khoi Fold system. *Struktura Fundamenta Platformennykh Oblastey SSSR: Nauka, Leningrad, USSR*, 253-258. (In Russian).

Porten, H.W. (2012). *Petrography, diagenesis, and reservoir quality of the triassic Fruholmen, Snadd, and Kobbe formations, southern Barents Sea* (Master's thesis).

Powers, M. C. (1953). A new roundness scale for sedimentary particles. *Journal of Sedimentary Research*, *23*(2), 117-119.

Reading, H. G., & Levell, B. K. (1996). Controls on the sedimentary rock record. *Sedimentary environments: processes, facies and stratigraphy*, 5-36.

Reed, S. J. B. (2005) 'Electron microprobe analysis and scanning electron microscopy in geology'. Cambridge: Cambridge University Press.

Reineck, H. E., & Wunderlich, F. (1968). Classification and origin of flaser and lenticular bedding. *Sedimentology*, *11*(1-2), 99-104.

Reineck, H. E., & Singh, I. B. (1980). Tidal flats. In *Depositional Sedimentary Environments* (pp. 430-456). Springer, Berlin, Heidelberg.

Rider, M. H. (1986). *The geological interpretation of well logs.* New York, NY: John Wiley and Sons.

Ritzmann, O., & Faleide, J. I. (2009). The crust and mantle lithosphere in the Barents Sea/Kara Sea region. *Tectonophysics*, *470*(1-2), 89-104.

Ronkina, Z.Z., Vishnevskaya, T.N. and Efremova, V.l., (1985). Vescestvennyj sostav mezozojskich ottozenij ostrovo Kolguev (Substance composition of the Mesozoic deposits of the island of Kolgujev). *Geologiceskoe stroenie Barencevo-Karskoga sel'fa (Geological Structure of the Barents-Kara Shelf, Collection of Scientific Papers).* (In Russian)

Ryseth, A. (2014). Sedimentation at the Jurassic–Triassic boundary, south-west Barents Sea: indication of climate change. *From Depositional Systems to Sedimentary Successions on the Norwegian Continental Margin*, *187*, 214.

Sales, J. K. (1993). Closure vs. seal capacity-A fundamental control on the distribution of oil and gas. *Basin modeling: Advances and application: Norwegian Petroleum Society (NPF) Special Publication*, 3, 399-414.

Slater, S. M., McKie, T., Vieira, M., Wellman, C. H., & Vajda, V. (2017). Episodic river flooding events revealed by palynological assemblages in Jurassic deposits of the Brent Group, North Sea. *Palaeogeography, Palaeoclimatology, Palaeoecology*, *485*, 389-400.

Skretting, S.R. (*in prep*). *Reservoir Characterization of the Realgrunnen Subgroup (Fruholmen and Stø Formations) in well 7325/4-1 within the Hoop Fault Complex* (Master's thesis)

Smelror, M., Petrov, O., Larssen, G. B. & Werner, S. (2009). Geological history of the Barents Sea. *Norges Geologiske Undersøkelse.*

Sneed, E. D., & Folk, R. L. (1958). Pebbles in the lower Colorado River, Texas a study in particle morphogenesis. *The Journal of Geology*, *66*(2), 114-150.

Stemmerik, L., & Worsley, D. (2005). 30 years on-Arctic Upper Palaeozoic stratigraphy, depositional evolution and hydrocarbon prospectivity. *Norwegian Journal of Geology/Norsk Geologisk Forening*, *85*.

Swapp, S. (2019). Scanning Electron Microscopy (SEM). Available from: https://serc.carleton.edu/research_education/geochemsheets/techniques/SEM.html [Accessed 12.03.2019].

Tamrakar, N. K., Yokota, S., & Shrestha, S. D. (2007). Relationships among mechanical, physical and petrographic properties of Siwalik sandstones, Central Nepal Sub-Himalayas. *Engineering Geology*, *90*(3-4), 105-123.

Taylor, J.M., 1950. Pore space reduction in sandstone. *Bulletin of the American Association of Petroleum Geologists* 34, 701–716.

Thyberg, B., Jahren, J., Winje, T., Bjørlykke, K., Faleide, J. I., & Marcussen, Ø. (2010). Quartz cementation in Late Cretaceous mudstones, northern North Sea: changes in rock properties due to dissolution of smectite and precipitation of micro-quartz crystals. *Marine and Petroleum Geology*, *27*(8), 1752-1764.

Tissot, B. P., & Welte, D. H. (1984). *Petroleum formation and occurrence: a new approach to oil and gas exploration*. Berlin: Springer.

Ulmer-Scholle, D. S., Scholle, P. A., Schieber, J., & Raine, R. J. (2014). *A color guide to the petrography of sandstones, siltstones, shales and associated rocks*. American Association of Petroleum Geologists.

Van Houten, F. B., & Purucker, M. E. (1984). Glauconitic peloids and chamositic ooids-favorable factors, constraints, and problems. *Earth-Science Reviews*, *20*(3), 211-243.

Wadell, H. (1932). Volume, shape, and roundness of rock particles. *The Journal of Geology*, *40*(5), 443-451.

Walderhaug, O. (1996). Kinetic modeling of quartz cementation and porosity loss in deeply buried sandstone reservoirs. *AAPG bulletin*, *80*(5), 731-745.

Walderhaug, O., & Bjørkum, P. A. (1998). Calcite cement in shallow marine sandstones: growth mechanisms and geometry. In Morad, S. (Ed) *Carbonate Cementation in Sandstones: Distribution Patterns and Geochemical Evolution* (pp. 179-192). Oxford: Blackwell Science.

Walderhaug, O., Bjørkum, P. A., Nadeau, P. H., & Langnes, O. (2001). Quantitative modelling of basin subsidence caused by temperature-driven silica dissolution and reprecipitation. *Petroleum Geoscience*, *7*(2), 107-113.

Walker, R.G., & Plint, A.G. (1992). Wave- and storm-dominated shallow marine systems. In: Walker, R.G., & James, N.P. (Eds.). *Facies Models: Response to Sea Level Change*. Geological Association of Canada, p. 219–238.

Wentworth, C. K. (1922). A scale of grade and class terms for clastic sediments. *The journal of geology*, *30*(5), 377-392.

Wilkin, R. T., & Barnes, H. L. (1997). Formation processes of framboidal pyrite. *Geochimica et Cosmochimica Acta*, *61*(2), 323-339.

Williams, L. A., & Crerar, D. A. (1985). Silica diagenesis; II, General mechanisms. *Journal of Sedimentary Research*, *55*(3), 312-321.

Wilson, M. D., & Pittman, E. D. (1977). Authigenic clays in sandstones; recognition and influence on reservoir properties and paleoenvironmental analysis. *Journal of Sedimentary Research*, *47*(1), 3-31.

Wilson, M.D. (1992). Inherited grain-rimming clays in sandstones from eolian and shelf environments: their origin and control on reservoir properties. In Houseknecht, D.W. & Pittman, E.D.(Eds.) Origin, Diagenesis, and Petrophysics of Clay Minerals in Sandstones (pp.209-225). Tulsa, OK: Society for Sedimentary Geology

Worden, R. H., & Morad, S. (2003). *Clay mineral cements in sandstones*. Malden, MA: Blackwell Publishing.

Worden, R.H. & Burley, S.D. (2003). Sandstone diagenesis: the evolution of sand to stone. *Sandstone Diagenesis: Recent and Ancient*, *4*, 3-44

Worsley, D. (2008). The post-Caledonian development of Svalbard and the western Barents Sea. *Polar Research*, *27* (3), 298-317.

Wright, L.D., Wiseman, W.J., Bornhold, B.D., Prior, D.B., Suhayda, J.N., Keller, G.H., Yang, Z.S., & Fan, Y.B.(1988), Marine dispersal and deposition of Yellow River silts by gravity-driven underflows. *Nature*, v. 332, p. 629–632.

Young, S. W., (1976), Petrographic textures of detrital polycrystalline quartz as an aid to interpreting crystalline source rocks. *Journal of Sedimentary Research*, *46*(3), 595-603.

Zaitlin, B. A., Dalrymple, R. W., & Boyd, R. (1994). The stratigraphic organization of incised-valley systems associated with relative sea-level change. In*: Incised-Valley Systems: Origin and Sedimentary sequences*

Zoltai, T., & Stout, J. H. (1984). *Mineralogy: concepts and principles*. Burgess Publishing Company.

# Appendix A

Summary of well data used in this thesis from Wisting Central III (7324/8-3) (compiled from NPD, 2018).

| | |
|---|---|
| **Wellbore Name** | Wisting Central III (7324/8-3) |
| **Purpose** | Appraisal |
| **Content** | Oil |
| **Latitude and Longitude Coordinates** | 73° 26' 4" N<br>24° 23' 21.67" E |
| **UTM Zone** | 35 |
| **UTM Coordinates** | 8150984.02<br>416938.84 |
| **Structural Element** | Hoop Fault Complex |
| **Completion date** | 17.09.2017 |
| **Publication date** | 17.09.2019 |
| **KB Elevation (m)** | 23 |
| **Water Depth (m)** | 400 |
| **Total Depth (MD) (mRKB)** | 805 |
| **Bottom Hole Temperature (°C)** | 17 |

# Appendix B

Summary of samples extracted from the Wisting Central III (7324/8-3) drill core, indicated with their depth and petrographic analysis carried out. Samples saturated with oil are also marked.

KM = Kara Meunier

| Well | Formation | Sample code | Sample depth [m MD] | Bulk XRD | Clay XRD | Point Count | SEM | Oil stain |
|---|---|---|---|---|---|---|---|---|
| 7324/8-3 (Wisting Central III) | Fruholmen Fm. | V1 | 758.40 | KM | | KM | | |
| | | V2 | 756.90 | KM | | KM | | |
| | | V3 | 754.80 | KM | | KM | KM | |
| | | V4 | 748.65 | KM | | KM | | |
| | | V5 | 745.00 | KM | | KM | | |
| | | V6 | 743.65 | KM | | KM | | |
| | | V7 | 729.70 | KM | | KM | | |
| | | V8 | 719.10 | KM | | KM | KM | X |
| | | V9 | 716.62 | KM | | KM | | X |
| | | V10 | 715.44 | KM | | KM | | |
| | | V11 | 712.90 | KM | | KM | KM | X |
| | | V12 | 711.68 | KM | | KM | | |
| | | V13 | 705.10 | KM | | KM | | X |
| | | V14 | 698.10 | KM | | KM | | X |
| | | V15* | 691.35 | KM | | | | |
| | Nord. Fm. | V16 | 687.56 | KM | | KM | KM | X |
| | | V17 | 686.05 | KM | | KM | | X |
| | Stø Fm. | V18 | 680.95 | KM | | KM | KM | X |
| | | V19 | 675.51 | KM | | KM | KM | X |
| | | V20 | 666.70 | KM | | KM | | X |

* Shale/mudstone

# Appendix C

Petrophysical well logs available from Wisting Central III, provided by OMV Norge AS.

| Well Log | Wisting Central III (7324/8-3) |
|---|---|
| **Caliper** | X |
| **Bit Size** | X |
| **Gamma Ray** | X |
| **Neutron** | X |
| **Bulk Density** | X |
| **Deep Resistivity** | X |
| **Medium Resistivity** | X |
| **Shallow Resistivity** | X |
| **Sonic Compressional** | X |
| **Sonic Shear** | X |
| **Photoelectric Factor** | X |
| **Density Correction** | X |

# Appendix D

## XRD Analytical Parameters

| | |
|---|---|
| Diffractometer: | Bruker D8 ADVANCE diffractometer |
| Detector: | Lynxeye 1-dimensional position-sensitive detector (PSD) |
| Generator: | CuKα at 40mA, 40kV |
| Application: | Bulk - 0.01º/0.3s; 2º -65º (2θ) |
| | Clay Air Dried - 0.01º/0.3s; 2º -66º (2θ) |
| | Clay Treated - 0.01º/0.3s; 2º -34º (2θ) |

# Appendix E

**Table 1:** Grain size analysis and sorting results for Wisting Central III.

| Strat. | Sample | Phi Average | Wentworth Size Class | Phi Standard Deviation | Folk Sorting Class |
|---|---|---|---|---|---|
| **Akkar Mbr** | V1 | 4.20 | Course Silt | 0.44 | Well Sorted |
| | V2 | 4.02 | Course Silt | 0.40 | Well Sorted |
| **Reke Mbr.** | V3 | 3.24 | Very Fine Sand | 0.53 | Moderately Well Sorted |
| | V4 | 3.26 | Very Fine Sand | 0.48 | Well Sorted |
| | V5 | 3.12 | Very Fine Sand | 0.43 | Well Sorted |
| | V6 | 3.55 | Very Fine Sand | 0.55 | Moderately Well Sorted |
| | V7 | 3.20 | Very Fine Sand | 0.54 | Moderately Well Sorted |
| | V8 | 2.72 | Fine Sand | 0.48 | Well Sorted |
| | V9 | 2.76 | Fine Sand | 0.45 | Well Sorted |
| | V10 | 3.09 | Very Fine Sand | 0.71 | Moderately Sorted |
| | V11 | 2.99 | Fine Sand | 0.46 | Well Sorted |
| | V12 | 3.88 | Very Fine Sand | 0.62 | Moderately Well Sorted |
| | V13 | 2.75 | Fine Sand | 0.52 | Moderately Well Sorted |
| | V14 | 3.39 | Very Fine Sand | 0.47 | Well Sorted |
| **Nord. Fm.** | V16 | 2.41 | Fine Sand | 0.46 | Well Sorted |
| | V17 | 2.07 | Fine Sand | 0.37 | Well Sorted |
| **Stø Fm.** | V18 | 2.28 | Fine Sand | 0.44 | Well Sorted |
| | V19 | 2.33 | Fine Sand | 0.36 | Well Sorted |
| | V20 | 2.63 | Fine Sand | 0.34 | Very Well Sorted |

| | Sample | Quartz | | Feldspar | | | Lithic Rock Fragments | | | | | | | | | Cements | | | | | | | |
|---|---|---|---|---|---|---|---|---|---|---|---|---|---|---|---|---|---|---|---|---|---|---|---|
| | | Mono | Poly | Plag | K | Altered | Chert | Mica | Igneous | Organic | Mud Rock | Sec. Porosity | Pseudo. | Other | Matrix | Chlorite | Kaolin | Calcite | Quartz | Siderite | Total Cement | Porosity | IGV |
| Akkar Mbr | V1 | 47.33 | 3.33 | 4.67 | 0.33 | 9.00 | 0.33 | 3.00 | 3.67 | 0.00 | 1.67 | 0.33 | 1.33 | 0.67 | 6.00 | 8.33 | 3.00 | 0.00 | 0.67 | 0.67 | 12.67 | 5.67 | 24.33 |
| | V2 | 38.00 | 2.33 | 4.33 | 0.33 | 6.67 | 1.00 | 2.67 | 6.33 | 0.00 | 2.00 | 0.33 | 1.00 | 2.67 | 6.67 | 9.67 | 4.00 | 1.67 | 0.00 | 3.33 | 18.67 | 10.00 | 34.30 |
| Reke Mbr | V3 | 40.00 | 4.00 | 4.67 | 0.67 | 8.00 | 1.00 | 3.33 | 9.67 | 1.00 | 7.00 | 0.00 | 0.33 | 0.33 | 3.00 | 3.33 | 3.33 | 0.00 | 0.67 | 0.33 | 7.67 | 9.33 | 20.00 |
| | V4 | 42.00 | 3.67 | 4.00 | 0.33 | 9.00 | 0.67 | 1.33 | 8.33 | 1.67 | 5.00 | 0.00 | 0.67 | 1.00 | 2.67 | 2.00 | 4.00 | 0.00 | 0.00 | 0.00 | 6.00 | 13.67 | 22.33 |
| | V5 | 43.33 | 5.00 | 6.33 | 0.67 | 5.67 | 0.33 | 1.33 | 8.00 | 0.67 | 6.00 | 0.00 | 1.33 | 0.00 | 4.33 | 2.67 | 3.33 | 0.00 | 0.00 | 2.00 | 8.00 | 9.00 | 21.33 |
| | V6 | 43.00 | 2.00 | 5.67 | 0.33 | 7.67 | 0.00 | 1.00 | 6.00 | 0.33 | 1.67 | 0.00 | 1.67 | 0.00 | 12.33 | 2.67 | 3.33 | 0.00 | 1.00 | 0.33 | 7.33 | 11.00 | 30.67 |
| | V7 | 41.33 | 2.33 | 8.33 | 0.00 | 6.33 | 0.00 | 2.00 | 5.00 | 0.33 | 1.00 | 0.00 | 2.33 | 0.33 | 18.00 | 1.67 | 2.00 | 0.00 | 1.33 | 0.33 | 5.33 | 7.33 | 30.67 |
| | V8 | 44.00 | 3.33 | 7.33 | 1.67 | 7.00 | 0.33 | 0.00 | 9.00 | 0.00 | 1.67 | 0.67 | 2.67 | 0.00 | 1.00 | 0.67 | 2.33 | 0.00 | 1.67 | 1.00 | 5.67 | 15.67 | 22.33 |
| | V9 | 41.33 | 3.33 | 7.00 | 1.00 | 8.33 | 0.00 | 0.67 | 8.00 | 0.00 | 3.33 | 0.00 | 0.67 | 0.00 | 5.00 | 0.67 | 3.67 | 0.00 | 2.00 | 1.33 | 7.67 | 13.67 | 26.33 |
| | V10 | 42.67 | 1.67 | 4.67 | 1.33 | 5.67 | 0.00 | 0.67 | 6.00 | 0.00 | 5.00 | 0.33 | 1.00 | 0.00 | 11.67 | 1.33 | 2.33 | 0.00 | 1.33 | 0.33 | 5.33 | 14.00 | 31.00 |
| | V11 | 40.33 | 3.67 | 5.00 | 1.00 | 9.67 | 0.00 | 0.00 | 8.67 | 0.00 | 2.67 | 0.00 | 2.00 | 0.67 | 3.33 | 1.67 | 3.33 | 0.00 | 2.33 | 0.00 | 7.33 | 15.67 | 26.33 |
| | V12 | 30.33 | 1.00 | 4.33 | 1.00 | 9.33 | 0.00 | 0.67 | 6.33 | 0.00 | 6.00 | 1.33 | 1.67 | 0.00 | 1.33 | 0.00 | 3.67 | 32.67 | 0.00 | 0.00 | 36.33 | 0.33 | 38.00 |
| | V13 | 46.33 | 3.00 | 7.00 | 0.67 | 8.67 | 0.00 | 0.33 | 7.33 | 0.00 | 3.00 | 0.00 | 1.33 | 0.00 | 1.67 | 0.67 | 3.00 | 0.00 | 0.33 | 0.00 | 4.00 | 16.67 | 22.33 |
| | V14 | 42.67 | 2.33 | 6.33 | 1.00 | 5.33 | 0.00 | 2.00 | 9.33 | 0.00 | 5.33 | 0.00 | 0.67 | 0.00 | 10.00 | 0.67 | 2.00 | 0.00 | 2.00 | 0.33 | 5.00 | 10.00 | 25.00 |
| Nordmela Fm | V16 | 63.67 | 3.00 | 1.00 | 0.00 | 1.00 | 0.00 | 0.00 | 1.67 | 0.00 | 0.00 | 0.00 | 1.33 | 0.33 | 0.33 | 0.00 | 0.33 | 0.00 | 2.00 | 0.00 | 2.33 | 25.00 | 27.67 |
| | V17 | 60.67 | 4.33 | 2.00 | 0.00 | 2.33 | 0.00 | 0.00 | 1.67 | 0.00 | 0.00 | 0.67 | 0.33 | 0.00 | 0.00 | 1.33 | 0.33 | 0.00 | 1.00 | 0.00 | 2.67 | 25.33 | 28.00 |
| Stø Fm | V18 | 67.67 | 0.67 | 1.00 | 0.00 | 2.00 | 0.00 | 0.00 | 0.67 | 0.00 | 0.00 | 0.33 | 0.00 | 0.00 | 0.33 | 0.00 | 0.00 | 1.00 | 2.33 | 0.00 | 3.33 | 24.00 | 27.67 |
| | V19 | 73.33 | 1.33 | 0.33 | 0.00 | 1.00 | 0.00 | 0.00 | 0.00 | 0.00 | 0.00 | 0.33 | 0.00 | 0.00 | 0.00 | 0.33 | 0.00 | 0.00 | 1.33 | 0.00 | 1.67 | 22.00 | 23.67 |
| | V20 | 69.33 | 0.67 | 0.33 | 0.33 | 3.00 | 0.00 | 0.00 | 0.67 | 0.00 | 0.00 | 0.00 | 1.00 | 0.00 | 0.00 | 0.67 | 0.00 | 0.00 | 1.00 | 0.00 | 1.67 | 23.00 | 24.67 |

**Table 2:** Point counting results for Wisting Central III. Colours correspond to facies associations as seen in the sedimentary log. A thin section was not prepared for V15 from FA7.

| | Sample | Quartz | Plag | K | Musc/Illite | Kaolin | Chlorite | Calcite | Siderite | Fluorapatite | Pyrite | Rutile |
|---|---|---|---|---|---|---|---|---|---|---|---|---|
| Akkar Mbr | V1 | 53.10 | 20.12 | 2.40 | 9.34 | 3.06 | 9.30 | 0.00 | 2.68 | 0.00 | 0.00 | 0.00 |
| | V2 | 49.32 | 12.81 | 2.94 | 7.61 | 3.63 | 7.65 | 0.00 | 14.71 | 1.32 | 0.00 | 0.00 |
| Reke Mbr | V3 | 66.02 | 13.87 | 4.68 | 5.75 | 3.70 | 3.64 | 0.00 | 2.34 | 0.00 | 0.00 | 0.00 |
| | V4 | 62.71 | 16.68 | 5.28 | 5.94 | 4.30 | 3.96 | 0.00 | 1.13 | 0.00 | 0.00 | 0.00 |
| | V5 | 60.78 | 15.44 | 6.14 | 6.32 | 5.73 | 3.33 | 0.00 | 2.26 | 0.00 | 0.00 | 0.00 |
| | V6 | 62.15 | 17.67 | 2.49 | 6.62 | 3.81 | 5.18 | 0.00 | 2.08 | 0.00 | 0.00 | 0.00 |
| | V7 | 55.26 | 16.98 | 4.08 | 9.01 | 5.57 | 5.67 | 0.64 | 2.36 | 0.00 | 0.00 | 0.43 |
| | V8 | 66.36 | 12.46 | 7.38 | 5.12 | 4.71 | 1.89 | 1.98 | 0.10 | 0.00 | 0.00 | 0.00 |
| | V9 | 62.72 | 14.47 | 5.86 | 5.88 | 4.04 | 5.57 | 1.46 | 0.00 | 0.00 | 0.00 | 0.00 |
| | V10 | 56.24 | 12.88 | 10.31 | 8.80 | 6.71 | 3.92 | 0.38 | 0.75 | 0.00 | 0.00 | 0.00 |
| | V11 | 64.99 | 15.38 | 5.22 | 5.08 | 4.31 | 5.02 | 0.00 | 0.00 | 0.00 | 0.00 | 0.00 |
| | V12 | 31.20 | 14.16 | 7.65 | 3.29 | 8.27 | 0.00 | 32.90 | 2.53 | 0.00 | 0.00 | 0.00 |
| | V13 | 66.37 | 12.12 | 8.07 | 3.96 | 4.65 | 3.15 | 1.68 | 0.00 | 0.00 | 0.00 | 0.00 |
| | V14 | 55.37 | 14.27 | 9.63 | 9.54 | 5.39 | 5.09 | 0.71 | 0.00 | 0.00 | 0.00 | 0.00 |
| | V15 | 32.88 | 8.39 | 4.91 | 20.54 | 25.05 | 4.40 | 0.00 | 1.86 | 0.00 | 1.98 | 0.00 |
| Nordmela Fm | V16 | 93.96 | 1.50 | 0.00 | 0.61 | 2.01 | 0.21 | 1.42 | 0.00 | 0.00 | 0.28 | 0.00 |
| | V17 | 92.56 | 6.30 | 0.00 | 0.00 | 1.10 | 0.00 | 0.00 | 0.00 | 0.00 | 0.04 | 0.00 |
| Stø Fm | V18 | 92.22 | 5.89 | 0.56 | 0.00 | 0.27 | 0.00 | 0.58 | 0.00 | 0.08 | 0.40 | 0.00 |
| | V19 | 93.42 | 6.06 | 0.38 | 0.00 | 0.00 | 0.14 | 0.00 | 0.00 | 0.00 | 0.00 | 0.00 |
| | V20 | 97.58 | 0.00 | 0.59 | 0.00 | 0.76 | 0.27 | 0.80 | 0.00 | 0.00 | 0.00 | 0.00 |

**Table 3:** XRD results for Wisting Central III, normalized with respect to drill fluids (e.g. sylvite). Colours correspond to facies associations as seen on the sedimentary logs.

| | Sandstone Classification | | |
|---|---|---|---|
| | Quartz | Feldspar | Lithics |
| V1 | 66.96 | 18.50 | 14.54 |
| V2 | 59.61 | 16.75 | 23.65 |
| V3 | 55.00 | 16.67 | 28.33 |
| V4 | 58.80 | 17.17 | 24.03 |
| V5 | 61.44 | 16.10 | 22.46 |
| V6 | 64.90 | 19.71 | 15.38 |
| V7 | 62.98 | 21.15 | 15.87 |
| V8 | 60.94 | 20.60 | 18.45 |
| V9 | 60.63 | 22.17 | 17.19 |
| V10 | 64.25 | 16.91 | 18.84 |
| V11 | 59.73 | 21.27 | 19.00 |
| V12 | 50.54 | 23.66 | 25.81 |
| V13 | 63.52 | 21.03 | 15.45 |
| V14 | 60.00 | 16.89 | 23.11 |
| V16 | 92.59 | 2.78 | 4.63 |
| V17 | 90.28 | 6.02 | 3.70 |
| V18 | 94.47 | 4.15 | 1.38 |
| V19 | 97.82 | 1.75 | 0.44 |
| V20 | 92.92 | 4.87 | 2.21 |

**Table 4:** Relative proportions of quartz, feldspar, and lithics from point counting to plot on the QFL ternary diagram.

| | Sample | Very Angular | Angular | Sub-angular | Sub-rounded | Rounded | Very Rounded |
|---|---|---|---|---|---|---|---|
| Akkar Mbr. | V1 | 14 | 61 | 87 | 43 | 22 | 0 |
| | V2 | 12 | 57 | 77 | 39 | 18 | 0 |
| Reke Mbr | V3 | 7 | 33 | 111 | 61 | 23 | 5 |
| | V4 | 9 | 37 | 107 | 51 | 22 | 6 |
| | V5 | 7 | 45 | 109 | 49 | 21 | 5 |
| | V6 | 2 | 32 | 80 | 64 | 27 | 3 |
| | V7 | 4 | 35 | 75 | 68 | 23 | 4 |
| | V8 | 5 | 30 | 75 | 80 | 36 | 7 |
| | V9 | 4 | 29 | 71 | 84 | 31 | 2 |
| | V10 | 0 | 27 | 61 | 84 | 29 | 6 |
| | V11 | 0 | 29 | 68 | 80 | 34 | 10 |
| | V12 | 20 | 40 | 80 | 26 | 20 | 0 |
| | V13 | 0 | 30 | 72 | 83 | 40 | 8 |
| | V14 | 4 | 31 | 72 | 90 | 28 | |
| Nord. Fm. | V16 | 0 | 13 | 55 | 81 | 57 | 10 |
| | V17 | 0 | 13 | 65 | 83 | 50 | 5 |
| Stø Fm. | V18 | 0 | 11 | 48 | 82 | 67 | 9 |
| | V19 | 0 | 7 | 54 | 87 | 73 | 8 |
| | V20 | 0 | 11 | 50 | 86 | 70 | 9 |

**Table 5:** Angularity of framework grains from point counting. Colours correspond to facies associations as seen on the log.

| Strat. | Sample | Floating | Tangential | Long | Concavo-convex | Sutured |
|---|---|---|---|---|---|---|
| Akkar Mbr | V1 | 6 | 56 | 116 | 49 | 2 |
| | V2 | 9 | 44 | 84 | 66 | |
| Reke Mbr. | V3 | 15 | 71 | 102 | 50 | 2 |
| | V4 | 3 | 87 | 102 | 40 | 1 |
| | V5 | 6 | 45 | 107 | 75 | 3 |
| | V6 | 2 | 40 | 86 | 80 | 8 |
| | V7 | 7 | 52 | 87 | 60 | 2 |
| | V8 | 4 | 82 | 101 | 44 | 2 |
| | V9 | 3 | 76 | 105 | 31 | 6 |
| | V10 | 1 | 79 | 100 | 27 | |
| | V11 | 3 | 88 | 106 | 24 | |
| | V12 | 56 | 97 | 33 | | |
| | V13 | 2 | 91 | 107 | 30 | 3 |
| | V14 | 6 | 57 | 126 | 31 | 5 |
| Nord. Fm | V16 | 13 | 112 | 77 | 14 | |
| | V17 | 12 | 116 | 83 | 5 | |
| Stø Fm. | V18 | 12 | 104 | 80 | 17 | 4 |
| | V19 | 16 | 110 | 74 | 26 | 3 |
| | V20 | 8 | 114 | 82 | 22 | |

**Table 6:** Grain contacts.

| Strat. | Sample | High | Low |
|---|---|---|---|
| Akkar Mbr | V1 | 45 | 182 |
| | V2 | 47 | 156 |
| Reke Mbr | V3 | 70 | 170 |
| | V4 | 76 | 157 |
| | V5 | 64 | 172 |
| | V6 | 54 | 162 |
| | V7 | 35 | 173 |
| | V8 | 98 | 135 |
| | V9 | 95 | 126 |
| | V10 | 84 | 123 |
| | V11 | 90 | 131 |
| | V12 | 38 | 148 |
| | V13 | 95 | 133 |
| | V14 | 94 | 130 |
| Nord Fm. | V16 | 115 | 101 |
| | V17 | 122 | 94 |
| Stø Fm. | V18 | 130 | 87 |
| | V19 | 124 | 105 |
| | V20 | 136 | 90 |

**Table 7:** Grain sphericity.

# Appendix F

Summary of diagenetic processes inferred to have taken place in sandstones in Wisting Central III. Diagram applies primarily to the Fruholmen Formation. Jurassic sandstones are seen to almost exclusively contain evidence for quartz overgrowths, with an absence of most other diagenetic reactions below.

| STARTING MINERALS/ DIAGENETIC PROCESS | TEMPERATURE and PRODUCTS (degrees centigrade) 30 60 90 | OTHER PRODUCTS | SOURCE |
|---|---|---|---|
| Mechanical Compaction | | | Bjørlykke and Jahren (2015) |
| Carbonate Cement | | | Bjørlykke (2015) |
| Pyrite | | | Berner (1984) |
| Feldspar and Mica | Kaolinite | Silicic acid, K, Na, Ca ions | Bjørlykke (2015) |
| Volcanic Ash? | Smectite | Na, Ca, Fe, Mg, Si ions | Bjørlykke (2015) |
| Quartz Overgrowths | | | Bjørlykke and Jahren(2015) |
| Dioctahedral Smectite + K and Al ions | Illite | microquartz | Thyberg et al. (2010) McKinley et al. (2003) |
| Trioctahedral Smectite | Chlorite | quartz | McKinley et al. (2003) |
| Ferromagnesian Grains | Chlorite | | De Ros et al. (1994), Worden and Morad (2003) |

# Appendix G

XPL image from sample V12, which is calcite cemented. Note high angularity of grains, dominance of tangential contacts, and high IGV.

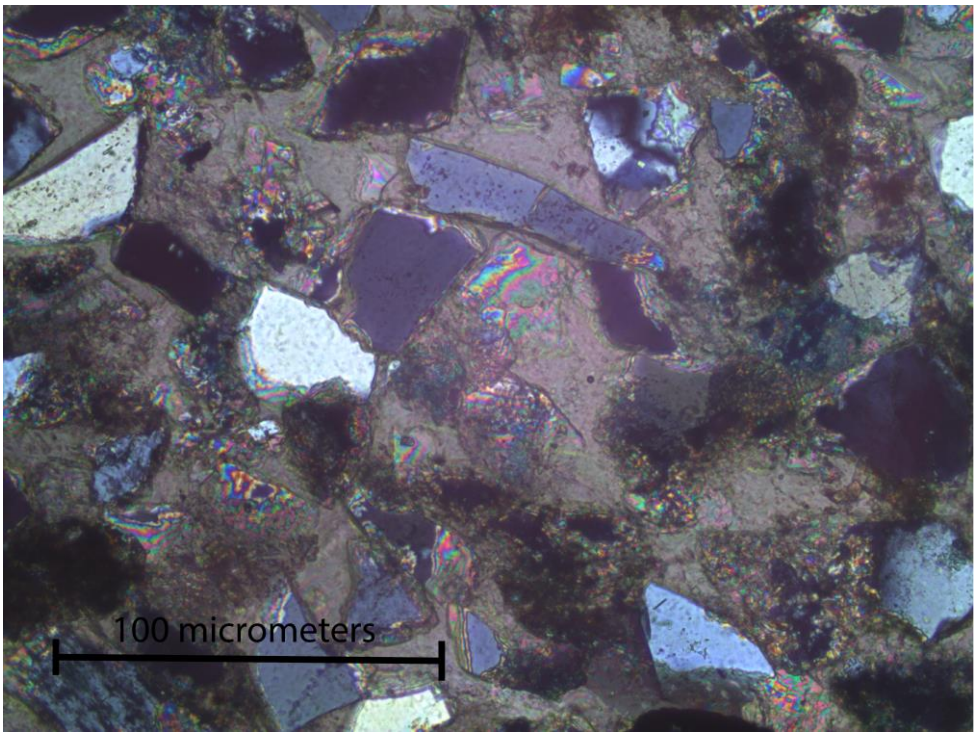

# Appendix H

XRD results demonstrating the higher kaolinite to feldspar ratio observed in the Fruholmen Formation of Gemini North as Compared to Wising Central III, discussed in section 6.3.1.1. Horizontal axis is the proportion of these components in the sample.

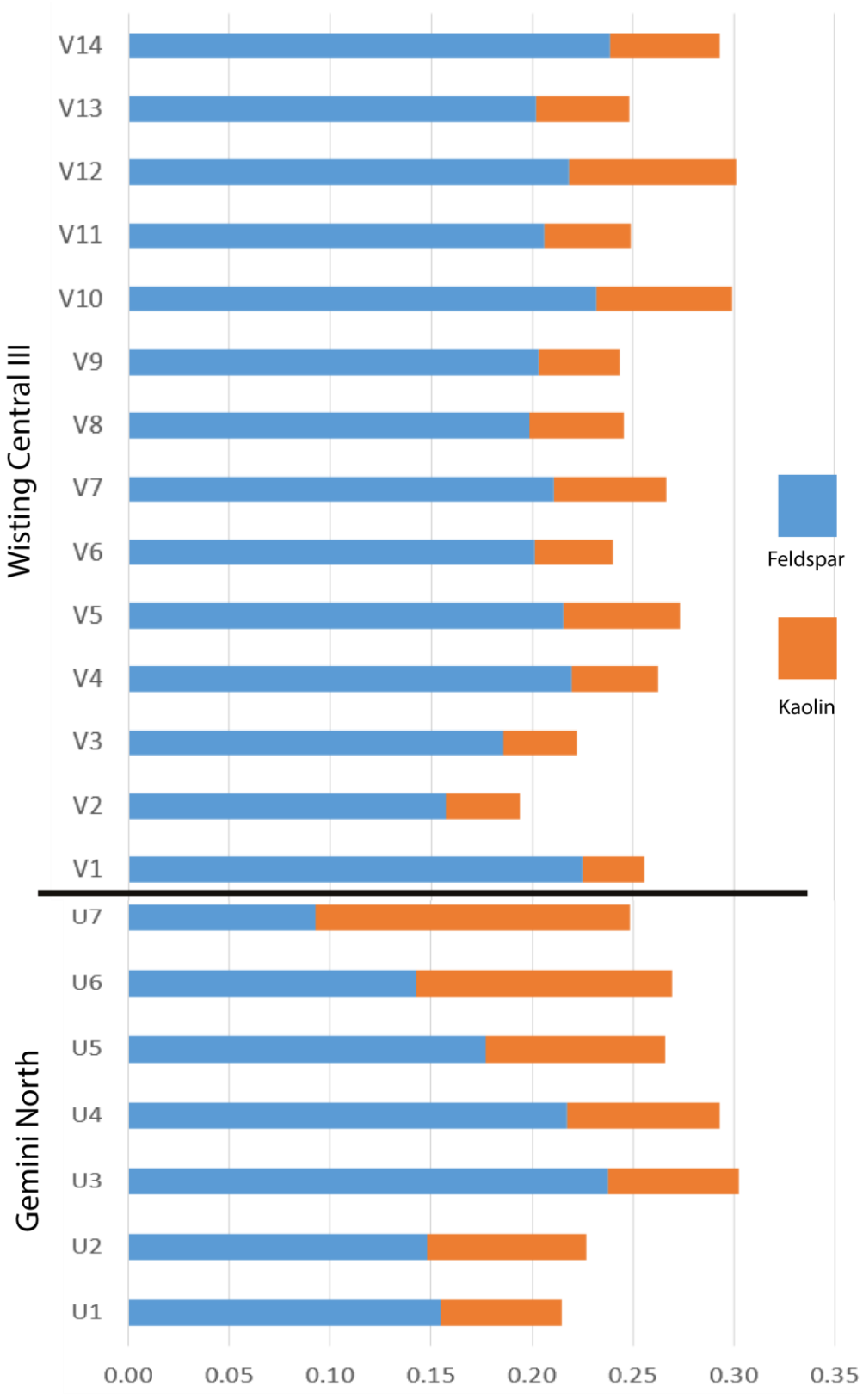

# Appendix I

Digital sedimentary logs prior to compression. Note that details such as sample number and oil content were added subsequent to compression, as such logs displayed here are very rudimentary. However they capture a higher resolution of details than the compressed log, especially with respect to sedimentary structures. The detailed log sheets from which these logs were derived upon can be found here:
https://drive.google.com/open?id=1zDMaAcD7Xqm83l7trHNt8LVLkRs0bHhZ

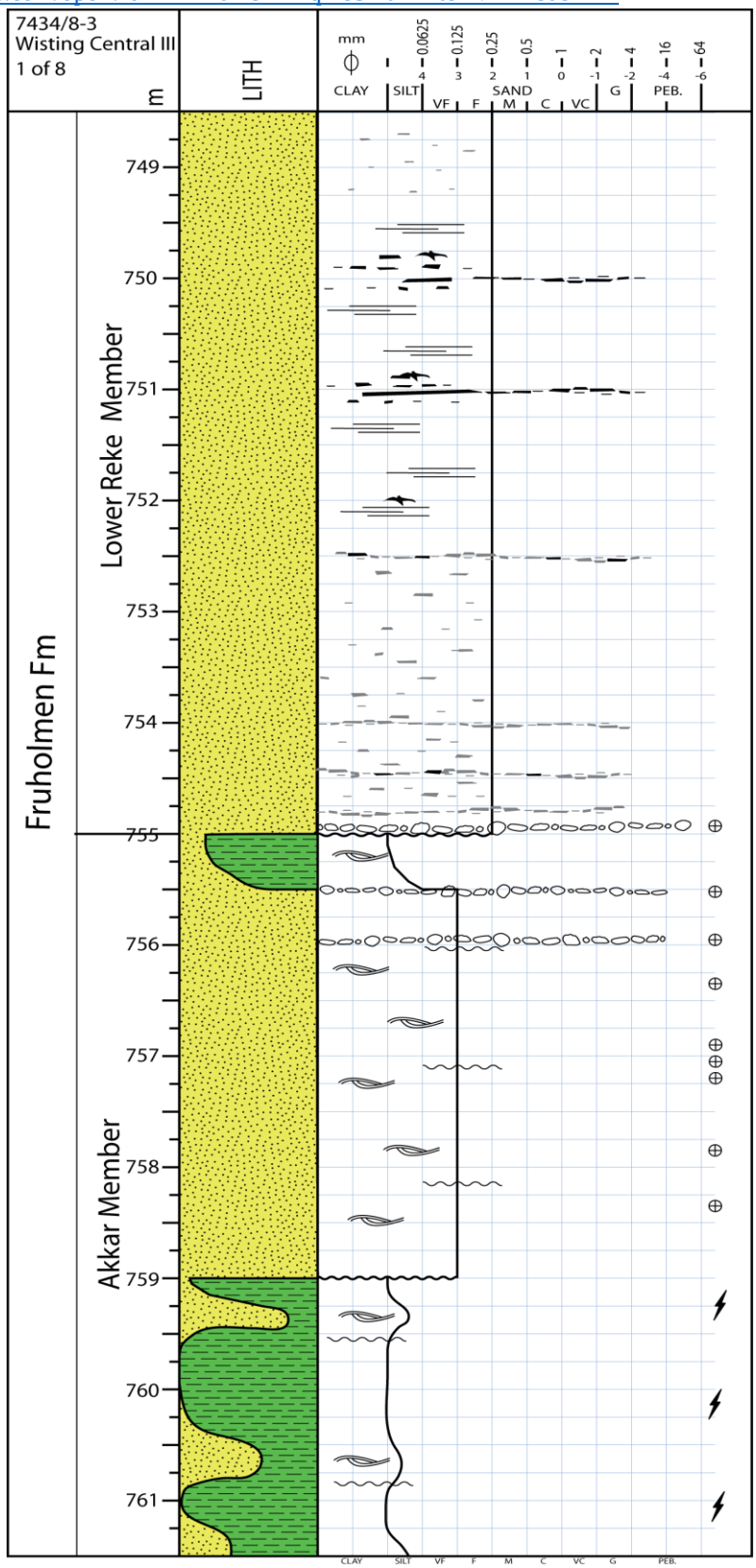

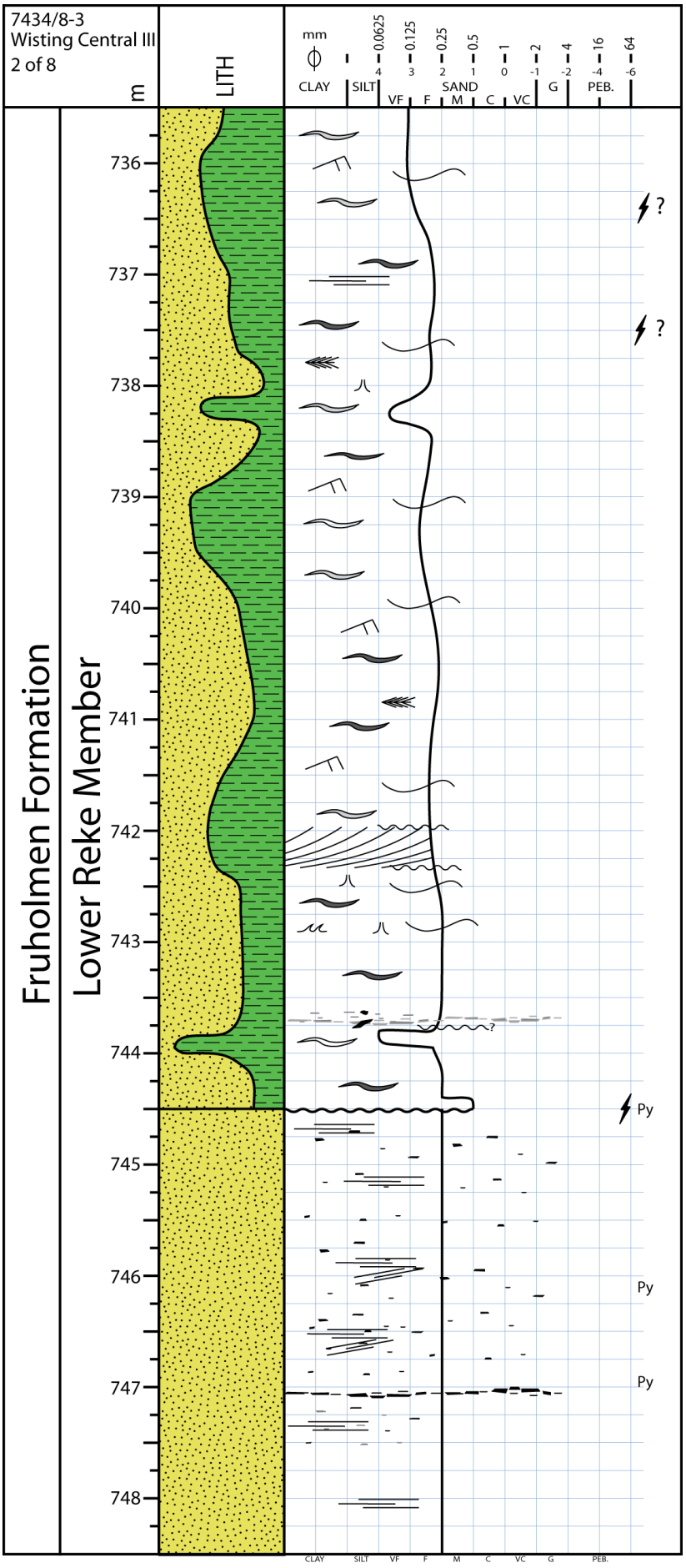
7434/8-3
Wisting Central III
2 of 8
m
LITH
mm
ϕ
0.0625
0.125
0.25
0.5
1
2
4
16
64
4
3
2
1
0
-1
-2
-4
-6
CLAY
SILT
SAND
VF
F
M
C
VC
G
PEB.
Fruholmen Formation
Lower Reke Member
736
737
738
739
740
741
742
743
744
745
746
747
748
?
?
?
Py
Py
Py

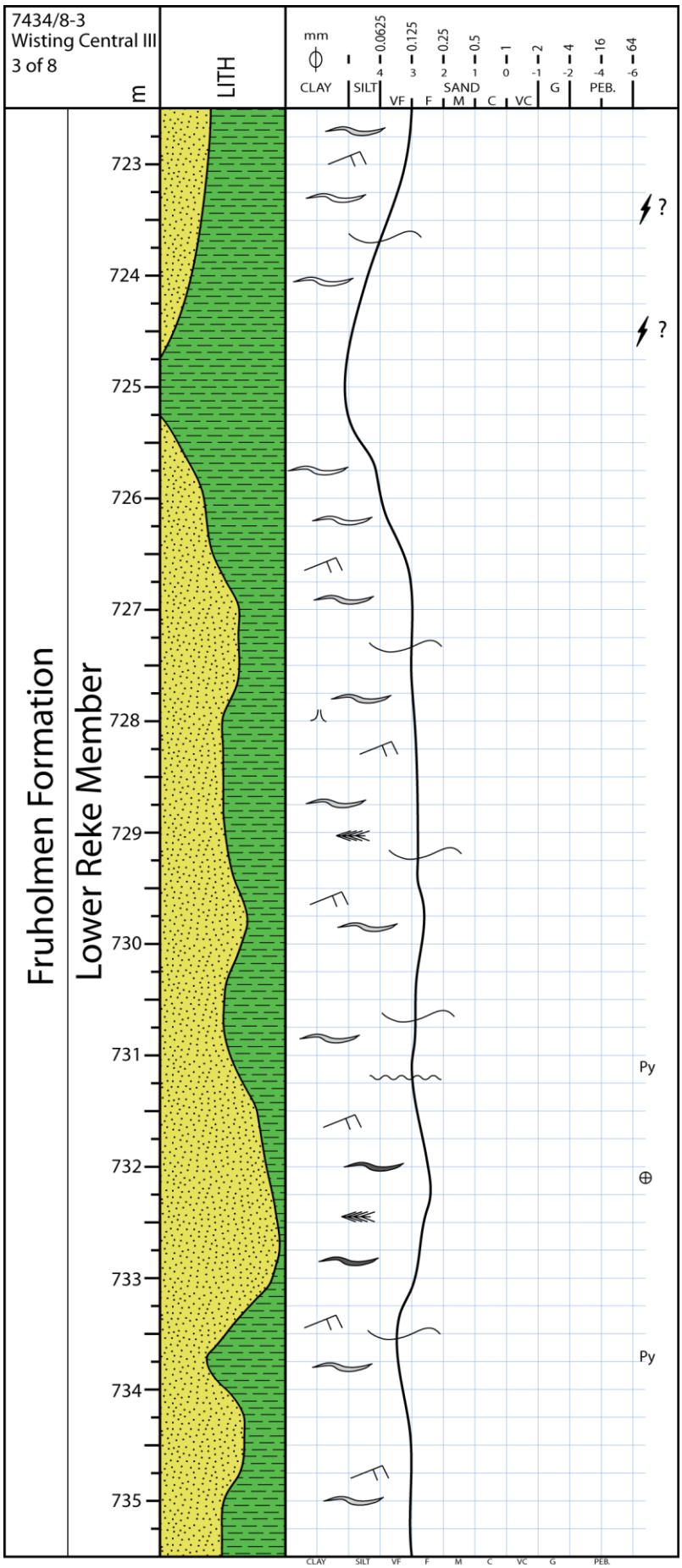
7434/8-3
Wisting Central III
3 of 8
m
LITH
mm
0.0625
0.125
0.25
0.5
1
2
4
16
64
CLAY
SILT
SAND
VF
F
M
C
VC
G
PEB.
723
724
725
726
727
728
729
730
731
732
733
734
735
Fruholmen Formation
Lower Reke Member
?
?
Py
Py

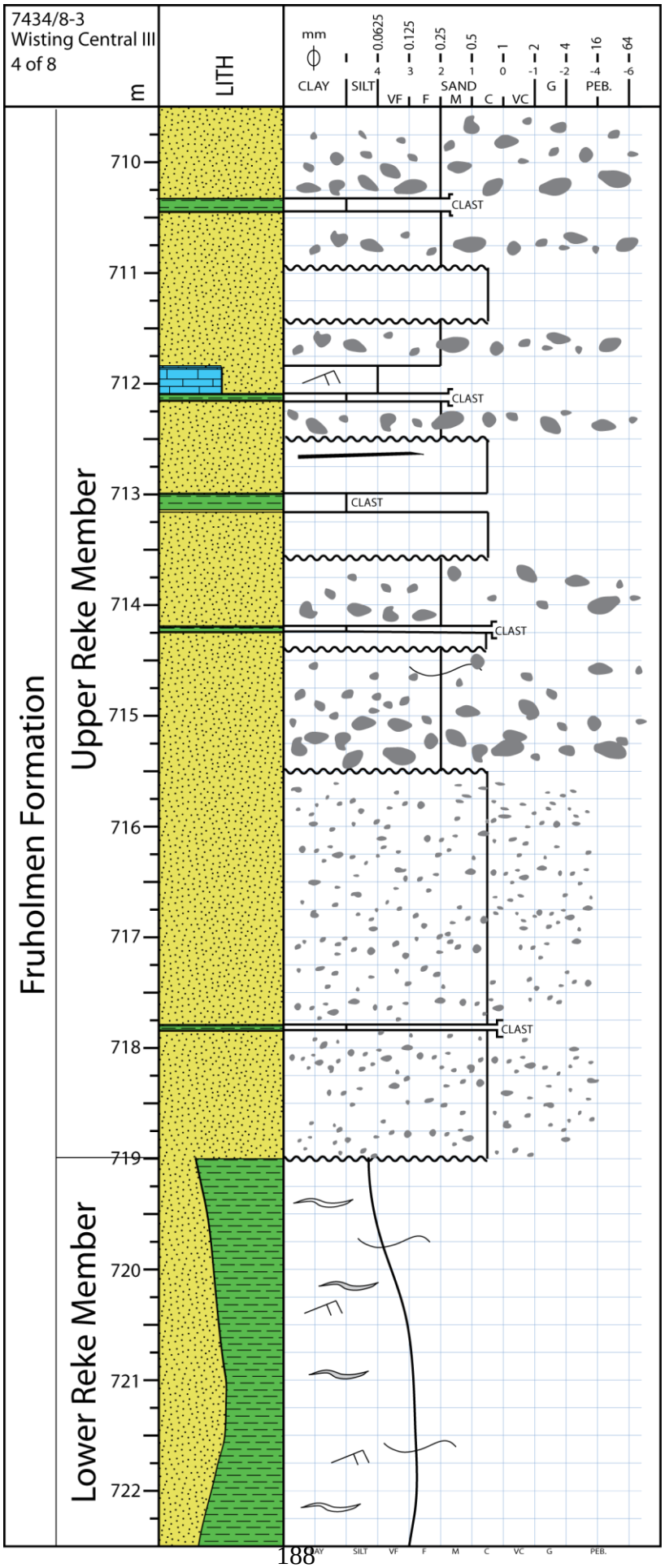
7434/8-3
Wisting Central III
4 of 8
m
LITH
mm
CLAY
SILT
SAND
VF
F
M
C
VC
G
PEB.
Fruholmen Formation
Upper Reke Member
Lower Reke Member
CLAST

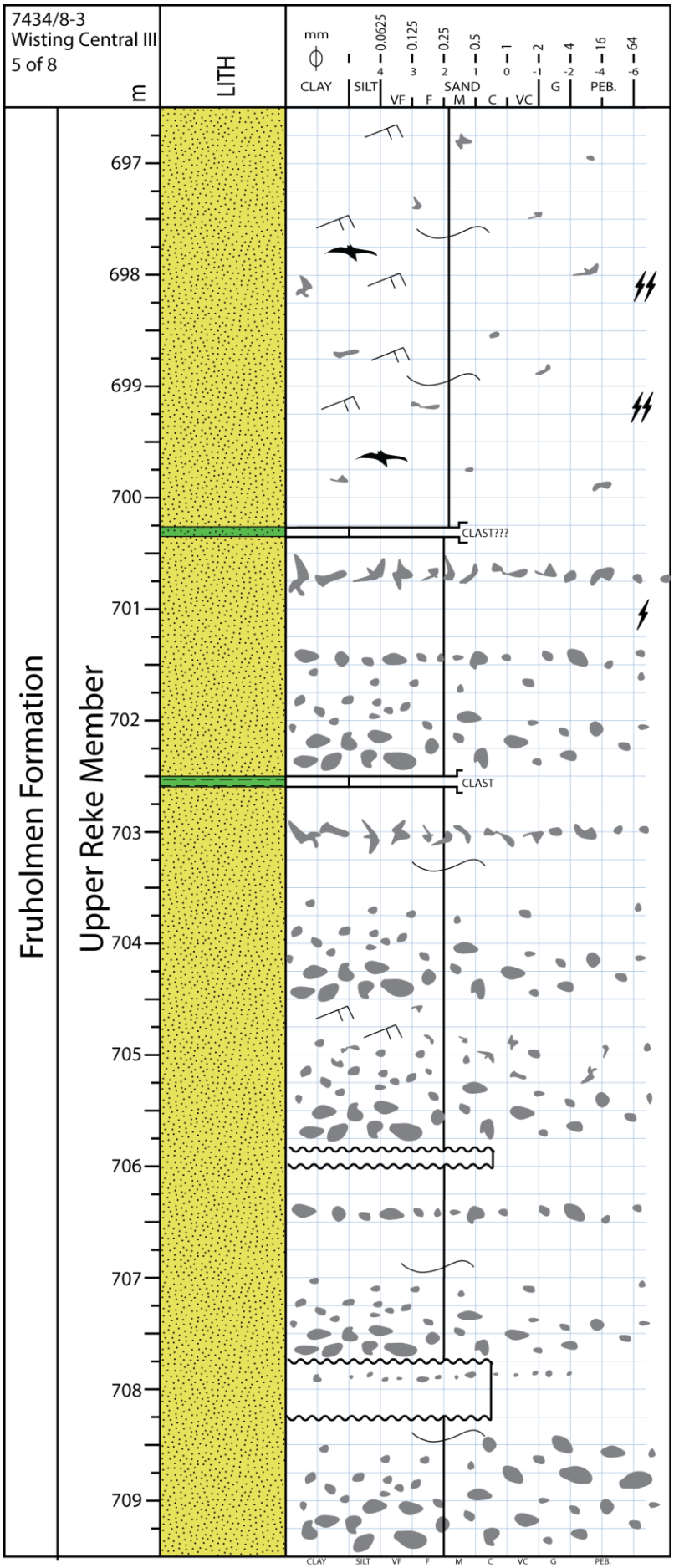
7434/8-3
Wisting Central III
5 of 8
m
LITH
mm
CLAY
SILT
VF
F
M
C
VC
G
PEB.
SAND
0.0625
0.125
0.25
0.5
1
2
4
16
64
697
698
699
700
701
702
703
704
705
706
707
708
709
CLAST???
CLAST
Fruholmen Formation
Upper Reke Member

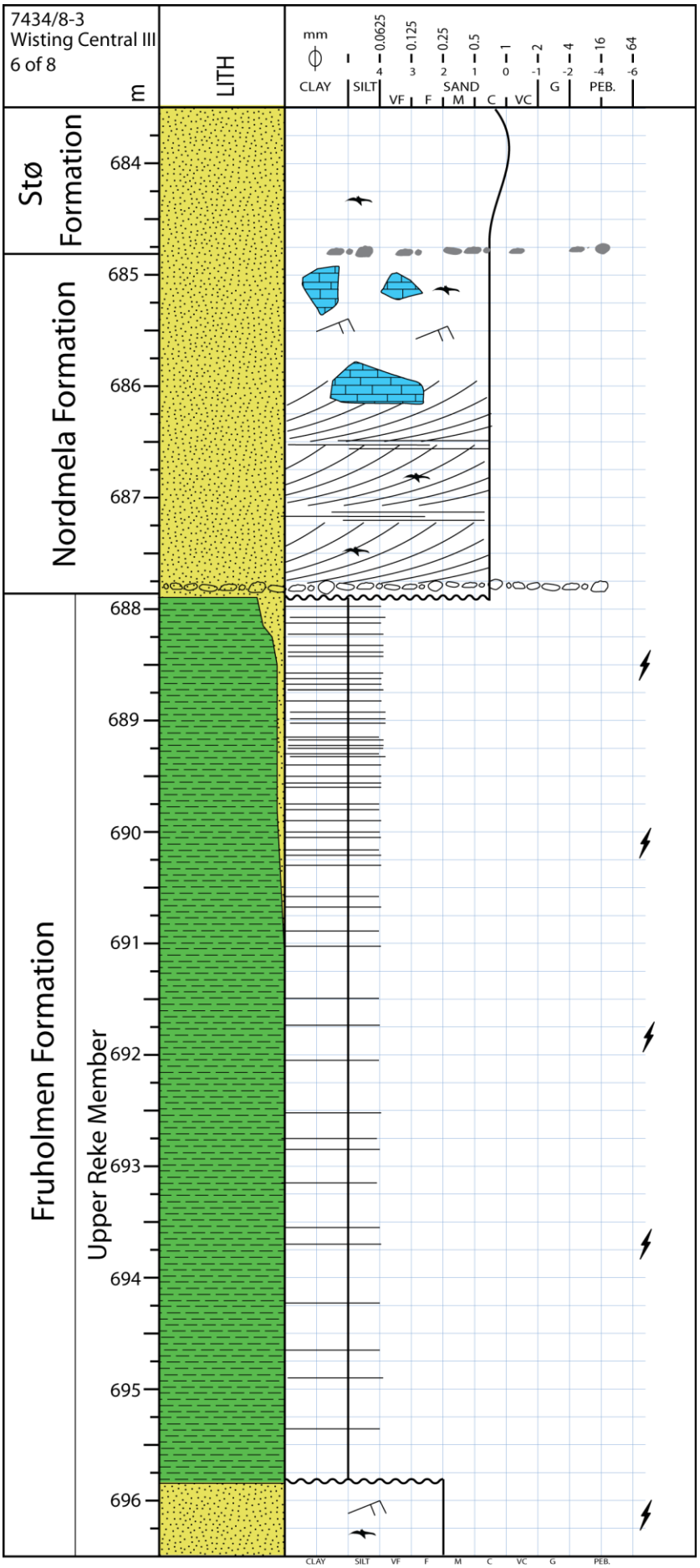
7434/8-3
Wisting Central III
6 of 8
m
LITH
mm
CLAY
SILT
SAND
VF
F
M
C
VC
G
PEB.
Stø Formation
Nordmela Formation
Fruholmen Formation
Upper Reke Member
684
685
686
687
688
689
690
691
692
693
694
695
696

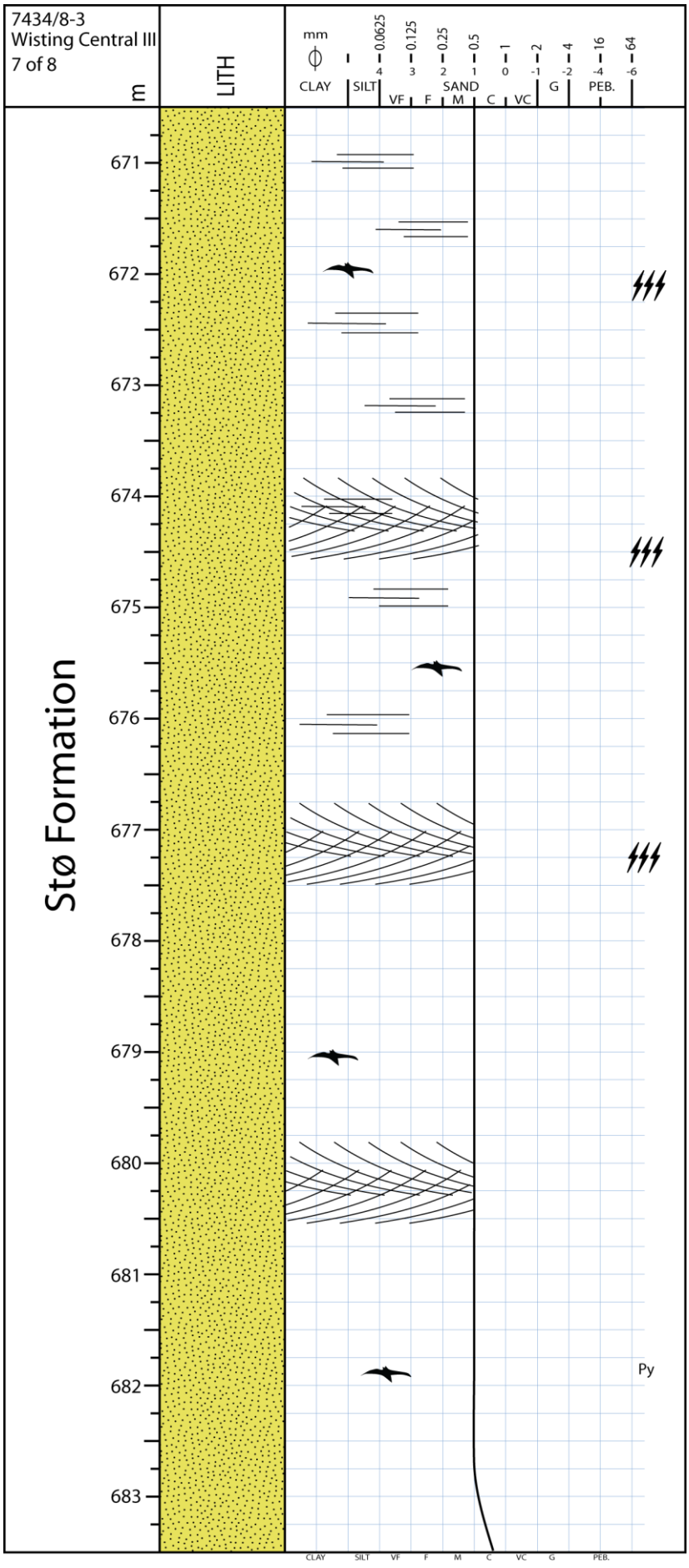
7434/8-3
Wisting Central III
7 of 8
m
LITH
mm
Φ
0.0625
0.125
0.25
0.5
1
2
4
16
64
CLAY
SILT
SAND
VF
F
M
C
VC
G
PEB.
671
672
673
674
675
676
677
678
679
680
681
682
683
Stø Formation
Py